VOLUME OF INTEREST IMAGING FOR IMAGE GUIDED RADIOTHERAPY

by

David D. M. Parsons

Submitted in partial fulfilment of the requirements
for the degree of Doctor of Philosophy

at

Dalhousie University
Halifax, Nova Scotia
April 2017

Table of Contents

LIST OF TABLES

LIST OF FIGURES

ABSTRACT

Image guidance has become a vital tool for accurate positioning and monitoring of a patient during radiation therapy. However, the current clinical standard is limited to a large static imaging field and constant x-ray tube current. In cone beam computed tomography (CBCT), this results in high scatter radiation and increased patient dose. During kilovoltage intrafraction monitoring of prostate patients with fiducial marker implants, this gives rise to periods of limited fiducial marker detectability. This work proposes a novel current-modulated volume-of-interest (VOI) approach to address these deficiencies and to improve the available image quality for image-guided radiation therapy (IGRT) with a considerably lower peripheral dose to the patient.

A series of three manuscripts form the foundation of this thesis. The first manuscript entitled, "*An investigation of kV CBCT image quality and dose reduction for volume-of-interest imaging using dynamic collimation*", demonstrates the advantages of a dynamic collimator approach for VOI CBCT, in which image quality is improved as imaging aperture decreases for a given dose to the VOI, with significant reductions in dose outside the VOI compared to full-field imaging. The second manuscript, "*Volume of Interest CBCT and tube current modulation for image guidance using dynamic kV collimation*", demonstrates how current modulation can be used in combination with VOI to further improve the available image quality for CBCT at a given dose to the VOI or maintain image quality at a reduced dose. The third and final manuscript, "*Current modulated volume-of-interest imaging for kilovoltage intrafraction monitoring of the prostate*", demonstrates how current modulated VOI can be used to provide constant intrafraction fiducial detectability for non-ideal imaging conditions (i.e. high kilovoltage attenuation and megavoltage scatter). The associated dosimetric trade-offs required for current modulation are also examined.

Overall, this thesis demonstrates that the current modulated VOI approach provides enhanced image quality for guidance in radiation therapy, while sparing tissue extraneous to the image guidance task of unnecessary dose. This is accomplished through quantitative measurement of contrast-to-noise ratio or fiducial position and corresponding Monte Carlo modeled dose distributions.

LIST OF ABBREVIATIONS AND SYMBOLS USED

1D	One dimensional
2D	Two dimensional
3D	Three dimensional
4D	Four dimensional
AAPM	American association of physicists in medicine
ADD	Axis-to-detector distance
AP	Anterior-posterior
CBCT	Cone beam computed tomography
CMVOI	Current modulated volume-of-interest
CNR	Contrast-to-noise ratio
CT	Computed tomography
CTV	Clinical target volume
$D_{95\%}$	Dose to 95% of the volume
$D_{99\%}$	Dose to 99% of the volume
DRR	Digitally reconstructed radiograph
DSB	Directional bremsstrahlung splitting
EBRT	External beam radiation therapy
ECUT	Electron transport cut-off energy
EGS	Electron gamma shower
FDK	Feldkamp Davis Kress
FFMCT	Fluence field modulated CT
GI	Gastrointestinal
GU	Genitourinary
ICRU	International Commission on Radiation Units and Measurements
ICRP	International Commission on Radiological Protection
IGRT	Image guided radiation therapy
keV	kiloelectron volt

KIM	kilovoltage intrafraction monitoring
kV	kilovoltage
kVp	Peak kilovoltage
Linac	Linear accelerator
mAs	milliampere-second
MeV	Megaelectron volt
MLC	Multileaf collimator
MU	Monitor unit
MV	Megavoltage
MVFFF	Megavoltage flattening filter free
NIST	National Institute of Standards and Technology
NRC	National Research Council of Canada
OBI	On-board imaging
PCUT	Photon transport cutoff energy
PMMA	Poly(methyl methacrylate)
PTV	Planning target volume
RF	Radiofrequency
RLP	Radiological path
SAD	Source-to-axis distance
SBRT	Stereotactic body radiation therapy
SDD	Source-to-detector distance
SI	Superior-inferior
SNR	Signal-to-noise ratio
SPR	Scatter-to-primary ratio
SSD	Source-to-surface distance
TCM	Tube current modulation
TPS	Treatment planning system
$V_{65\%}$	Volume receiving 65% of the prescribed dosimetric value
VMAT	Volumetric modulated arc therapy

VOI	Volume-of-interest
XML	Extensible markup language
Z	Atomic number

ACKNOWLEDGEMENTS

CHAPTER 1 INTRODUCTION

In Canada, cancer is the leading cause of all deaths at 74 361 and an incidence of approximately 196 900 in 2012[1, 2]. Globally in 2012, 14.1 million cases of cancer were diagnosed and 8.2 million deaths were recorded, with the incidence expected to eclipse 20 million per year by 2025[3].

Cancer is the general name for more than 100 diseases in which abnormal cells grow out of control and have the ability to infiltrate and destroy normal body tissue[4]. The three main treatment modalities are surgery, radiation therapy and chemotherapy. The course of treatment often depends on the site origin, histological consideration and the extent of disease, in which each treatment modality can be used concurrently. Currently, between 50% and 60% of patients diagnosed with cancer receive radiation therapy as part of their care[5, 6].

Radiation therapy utilizes ionizing radiation in an attempt to control or cure the disease or improve the symptoms of patients, through the damaging of DNA and subsequent cellular death. The objective is to deliver a precise dose of radiation to a defined target volume while delivering as low of a dose as reasonably achievable to the surrounding healthy tissue, with the goals of eradicating the malignant cells with minimal side effects. This branch of medicine is known as radiation oncology.
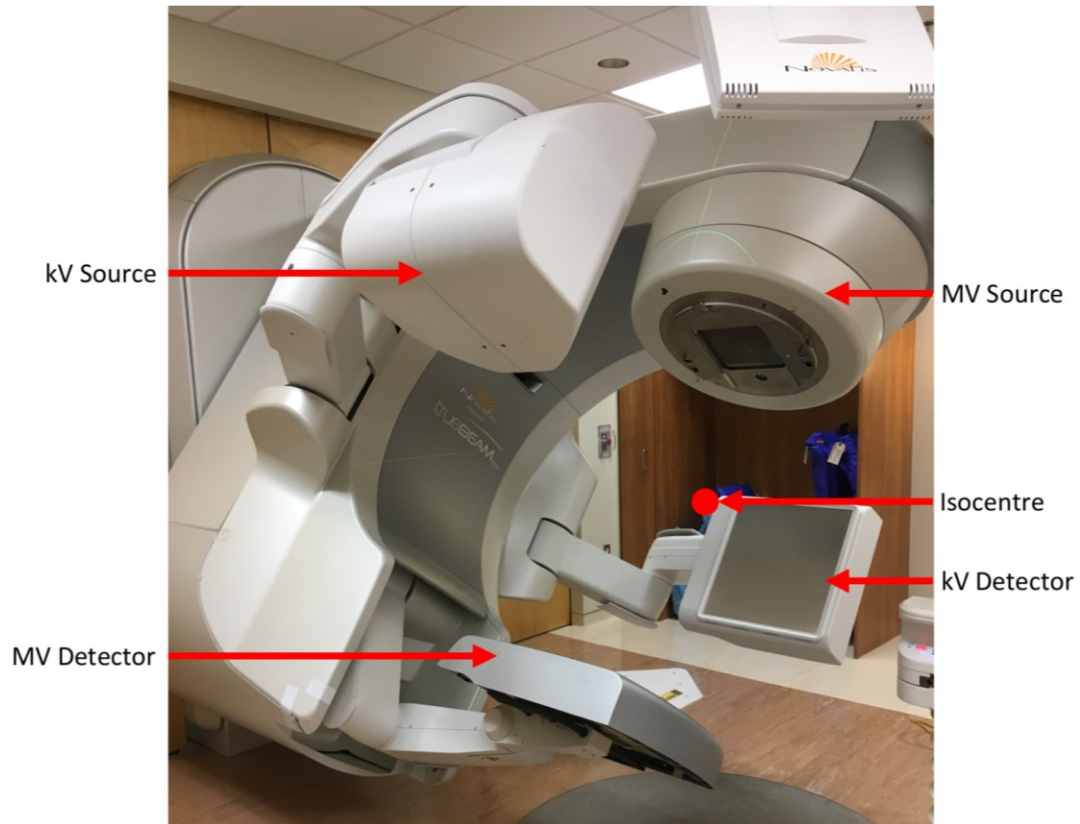
Figure 1.1   Picture of the TrueBeam STx linear accelerator platform (Varian Medical Systems, Inc., Palo Alto, CA) at the Nova Scotia Health Authority, highlighting the MV and kV systems as well as the approximate location of isocentre.

For the purposes of this work, radiation is delivered from an x-ray source external to the patient. This is known as teletherapy or external beam radiation therapy (EBRT). This is commonly achieved through the acceleration of electrons in a medical linear accelerator (linac, Figure 1.1) and colliding them on a high atomic number (Z) target to produce megavoltage (MV) bremsstrahlung photons. One technique to deliver a precise dose of radiation is known as volumetric modulated arc therapy (VMAT). In this technique, the photon beam is collimated using jaws and a multi-leaf collimator (MLC) and modulated

as the linac rotates about the patient. Thus, sharp dose gradients are produced at the

interface between the target volume and healthy tissue (Figure 1.2).
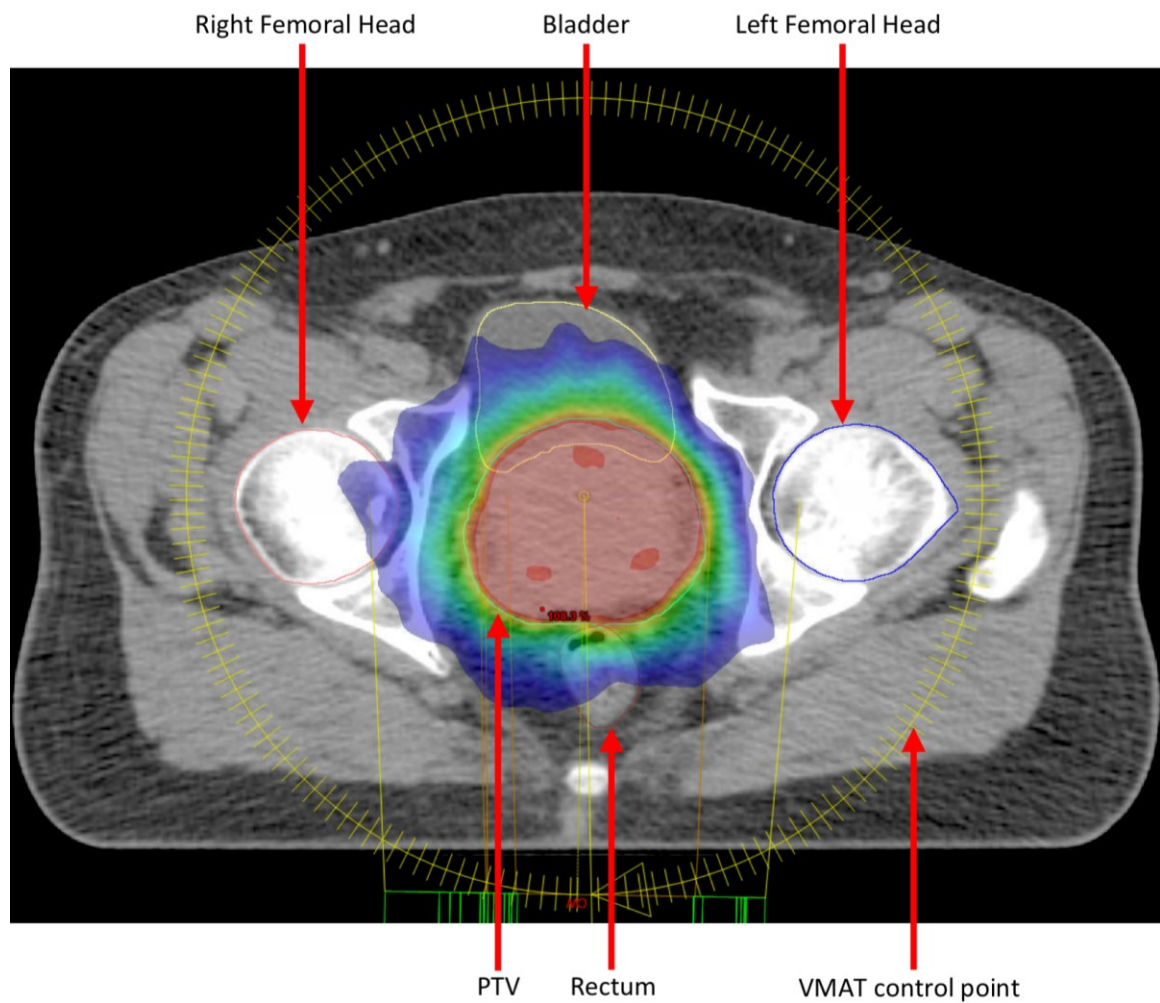
Figure 1.2   VMAT dose distribution for a patient with prostate cancer. The planning target volume (PTV) and surrounding organs at risk (OAR) are highlighted. The dose wash ranges from 50% to 100% of the prescription dose. The lines intersecting the yellow circle represent a VMAT control point. Each control point contains a unique MLC and jaw pattern as well as the number of monitor units (MU) to deliver.

Due to the focal nature of EBRT and the variation in target position between or during treatments (inter- or intrafraction motion), localization of the target volume prior to, and during treatment delivery is crucial. Further, as a result of the high dose gradients created, misalignment of the patient by as low as just several millimeters could result in severe complications. This is especially important for hypofractionated radiation therapy, i.e., where the number of treatment fractions is greatly reduced and the dose per fraction is increased, relative to those used in conventionally fractionated radiation therapy. The current standard to achieve alignment of the target volume is kilovoltage (kV) imaging prior to treatment, either using orthogonal planar image pairs or cone beam computed tomography (CBCT) with comparison to digitally reconstructed radiographs (DRR) or the computed tomography (CT) image set that was used in treatment planning, respectively. This may be achieved through the use of on-board imaging (OBI), an auxiliary system on a linear accelerator which includes a kV x-ray beam line placed orthogonal to the MV treatment beam line (Figure 1.1). A kV photon beam (photon energies ranging from 25 to 140 keV) is preferred for imaging compared to an MV photon beam (photon energies up to 6 MeV for 6 MV) due to the increased probability of photoelectric compared to Compton interactions (Figure 1.3). This difference in image quality is demonstrated in Figure 1.4 for a 6 MV and 125 kVp projection of the ATOM head phantom (701-A, Computerized Imaging Reference Systems, Inc., Norfolk, VA). The approach of adjusting patient position based on images acquired *in situ* is referred to as image guided radiotherapy (IGRT).
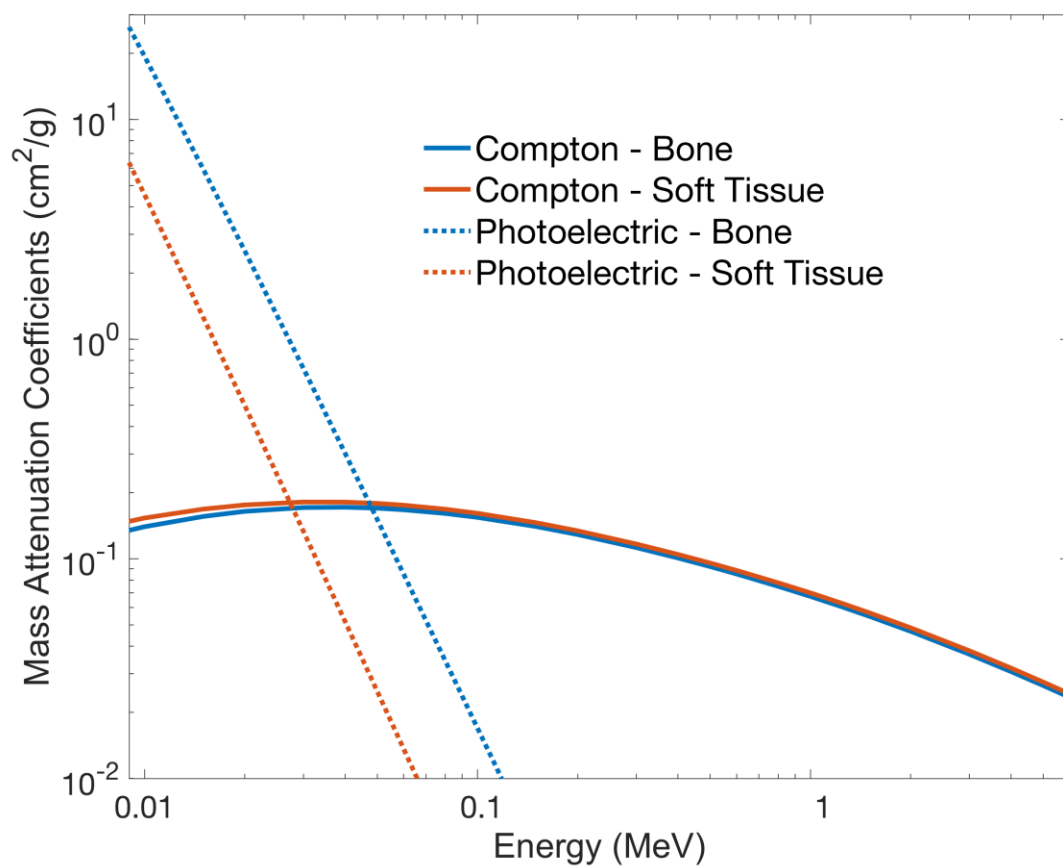
Figure 1.3   Mass attenuation coefficients for Compton and Photoelectric interactions in bone and soft tissue as a function of photon energy.

6 MV　　　　　　　　　　　　　　**125 kVp**
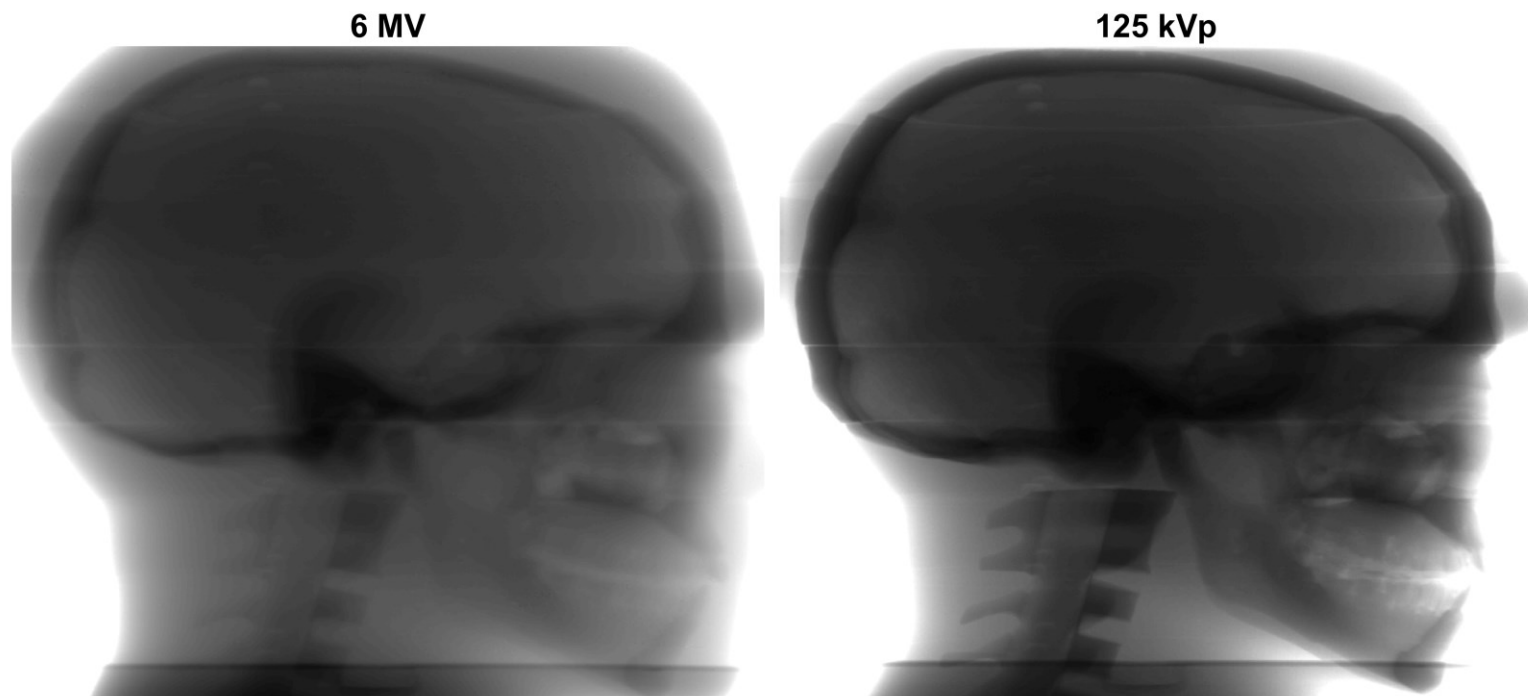
Figure 1.4　　　6MV and 125 kVp projection image on the ATOM head phantom, acquired on a TrueBeam platform.
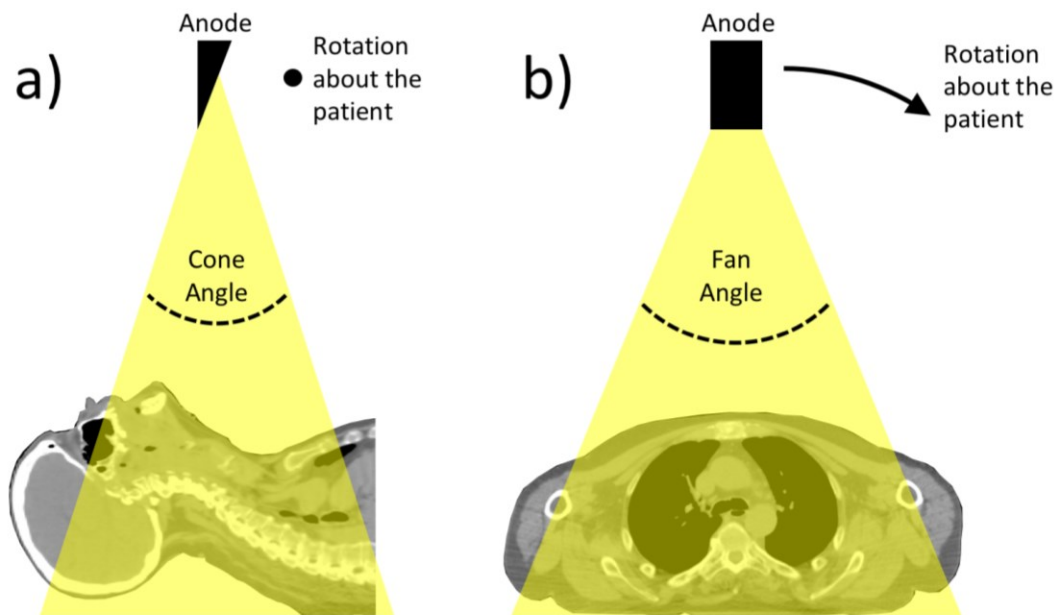
Figure 1.5   CBCT geometry describing the a) cone and b) fan angles relative to the patient and axis of rotation.

1.1   VOLUMETRIC IMAGING IN RADIATION THERAPY

1.1.1   CONE BEAM COMPUTED TOMOGRAPHY

The first integration of a kV image system on a MV linac was demonstrated in 1999 by Jaffray *et al*.[7] However, the image contrast-to-noise ratio (CNR) was low for CBCT compared to traditional fan-beam CT (Figure 1.5) due to the higher scattered photon population, which is enhanced by the larger field of view. Siewerdsen and Jaffray[8] initially characterized the magnitude and effects of scattered photons on CBCT image quality. This was demonstrated by varying the cone angle from 0.5° to 10.5° while keeping the fan angle constant at either 14° or 22° for the same imaging parameters. The phantom

consisted of a water-filled, 11 cm diameter cylinder, surrounded by slabs of poly(methyl methacrylate) (PMMA), with bone or breast tissue equivalent inserts. Siewerdsen and Jaffray[8] demonstrated that as the thickness of tissue or cone angle increases scatter-to-primary photon ratio (SPR) increases as well. Similar to a fan-beam geometry, for small cone angles (less than 1.6°) more scatter is produced towards the periphery compared to the centre of the detector plane. This is due to attenuation of secondary photons (for phantom diameters greater than μ^{-1})[9] toward the center of the detector plane. However, for large cone angles (greater than 1.6°), scatter is greatest toward the center of the detector plane. This is due to the contribution of scattered photons generated outside the central imaging plane. The practical consequence is the introduction of more severe shading artifacts as scatter increases.

Methods to reduce the effects of scatter involve a combination of increased separation between the patient and detector, anti-scatter grids and model based corrections[10, 11]. These methods attempt to reduce the amount scatter reaching the detector or subtracted the scatter from the image. Neither of these approaches reduces the amount of scatter generated in the patient and associated imaging dose. However, in 2007 Chen *et al.*[12] demonstrated the feasibility of using a truncated field that acquired information in a volume-of-interest (VOI) for breast CBCT. Chen *et al.*[12] used a static copper plate with a 2.4 cm diameter opening as a collimator to attenuate the beam outside the VOI. As a result of the reduced fan and cone angle, the scatter contribution was reduced by approximately a factor of 7.3 inside the VOI compared to full-field, which in turn increased CNR by a factor of 1.45. The decrease in scatter generation also reduced

the dose within the VOI by a factor of 4.4 compared to full-field. This was in addition to the significant dose reduction observed outside the VOI, up to a factor of 24.9 out of plane. Lai *et al.*[13] expanded this work by providing information outside the VOI at a reduced image quality. A two-acquisition approach was used, in which a first image set was acquired using low exposure full-field and followed by a high exposure VOI image set. The exposure ratio between full-field and VOI ranged between 1:20 and 1:3.9. A composite image set was then produced and used for reconstruction, in which the full-field data replaced the collimated information outside the VOI. Using this technique, Lai *et al.*[13] observed a similar SPR reduction by a factor 6.6 and 10.3 for an 11 and 15 cm diameter polycarbonate phantom, respectively. However, as a result of the two acquisitions dose reduction was inferior compared to that reported by Chen *et al.*[12], with reductions being limited to a factor of 1.2 to the VOI compared to full-field (for an exposure ratio of 1:3.9) and a reduction of 2.7 to the periphery. Similarly, Kolditz *et al.*[14] have developed a two arc VOI technique for C-arm CBCT, using a static collimator and two isocentres, one arc for a low exposure full field acquisition with less projections and the second for a high exposure collimated VOI acquisition. A lengthy process was used to combine the two image sets that involved reconstructing the full-field acquisition, followed by forward projection using the VOI geometry. Thereafter, the VOI and full-field projections were weighted and combined. Kolditz *et al.*[14] demonstrated that an integral dose reduction of 93.1% was possible while maintaining equivalent noise and spatial resolution as a full-field acquisition. Cho *et al.*[15] demonstrated a similar approach: instead of two acquisitions, the collimator allowed for partial attenuation outside the VOI within

9

the fan angle, while still fully attenuating superior-inferiorly, within the cone angle. This offered a high quality VOI image and low quality outside, with CNR improvement in the VOI increasing with collimator thickness and atomic number.

The VOI approach has also been implemented and functionality extended to allow imaging of arbitrary shaped and located VOI using an MV beam line. Robar *et al.*[16] developed a dynamic collimation VOI method using the MLC in a linac with a 2.35 MeV electron beam incident on a carbon target[17]. In this work, the MLC was used to track an arbitrarily VOI throughout the rotation of the linac, in a fashion analogous to dynamic conformal arc radiotherapy. To minimize the truncation artifact at the boundary of the VOI caused by the near complete attenuation (less than 2% transmission) outside the VOI by the MLC, two methods were investigated. The first used DRRs calculated in the treatment planning system (TPS) to fill information outside the VOI. The second extrapolated the data beyond the boundary of the VOI to apodize projection data. Both methods resulted in minimization of the truncation artifact, with extrapolation being more efficient and obviating the need for *a priori* data from the treatment planning CT. Similar to the kV implementation, dose was reduced inside and outside the VOI by factors of 1.15 and 1.70, respectively, compared to full-field for equivalent number of monitor units. However, unlike kV no improvement in CNR or noise was observed compared to full-field. This is likely attributed to the low-Z spectrum, which, compared to a kV beam, features a low, and thus favourable, SPR. Leary and Robar[18] further expanded this concept to modulate the collimation throughout the acquisition to allow high and low exposures corresponding to central and peripheral VOIs, respectively. This resulted in a

higher dose and image quality in the central VOI, with reduced CNR and dose to the peripheral VOI. Similarly, Szczykutowicz *et al.*[19] implemented this concept on a tomotherapy unit using the 3.5 MV beam and the binary MLC.

It is clear that the VOI approach results in significant dose reductions and when implemented with a kV system, image quality can be improved as well. However, the use of static rectangular fields for either cone beam CT or planar imaging generally delivers unnecessary peripheral dose to anatomy that is not relevant to the image guidance task. The first objective of this thesis is to develop a dynamic collimator for kV VOI CBCT. This will remove the aperture limitations of previous static kV collimators used for VOI CBCT and similar to MV implementations, the collimator will be able to track a variety of arbitrarily located VOIs. This will greatly expand the VOI approach, in which non-cylindrical VOIs can be acquired eccentric to the axis-of-rotation, with expected improved kV image quality compared to the full-field approach. This implementation is hypothesized to have the benefits of improved dose reduction and increased image quality. Additionally, we propose to leverage the dose reduction to the VOI to further improve image quality, in which equivalent doses as the full-field implementation can be delivered to the VOI.

1.1.2 FLUENCE MODULATION IN CBCT

The MV VOI implementations may be considered a simple form of fluence field modulated CT (FFMCT). Bartolac *et al.*[20] initially described a framework for FFMCT, in which the fluence distribution is optimized as a function of angle to meet prescribed

image quality and dose objectives to various VOI in the patient. Various groups have since begun development on apparatus which can implement FFMCT. Szczykutowicz and Mistretta[21–23] described an approach in which fluence is modulated for CBCT. This is achieved by ten overlapping iron wedge pairs creating a piecewise-constant dynamic attenuator. By modulating fluence as a function of projection angle and wedge position, Szczykutowicz and Mistretta[21–23] have demonstrated that this technique is capable of decreasing dose and image noise while providing regions of high signal-to-noise ratio (SNR) compared to unmodulated CBCT.   Similarly for CT, Hsieh *et al.*[24] and Hsieh and Pelc[25] have described a piecewise-linear dynamic attenuator using two sets of abutting triangular wedges composed of iron, one offset laterally from the other by half of the triangle base. With this fluence could be modulated as a function of position and projection angle, resulting in a decrease in dose and a more uniform noise distribution for equivalent peak voxel noise as standard CT.

Attenuation based tube current modulation (TCM), which has widely been used in CT for the last several decades[26–30], is considered a simplistic form of fluence modulation. TCM alters the fluence as a function of beam angle in accordance with the amount of attenuation at that angle, and therefore can take into account the geometry of the patient during imaging. This ideally minimizes the variation of total fluence at the detector plane over all projection angles. However, the implementation of TCM in full-field CBCT has yet to be fully implement on the clinical system. However, the combination of TCM and VOI may be suitable in the context of CBCT as the FOV solid angle approaches that for fan-beam CT.

12

The second objective is to enhance the VOI approach using TCM. The introduction of TCM for VOI CBCT is hypothesized to reduce noise (thereby improving CNR) by reducing the variation in projection SNR for approximately equivalent x-ray tube milliampere-second (mAs) and dose. Additionally, similar to work of Greese et al.[26] for TCM in CT, the image quality for current modulated VOI should be similar to an unmodulated VOI acquired with a reduced total mAs and dose. This could be further expanded to improve image quality, by acquiring the modulated approach with equal total mAs as the unmodulated acquisition. Additionally, this completed work can be applied to kV projection imaging used for intrafraction monitoring of patient motion.

1.2   INTRAFRACTION IMAGING IN RADIATION THERAPY

Prostate cancer is currently the first most common cancer in men with an incidence and mortality of approximately 1.1 million and 307 000, respectively, in 2012[3]. The percentage of prostate patients treated with radiation therapy ranges between 25% to 48%, depending on disease severity, age and comorbidity as well as personal preference[31]. Pisansky et al.[32] reported a clinical disease free survival at five years of 97% and 91% for low and intermediate risk prostate patients treated with at least 35 fractions of 2 Gy. Separately, Zelefsky et al.[33] reported gastrointestinal (GI) and genitourinary (GU) late grade 3 toxicities or greater in 0.5% of patients treated IMRT (45 fractions of 1.8 Gy). In traditional fractionation schemes (greater than ten fractions, e.g.), the assumption has been that the consequence of geographic miss during a single fraction is limited by the low dose per fraction (approximately 2 Gy). However, as the number of fractions is

decreased (and dose increased) the consequences of a geographic miss appreciably increase. Prostate cancer has become an interesting indication for hypofractionation due to a low α/β ratio of approximately 1.5 Gy[4, 34, 35] compared to α/β of 4 to 6 Gy[4, 34] for the proximal organs at risk of bladder and rectum. As demonstrated in Figure 1.6, this scenario suggests a greater therapeutic ratio for a reduced number of fractions with a larger dose compared to conventional 2 Gy fractionation for cancers with an α/β of 10 Gy[4].
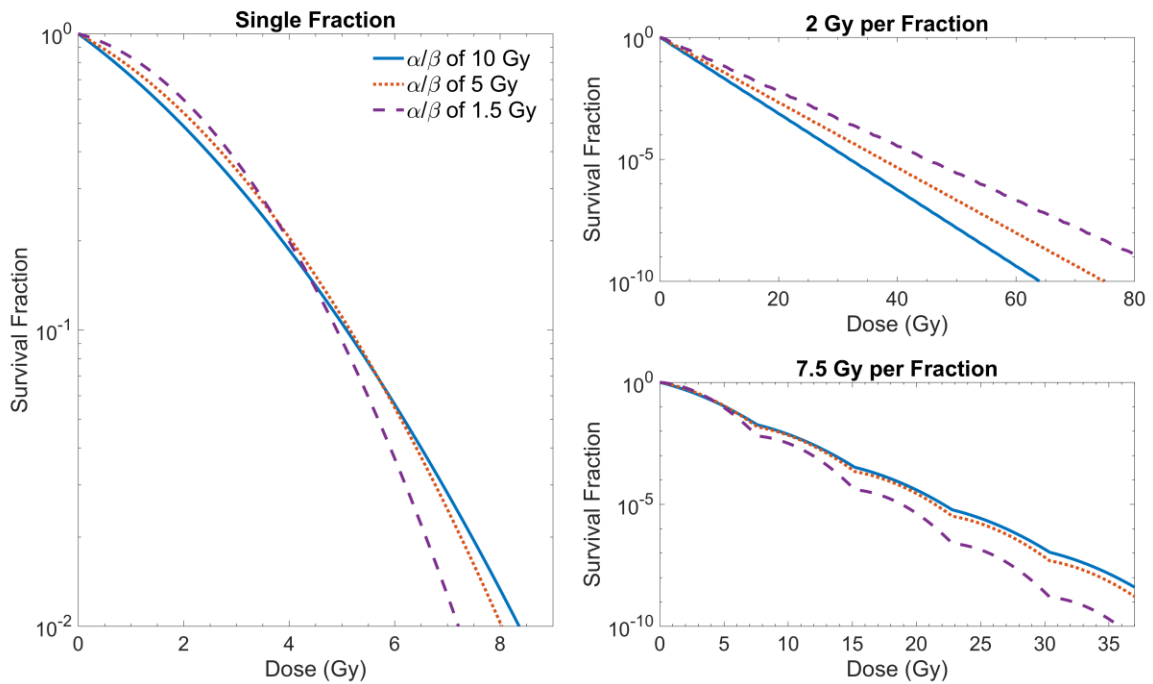
Figure 1.6   Survival fraction for tissues with an α/β ratio of 1.5, 5 and 10 Gy for a single fraction. Fractionated survival fraction demonstrated for 2 and 7.5 Gy per fraction (assuming no repopulation or repair).

Additionally, the benefit of hypofractionation relative to conventional can be observed in the biologically effective dose (BED)

$$BED = nd\left(1 - \frac{d}{\alpha/\beta}\right)$$ Eq 1.1

where n is the number of fractions and d is the dose per fraction. As reported in Table 1.1, a hypofractionation (7.5 Gy with five fractions) scheme increases the effective dose to the prostate by a factor of 1.2 and similarly decreases the effective dose to the rectum and bladder by a factor of 1.2 compared to a conventional 2 Gy per fraction scheme with 40 fractions.

Table 1.1   Biologically effective dose for prostate and rectum for conventional (2 Gy with 40 fractions) and hypofractionation (7.5 Gy with 5 fractions) schemes.

Organ/Cancer (α/β)	2 Gy (40 fractions)	7.5 Gy (5 fractions)
Prostate cancer (1.5 Gy)	187 Gy	225 Gy
Rectum/bladder (5 Gy)	112 Gy	94 Gy

However, the prostate can be relatively mobile, motion is the result of the force of the bladder and rectum pushing against the prostate[36]. This varies due to the amount of filling in the bladder and rectum, and displacement can exceed 1-2 cm for prolong periods of time relative the position of the planning CT[37]. Prostate motion can be categorized into six groups: stable, continuous drift, transient excursion, persistent excursion, high frequency excursion and erratic[38]. As demonstrated in Figure 1.7, the types of motion possible for a prostate have an extensive range. Langen *et al.*[37] have reported that for 550

monitored prostate fractions, one-third were never displaced more than 3 mm from baseline, with only 13.2% of the total time (for all fractions) displaced more than 3 mm from the initial setup position. However, as demonstrated this is motion during a single fraction can be substantial and volatile.
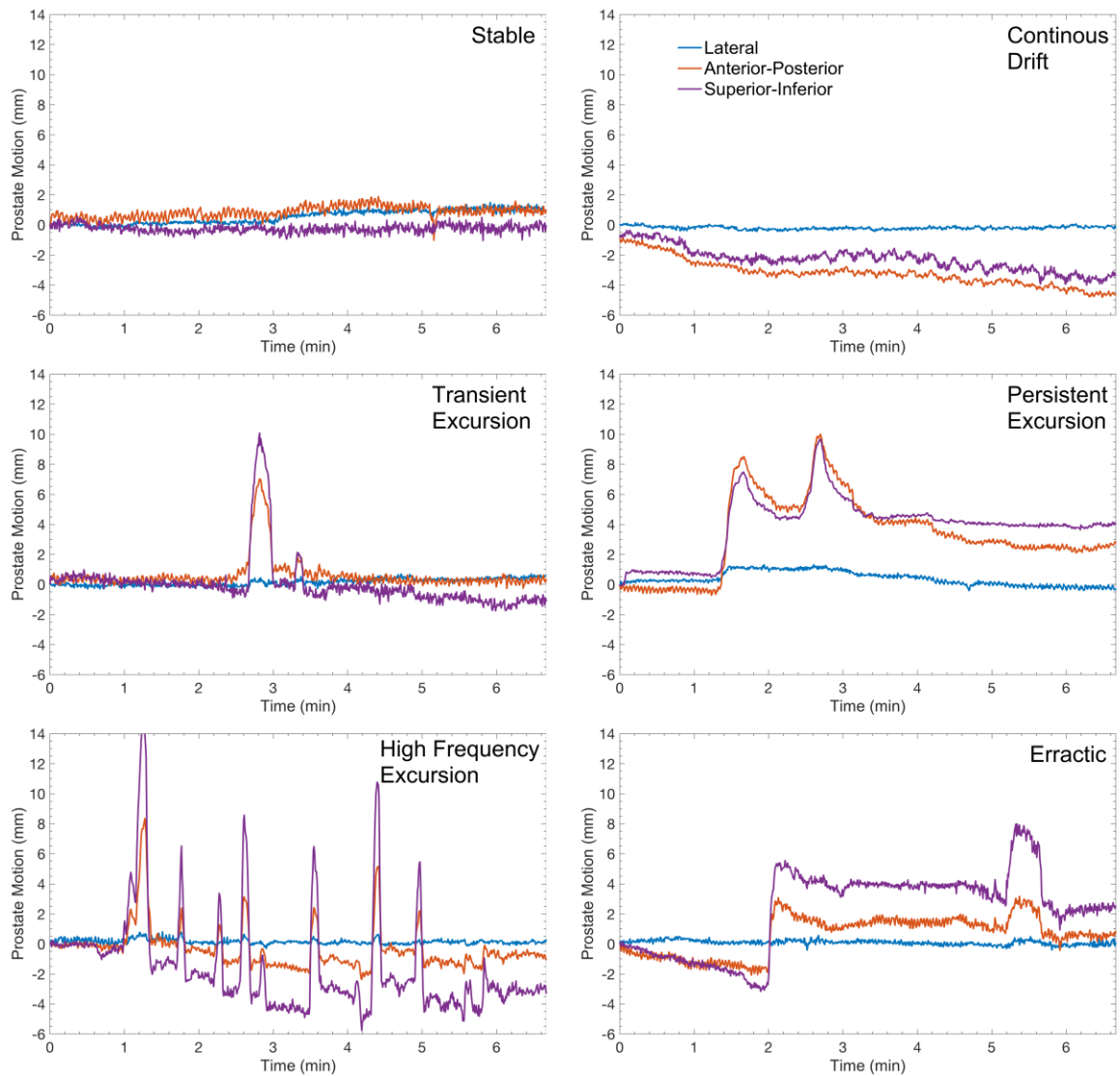
Figure 1.7   Selected prostate motions highlighting the range of motions. Data provided by Langen *et al.*[37] and collected using a Calypso system (Varian Medical System, Inc., Palo Alto, CA) for 550 fractions.

Table 1.2   Clinical trials for prostate hypofractionated RT for localized prostate cancer.

Reference	Number of patients	Dose per fraction (Gy)	Number of fractions	Median follow-up (months)	Freedom from biochemical failure (%)	Late GU/GI toxicity grade $\geq$3(%)
Tang et al.[39] & Quon et al.[40, 41]	84	7	5	74	95.6	1.2/0
	30	8	5	36	100	0/0
Katz and Kang[42]	477	7-7.25	5	72	93.5	1.7/0
King et al.[43]	67	7.25	5	32	94.0	3.0/0
Bolzicco et al.[44]	100	7	5	36	94.4	1.0/0
Chen et al.[45]	100	7-7.25	5	28	99.0	1.0/0
Hannan et al.[46]	91	9-10	5	54	98.6	6.0/6.8
Oliai et al.[47]	70	7-7.5	5	37	94.5	2.8/0
McBride et al.[48]	45	7-7.5	5	44	97.7	2.2/4.4

Typical stereotactic body radiation therapy (SBRT) fractionation schemes used in clinical prostate trials and their outcomes are summarized in Table 1.2. Many trials utilize between 35 and 36.25 Gy in five fractions with low incidence of late grade three GU and GI toxicities. However, for SBRT, when escalating the dose per fraction beyond 7.5 Gy the incidence of late toxicities sharply increases. Musunuru et al.[49] reported an increase in GI toxicities greater than grade two when the volume of the rectum receiving 38 Gy (V_{38Gy}) exceeds 2 cm^3 to the rectum. Similarly, several groups[47, 50, 51] have adopted a more conservative rectal dose constraint of the V_{36Gy} be less than 1 cm^3. Additionally, King et al.[52] have demonstrated meaningful reductions in late toxicities when treating every other day compared to five consecutive days. Despite this, 19% of patients (from n=258) develop high-grade hematochezia at some point after treatment, with 11% requiring

argon plasma coagulation, an additional 2% requiring blood transfusion, or a course of hyperbaric oxygen. Ultimately, an additional 2% develop a visceral fistula[49]. All trials cited in Table 1.2 used several gold fiducial markers implanted within the prostate to facilitate alignment of the target volume prior to treatment. However, most of these studies were taken prior to the availability of active intrafraction monitoring methods. Recently, Colvill et al.[53] demonstrated that a persistent excursion with a mean displacement of 9.9 mm during VMAT reduces the clinical target volume (CTV) coverage, with the dose to 99% of the volume ($D_{99\%}$) and PTV dose to 95% of the volume ($D_{95\%}$) degrading by 19.2% and 34.2%, respectively, while increasing rectum volume receiving 65% of the prescription dose ($V_{65\%}$) by 100.7%. Similar to the observations by Langen et al.[37], Wu et al.[54] have reported that the number of patients that require intrafraction monitoring is small with limited benefit for SBRT. However, for the population (~10%) that exhibits substantial motion and requires intervention the benefit can be significant. Additionally, there is currently no clear indication, prior to treatment, of whether, and when a prostate may exhibit sudden or prolonged displacement.

Current intrafraction monitoring techniques include implanted radio frequency (RF) transponders[37, 55, 56], stereoscopic x-ray imaging[57–59], or monoscopic imaging[38, 58, 60]. RF transponders are arguably the optimal solution due to no additionally ionizing radiation and an accuracy of 0.5 mm. Stereoscopic x-ray imaging utilizes two orthogonal kV x-ray tubes or the kV-MV imaging system on the linac to triangulate fiducial marker locations. However, in some systems, the two kV x-ray tube systems are often blocked by the linac and resort to monoscopic techniques during these periods[58]. Additionally, the two kV x-ray tubes require a substantial investment in the additional hardware and are not readily available on all treatment units. Triangulation using kV-MV imaging is an on-

going research topic which could also benefit from the VOI approach. However, the

challenge is in detecting the fiducial markers in a potentially modulated MV field. For

example, Keall *et al.*[61] reported for 47320 MV projections (52 VMAT fractions), only 6461

projections had a single fiducial marker visible. In any given fraction, the number of

projections with at least a single fiducial marker visible ranged from 66 to 167.

Monoscopic imaging is the most readily available as it uses the kV imaging system on

gantry based linacs as part of the OBI system and deposits equal imaging dose as kV-MV

triangulation. In 2008, Poulsen *et al.*[60] developed a method to estimate the position of

fiducial marker for monoscopic imaging. At any point in time, this technique provides

absolute localization in two dimensions i.e., those of the detector plane and relies on

correlations between the superior-inferior (SI) and anterior-posterior (AP) prostate

motion to determine the unresolved dimension with a mean error less than 0.6 mm[61].

The SI and AP correlations are such that a superior motion occurs with simultaneous an

anterior motion as well, similarly, inferior motion occurs with posterior motion. However,

since the main application of the method is to provide guidance during treatment, the

effects of MV scatter from the patient to the kV detector and kV beam attenuation have

undesirable effects on localizing a fiducial marker. The magnitude of MV scatter can vary

throughout the treatment delivery, more specifically it depends on patient geometry,

dose rate and field shape[62, 63]. Van Herk *et al.*[63] have estimated that upwards of 45% of

the total signal at the centre of the kV detector panel is due to MV scatter during VMAT

using a 6 MV beam. However, these effects have yet to be fully investigated.

Similar to VOI CBCT, it is clear that the application of VOI to intrafraction monitoring should decrease imaging dose[64]. Additionally, TCM when fully implement will allow for further dose reduction with improved image quality and therefore fiducial marker detection. The third objective is to implement current modulated VOI for intrafraction monitoring of the prostate, in which the VOI contains a single or several fiducial markers. We hypothesize that the reduced imaging aperture, akin to VOI CBCT, will decrease kV image noise and peripheral dose for equal dose to the VOI. Additionally, TCM can be utilized to improve fiducial marker detectability with the aim of mitigating the impact of kV attenuation and MV scatter.

1.3   RESEARCH OBJECTIVES

This thesis implements a dynamic VOI approach for inter- (CBCT) and intrafraction (monitoring fiducial markers) IGRT. This thesis consists primarily of a series of manuscripts, each addressing a key objective, as follows.

- **Manuscript 1 is presented in Chapter 3 and addresses the first objective**. It describes the development of dynamic iris collimator for kV CBCT that can track an arbitrarily located VOI within the patient anatomy. In this work, we quantify the gains in image quality for a given dose as a function of VOI size. We demonstrate the functionality of dynamic collimation through phantom studies.

- **Manuscript 2 is presented in Chapter 4 and addresses the second objective.** It expands the VOI approach by introducing TCM. In this work, we develop a dynamic blade collimator for the TrueBeam STx platform and utilize Developer Mode

(Varian Medical Systems, Inc., Palo Alto, CA) to implement TCM. Advantages are assessed with regard to image quality and dose for equal or reduced x-ray tube mAs compared to an unmodulated VOI acquisition.

- **Manuscript 3 is presented in Chapter 5 and addresses the third objective.** It extends the combination of TCM and VOI to intrafraction monitoring of the prostate. In this work, current modulated VOI is utilized to maintain accurate fiducial marker detectability in non-ideal image conditions for equivalent mAs as an unmodulated VOI approach. Additionally, MV scatter on the kV detector plane is modeled using Monte Carlo to determine whether this source of image degradation is sufficiently variable with gantry angle, and significant to be integrated into kV modulation.

Throughout these manuscripts, the advantages of VOI imaging with regard to image quality improvement and dose reduction will be emphasized.

The second chapter describes background theory, algorithms, concepts and devices used to accomplish the work presented. The sixth chapter concludes the thesis by summarizing the key findings of the manuscripts and hypothesizes on the future work surrounding VOI imaging.

CHAPTER 2   METHODOLOGY

This chapter contains descriptions of the various algorithms, concepts and devices used throughout this thesis that were not detailed in the manuscripts. This chapter starts with the background theory on image formation and reconstruction and leads into VOI CBCT and the truncation artifact. The chapter then expands into the methodology and devices used to enable dynamic collimation for VOI, tube current modulation and intrafraction imaging. The chapter ends with a brief introduction to Monte Carlo simulation and the specific tools utilized in this thesis.

2.1   X-RAY IMAGING

The use of x-rays for imaging in medicine was first explored in 1896, six months after the first image was taken by Wilhelm Röntgen[11]. This technology has evolved to be one of the most important imaging modalities in medicine, with 4.3 and 82 million CT examinations taken in 2010 in Canada and the United States, respectively[65].

2.1.1 RADON TRANSFORM AND THE FOURIER SLICE THEOREM

The simplest x-ray image is a projection, in which the variation of attenuation through the object is measured for a given angle. Attenuation varies through the body due to differences in composition of tissues and therefore linear attenuation coefficients. This is demonstrated in Figure 2.1 for three tissues and air, over the energy range of 10 to 125

keV. The attenuation of photons through a heterogeneous object decreases exponentially with distance travelled through the object

$$N = N_o \exp\left(-\int_0^L \mu(x)dx\right)$$

Eq 2.1

where N_o is the initial number of photons and $\mu(x)$ is the linear attenuation coefficient at each position in the object. In two dimensions, the object is composed of an array of linear attenuation coefficients, $\mu(x, y)$.
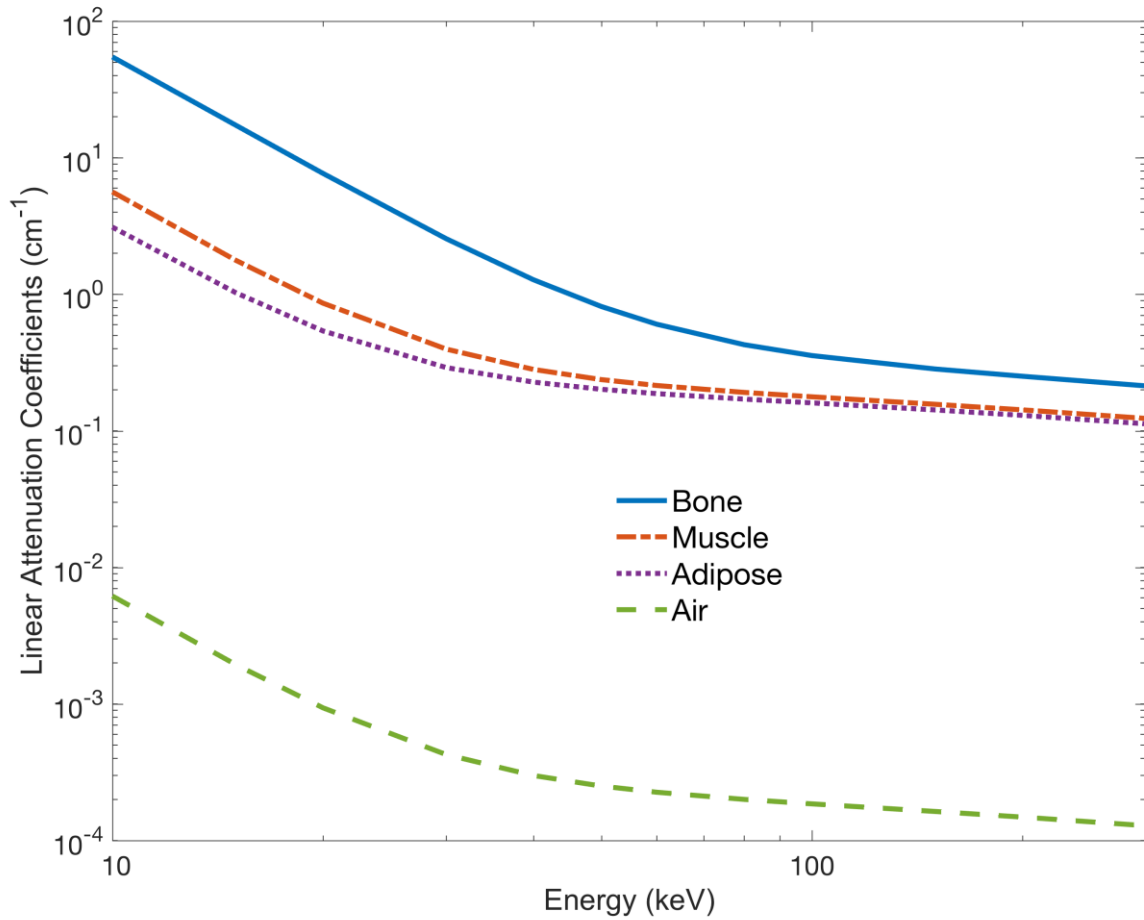
Figure 2.1   Linear attenuation coefficients for bone, muscle, adipose and air.

The projection integral through a two dimensional (2D) object, as described in Figure 2.2, is represented mathematically as a series of line integrals of the linear attenuation coefficients using the Radon transform. The Radon transform at a measurement position s and projection angle θ is described using

$$P_\theta(s) = \ln\left(\frac{N_o}{N}\right) = \int_{-\infty}^{\infty} \int_{-\infty}^{\infty} \mu(x, y)\delta(x \cos\theta + y \sin\theta - s)dxdy \qquad \text{Eq 2.2}$$

where δ is the Dirac delta function[30, 66, 67]. The Radon transform of the object over the angular range of 0 to π form the Radon domain of the object. The Radon domain is more commonly referred to as a sinogram of the object (Figure 2.3).
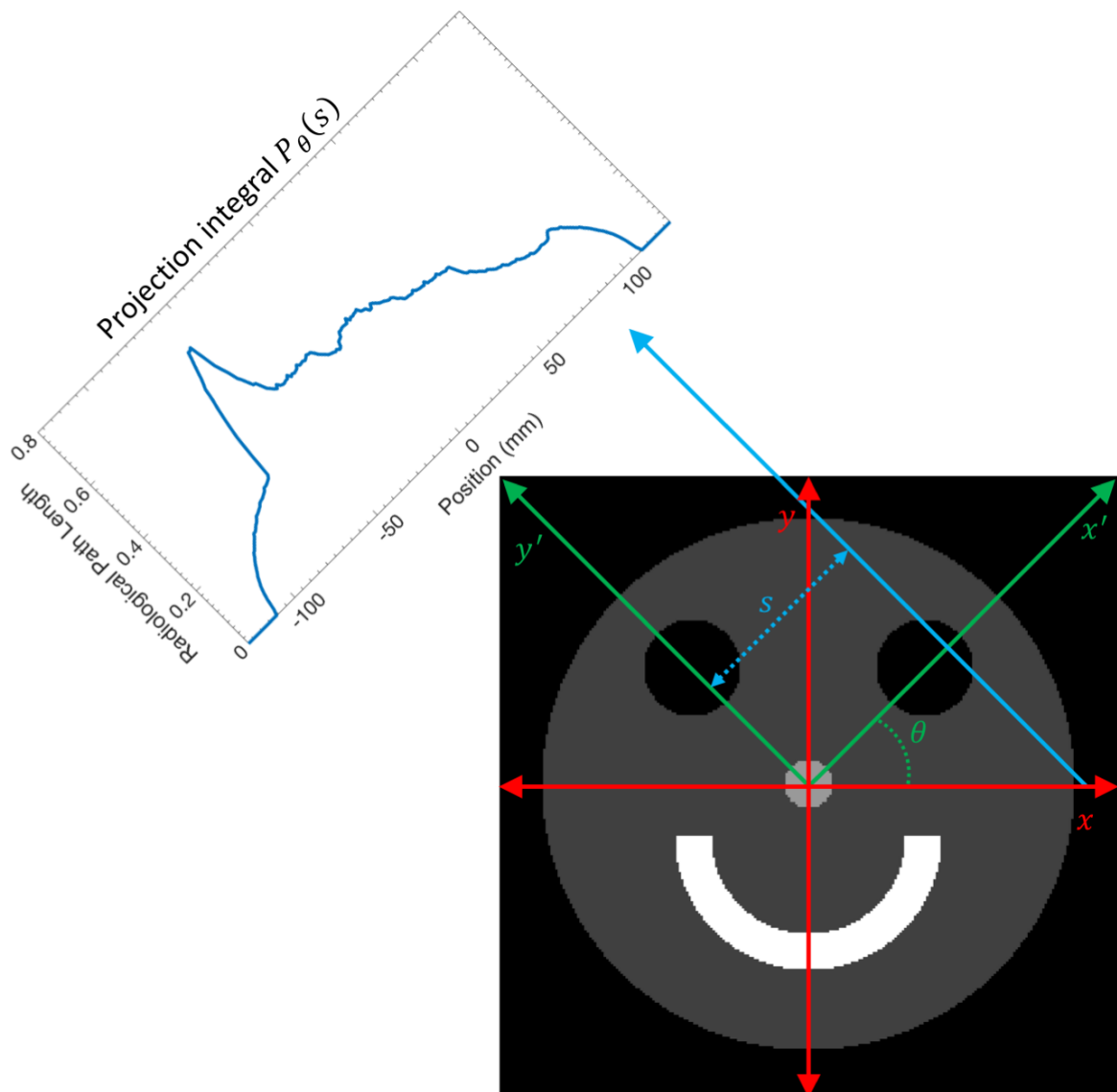
Figure 2.2   Projection geometry for parallel x-ray beam reconstruction using filtered backprojection. The angle θ defines rotation of the xy frame to the rotated frame $x'y'$. The variable s defines the measurement location of the projection integral $P_\theta(s)$.
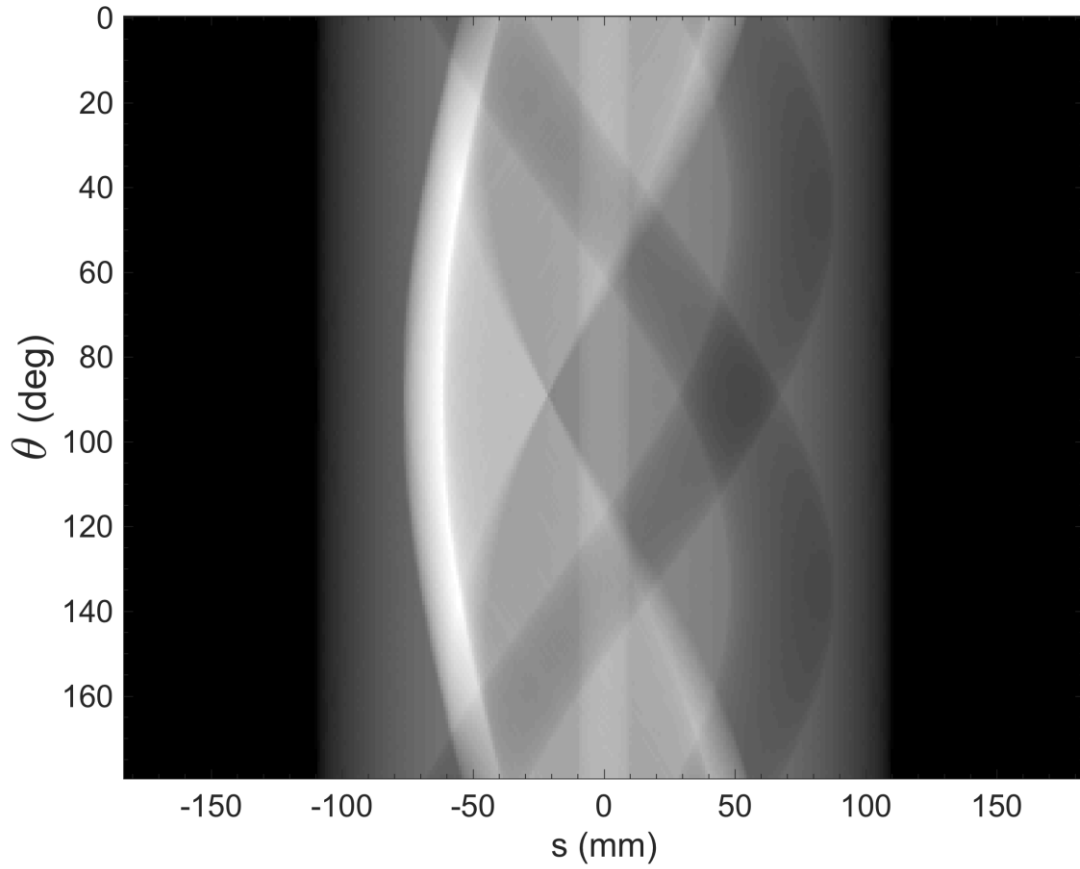
Figure 2.3   Radon transform of the object over the angular range of 0 to π.

The Radon transform and the Fourier transform of the array of linear attenuation coefficients can be related using the following. The Fourier transform of $\mu(x, y)$ is defined by

$$U(u,v) = \int_{-\infty}^{\infty}\int_{-\infty}^{\infty} \mu(x,y)\exp\big(-2\pi i(ux + vy)\big)dxdy \qquad \text{Eq 2.3}$$

Using polar coordinates of $u = r\cos\theta$ and $v = r\sin\theta$, Eq 2.3 becomes

$$U(r,\theta) = \int_{-\infty}^{\infty}\int_{-\infty}^{\infty} \mu(x,y)\exp\big(-2\pi ir(x\cos\theta + y\sin\theta)\big)dxdy \qquad \text{Eq 2.4}$$

The sifting property of the Dirac delta function can be applied to Eq 2.4, such that

26

$$f(x') = \int_{-\infty}^{\infty} f(x)\delta(x - x')dx \qquad \text{Eq 2.5}$$

$$\exp\big(-2\pi i r(x\cos\theta + y\sin\theta)\big)$$

$$= \int_{-\infty}^{\infty} \exp(-2\pi i r s)\delta(x\cos\theta + y\sin\theta - s)ds \qquad \text{Eq 2.6}$$

And substituted into Eq 2.4 to give

$$U(r,\theta) = \int_{-\infty}^{\infty}\int_{-\infty}^{\infty}\int_{-\infty}^{\infty} \mu(x,y)\,\delta(x\cos\theta + y\sin\theta$$

$$- s)\exp(-2\pi i r s)ds\,dx\,dy \qquad \text{Eq 2.7}$$

$$U(r,\theta) = \int_{-\infty}^{\infty} P_\theta(s)\exp(-2\pi i r s)ds \qquad \text{Eq 2.8}$$

$$U(r,\theta) = \mathcal{F}[P_\theta(s)] \qquad \text{Eq 2.9}$$

$$P_\theta(s) = \mathcal{F}^-[U(r,\theta)] \qquad \text{Eq 2.10}$$

where $\mathcal{F}$ and $\mathcal{F}^-$ are the forward and inverse Fourier transform. This relationship with the one dimensional (1D) Fourier transform of the object evaluated at an angle θ and the Radon transform at an angle θ, is known as the *Fourier slice theorem, projection slice theorem* or *central slice theorem*. The Fourier slice theorem can be used to reconstruct the array of linear attenuation coefficients by taking the Fourier transform and interpolating on to Fourier space, followed by calculating the inverse Fourier transform to retain $\mu(x,y)$. However, this method is not preferred to reconstruct the object due to the large number of projections required to fill the Fourier domain without causing interpolation errors in the high frequency image components[66].

2.1.2 Filtered Backprojection

Fourier slice theorem can be applied to backprojection of $P_\theta(s)$ between 0 and π, where backprojection is defined by[30, 66, 67]

$$\mu(x,y) = \int_0^\pi \int_{-\infty}^\infty P_\theta(s)\delta(x\cos\theta + y\sin\theta - s)dsd\theta \qquad \text{Eq 2.11}$$

Substituting for $P_\theta(s)$ using the Fourier slice theorem Eq 2.11 becomes

$$\mu(x,y) = \int_0^\pi \int_{-\infty}^\infty \int_0^\infty U(r,\theta)\exp(2\pi irs)\delta(x\cos\theta + y\sin\theta - s)drdsd\theta \qquad \text{Eq 2.12}$$

Applying the sifting function of the Dirac delta, Eq 2.12 can be simplified to

$$\mu(x,y) = \int_0^\pi \int_0^\infty U(r,\theta)\exp\big(2\pi ir(x\cos\theta + y\sin\theta)\big)drd\theta \qquad \text{Eq 2.13}$$

However, this method results in the blurred version of the object as illustrated in Figure 2.4. The solution to correct this error can be found by comparing to the inverse Fourier transform of $U(u,v)$ in polar coordinates with integration limits between 0 and π, where $dudv = rdrd\theta$

$$\mu(x,y) = \int_{-\infty}^\infty \int_{-\infty}^\infty U(u,v)\exp\big(2\pi i(xu + yv)\big)dudv \qquad \text{Eq 2.14}$$

$$\mu(x,y) = \int_0^\pi \int_0^\infty U(r,\theta)\exp\big(2\pi ir(x\cos\theta + y\sin\theta)\big)rdrd\theta \qquad \text{Eq 2.15}$$

As demonstrated, Eq 2.13 and Eq 2.15 differ by the value of r. The blurred object reconstructed using Eq 2.13 could then be rectified by multiplication by r to give the correct reconstruction of the object, such that

$$\mu(x,y) \quad = \quad \int_0^\pi \int_{-\infty}^\infty \left[\int_0^\infty \left[\int_{-\infty}^{-\infty} P_\theta(s) \exp(-2\pi i r s) ds \right] |r| \exp(2\pi i r s) dr \right]$$

Eq 2.16

$$\delta(x \cos\theta + y \sin\theta - s) ds d\theta$$

$$\mu(x,y) = \int_0^\pi \int_{-\infty}^\infty \mathcal{F}'[\mathcal{F}[P_\theta(s)]|r|] \, \delta(x \cos\theta + y \sin\theta - s) ds d\theta \qquad \text{Eq 2.17}$$

Eq 2.17 represents the equation for filtered back-projection (FBP) and is illustrated in

Figure 2.4. The reconstruction chain for FBP can therefore be summarized as:

  i. Log normalize the projection by an unattenuated projection

  ii. Fourier transform of the normalized projection

  iii. Multiplication by a ramp filter, $|r|$

  iv. Inverse Fourier transform of the filtered projection

  v. Backproject

  vi. Repeat over 180 degrees

Alternatively, Eq 2.17 could be achieved through convolution in the spatial domain

$$\mathcal{F}'[\mathcal{F}[P_\theta(s)]|r|] = \int_{-\infty}^\infty P_\theta(s') h(s - s') ds' \qquad \text{Eq 2.18}$$

where $h(s)$ is the ramp filter in the spatial domain defined by

$$h(s) = 2r_{max} \operatorname{sinc}(2r_{max}s) - r_{max}^2 \operatorname{sinc}^2(r_{max}s) \qquad \text{Eq 2.19}$$

where r_{max} is the maximum frequency.
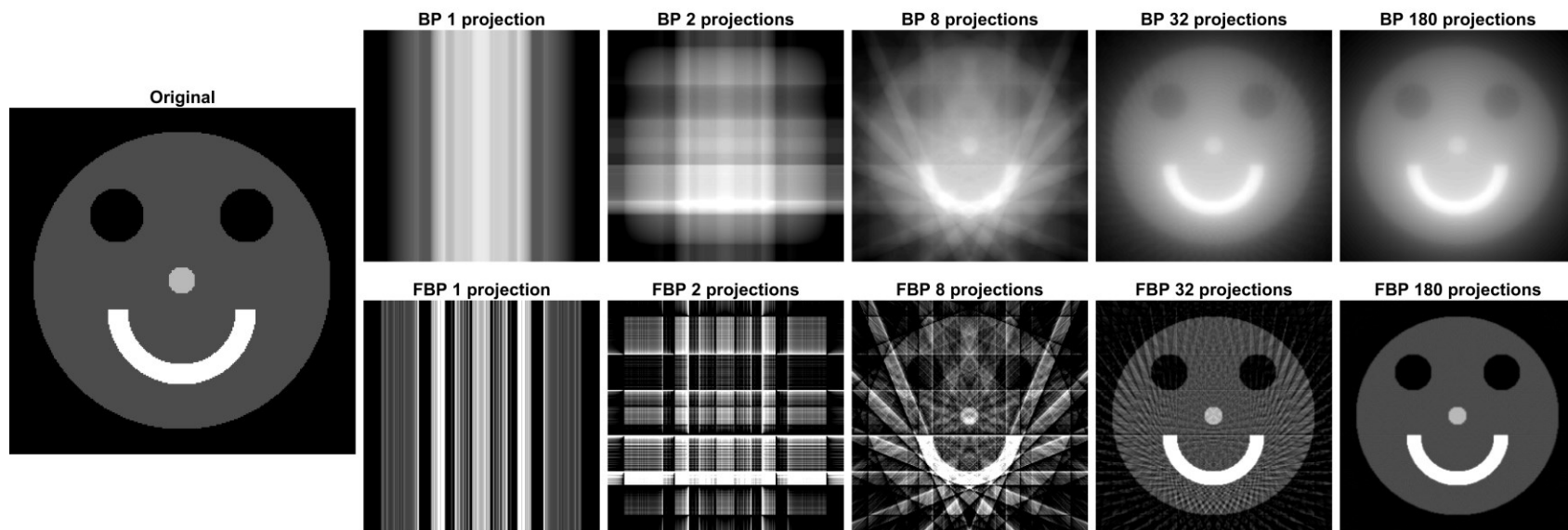
Figure 2.4   Backprojection (BP) and filtered backprojection (FBP) of a synthetic phantom using a parallel x-ray beam source with 1, 2, 8, 32 and 180 projections.

2.1.3 CT GENERATIONS

First generation CT utilized a pencil beam x-ray source collimated to approximately 1.3 mm long (in plane) and 3 mm wide (out of plane) with a single detector[30] (Figure 2.5). In which the source and detector translated across the patient acquiring individual measurements. After a complete translation across the patient, the source and detector rotated one degree and acquired the next angle of the sinogram. This setup mimics the parallel geometry illustrated in Figure 2.2. A complete acquisition would require approximately 4.5 minutes. Due to the long acquisition time, patient motion limited image quality[30]. This led to the development of second generation CT, which used an expanded collimation in plane and multiple detectors that translated and rotated like first generation. This reduced acquisition time for a single plane to under 20 seconds[30].

Third generation represents the geometry for modern CT in which the x-ray source is collimated to a fan beam, which is wide enough to irradiate the whole patient at a given angle. In this generation, the x-ray source and detector are contained in a gantry which rotates about the patient. With the introduction of slip ring technology (eliminating the need for cables between the stand and gantry), the scan time for a single plane was reduced to under 0.5 seconds[30]. However, this geometry deviates from the parallel beam geometry as illustrated in Figure 2.5. The simplest approach to reconstruct the fan beam geometry is to re-bin to a parallel beam geometry. Re-binning is possible since each ray line within the fan at a given angle, can be imagined as a parallel beam ray line acquired at a different angle of rotation. However, this method is typically not used since it requires that all projections are acquired before reconstruction can commence. Additionally, the

interpolation between the two geometries may limit spatial resolution[67]. The alternative, and preferred approach is to utilize direct weighted FBP. The detailed derivation for a curved or flat detectors can be found in chapter three of the textbook *Principles of Computerized Tomographic Imaging* by Kak and Slaney[66].
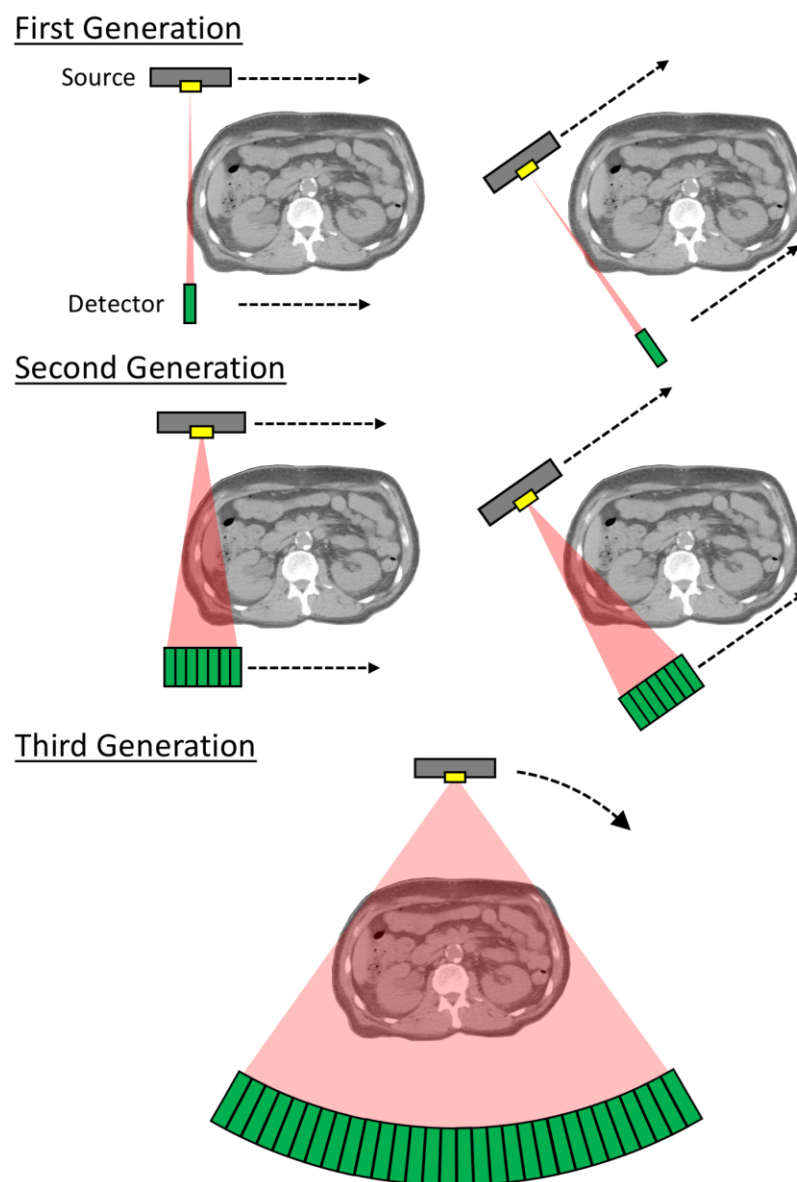
Figure 2.5   Illustration of the evolution of CT from first to third generation.

2.1.4 CONE-BEAM CT

A cone beam geometry extends this geometry with the expansion of the beam along the axis of rotation, creating a cone of photons irradiating the object (Figure 1.5). However, this data does not sufficiently fill the Radon domain to allow for correct reconstruction of the whole object. However, Feldkamp, Davis and Kress[68] (FDK) have developed a filtered backprojection approximation of the object. The FDK algorithm has since become the current standard CBCT reconstruction.

In CBCT, the projections are acquired through either a 180° plus the fan angle[69] or 360° rotation with the patient centered on the axis of rotation for equipment used. The cone beam geometry introduces corrections to the raw projection data. On Varian C-Series and TrueBeam platforms (Varian Medical Systems, Inc., Palo Alto, CA) for example, gain, offset and defect corrections (e.g. flood field, dark current and dead pixel corrections) are applied to every projection prior to writing to the hard drive. These processed projections are then log normalized by an unattenuated air projection. Thereafter, two additional corrections are applied. The first is Feldkamp or Cosine weighting[68], which accounts for the variation of the density of photons incident on a flat detector geometry, and is written as

$$p_2(u, v; \theta) = p_1(u, v; \theta) \left[\frac{SDD}{\sqrt{SDD^2 + u^2 + v^2}} \right] \qquad \text{Eq 2.20}$$

where SDD is the source-to-detector distance (intersecting the axis of rotation), u and v are positions within the projection, p_1 and p_2 are the original and corrected projection

data, respectively. As demonstrated in Figure 2.6, this is a relatively small but non-negligible correction.
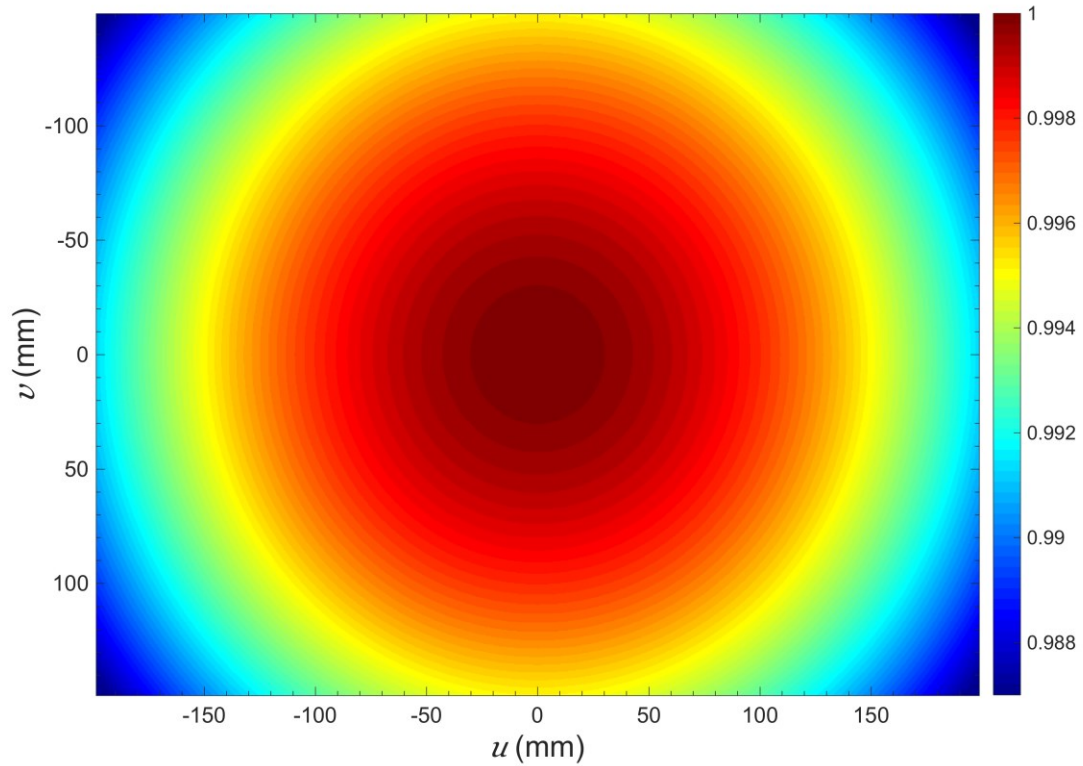
Figure 2.6   Feldkamp weighting for the setup used in this work.

The second is Parker weighting[69], this accounts for redundant or overlapping data in the Radon domain for short scans (e.g., those less than 360°) as illustrated in Figure 2.7 and Figure 2.8. As illustrated, for the fan beam geometry acquired from 0 to π, Radon space is incomplete for reconstruction in conventional CT or CBCT. As such, the arc is extended by the fan angle. However, this results is redundant (or double scanned) data which

causes artifacts in the reconstructed image[69]. Parker weighting, w_p, accounts for the

redundant data and is written as

$$
w_p = \begin{cases} \sin^2\left[\dfrac{\pi\theta}{\left(2\phi_{fan} - 4\phi_u\right)}\right], & \text{for } 0 \le \theta \le \phi_{fan} - 2\phi_u \\[4mm] 1, & \text{for } \phi_{fan} - 2\phi_u < \theta < \pi - 2\phi_x \\[4mm] \sin^2\left[\dfrac{\pi\left(\pi + \phi_{fan} - \theta\right)}{\left(2\phi_{fan} - 4\phi_u\right)}\right], & \text{for } \pi - 2\phi_u \le \theta \le \pi - \phi_{fan} \end{cases} \qquad \text{Eq 2.21}
$$

where ϕ_{fan} is the fan angle and ϕ_u is the fan angle at position u in the projection. This

correction is constant along the cone angle for each projection θ. This is used for

acquisitions that are less than 360° and is a result of the fan beam geometry. Parker

weights are demonstrated in Figure 2.9 for a 200° acquisition with a 15° fan angle and

SDD of 150 cm.
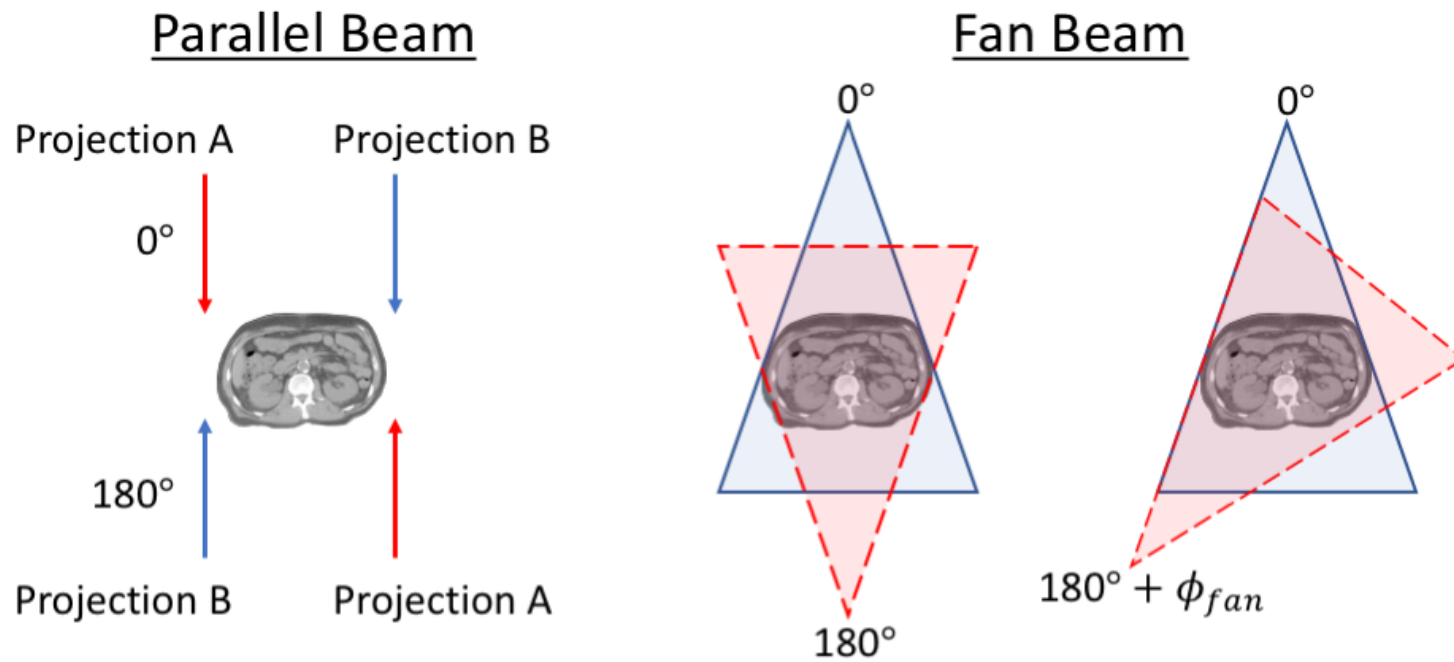
Figure 2.7   Illustration of conjugate sampling pair in parallel beam and fan beam CT. In which for parallel beam this pair is acquired after a 180°, whereas for a fan beam geometry this is acquired after a rotation of $180° + \phi_{fan}$. In acquiring extra data in ϕ_{fan}, duplicate or redundant conjugate pairs are acquired and results in artifacts if not corrected for. This correction is referred to as Parker weighting.
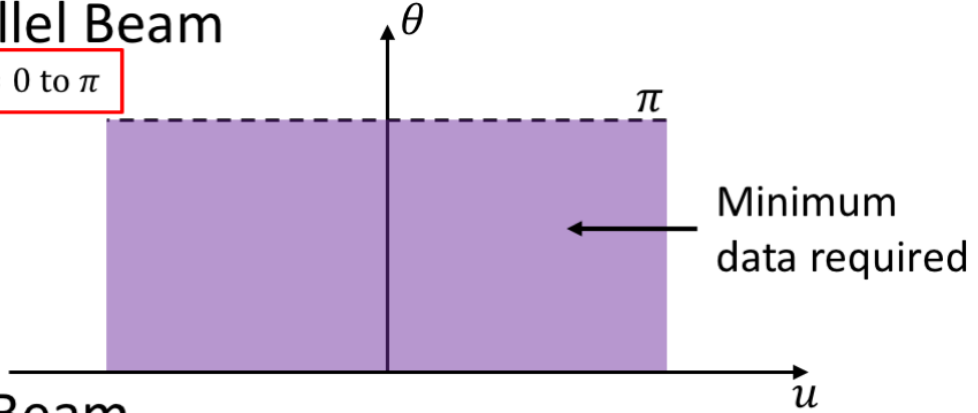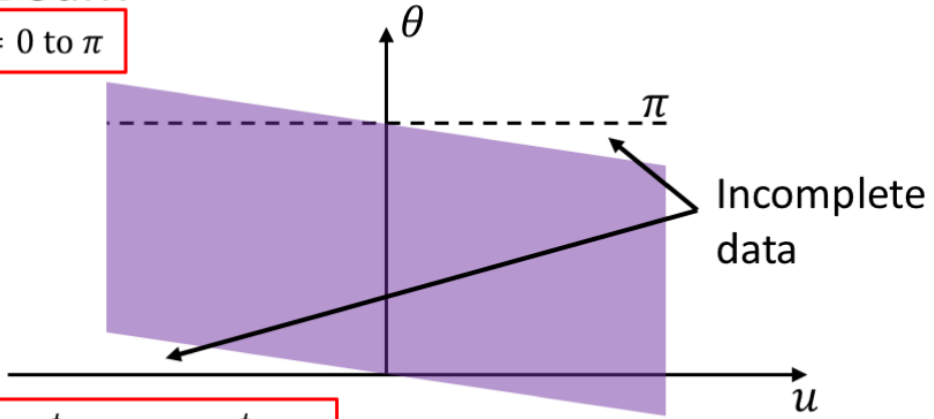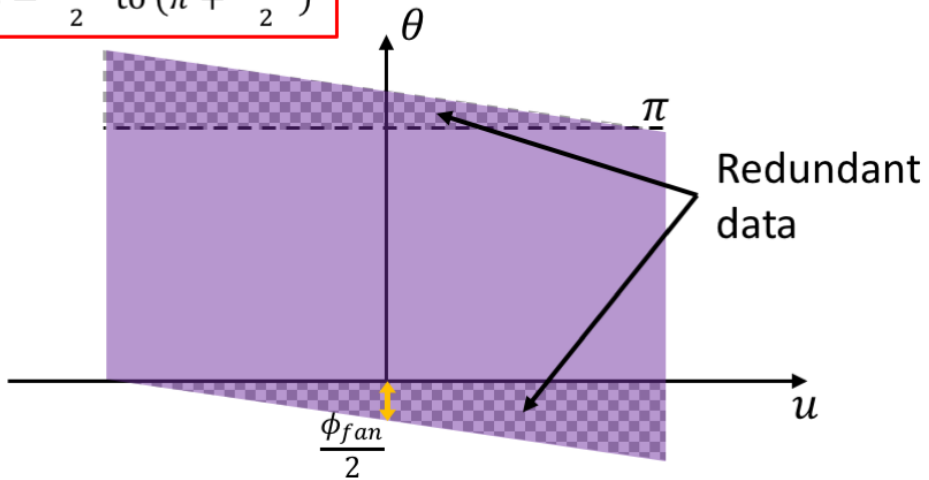
Figure 2.8   a) Parallel beam geometry illustrated in Radon space from 0 to π, representing the mimimum required amount of data for accurate reconstruction. b) Fan beam geometry acquired from 0 to π, in which the data is incomplete for reconstruction. c) Fan Beam geometry acquired from $-\phi_{fan}/2$ to $\pi + \phi_{fan}/2$. The minimum data is acquired; however, the redundant data would cause artifacts in the reconstructed image.
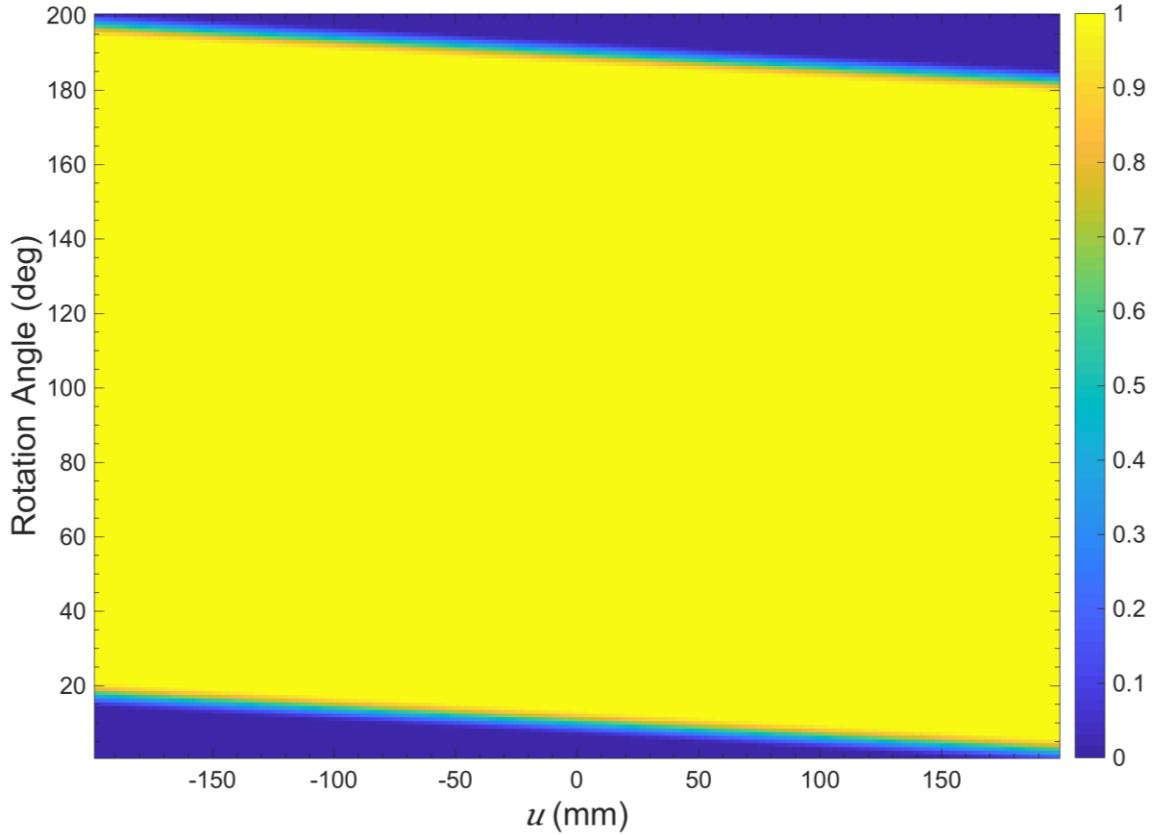
Figure 2.9   Parker weights for a 200° acquisition using the setup in this thesis.

Additionally, the ramp filter can be apodized to control the noise within the projection. The higher noise is due to retaining high frequencies in the ramp filter, and apodizing suppresses the high frequency amplification. Commonly used filters used are Shepp-Logan, cosine, Hanning and Hamming (Figure 2.10), however, between cosine, Hanning and Hamming the resulting difference is minimal.

These processing steps are demonstrated in Figure 2.11 for a projection of an ATOM head phantom taken on a TrueBeam STx unit. The steps highlighted in Figure 2.11 represent the minimum required, commercial systems commonly apply additional corrections (i.e. for scatter and beam hardening).
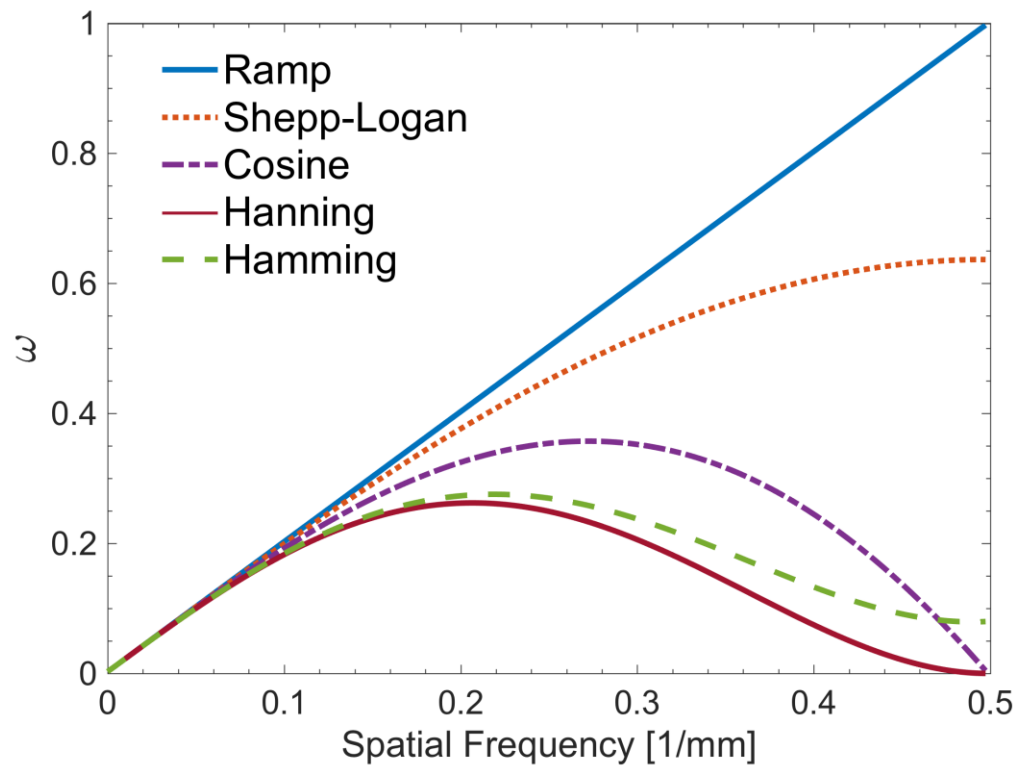
Figure 2.10   Ramp, Shepp-Logan, cosine, Hanning and Hamming filters.
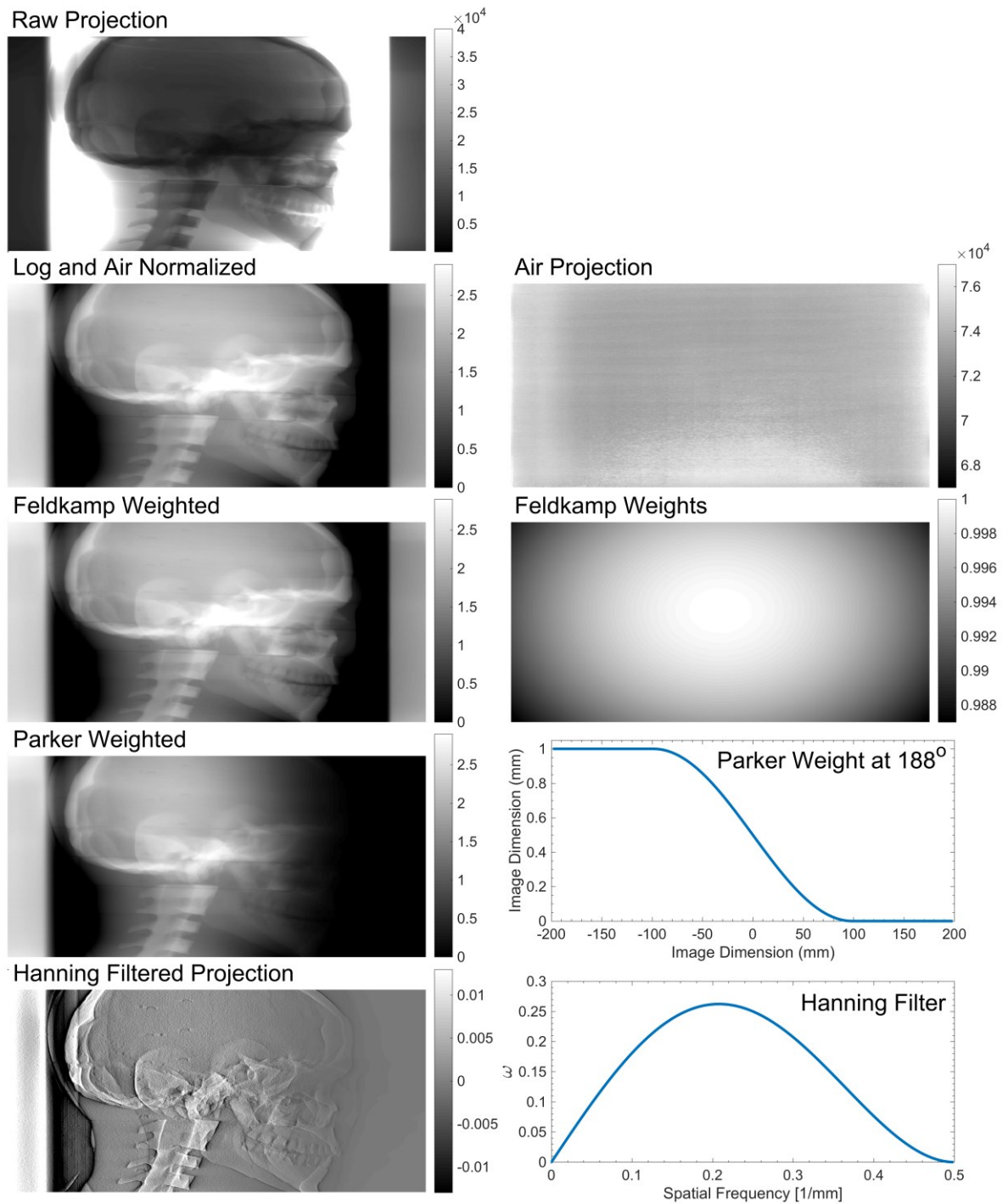
Figure 2.11   CBCT processing steps: log normalization by an unattenuated projection, Feldkamp and Parker weighting and filtering by a Hanning filter, for a projection of an ATOM head phantom taken on a TrueBeam STx unit.

2.1.5 COMPTON SCATTER

The extended cone angle used in CBCT, has adverse consequences compared to traditional fan-beam CT, which uses a limited cone-angle. For example, a 16 multi-detector row CT system[70] use a cone angle less than 1°. For comparison, the imaging system on a Varian Clinac or TrueBeam platform use a standard cone-angle of 11.4°. This increase in cone angle and therefore the volume of tissue irradiated increases the amount of scattered radiation generated.
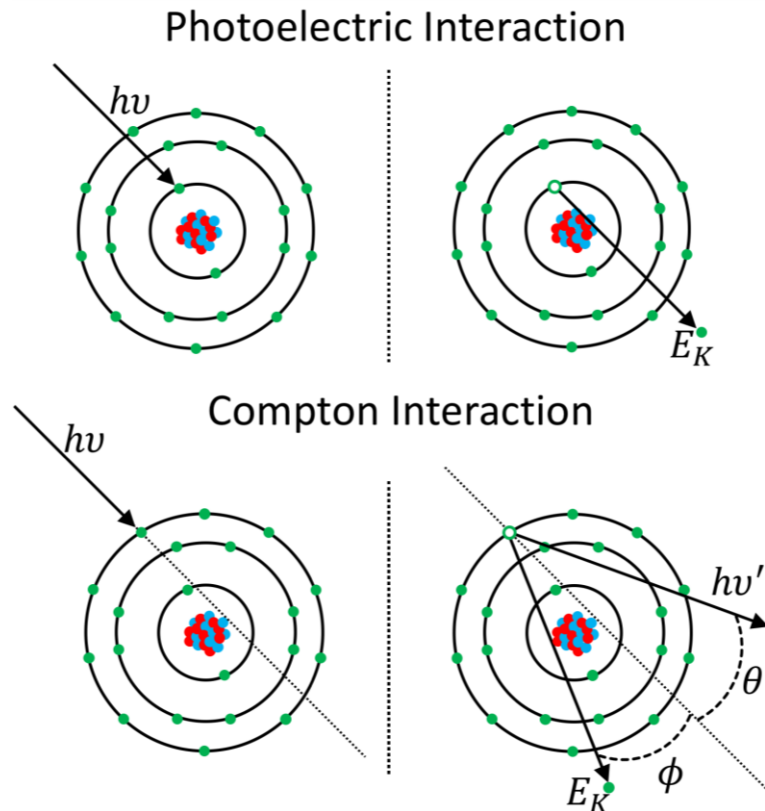
Figure 2.12   Illustration of photoelectric and Compton interactions for a photon with incident energy $h\upsilon$. The product of a photoelectric interaction is an electron with energy E_k. The products of a Compton interaction are a photon with energy $h\upsilon'$ scattered by an angle θ and an electron with energy E_k scattered by an angle ϕ.

The mechanism behind scatter generation is the high volume of Compton interactions relative to photoelectric interactions that occur in tissue for the photon energies used clinically. As illustrated in Figure 2.12, a recoil electron and a secondary (scattered) photon are products of the Compton event. The differential Klein-Nishina cross section, as highlighted in Figure 2.13, describes the probability of secondary photon scattering angle, θ, relative to the incident, in a cone $d\Omega$. As illustrated, the bulk of these secondary photons are in the forward direction, i.e. toward the detection plane. Siewerdsen and Jaffray[8] initially demonstrated that SPR increases by 17.7% per degree of cone angle for a 30 cm diameter PMMA phantom. This results in lower than expected calculated linear attenuation coefficients towards to center of the image and noise within the projection, both of which decrease the available image quality and increase reconstruction artifacts (such as shading artifacts, Figure 2.14).
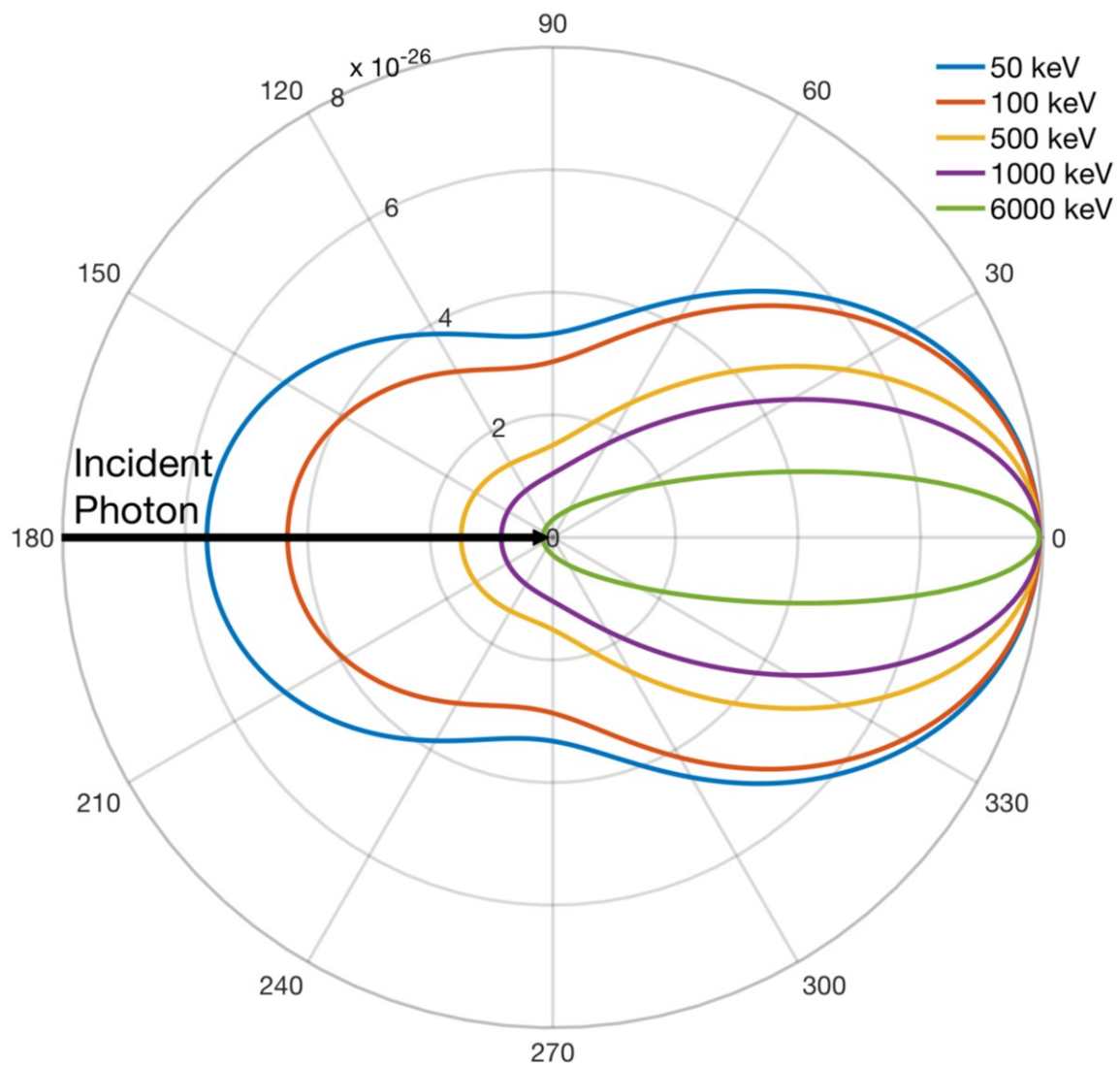
Figure 2.13   Differential Klein-Nishina cross section as a function of secondary photon scattering angle, θ, relative to the incident photon for various incident photon energies within the diagnostic and therapeutic energy domain, in cm^2 per steradian.
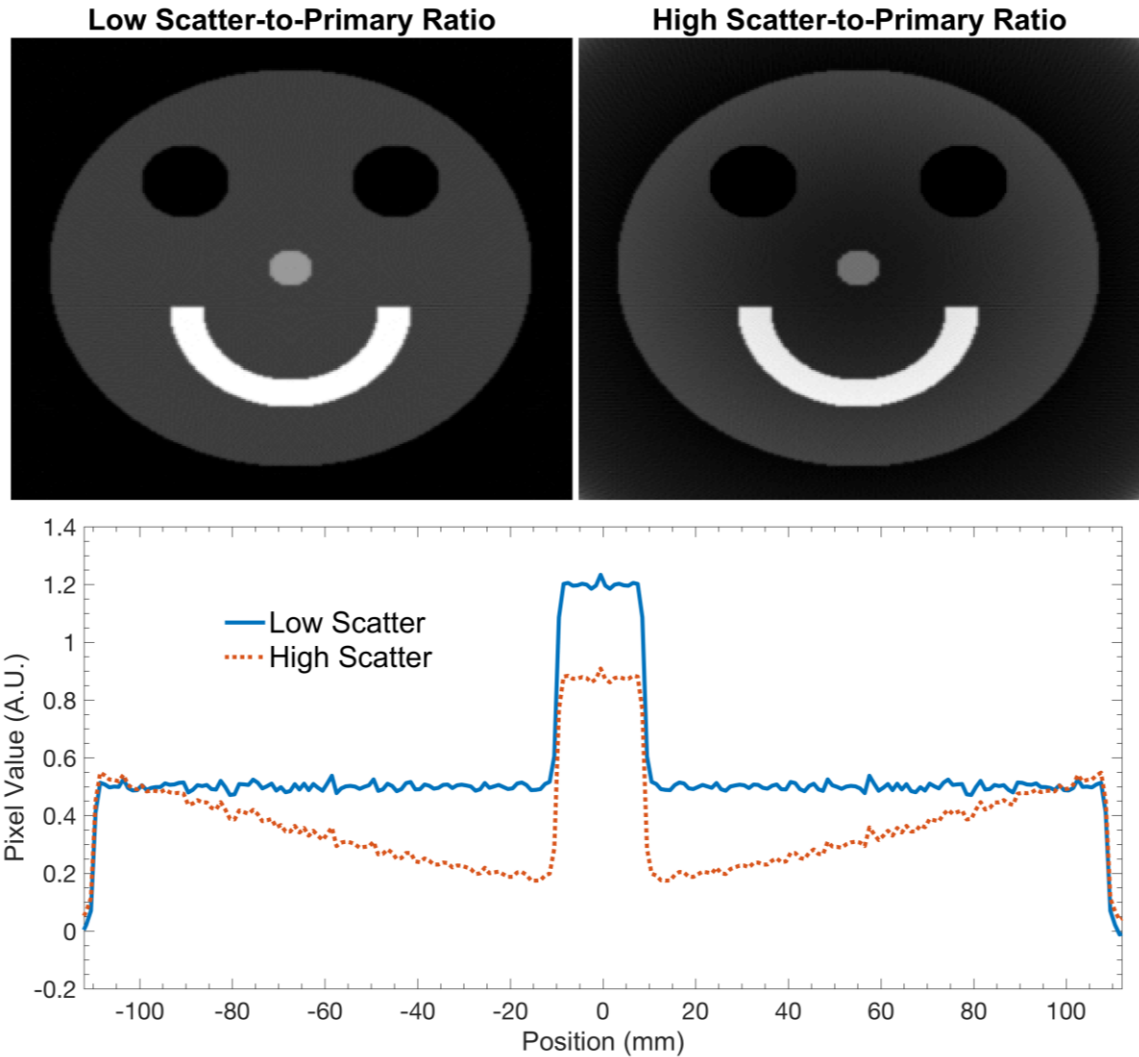
Figure 2.14   FBP of a synthetic phantom with simulated low and high SPR. This demonstrates the shading artifact that could result for a scenario with high SPR towards the center of the detector plane.

2.2 VOI Cone Beam CT

The method used to minimize the effect of scatter is to reduce the volume of tissue irradiated, such that only the relevant anatomy is exposed by the imaging beam. This involves truncating the measured data by attenuating the beam outside the VOI. However, truncating the data violates the completeness of the Radon domain, in that

Radon transform is not evaluated on the domain $[-\infty, \infty]$, with respect to s. Thus, the Fourier slice theorem is no longer valid,

$$U(r,\theta) \neq \mathcal{F}[P_\theta(s)]$$

Eq 2.22

The consequence of this, is that $|r|$ is no longer supported for $\mathcal{F}[P_\theta(s)]$ in Eq 2.17, as the Fourier slice theorem was implicit in arriving at this result. Specifically, ramp filtering at the sharp transition of measured and truncated data introduces artificial frequencies (Figure 2.16). This results in elevated values of $\mu(x,y)$ at the boundary (Figure 2.17), and is commonly referred as truncation induced cupping[14, 30]. When backprojected over all angles, the result is a ring artifact at the boundary and cupping toward the centre of the VOI. This is the same mechanism for photon starvation artifacts in FBP due to metallic objects, in which $P_\theta(s)$ behind the metal is fully attenuated and therefore incomplete.

The truncation artifact can be mitigated by extrapolation of the boundary value on either side of the truncation by the function

$$P'_\theta(s) = \begin{cases} P_\theta(s_{low}) \dfrac{1 - \exp(ks)}{1 - \exp(ks_{low})} & s < s_{low} \\ P_\theta(s_{up}) \dfrac{1 - \exp(ks)}{1 - \exp(ks_{up})} & s > s_{up} \\ P_\theta(s) & s_{low} \leq s \leq s_{up} \end{cases}$$

Eq 2.23

where s_{low} and s_{up} are the lower and upper bounds of the truncation boundary, respectively and k controls the exponential fall off[16]. This approach reduces the generation of higher frequencies and results in an approximation of the object within the VOI (Figure 2.17).
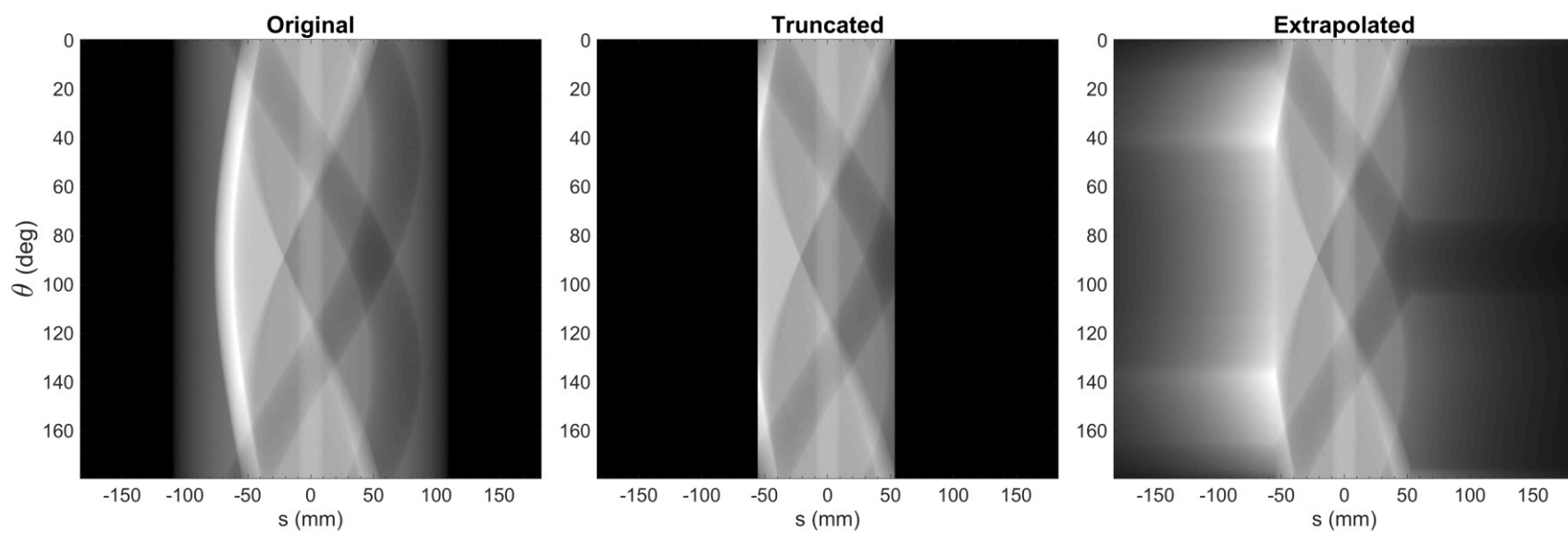
Figure 2.15   Original, truncated and extrapolated sinograms of the phantom in Figure 2.2.
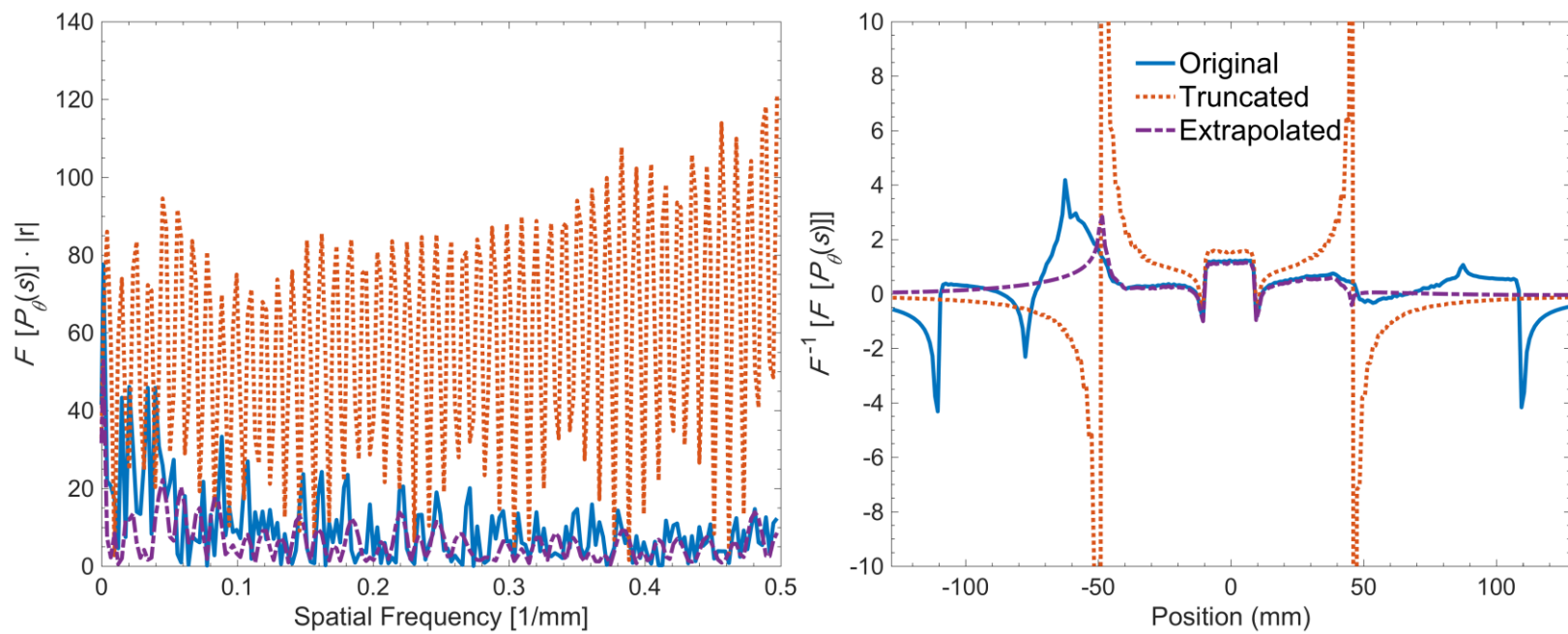
Figure 2.16   Original, truncated and extrapolated $\mathcal{F}[P_\theta(s)]|r|$ and $\mathcal{F}'[\mathcal{F}[P_\theta(s)]|r|]$ for an angle of 0 degrees.
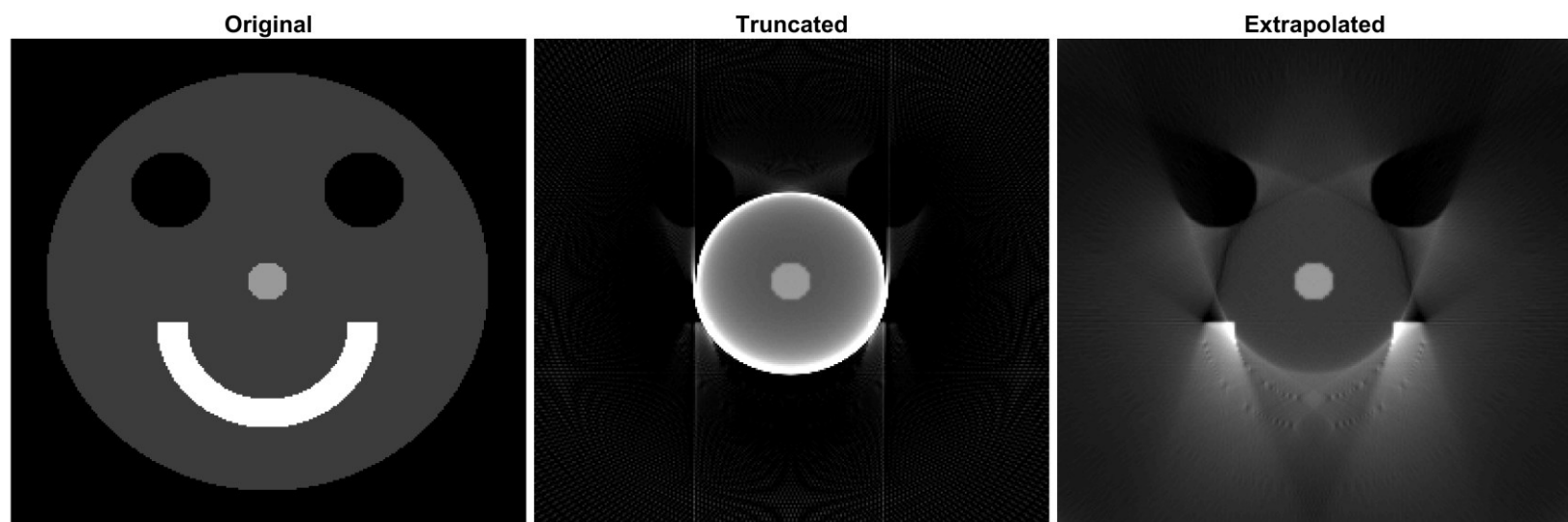
Figure 2.17   Original phantom with reconstructions of truncated and extrapolated sinogram data.

2.3 DYNAMIC COLLIMATORS FOR VOI IMAGING

2.3.1 IRIS COLLIMATOR

Two novel dynamic kV photon collimators were developed to enable VOI CBCT, given a VOI of arbitrary location and dimension within the patient. An iris collimator was the first dynamic collimator developed in this work to facilitate VOI imaging. Two versions exist, Figure 2.18 and Figure 3.1 displays the components of the first-generation and second-generation iris collimators, respectively. Figure 2.18 provides more information of the design of the iris collimator by highlighting the mechanisms that allow it to function. Chapter 3 describes in detail the design, function and advantages of the second-generation iris collimator for VOI CBCT in terms of image CNR and dose reduction compared to full-field.
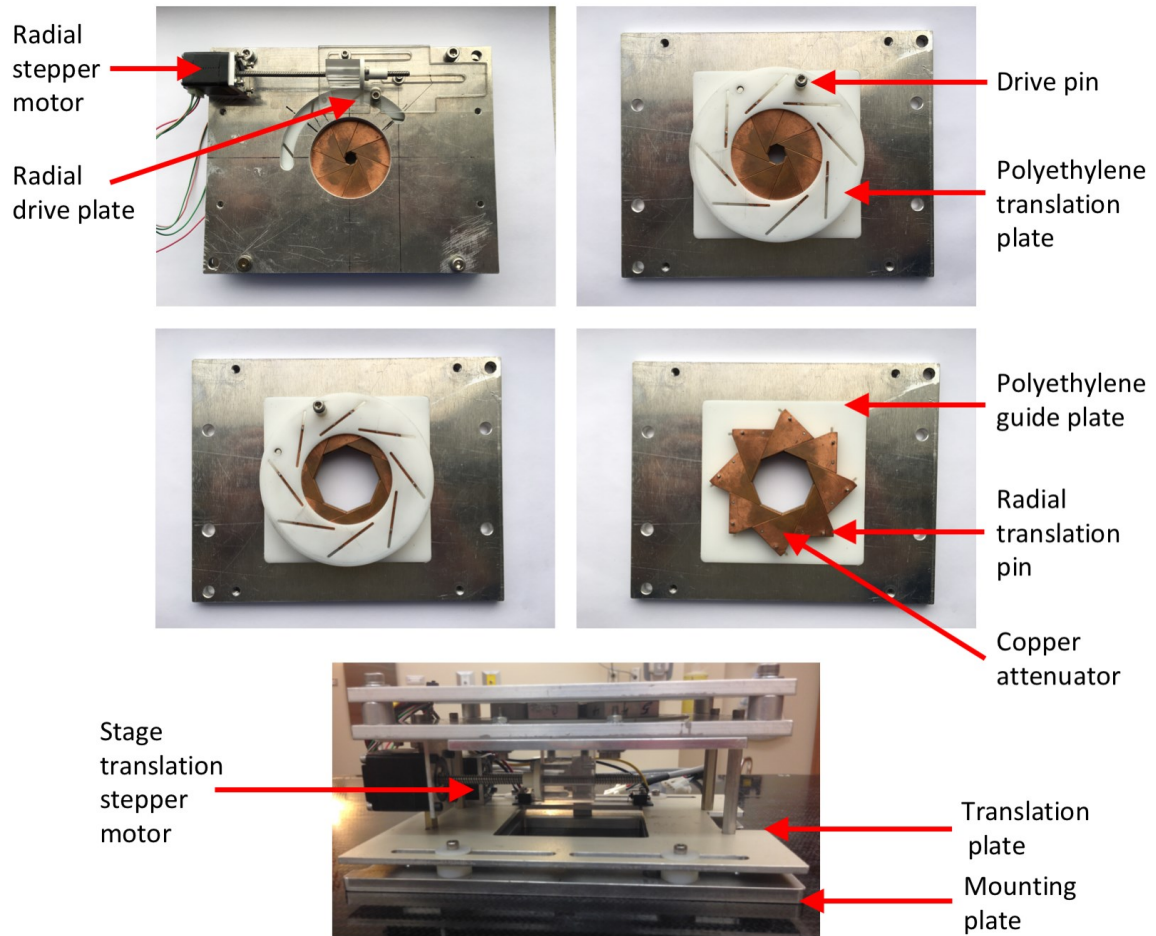
Figure 2.18   First generation iris collimator, highlighting the copper attenuators, the polyethylene guiding plates and drive pins. Also displayed are the linear translation stage and mounting plate.

2.3.2 Blade Collimator

A four-blade system was manufactured to allow dynamic collimation of the imaging system on a TrueBeam STx platform. Chapter 4 describes in detail the design and function of the blade collimator for VOI CBCT. Briefly, this system mimics the design of the commercial collimation system on TrueBeam, with 2 mm lead and 3 mm steel blades, 17.8 cm in length and 7.0 cm in width. These are attached to linear rail bearings on both sides

of each blade. (Figure 4.1). As illustrated in Figure 2.19, blade motions are controlled using a microcomputer (Raspberry Pi 2 model B V1.1, Raspberry Pi Foundation, Caldecote, UK) and a triple-axis digital accelerometer (ADXL345, Analog Devices, Inc., Norwood, MA) located within the gantry. This connects to four Big Easy Driver boards (SparkFun Electronics, Niwot, CO), each controlling a stepper motor (E28H43-05-900, Haydon Kerk Motion Solutions, Inc., Waterbury, CT). This allowed for simultaneous motion of each blade, with a maximum imaging aperture of 27.2 by 27.2 cm^2 and complete over-travel of each blade. The steppers were run using a full step resolution of 0.0127 mm at a frequency of 1 kHz. The absolute position of each blade was determined using a limit switch placed at the end of travel, near the stepper motor. The system was constructed on a 6.7 mm thick aluminum plate and attached to the source arm of TrueBeam using two custom aluminum mounting brackets, allowing for easy and reproducible set up. The blades and controlling electronics were connected using a 25-pin serial cable through the gantry and kV source arm. The system is then controlled using remote connection to the Raspberry Pi and a Python GUI (Figure 2.20). The use of this collimator is described in detail in Chapter 4 and Chapter 5.
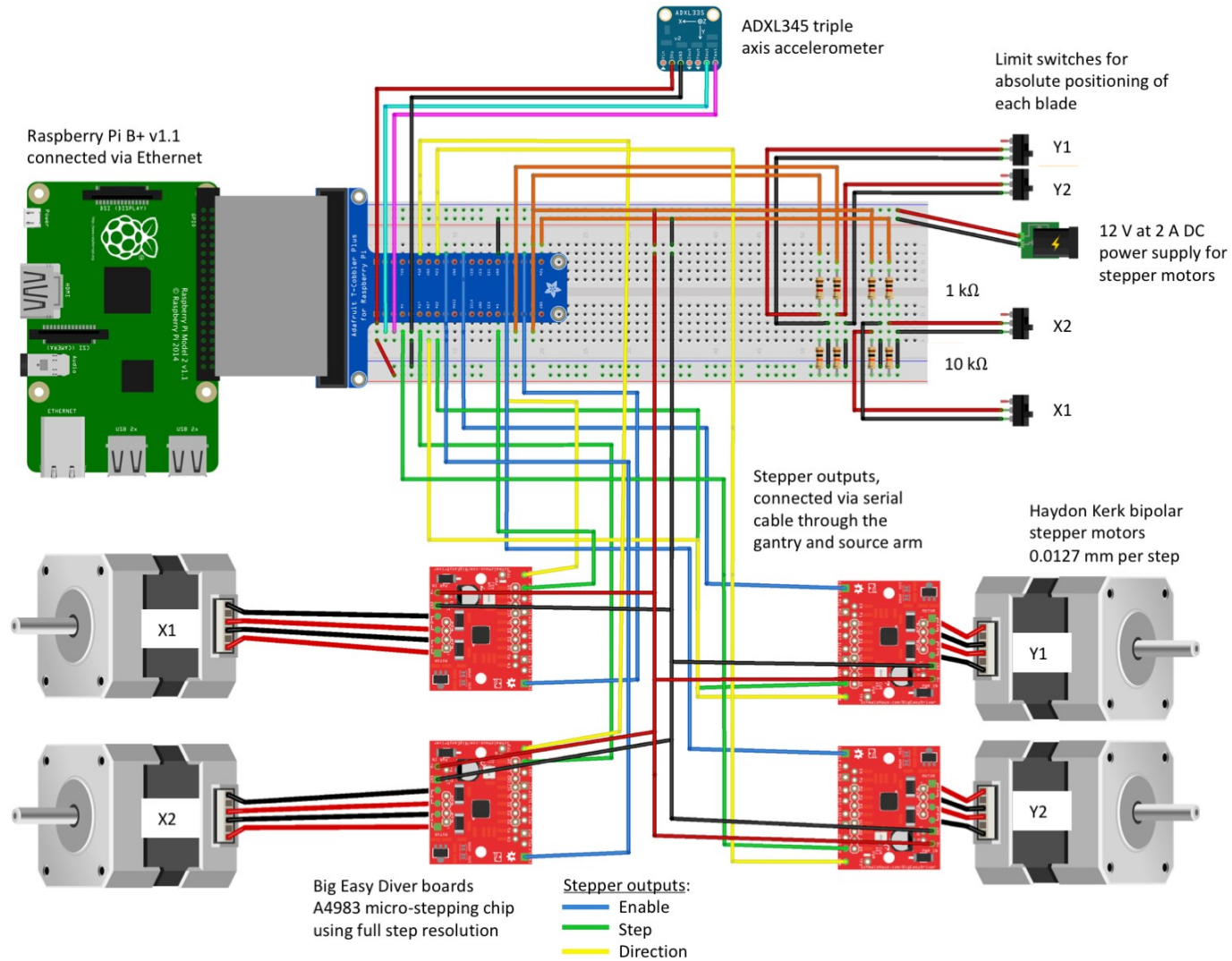
Figure 2.19   Robotic blade system wiring and component diagram.
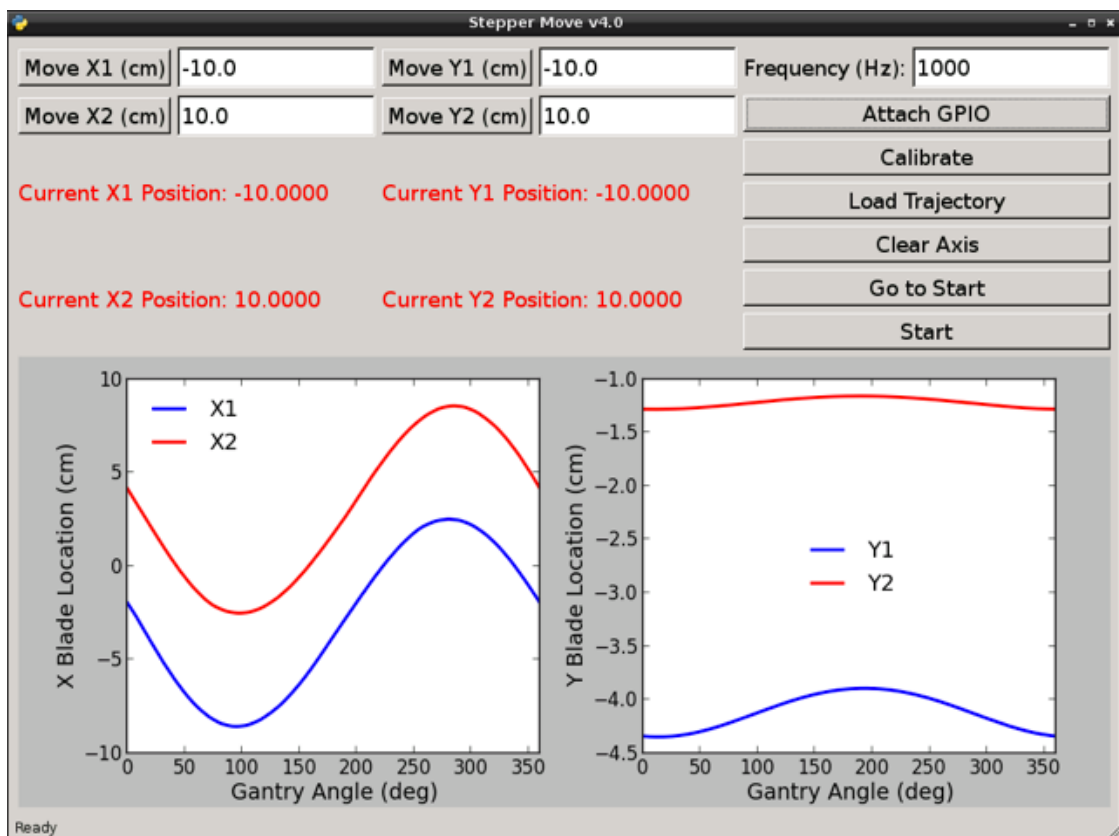
Figure 2.20   Robotic blade GUI in Python on the Raspberry Pi.
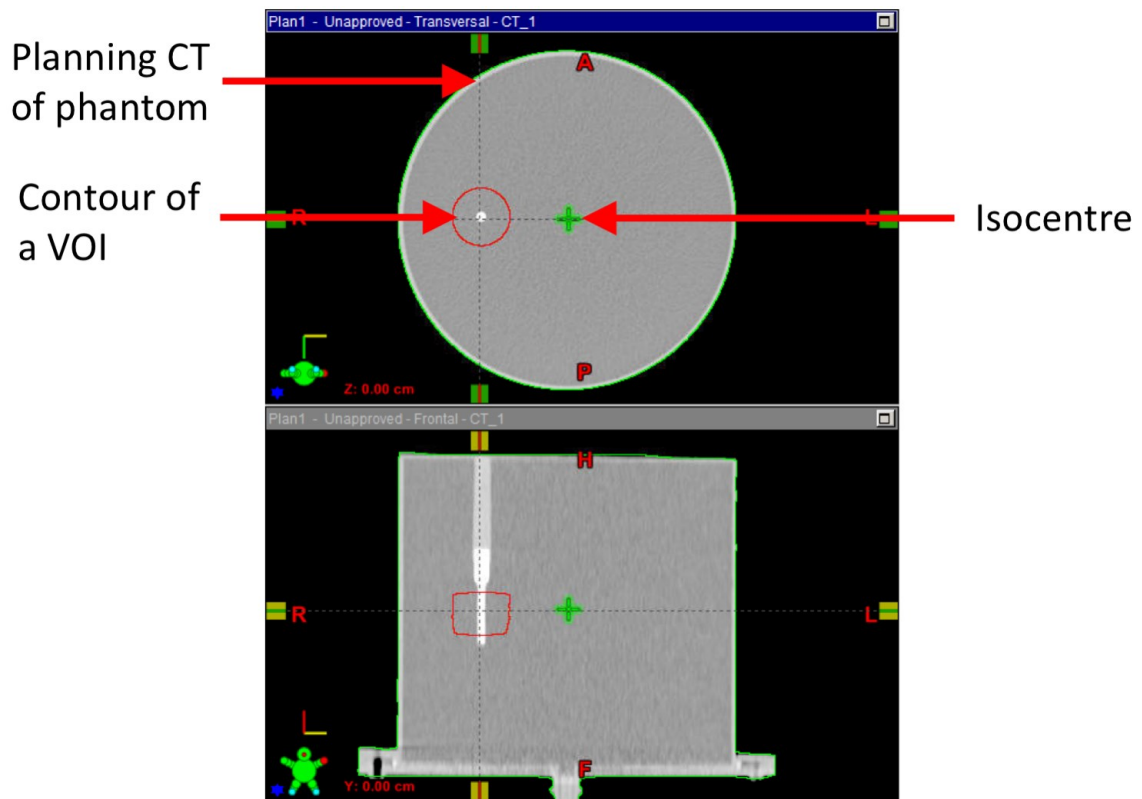
Figure 2.21   VOI drawn in the TPS for a bone insert located off axis in a uniform cylinder of water.

2.3.3 VOI Trajectory Calculation

To determine the trajectory of the iris or blades throughout the gantry rotation (such as that illustrated on the blade GUI in Figure 2.20), a VOI was first designed (Figure 2.21) in the Eclipse TPS (Varian Medical Systems, Inc., Palo Alto, CA). The structure metadata and contour coordinates are exported in DICOM RT format. These data were then used to determine the projection of structure vertices from a rotated point source onto a plane perpendicular to central axis and intersecting isocentre (Figure 2.22). The initial coordinates of the source (S), a contour (C), isocentre and the initial points on the plane

(P_1 and P_2) are described below as (note all coordinate points are transposed from how they are written below)

$$S = [x_s \quad y_s \quad z_s] = [1000 \quad 0 \quad 0] \qquad \text{Eq 2.24}$$

$$C = [x_c \quad y_c \quad z_c] \qquad \text{Eq 2.25}$$

$$P_1 = [0\ 1\ 0] \qquad \text{Eq 2.26}$$

$$P_2 = [0\ 1\ 1] \qquad \text{Eq 2.27}$$

$$iso = [0\ 0\ 0] \qquad \text{Eq 2.28}$$

The equation for the plane contain the points P_1, P_2 and isocentre is written as

$$0 = ax + by + cz \qquad \text{Eq 2.29}$$

where the coefficients a, b and c are defined by the vector normal to the plane, and is determined by

$$\vec{N} = \langle iso - P_1 \rangle \times \langle iso - P_2 \rangle \qquad \text{Eq 2.30}$$

At any angle θ, the source point and parallel plane intersecting isocentre can be determined by the rotation matrix

$$R = \begin{bmatrix} \cos\theta & \sin\theta & 0 \\ -\sin\theta & \cos\theta & 0 \\ 0 & 0 & 1 \end{bmatrix} \qquad \text{Eq 2.31}$$

$$\vec{S_R} = R(S - iso) \qquad \text{Eq 2.32}$$

$$\vec{N_R} = \langle iso - RP_1 \rangle \times \langle iso - RP_2 \rangle \qquad \text{Eq 2.33}$$

The projection line connecting each point C and S_R can be described as

$$x_L = Rx_s + t(x_c - Rx_s) \qquad \text{Eq 2.34}$$

$$y_L = Ry_s + t(y_c - Ry_s) \qquad \text{Eq 2.35}$$

$$z_L = Rz_s + t(z_c - Rz_s) \qquad \text{Eq 2.36}$$

the value t describes position along the projection. These set of equations can be simplified to

$$L = \overrightarrow{S_R} + t(\vec{C} - \overrightarrow{S_R})$$
Eq 2.37

where the vector $\vec{C}$ is defined as $(C - iso)$. The projection line intersects the rotated plane when

$$0 = ax_L + by_L + cz_L$$
Eq 2.38

$$0 = a(Rx_s + t(x_c - Rx_s)) + b(Ry_s + t(y_c - Ry_s))$$
$$+ c(Rz_s + t(z_c - Rz_s))$$
Eq 2.39

The above equation can then be rearranged using dot products and solved for t

$$0 = \vec{N}_R \cdot \overrightarrow{S_R} + t\vec{N}_R \cdot (\vec{C} - \overrightarrow{S_R})$$
Eq 2.40

$$t = \frac{\vec{N}_R \cdot \overrightarrow{S_R}}{\vec{N}_R \cdot (\vec{C} - \overrightarrow{S_R})}$$
Eq 2.41

With this the projected coordinates are determined and stored and the process repeated for each value of C. The convex hull of the projected points is then taken. Thereafter, the collimation is fitted to, for the iris specifically, the center of the iris is positioned at the centroid of the projected points and radius extended to the outer most surface of the convex hull. This process is then repeated in one degree increments of θ.
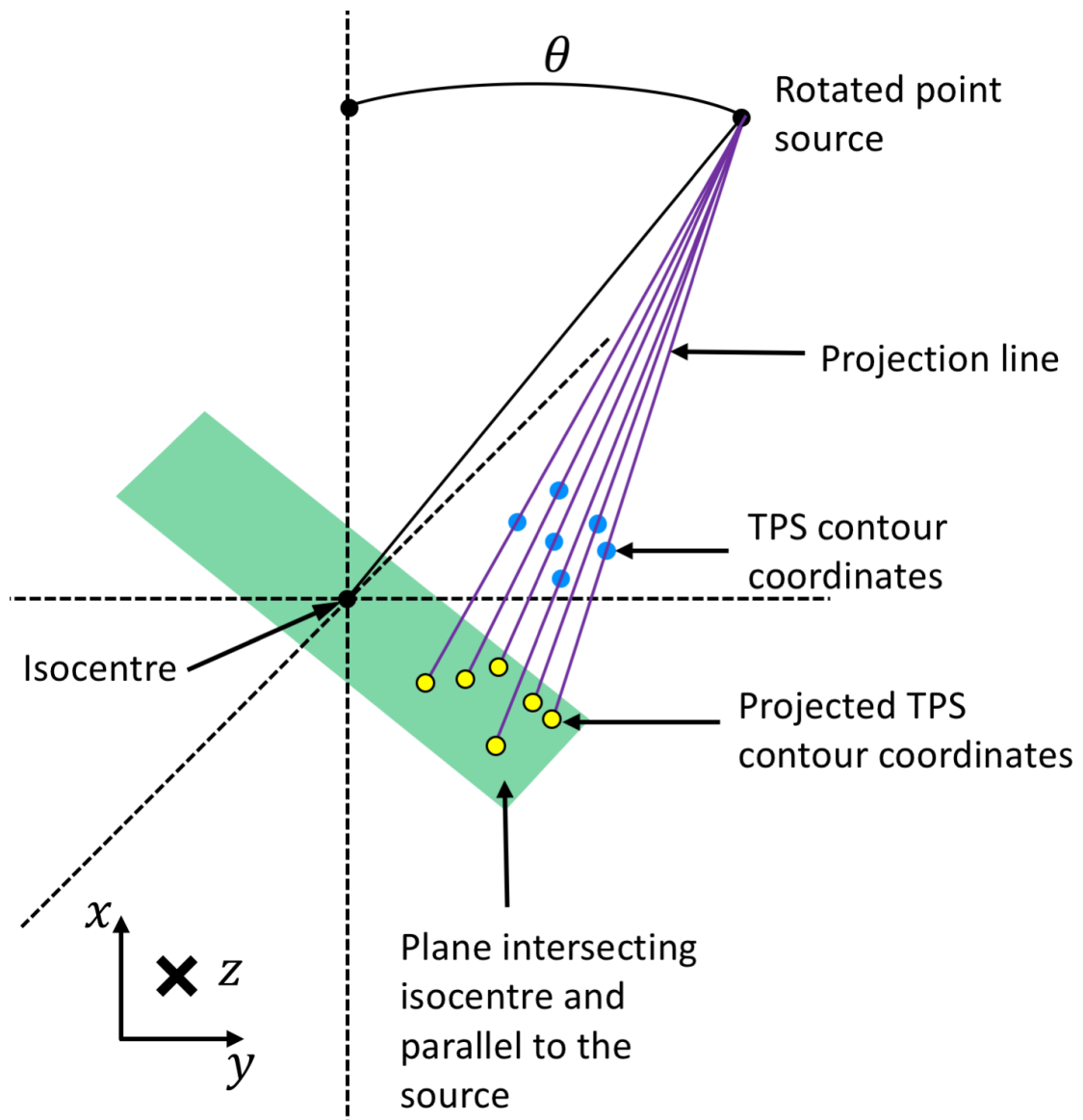
Figure 2.22   Illustration of the VOI structure set being projected onto a plane which intersects isocentre and perpendicular to central axis .

2.4   Tube Current Modulation

The robotic blade collimator was used in combination with TCM to further improve the available image quality for a given dose to the VOI. This is described in detail in Chapter 4. This technique aims at adapting tube current in proportion with the attenuation through the patient at a given angle, thereby reducing imaging dose yet maintaining image quality (Figure 2.23). TCM is a well-established technique in CT[71], but has been yet to introduced to conventional (non-VOI) CBCT.
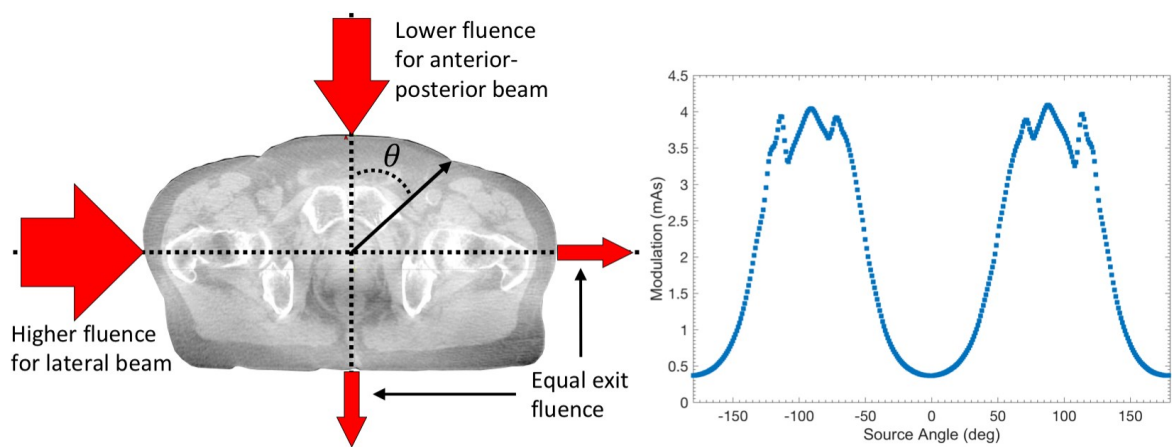
Figure 2.23   Illustrating the premise of tube current modulation, in which the incident fluence is increased or decreased in accordance with attenuation. This ideally results in approximately equal fluence at the detector plane.

2.4.1 Attenuation Calculation

To calculate tube current modulation curves as a function of tube angle, attenuation maps were calculated using the pre-existing CT data from the TPS. Using CT data, the radiologic path length through the phantom was determined from a setup that mimicked the

experimental setup, i.e. a source location 100 cm and detector plane 50 cm from the axis

of rotation. Siddon's method[72] was used to calculate all attenuation maps. For

simplification, the algorithm is demonstrated for the 2D example in Figure 2.24.
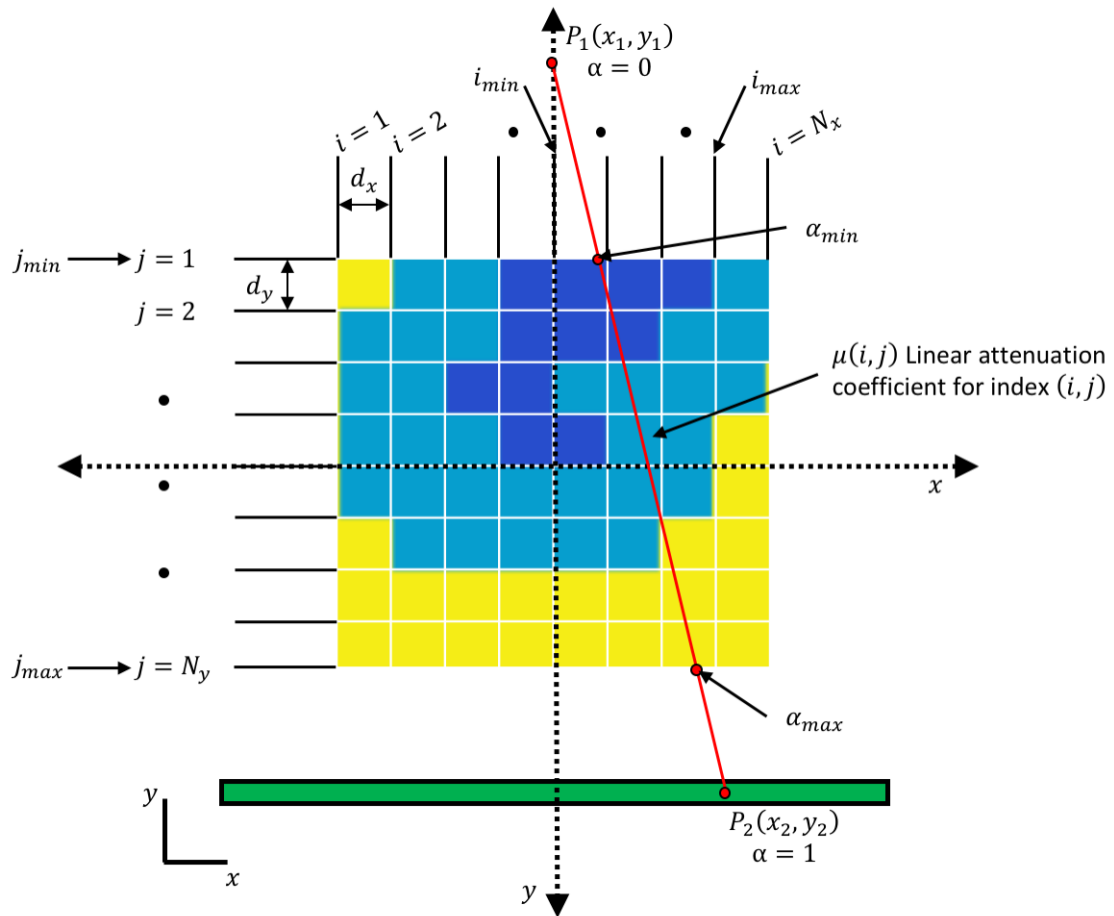
Figure 2.24   Illustration of Siddon's method for calculating the radiologic path through a 2D array of linear attenuation coefficients from P_1 to P_2.

Figure 2.24 describes Siddon's method for a ray emitted at P_1 (the source) and travelling

to P_2 (a point on the detector plane) through an array of linear attenuation coefficients

$\mu(i,j)$, at a pixel index i,j. The coordinates of the array are described as a series of planes

X_i and Y_j separated by a distance d_x and d_y (the x- and y- pixel dimensions).

$$X_i = X_o + id_x \qquad for \; i = 1, 2, \dots, N_i \qquad\qquad \text{Eq 2.42}$$

$$Y_j = Y_o + jd_y \qquad for \; j = 1, 2, \dots, N_j \qquad\qquad \text{Eq 2.43}$$

The path of the ray through the image from $P_1(x_1, y_1)$ to $P_2(x_2, y_2)$ can be represented

parametrically as α. In which α describes the position along the line from P_1 to P_2 and is

zero at P_1 and one at P_2. In this system, P_1 and P_2 represent a point source and detector

plane, respectively.

$$x(\alpha) = x_1 + \alpha(x_2 - x_1) \qquad\qquad \text{Eq 2.44}$$

$$y(\alpha) = y_1 + \alpha(y_2 - y_1) \qquad\qquad \text{Eq 2.45}$$

where x and y are coordinates along the ray line. The parameter α can then be used to

determine the intersection of the ray line with planes X_i and Y_j (i.e. a change in μ)

$$\alpha_x(i) = \frac{X_o + id_x - x_1}{x_2 - x_1} \qquad\qquad \text{Eq 2.46}$$

$$\alpha_y(j) = \frac{Y_o + jd_y - y_1}{y_2 - y_1} \qquad\qquad \text{Eq 2.47}$$

The values of α are calculated for all the intersections between the ray and 2D array of

coefficients, such that

$$\alpha_x = [\alpha_x(i_{min}), \dots, \alpha_x(i_{max})] \qquad\qquad \text{Eq 2.48}$$

$$\alpha_y = [\alpha_y(j_{min}), \dots, \alpha_y(j_{max})] \qquad\qquad \text{Eq 2.49}$$

where min and max are the first and last planes to intersect the array. In the algorithm

Siddon[72] subsequently, merges α_x and α_y in ascending order, such that each increasing

value marks the interception with a plane (i.e. changing linear attenuation value)

60

$$\alpha_{xy} = \left[\alpha_{min}, \text{merge}(\alpha_x, \alpha_y), \alpha_{max}\right] \qquad \text{Eq 2.50}$$

α_{xy} is then used to calculate the length traveled in a pixel (voxel) from two consecutive

elements of α_{xy}, m and $m-1$, starting at the second index of α_{xy} to the last

$$l(m) = \left[\alpha_{xy}(m) - \alpha_{xy}(m-1)\right]d_{ray} \qquad \text{Eq 2.51}$$

where d_{ray} is length of the ray from P_1 to P_2. The indices of the 2D array are then

determined for each element m as

$$i(m) = \left\lfloor \frac{x_1 + \alpha_{mid}(x_2 - x_1) - X_0}{d_x} \right\rfloor \qquad \text{Eq 2.52}$$

$$j(m) = \left\lfloor \frac{y_1 + \alpha_{mid}(y_2 - y_1) - Y_0}{d_y} \right\rfloor \qquad \text{Eq 2.53}$$

$$\alpha_{mid} = \frac{\alpha_{xy}(m) + \alpha_{xy}(m-1)}{2} \qquad \text{Eq 2.54}$$

where $\lfloor \ \ \rfloor$ is floor function. The total radiological path (RLP) for the ray from P_1 to P_2 is

then

$$RLP = d_{ray} \sum_{m=2}^{N} \mu(i(m), j(m)) \left[\alpha_{xy}(m) - \alpha_{xy}(m-1)\right] \qquad \text{Eq 2.55}$$

This process can then be summarized as:

1. Load CT data and convert to linear attenuation coefficients

2. Determine min and max planes from CT data

3. Setup detector plane, i.e. 20 x 20 cm^2 with 4 mm grid spacing

4. For each element in detector space:

   i. Determine the min and max indices of planes that intersect the ray

   ii. Calculate the parametric values α_x, α_y and α_z and merge to form α_{xyz}

iii. From each index of α_{xyz} for $m \in [2 \dots N]$ calculate and sum the RLP of the ray

iv. Multiply by the length of the ray

5. Repeat for rotation of the source and detector plane, i.e. from 1° to 360° in 1° increments

Similar to Siddon[72], most of the calculation time is spent in steps ii and iii of the process. The calculation of the radiologic path is only an approximation as the linear attenuation coefficient arrays were formed for a 60 keV mono-energetic photon beam. This could be made more accurate by using a poly-energetic set of linear attenuation coefficients. The use of these attenuation maps for tube current modulation are explained in detail in Chapter 4 and Chapter 5.

2.5 INTRAFRACTION IMAGING

Intrafraction imaging simultaneous to the MV treatment beam delivery has become desirable for monitoring of internal motion of the target volume or of a surrogate structure. Similar to CBCT, intrafraction image quality varies throughout the rotation due to kV attenuation; however, it is additionally confounded by the presence of MV scatter radiation from the patient. Recently, van Herk *et al.*[63] and Ling *et al.*[62] demonstrated two methods to mitigate MV scatter for CBCT during VMAT, however they do not address the variation in image quality with kV attenuation. The combination of VOI and TCM were explored to improve the available image quality for intrafraction monitoring.

2.5.1 Monoscopic estimation of prostate motion

To determine prostate motion, gold fiducial markers were imaged and the three dimensional (3D) position estimated using the method described by Poulsen *et al*.[60] When imaging the projection of a fiducial marker with the setup illustrated in Figure 2.25 two directions of motion are resolvable, i.e., those of the detector plane. However, the position along a ray line is unresolved. In 2008, Poulsen *et al.*[60] recognized that due to i) the highly correlated motion that exists between SI and AP motion for the prostate, ii) the fact that the SI direction always being identified during imaging, and iii) minimal lateral motion of the prostate (Figure 1.7), the 3D position of the prostate could be estimated. The approach by Poulsen *et al.*[60] is described in detail in the following pages.
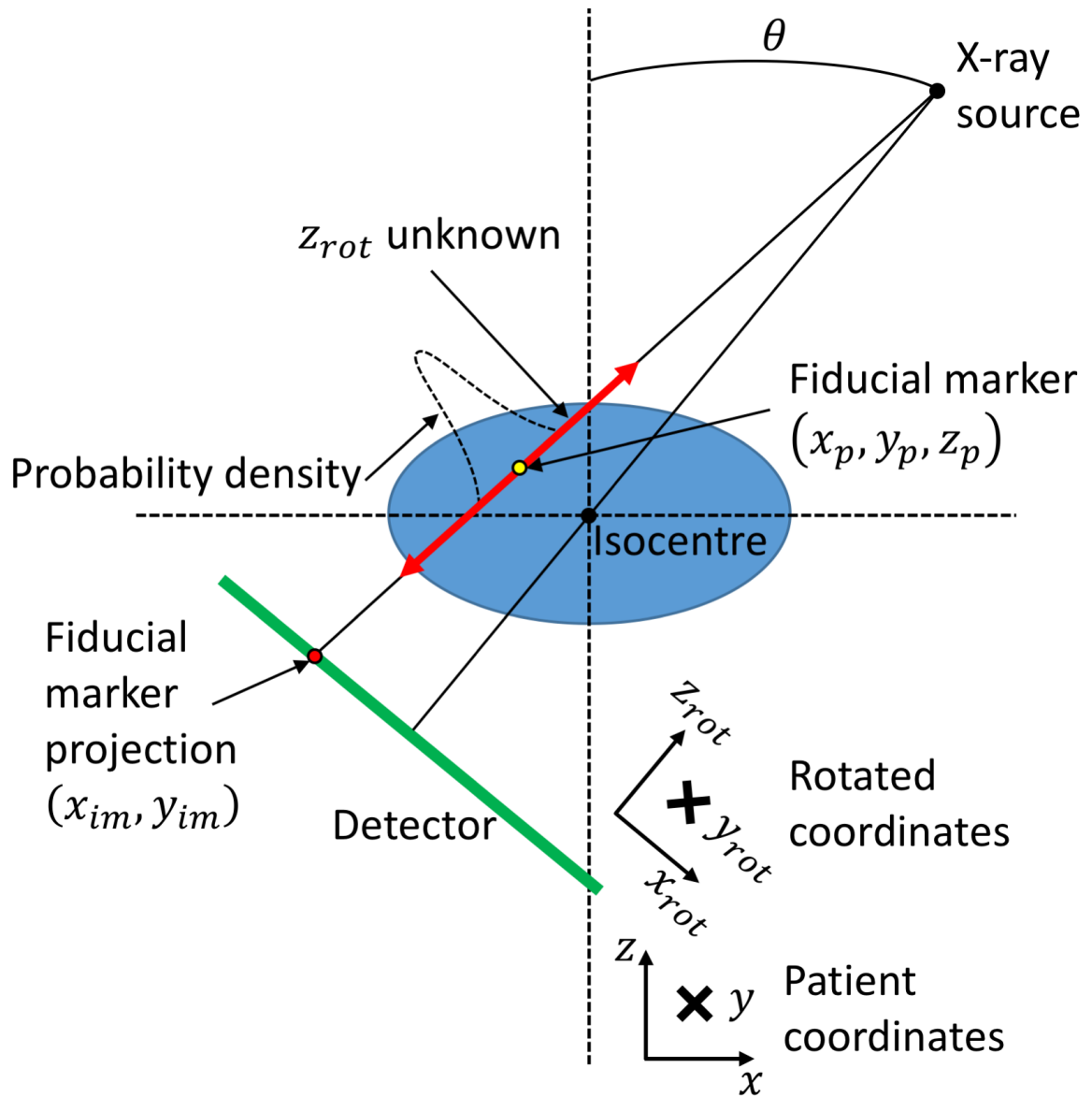
Figure 2.25   Monoscopic imaging at a source rotation θ of a fiducial marker at (x_p, y_p, z_p) in patient coordinates. This results in a projected fiducial marker at (x_{im}, y_{im}) in image coordinates, with an unknown location along the ray line, z_{rot} in rotated coordinates. Using a 3D Gaussian probability distribution, the unknown fiducial marker position is estimated. Figure adapted from Poulsen $et\ al.$[60]

The 3D Gaussian distribution describing the probability distribution of prostate motion as described by Poulsen *et al.*[60] in the patient coordinate system is

$$P(x_p, y_p, z_p) = \frac{\sqrt{det(\Sigma^{-1})}}{(2\pi)^{3/2}} exp(-\vec{r}^T \Sigma^{-1} \vec{r}) \qquad \text{Eq 2.56}$$

$$= \frac{\sqrt{det(\Sigma^{-1})}}{(2\pi)^{3/2}} exp\left(-\frac{1}{2}[Ax^2 + By^2 + Cz^2 + Dxy + Exz + Fyz]\right) \qquad \text{Eq 2.57}$$

where $\vec{r} = \begin{bmatrix} x_p \\ y_p \\ z_p \end{bmatrix}$ and Σ is the covariance matrix describing prostate motion

$$\Sigma = \begin{bmatrix} \sigma_x^2 & \sigma_x\sigma_y & \sigma_x\sigma_z \\ \sigma_x\sigma_y & \sigma_y^2 & \sigma_y\sigma_z \\ \sigma_x\sigma_z & \sigma_y\sigma_z & \sigma_z^2 \end{bmatrix} \qquad \text{Eq 2.58}$$

$$\Sigma = \begin{bmatrix} 0.32 & 0.01 & -0.08 \\ 0.01 & 1.88 & 1.51 \\ -0.08 & 1.51 & 2.47 \end{bmatrix} \qquad \text{Eq 2.59}$$

$$\Sigma^{-1} = \begin{bmatrix} A & D/2 & E/2 \\ D/2 & B & F/2 \\ E/2 & F/2 & C \end{bmatrix} \qquad \text{Eq 2.60}$$

The population covariance matrix from Poulsen *et al.*[60] was used (Eq 2.59) in this work. This was determined from 536 prostate trajectories recorded using the Calypso (Varian Medical Systems, Inc., Palo Alto, CA) RF beacon system. As demonstrated in Eq 2.59 and Figure 2.26, high correlation exists between AP and SI motion. For a source rotation of θ, and rotation matrix

$$R = \begin{bmatrix} \cos\theta & 0 & \sin\theta \\ 0 & 1 & 0 \\ -\sin\theta & 0 & \cos\theta \end{bmatrix} \qquad \text{Eq 2.61}$$

the distribution from Eq 2.57 in the rotated coordinate system becomes

$$P(x_{rot}, y_{rot}, z_{rot}) = \frac{\sqrt{det(\Sigma^{-1})}}{(2\pi)^{\frac{3}{2}}} exp(-\vec{r}_{rot}^T R\Sigma^{-1}R^{-1}\vec{r}_{rot})$$

Eq 2.62

$$P(x_{rot}, y_{rot}, z_{rot})$$

$$= \frac{\sqrt{det(\Sigma^{-1})}}{(2\pi)^{3/2}} exp\left(-\frac{1}{2}[A_{rot}x_{rot}^2 + B_{rot}y_{rot}^2\right.$$

$$+ C_{rot}z_{rot}^2 + D_{rot}x_{rot}y_{rot} + E_{rot}x_{rot}z_{rot}$$

$$\left. + F_{rot}y_{rot}z_{rot}]\right)$$

Eq 2.63

where

$$R\Sigma^{-1}R^{-1} = \begin{bmatrix} A_{rot} & D_{rot}/2 & E_{rot}/2 \\ D_{rot}/2 & B_{rot} & F_{rot}/2 \\ E_{rot}/2 & F_{rot}/2 & C_{rot} \end{bmatrix}$$

Eq 2.64

The line from the rotated source at $(0, 0, SAD)$ and the image point $(x_{im}, y_{im}, -ADD)$, where SAD is the source-to-axis distance and ADD is the axis-to-detector distance, in the rotated coordinate system can be used to write the fiducial marker location in terms of z_{rot} as

$$(x_{rot}, y_{rot}, z_{rot}) = \left(\frac{SAD - z_{rot}}{SDD} x_{im}, \frac{SAD - z_{rot}}{SDD} y_{im}, z_{rot}\right)$$

Eq 2.65

With Eq 2.65 the exponent from Eq 2.63 can be expanded by substituting for x_{rot} and y_{rot} in terms of the known x_{im} and y_{im} within the image.
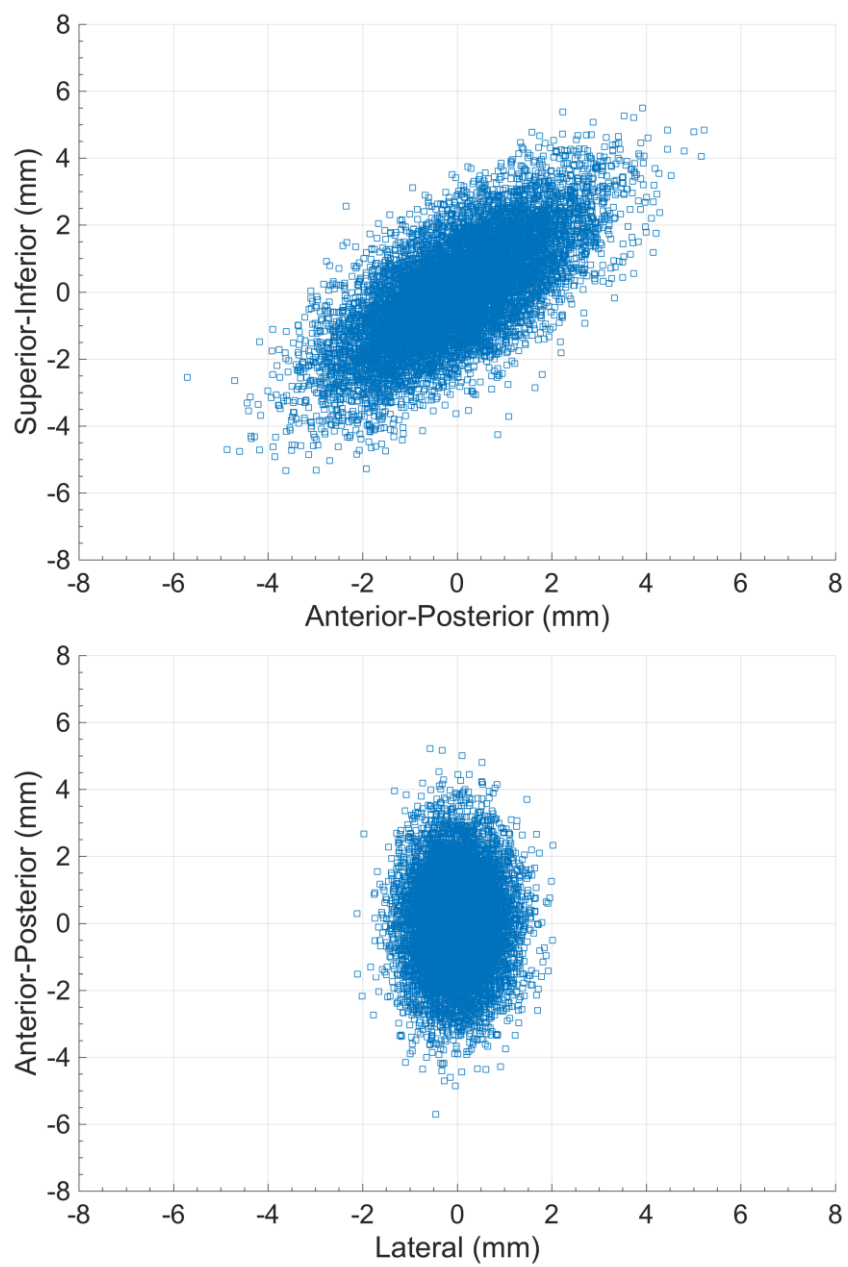
Figure 2.26   3D probability distribution of prostate motion for 10000 points. From the chosen view angle, the correlation between SI and AP motion can be observed.

$$2\vec{r}_{rot}^{T}R\Sigma^{-1}R^{-1}\vec{r}_{rot} \quad = \quad \frac{A_{rot}x_{im}^{2}}{SDD^{2}}(SAD - z_{rot})^{2} + \frac{B_{rot}y_{im}^{2}}{SDD^{2}}(SAD - z_{rot})^{2}$$

$$+ \; C_{rot}z_{rot}^{2} + \frac{D_{rot}x_{im}y_{im}}{SDD^{2}}(SAD - z_{rot})^{2}$$

Eq 2.66

$$+ \; E_{rot}\frac{SAD - z_{rot}}{SDD}x_{im}z_{rot}$$

$$+ \; F_{rot}\frac{SAD - z_{rot}}{SDD}y_{im}z_{rot}$$

This can then be grouped in terms of the unknowns $z_{rot}{}^{2}$, z_{rot} and known values

$$2\vec{r}_{rot}^{T}R\Sigma^{-1}R^{-1}\vec{r}_{ro} \quad = \quad z_{rot}^{2}\left[\frac{A_{rot}x_{im}^{2}}{SDD^{2}} + \frac{B_{rot}y_{im}^{2}}{SDD^{2}} + C_{rot} + \frac{D_{rot}x_{im}y_{im}}{SDD^{2}}\right.$$

$$\left. - \; \frac{E_{rot}x_{im}}{SDD} - \frac{F_{rot}y_{im}}{SDD}\right]$$

$$- \; 2z_{rot}SAD\left[\frac{A_{rot}x_{im}^{2}}{SDD^{2}} + \frac{B_{rot}y_{im}^{2}}{SDD^{2}}\right.$$

Eq 2.67

$$\left. + \; \frac{D_{rot}x_{im}y_{im}}{SDD^{2}} - \frac{E_{rot}x_{im}}{2SDD} - \frac{F_{rot}y_{im}}{2SDD}\right]$$

$$+ \; SAD^{2}\left[\frac{A_{rot}x_{im}^{2}}{SDD^{2}} + \frac{B_{rot}y_{im}^{2}}{SDD^{2}} + \frac{D_{rot}x_{im}y_{im}}{SDD^{2}}\right]$$

Poulsen *et al.* [60] then make two substitutions for the coefficients of z_{rot}^{2} and z_{rot}, such

that

$$\sigma^{2} = \left[\frac{A_{rot}x_{im}^{2}}{SDD^{2}} + \frac{B_{rot}y_{im}^{2}}{SDD^{2}} + C_{rot} + \frac{D_{rot}x_{im}y_{im}}{SDD^{2}} - \frac{E_{rot}x_{im}}{SDD} - \frac{F_{rot}y_{im}}{SDD}\right] \quad \text{Eq 2.68}$$

$$\langle z_{\parallel}\rangle = \sigma^{2}SAD\left[\frac{A_{rot}x_{im}^{2}}{SDD^{2}} + \frac{B_{rot}y_{im}^{2}}{SDD^{2}} + \frac{D_{rot}x_{im}y_{im}}{SDD^{2}} - \frac{E_{rot}x_{im}}{2SDD} - \frac{F_{rot}y_{im}}{2SDD}\right] \quad \text{Eq 2.69}$$

Eq 2.67 then becomes

$$2\vec{r}_{rot}^{T} R\Sigma^{-1}R^{-1}\vec{r}_{rot} \quad = \quad \frac{1}{\sigma^2}[z_{rot}^2 - 2z_{rot}\langle z_\parallel \rangle] +$$

$$SAD^2\left[\frac{A_{rot}x_{im}^2}{SDD^2} + \frac{B_{rot}y_{im}^2}{SDD^2} + \frac{D_{rot}x_{im}y_{im}}{SDD^2}\right]$$

Eq 2.70

$$2\vec{r}_{rot}^{T} R\Sigma^{-1}R^{-1}\vec{r}_{rot} \quad = \quad \frac{1}{\sigma^2}[z_{rot}^2 - 2z_{rot}\langle z_\parallel \rangle + \langle z_\parallel \rangle^2 - \langle z_\parallel \rangle^2] +$$

$$SAD^2\left[\frac{A_{rot}x_{im}^2}{SDD^2} + \frac{B_{rot}y_{im}^2}{SDD^2} + \frac{D_{rot}x_{im}y_{im}}{SDD^2}\right]$$

Eq 2.71

$$2\vec{r}_{rot}^{T} R\Sigma^{-1}R^{-1}\vec{r}_{rot} \quad = \quad \frac{1}{\sigma^2}(z_{rot} - \langle z_\parallel \rangle)^2 - \frac{\langle z_\parallel \rangle^2}{\sigma^2} +$$

$$SAD^2\left[\frac{A_{rot}x_{im}^2}{SDD^2} + \frac{B_{rot}y_{im}^2}{SDD^2} + \frac{D_{rot}x_{im}y_{im}}{SDD^2}\right]$$

Eq 2.72

At this point the exponents independent of z_{rot} are separated into a constant K such that

$$P(z_{rot}) = K exp\left(\frac{(z_{rot} - \langle z_\parallel \rangle)^2}{2\sigma^2}\right)$$

Eq 2.73

$$K = \frac{\sqrt{det(\Sigma^{-1})}}{(2\pi)^{3/2}} exp\left(\frac{1}{2}\left[SAD^2\left[\frac{A_{rot}x_{im}^2}{SDD^2} + \frac{B_{rot}y_{im}^2}{SDD^2} + \frac{D_{rot}x_{im}y_{im}}{SDD^2}\right] - \frac{\langle z_\parallel \rangle^2}{\sigma^2}\right]\right)$$

Eq 2.74

Eq 2.73 represents the 1D Gaussian probability distribution illustrated in Figure 2.25, for

z_{rot} on the ray line between the source and the image point (x_{im}, y_{im}), with $\langle z_\parallel \rangle$ giving

the expectation value for z_{rot}. With this, x_{rot} and y_{rot} can be determined (Eq 2.65) and

transformed to patient coordinates using inverse rotation matrix of Eq 2.61.

Using this approach Ng et al.[38] reported an accuracy of 0.46 mm after 4803

projections taken in a pre-clinical trial (seven patients) compared to triangulation with

MV projections. This was updated by Keall *et al.*[61] after 47320 projections into a clinical trial to give a mean error of 0.17, 0.55, and -0.61 mm, for lateral, SI and AP directions, respectively.

2.6 MONTE CARLO SIMULATION

In radiation therapy, Monte Carlo simulations are considered the gold standard for modeling the transport and interaction of ionizing radiation in matter. Monte Carlo simulations use uniform random number sampling of known probability distributions to model a stochastic process. The Monte Carlo process can be described using Figure 2.27 for simulation of photon transport and interaction in a medium. For a photon with a given energy and direction, the point of interaction within the medium is first simulated. This is determined by utilizing the probability of interacting after path length x in the medium

$$p(x)dx = \mu exp(-\mu x)dx$$

<div align="right">Eq 2.75</div>

The mean free path (or macroscopic cross section) can then be written as

$$\langle x \rangle = \int_0^\infty xp(x)dx = \int_0^\infty x\mu exp(-\mu x)dx$$

<div align="right">Eq 2.76</div>

The number of mean free paths would then be

$$\lambda = \frac{x}{\langle x \rangle} = \mu x$$

<div align="right">Eq 2.77</div>

Using Eq 2.77, x could then be substituted for in Eq 2.75 and expressed as the number of mean free paths

$$p(\lambda)d\lambda = exp(-\lambda)d\lambda \qquad\qquad \text{Eq 2.78}$$

$$p(\lambda) = \int_{0}^{\lambda} exp(-\lambda)d\lambda \qquad\qquad \text{Eq 2.79}$$

$$p(\lambda) = 1 - exp(-\lambda) \qquad\qquad \text{Eq 2.80}$$

In this form, it is independent of the medium traversed and $p(\lambda)$ can be expressed as a random number, ζ in the domain of $[0, 1)$. The number of mean free paths and therefore x, can then be determined as

$$\lambda = -ln(1 - \zeta) \qquad\qquad \text{Eq 2.81}$$

$$x = \frac{\lambda}{\mu} = \frac{-ln(1 - \zeta)}{\mu} \qquad\qquad \text{Eq 2.82}$$

$$x = \frac{-ln(1 - \zeta)}{\rho N_A \sum_i \left[\frac{\omega_i}{A_i}\mu_i\right]} \qquad\qquad \text{Eq 2.83}$$

where N_A is Avogadro's number, ρ is the density, ω_i and A_i are the proportion by mass and mass of a mole, respectively, of the ith element in the material. The use of Eq 2.82 is demonstrated in Figure 2.28 for 100 keV photons interacting in a uniform water medium. As demonstrated, as the number of events increases, the probability density approaches the expected attenuation for the medium.

Select energy, position, direction of initial photon for the stack

Take energy, position, direction of current particle from top of stack

Is stack empty? — Yes / No

Is energy < cut-off — Yes

Terminate transport

Select distance to next interaction (i.e. $x = -\ln(1 - \zeta)/\mu$)

Has particle left the region of interest? — Yes / No

Select interaction type (Rayleigh, PE, Compton or Pair)

Determine energies and direction of primary and secondary particles and put them on the stack

Figure 2.27   Simplistic flow chart of Monte Carlo simulation for photons. Adapted from *The Handbook of Radiotherapy Physics*[73].
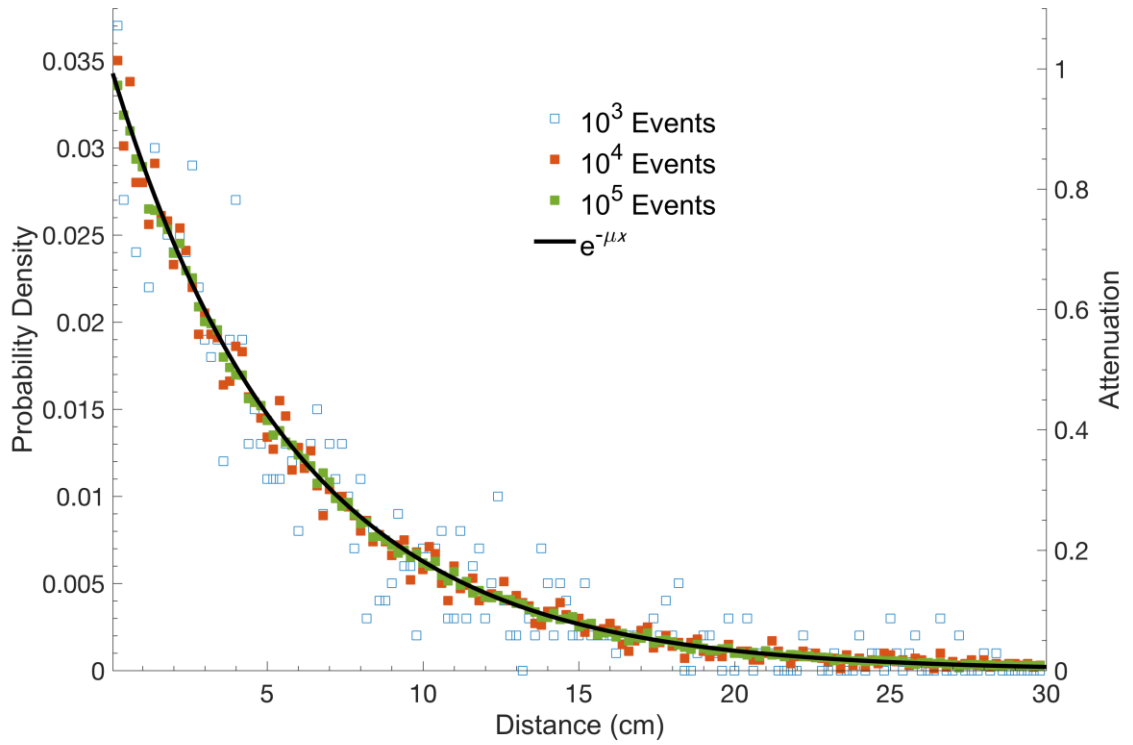
Figure 2.28   Sampled first interaction distance for 10^3, 10^4 and 10^5 100 keV photons in water. Overlaid with attenuation.

This is the implementation to determine the depth of photon interactions in the original

EGS (electron gamma shower) Monte Carlo code developed at the Stanford Linear

Accelerator Center (SLAC) and later at the National Research Council (NRC) as described

by Ford and Nelson[74] and Kawrakow *et al.*[75] After the depth of interaction is chosen, the

type of interaction is determined. Recognizing that the linear attenuation coefficient is

the sum of interaction coefficients for all interactions, a set of domains can be defined for

random sampling.

$$\mu(E) = \sigma_R(E) + \tau(E) + \sigma_C(E) + \kappa(E) \qquad \text{Eq 2.84}$$

where σ_R, τ, σ_C and κ are Rayleigh, photoelectric, Compton and pair production. These are similarly sampled using a uniform random number in the domain $[0, 1]$ such that

$$
\left[0, \frac{\sigma_R}{\mu}\right) \quad : \text{Rayleigh}
$$

$$
\left[\frac{\sigma_R}{\mu}, \frac{1}{\mu}(\sigma_R + \tau)\right) \quad : \text{Photoelectric}
$$

$$
\left[\frac{1}{\mu}(\sigma_R + \tau), \frac{1}{\mu}(\sigma_R + \tau + \sigma_C)\right) \quad : \text{Compton}
$$

$$
\left[\frac{1}{\mu}(\sigma_R + \tau + \sigma_C), 1\right] \quad : \text{Pair Production}
$$

Eq 2.85

From this point the kinematics of the individual process are simulated. For example, Compton interactions are sampled from the Klein-Nishina differential cross-section per atom

$$
\frac{d\sigma_C}{d\varepsilon} = \pi r_e^2 \frac{m_e c^2}{E_0} Z \left[\frac{1}{\varepsilon} + \varepsilon\right]\left[1 - \frac{\varepsilon \sin^2 \theta}{1 + \varepsilon^2}\right]
$$

Eq 2.86

$$
\varepsilon = \frac{E_1}{E_0} = \frac{1}{1 + \frac{E_0}{m_e c^2}(1 - \cos\theta)}
$$

Eq 2.87

where E_0 is the energy of the incident photon, E_1 is the energy of the scattered photon, θ is the angle of the scattered photon relative to the incident photon, $m_e c^2$ is the rest energy of an electron, Z is the atomic number and r_e is the classical electron radius (2.8179x10^{-15} m). As an illustration, this was used to generate Figure 2.29 for the secondary and Compton electron scatter angle for 200 000 Compton events at various energies. After simulating the interaction and obtaining the products of the interaction, the Monte Carlo process is repeated for those products (i.e. depth of interaction determined for the scattered photon from the Compton interaction).
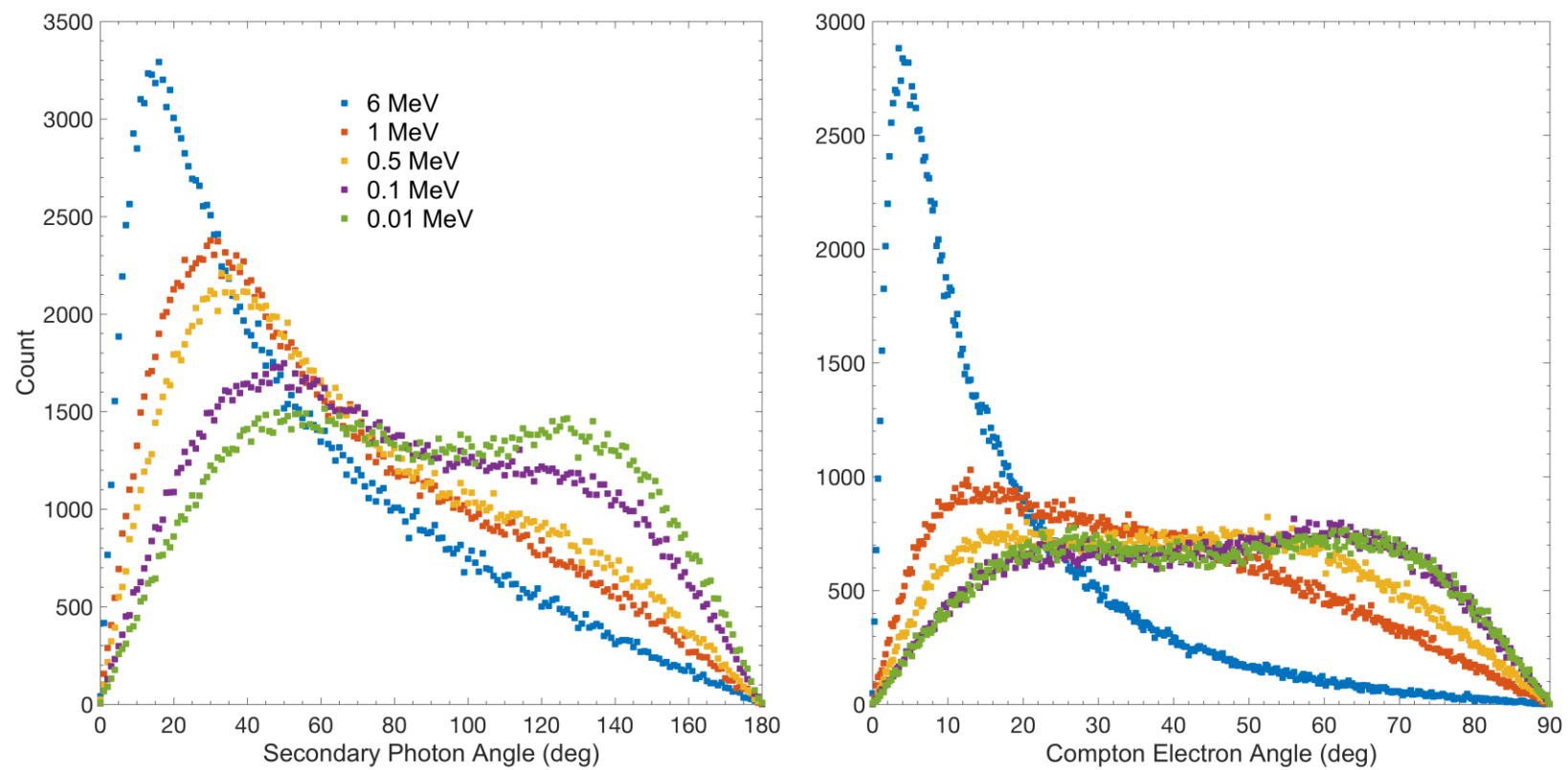
Figure 2.29   Sampled scattered photon and electron angle for various incident photon energies for 200 000 Compton events.

Monte Carlo simulations were primarily used to simulate kV imaging dose deposited in a

phantom. This was accomplished using the BEAMnrc[76] and DOSXYZnrc[77] user codes and

is described in detail in sections 3.4.3, 4.4.3, 5.4.7 and 0.
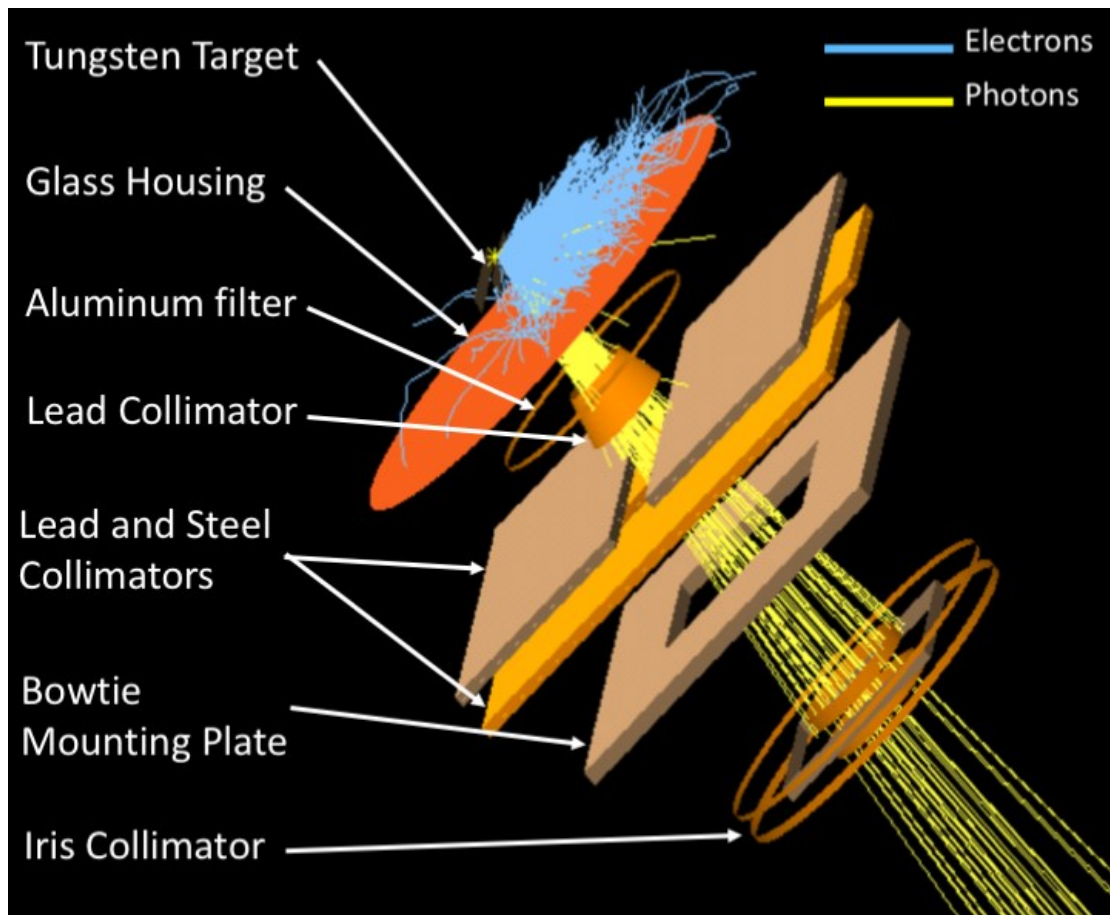
Figure 2.30   BEAMnrc model of the OBI with the dynamic iris collimator.

Figure 2.30 displays the BEAMnrc model of the OBI on a 2100 iX Varian linear accelerator

(Varian Medical Systems, Inc., Palo Alto, CA) with attached dynamic iris collimator. Figure

2.31 contains select measured and simulated relative depth dose curves of the OBI x-ray tube used in validating the Monte Carlo model with and without the iris collimator.
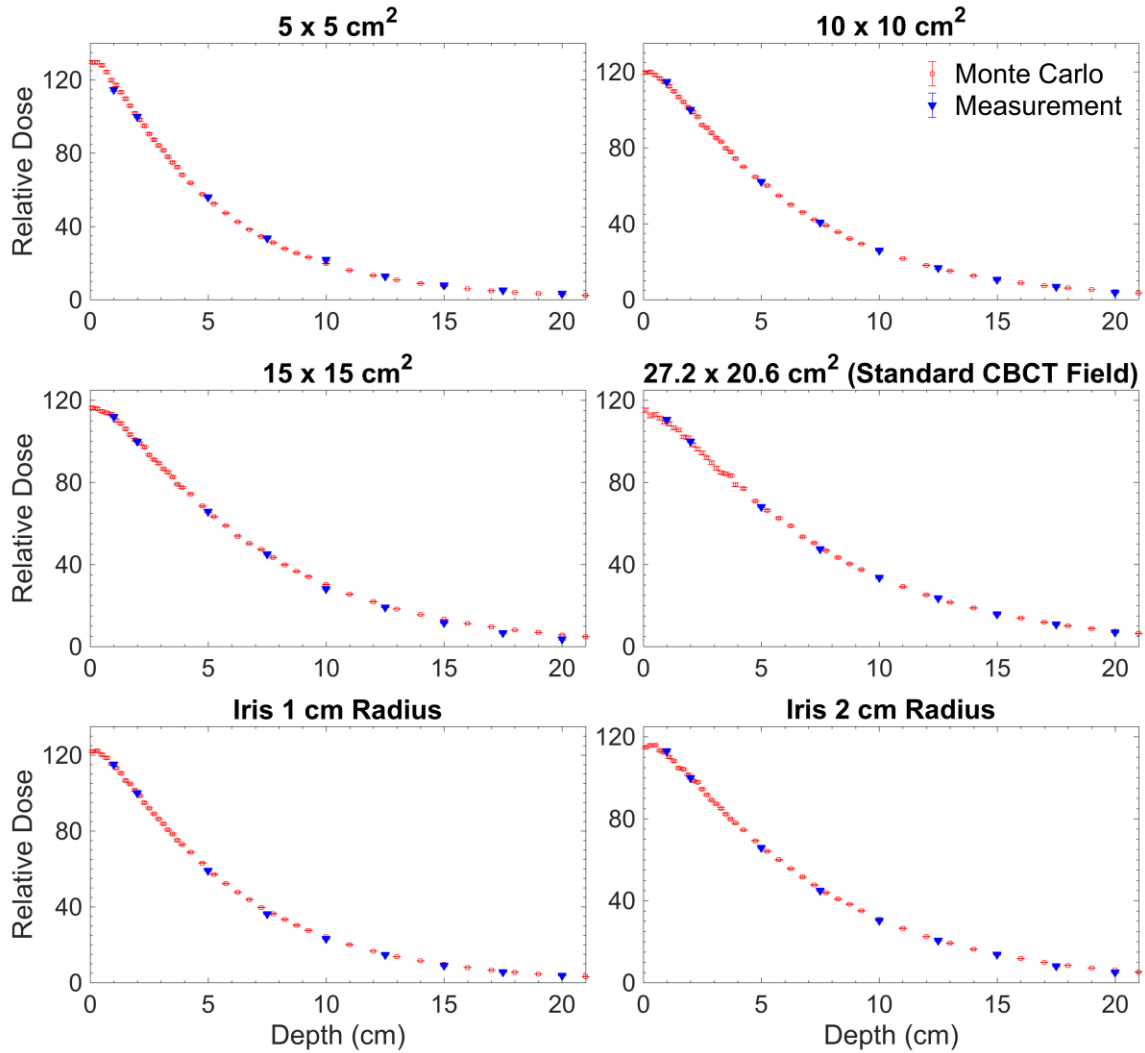
Figure 2.31   Comparison of measurement and Monte Carlo simulation of the On-Board Imager on a 2100 iX Varian linear accelerator with and without the dynamic iris collimator. Dose normalized at a depth of 2 cm.

Within this work, the output phase space was scored above the iris or blade collimator and used as the source for a four dimensional (4D) DOSXYZnrc simulation. The simulations

used an exported CT dicom data set from the TPS as the phantom in DOSXYZnrc, known as an EGSphant file. An example of the phantom used in Chapter 3, is demonstrated in Figure 2.32. Within the EGSphant file, each voxel contains information specifying the density and the assigned material. The material assignment was accomplished by setting cutoff CT values for AIR700ICRU, LUNG700ICRU, TISSUE700ICRU and ICRPBONE700ICRU and linear interpolating between the assigned CT values for the density. The cutoff CT values were taken from Kawrakow *et al.*[78] (and the DOSXYZnrc manual[79]) for 80 keV photons.

Standard BEAMnrc and DOSXYZnrc simulations model a static setup, i.e. an incident electron beam on a linac target with a set jaw and MLC collimation or an incident phase space on a phantom with a set distance and orientation. However, to simulate varying collimation, distance or orientation, such as those in VMAT or VOI CBCT, a 4D model is necessary. To generate a 4D model, Source 20 in DOSXYZnrc and the SYNCMLC or SYNCJAWS component module in BEAMnrc (for the iris or blades, respectively) developed by Lobo and Popescu[80] were used. The models were simulated with a control point resolution of one degree, with each control point specifying the position of the collimation, isocentre and angular location. To determine the weight of each control point, the arc distribution was sampled between zero and one. As demonstrated in Figure 2.33 for the modulation in Figure 4.7 of a VOI in the ATOM head phantom, this results in a complex distribution. For constant mAs, the variation of weight with control point is linear.
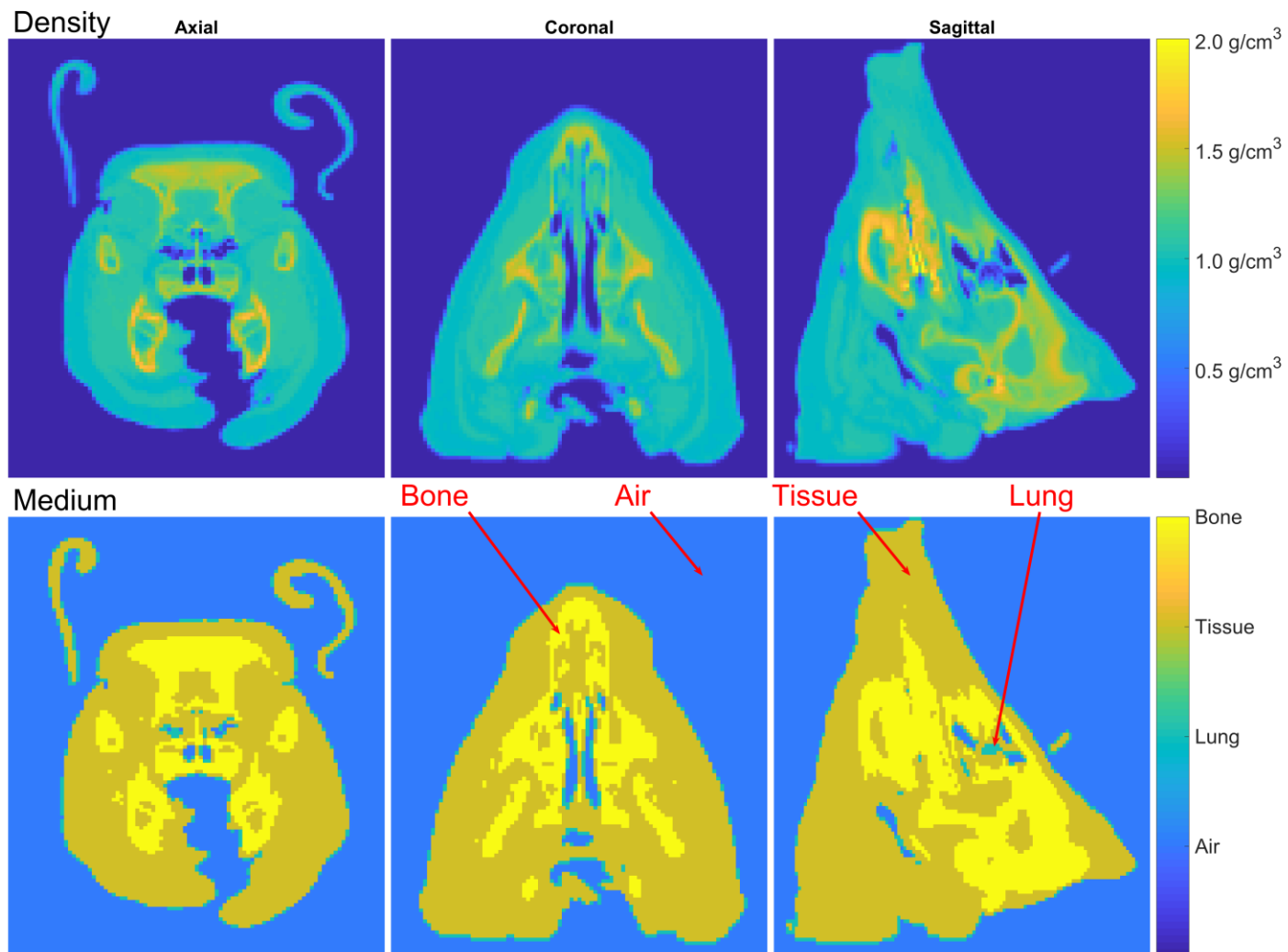
Figure 2.32   EGSphant file displaying the medium and density information for each voxel.
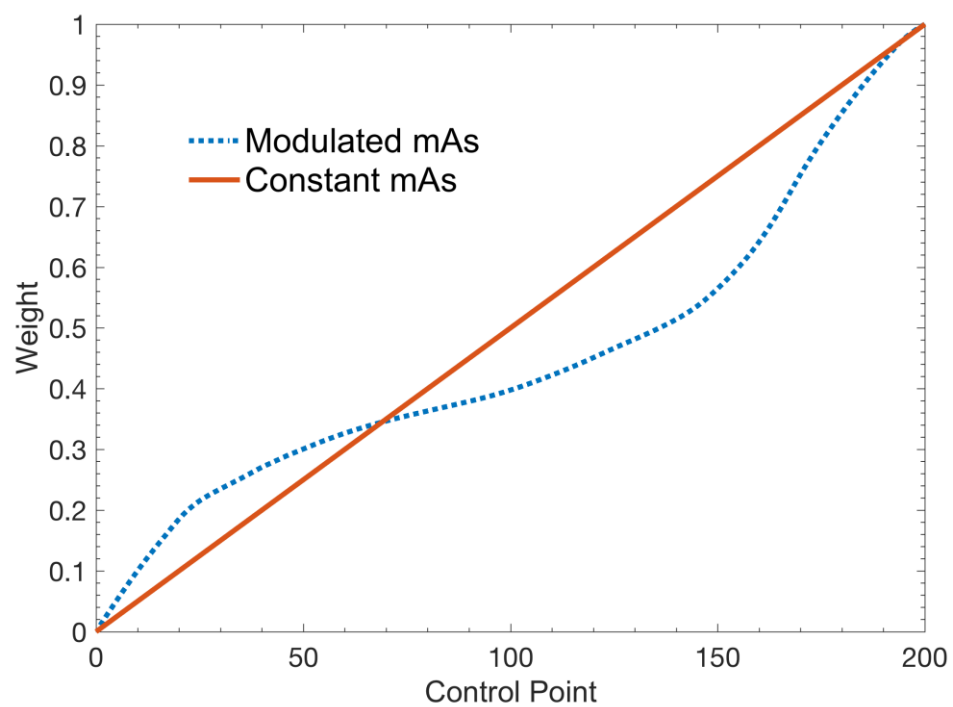
Figure 2.33   4D Monte Carlo control point distribution for modulated and constant mAs VOI
CBCT acquisitions of the ATOM Head phantom used in Chapter 4.

CHAPTER 3   MANUSCRIPT 1: AN INVESTIGATION OF KV CBCT IMAGE QUALITY AND DOSE REDUCTION FOR VOLUME-OF-INTEREST IMAGING USING DYNAMIC COLLIMATION

3.1   PROLOGUE

The following manuscript is the first foray into dynamic collimation for kV VOI CBCT. This manuscript introduces a novel iris collimator, capable of tracking VOI located off the axis of rotation. This paper demonstrates the substantial increases in image quality possible using a reduced imaging aperture compared to current practice with equivalent dose to the VOI. Additionally, 4D Monte Carlo is used to demonstrate the reductions in dose

outside the VOI. This manuscript lays much of the groundwork for the VOI method used throughout this work.

3.2 ABSTRACT

Purpose: The focus of this work was to investigate the improvements in image quality and dose reduction for VOI kV-CBCT using dynamic collimation.

Methods: A prototype iris aperture was used to track a VOI during a CBCT acquisition. The current aperture design is capable of one-dimensional translation as a function of gantry angle and dynamic adjustment of the iris radius. The aperture occupies the location of the bow-tie filter on a Varian OBI system. CBCT and planar image quality was investigated as a function of aperture radius, while maintaining the same dose to the VOI, for a 22.2 cm diameter cylindrical water phantom with a 9 mm diameter bone insert centered on isocentre. Corresponding SPR were determined at the detector plane with Monte Carlo simulation using EGSnrc. Dose distributions for various size VOI were modeled using a dynamic BEAMnrc library and DOSXYZnrc. The resulting VOI dose distributions were compared to full-field distributions.

Results: SPR was reduced by a factor of 8.4 when decreasing iris diameter from 21.2 cm to 2.4 cm (at isocentre). Depending upon VOI location and size, dose was reduced to 16%-90% of the full field value along the central axis plane and down to 4% along the axis of rotation, while maintaining the same dose to the VOI compared to full-field techniques. When maintaining constant dose to the VOI, this change in iris diameter corresponds to a factor increase of approximately 1.6 in image contrast, and a factor decrease in image

noise of approximately 1.7. This results in a measured gain in CNR by a factor of approximately 2.0.

Conclusions: The presented VOI technique offers improved image quality for image-guided radiotherapy while sparing the surrounding volume of unnecessary dose compared to full-field techniques.

3.3   INTRODUCTION

The use of CBCT for IGRT[81] is a standard which has been implemented on current generation linac platforms. This is commonly done through the addition of kV x-ray beam line placed orthogonal to the megavoltage treatment beam line. The use of CBCT provides accurate volumetric information about the patient's anatomy prior to treatment and allows for positioning of the patient relative to the treatment plan, generally compared to an image set taken with a conventional fan-beam CT. The characteristics of a CBCT x-ray beam differ substantially from that of a conventional CT. CBCT instead utilizes a radiation field typically 27.2 x 20.6 cm^2 at the isocentre plane located 100 cm from the source. Consequently, the amount of scattered radiation generated through primarily Compton interactions within the patient is greatly increased compared to a conventional CT leading to reconstruction artifacts such as shading artifacts, as well as a high image noise[81]. This in turn leads to a decrease in image quality, especially image CNR.

Siewerdsen and Jaffray[8] initially characterized the magnitude and effects of x-ray scatter in CBCT. This was done by varying the cone angle from 0.5° to 10.5° while keeping the fan angle constant at either 14° or 22° for the same tube parameters and phantom.

Siewerdsen and Jaffray[8] demonstrated that as cone angle increases, SPR increases greatly. For example, with a 30 cm diameter PMMA phantom, results in an increase in SPR of 17.7% per degree[8]. Contrast was reduced by half when changing from approximately 4% to 100% SPR conditions, this would correspond to a small and large cone angle, respectively. However, noise increased with decreasing SPR, due to the decreased scattered photon contribution to the integrated incident quanta. This has the effect of causing a trade-off between the gains in contrast and noise, resulting in a small gain in CNR.

Chen *et al.*[12] performed a preliminary study into the feasibility of VOI scanning in CBCT for breast imaging. Within the study, a 2.4 cm diameter static opening in a 2.0 mm thick copper plate, was placed 50 cm from the source to define a VOI. Chen *et al.*[12] demonstrated an improvement in CNR of a factor of approximately 1.45 for an 11 cm diameter breast phantom with an 80 kVp beam. This work was continued in a complete phantom study by Lai *et al.*[13] To minimize truncation artifacts produced in the reconstruction process, two sets of image projections were acquired. The first a high exposure VOI acquisition and the second a low exposure full field acquisition. The two projections were merged at each angle to form a composite image. With this technique, they observed scatter reductions by a factor of 6.6, compared to full field, for an 11 cm breast phantom, using the same 80 kVp beam. This resulted in a dose reduction by a factor of 1.2 and 2.7 inside and outside the VOI, respectively, compared to full field. Similar to Siewerdsen and Jaffray[8], a trade-off between the gain in contrast and noise was

observed, with a gain in CNR by a factor of 1.06 compared to full field. They also report further improvements with increasing phantom thickness.

Robar *et al.*[16] developed a dynamic collimation VOI CBCT method using the MLC in a linear accelerator with a 2.35 MeV electron beam incident on a carbon target. Tracking of the VOI was analogous to dynamic conformal arc therapy used commonly in radiation therapy. Two methods were examined to reduce truncation artifacts at the VOI boundary. The first used DRRs from the treatment planning system to fill in the information outside the VOI and the second extrapolated data beyond the boundary of the truncated region. Both methods resulted in equivalent images with minimal boundary artifacts, however the use of DRRs in the reconstruction process was less computationally efficient. For a 9x8x6 cm^3 VOI encompassing the ethmoid and sphenoid sinuses of an anthropomorphic head phantom, dose in the scan plane was reduced by factors of 1.15 and 1.7 inside and outside the VOI, respectively, compared to full field. However, no dependence of CNR on imaging aperture was observed. This is likely due to the use of a spectrum in which only 48% of photons have energies between 25 and 150 keV[17]. This also suggests that SPR changes little with imaging aperture.

It is clear that using the VOI approach results in significant dose reduction and when implemented with a kV spectrum, a gain in image quality is possible. This means relevant image quality is maintained with a reduced overall dose, this coincides with the goals of the Image Wisely[82] and Image Gently[83] campaigns. However, the collimation technique must be dynamic in order to track a variety of arbitrarily located VOI. Furthermore, the VOI CBCT concept is applicable to the IGRT paradigm, since most image guidance tasks

require imaging and alignment of a relevant sub-region of the anatomy. The

implementation of this technique in IGRT would accomplish the goals of dose reduction

and optimization set in Section V in the report by AAPM Task Group 75[84]. The specific

aims of the current work are to (i) develop dynamic collimation hardware and software

for a kV imaging system, (ii) examine dose reduction using measurement and Monte Carlo

techniques, and (iii) investigate the improvement in image quality afforded by VOI

methods.

3.4   MATERIALS AND METHODS

3.4.1 PROTOTYPE ROBOTIC IRIS COLLIMATOR

A robotic iris was developed to collimate the radiation field produced by the imaging

system as a function of gantry angle. The design has similarities to that used by Graves *et

al.*[85] which employed a hexagonal iris devised for conformal radiotherapy of small animals

using a micro-CT scanner. As demonstrated in Figure 3.1, the iris is formed by eight 45-

degree isosceles triangles composed of copper. The triangles are 6.4 mm thick with a 1.3

mm lap joint to minimize inter-wedge transmission. Copper was chosen due to the

machinability, while still being cost and space efficient. The thickness was greater than

necessary to allow for the lap joint. The two equivalent sides have a length of 32.5 mm

with a base width of 23.5 mm. To minimize friction between the triangles and the two

polyethylene guiding plates, the copper wedges are attached to a 7.6 mm aluminum

block, which has a length of 12.8 mm and is the same width as the copper triangles. The

whole assembly is sandwiched between two 6.0 mm thick aluminum plates. Iris

translations are accomplished using two stepper motors (E28H43-05-900, Haydon Kerk Motion Solutions, Inc., Waterbury, CT), one for stage translation and the second for radial translations. The iris mounting plate is similar to that of a bowtie filter and weighs only 0.7 kg more. This minimizes any potential gravitational sag effects.
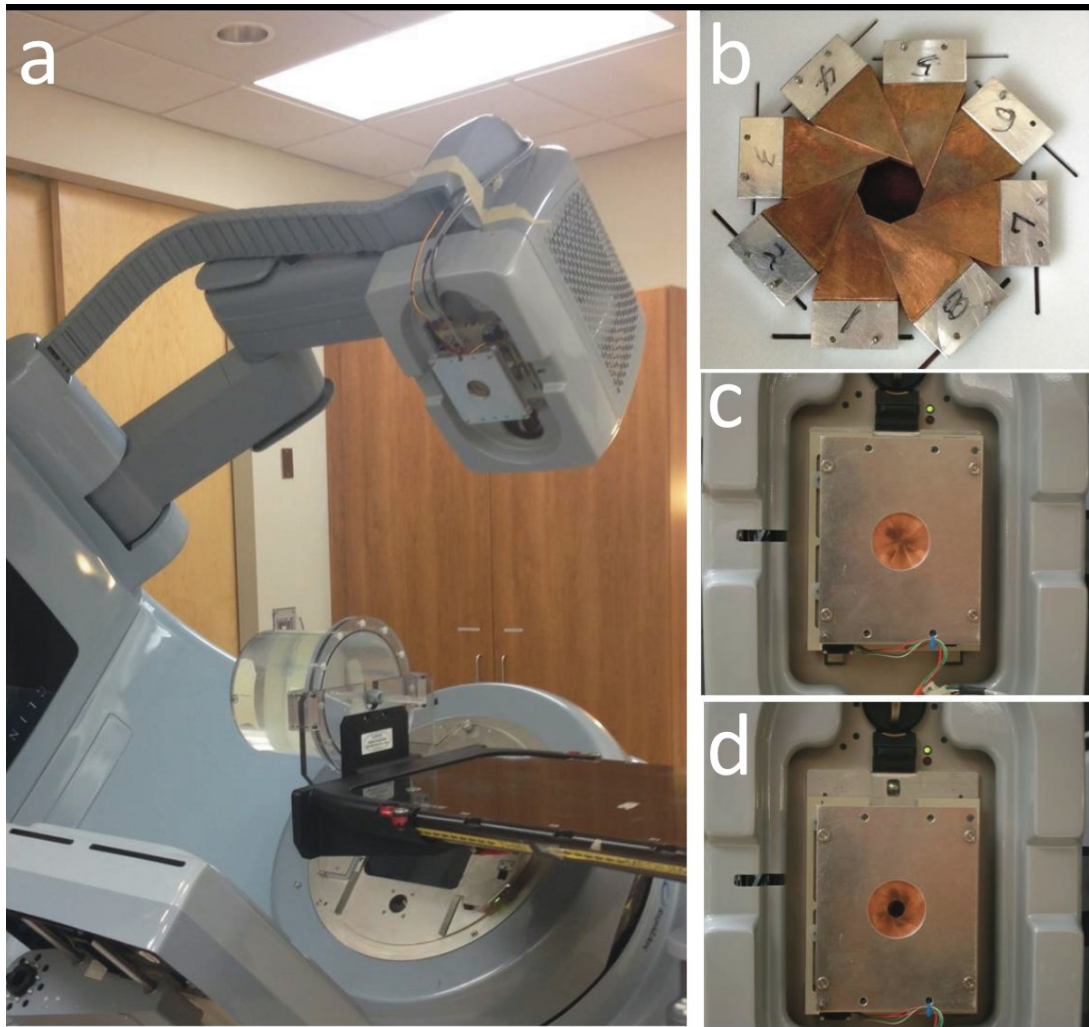
Figure 3.1   (a) Robotic iris attached to the On-Board Imager on a 2100 iX Varian linear accelerator (Varian Medical Systems, Inc., Palo Alto, CA). (b) Exposed iris, displayng the copper triangles, aluminum block and top polyethylene guide plate. Iris centered vertically (c) and closed (d). Iris translated down and opened radially.

The system is attached to the OBI on a 2100 iX Varian linear accelerator (Varian Medical Systems, Inc., Palo Alto, CA) using a bowtie filter mounting plate. To determine gantry angle, a triple-axis accelerometer (MMA7361, Freescale Semiconductor, Inc., Austin, TX) was mounted inside the gantry on the crossbar support between the two kV arms. The system is connected to an Arduino Uno microcontroller and controlled using MATLAB (Mathworks, Natick, MA). The iris stage can translate 22.1 cm and has a maximum radius of 11.1 cm defined at isocentre.

3.4.2 VOI IMAGING PROTOCOL

The previously described imaging paradigm by Robar *et al*.[16] was used within this work, in which the VOI was defined at the time of treatment planning using the Eclipse TPS (Varian Medical Systems, Inc., Palo Alto, CA). If used clinically, a margin expansion could be employed in VOI design to account for any initial uncertainty in positioning the anatomy of interest, i.e. similar to PTV margins. To calculate the radial and lateral translations of the iris, the DICOM structure set of the VOI was exported from the TPS and loaded into MATLAB. The structure set was projected onto a two-dimensional plane intersecting isocentre and perpendicular to central axis. The perimeter and centroid of the projected structure set were then calculated. The location of the centroid indicates the necessary stage translation relative to isocentre, and the maximum distance from the centroid to the projected perimeter determines the iris radius. Translation and radius trajectories were calculated in one-degree increments over a 360 degree arc. An example of this is demonstrated in Figure 3.2. The mean value of SI translations were taken to give

the necessary couch shift relative to isocentre. At the time of imaging, the calculated

translations served as a lookup table for the angular position of the gantry. Within this

work all iris diameters are defined at isocentre.
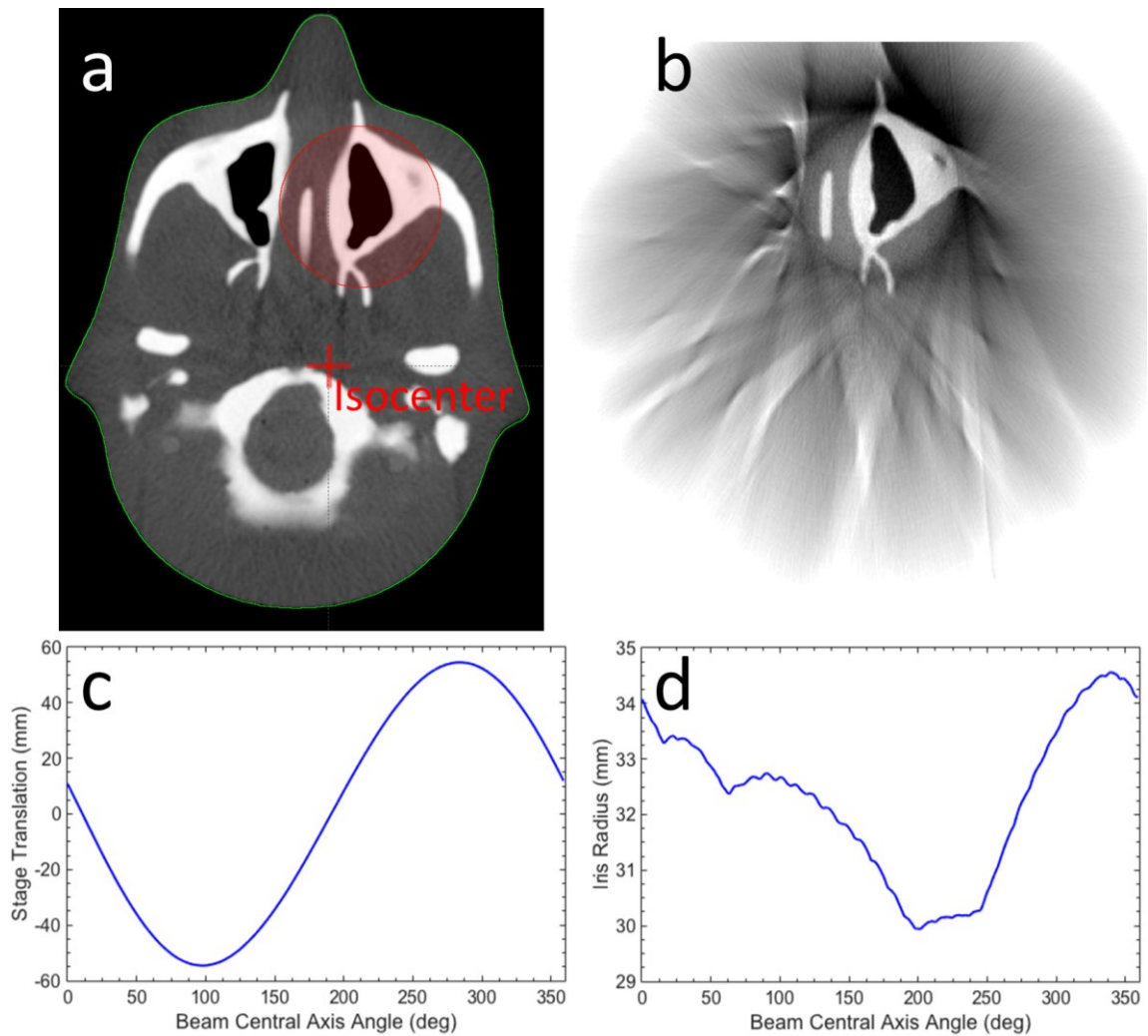
Figure 3.2   (a) CT volume of the ATOM head phantom in the Eclipse treatment planning
system (Varian Medical Systems, Inc., Palo Alto, CA), with the VOI to be imaged
in red. (c) Iris stage and (d) radial translations as a function of beam central axis
angle (using the Varian IEC coordinate system) calculated from the DICOM
structure using MATLAB. (b) Reconstructed VOI.

All images were acquired using the clinical OBI application. The clinical CBCT imaging protocol for head and neck patients was adapted for this work. Unless otherwise stated all imaging used the following x-ray tube parameters: a potential of 120 kVp, a current of 80 mA, a pulse width of 25 ms and a SDD of 150 cm. The clinical protocol of a 200° arc was extended to 360° to explore the full range of iris translations. Over a 360° arc this would result in approximately 660 projections.

The CBCT projections were reconstructed using the FDK algorithm[68]. Several preprocessing steps were added to the algorithm to account for the truncation artifacts associated when reconstructing VOI projections. Several authors have reported various methods to correct for these artifacts, including for example, using DRRs to fill the region outside the VOI[16], acquiring two sets of projections a VOI and either a reduced exposure or a sparse full-field projection[13, 86], pi-line reconstruction[87] or extrapolating the boundary of the VOI[16, 88]. Within this work the exponential extrapolation was utilized as defined previously by Robar *et al*.[16] This method was chosen as it is computationally simple, only requires a truncated projection and produces equivalent reconstructed images as DRR filling[16]. Previously[16], thresholding techniques were used to determine the location of the VOI boundary, however, this proved to be difficult when translating this approach from a megavoltage low-Z imaging beam to a dedicated kilovoltage image system. This deficiency was due to appreciable transmission through the lap joints in some projections. Additionally, the accelerometer has a precision of approximately 2° with the current experimental setup. Therefore, the *a priori* calculated iris translation data in combination with image co-registration was used to determine the location of the VOI within the

projection. The boundary of the VOI was then extrapolated and air normalized. The steps of this are illustrated in Figure 3.3. This process was accomplished using MATLAB executed in parallel using a computer cluster. The use of co-registration between the acquired and expected aperture location allows for the calculation of stage error as a function of gantry angle. The result of this workflow is demonstrated in Figure 3.2 for the ATOM head phantom. The corresponding stage error is displayed in Figure 3.4, which demonstrates that for the sample acquisition, regions of high translation stage error occur during the greatest stage velocity. This corresponds to a mean, median and mode (for several acquisitions) of 3.1, 2.0 and 0 mm, respectively. However, these errors can be greatly minimized with upgraded hardware or integration with the clinical system. Full-field images were reconstructed using the same methodology with the exception of the boundary correction. No additional corrections (e.g. for scatter) were used within this work.
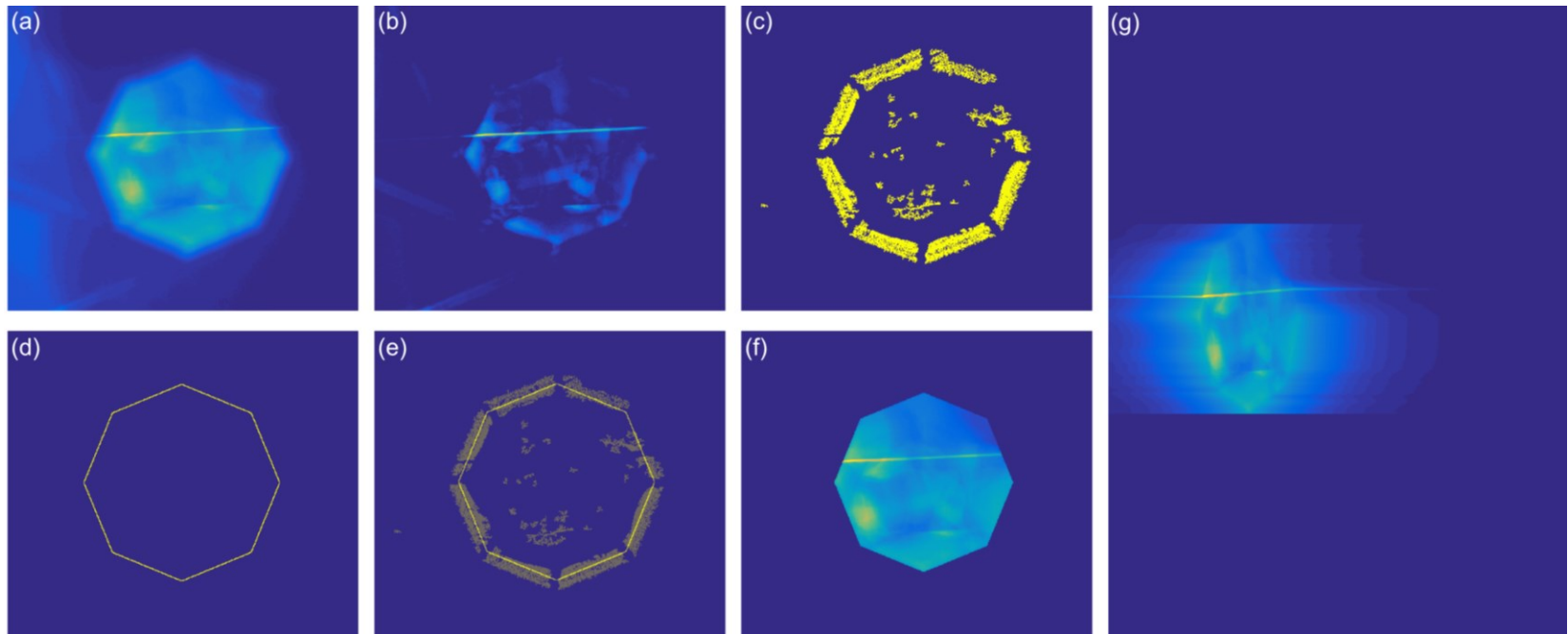
Figure 3.3   Process of identifying the truncated projection data. (a) Cropped data, (b) background subtraction (background found by erosion followed by a dilation), (c) binary conversion, inversion and area opening using 4-connected neighborhood, (d) expected aperture location, (e) co-registered match, (f) masked and eroded data, (g) projection data with extrapolation of the boundary.
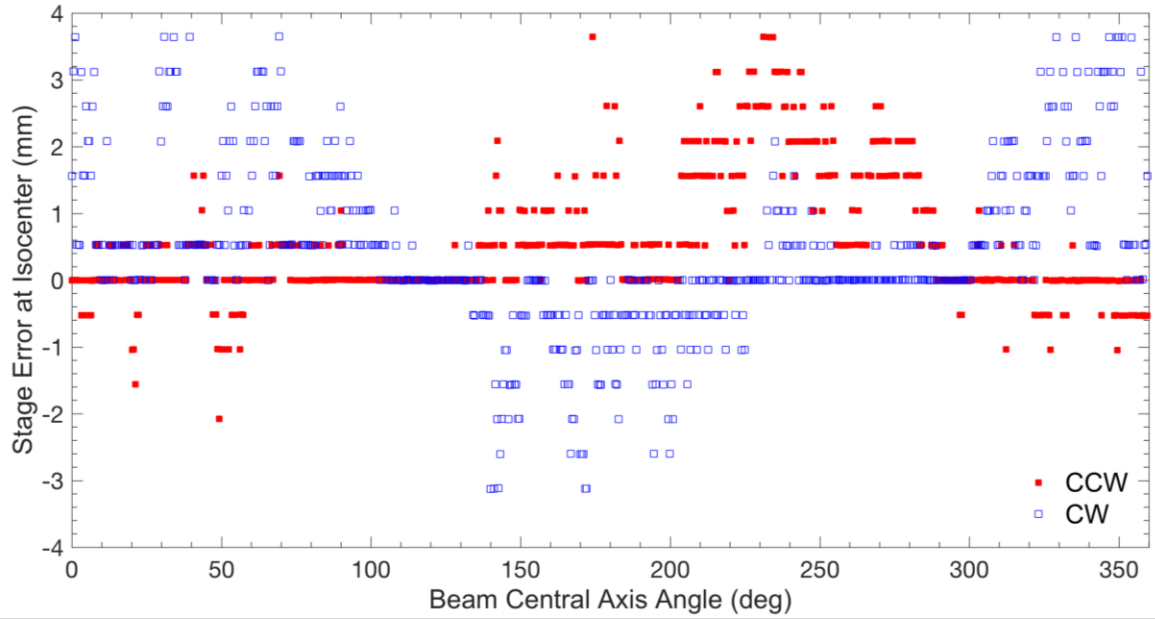
Figure 3.4   Translation stage error at isocentre as a function of beam central axis angle (using the Varian IEC coordinate system) for a counter-clockwise and clockwise rotation.

3.4.3 MONTE CARLO MODEL OF THE IMAGING SYSTEM

The OBI source was modeled in BEAMnrc[76] using exact geometric and material specifications provided by Varian Medical Systems. Two source models were simulated, the first with the bowtie filter and the second with the iris collimation system. A common phase-space was first generated just before the bowtie filter mounting plate without any additional filtration or tertiary collimation. This phase-space was then used as an input for the two simulations. A 120 keV mono-energetic electron beam was incident on the x-ray target, with spot size of 1.6 mm. The incident electron beam angle relative to the x-ray tube was simulated according to manufacturer's specifications. The directional bremsstrahlung splitting (DBS) variance reduction technique was used, with a splitting

radius of 17 cm for standard 27.2 x 20.6 cm^2 CBCT head and neck protocol, at a SSD of

100 cm, with a bremsstrahlung splitting number of 2000. Similar to the work done by Ding

et al.[89], the EGSnrc parameters listed in Table 3.1 were used; where not mentioned the

default values were used. Global electron (ECUT) and photon (PCUT) cut-off energies of

0.521 MeV and 0.010 MeV, respectively, were used. The models were validated through

depth dose measurements (Figure 2.31) acquired using a 50 x 50 x 50 cm^3 water tank (IBA

Dosimetry GmbH, Schwarzenbruck, Germany) and a 0.015 cm^3 cylindrical ion chamber

(PTW N31010, Freiburg, Germany) and compared to simulated depth dose using

DOSXYZnrc[77].

Table 3.1   Particle transport parameters used in the Monte Carlo simulations.

EGSnrc Parameter	kV System	MV System
Electron Impact Ionization	On	On
Bremsstrahlung Angular Sampling	Koch-Motz	Koch-Motz
Bremsstrahlung Cross Section	NIST	NIST
Bound Compton Scattering	On	Norej
Photoelectron angular sampling	On	Off
Rayleigh scattering	On	Off
Atomic Relaxations	On	Off
Photon cross-sections	NIST XCOM	NIST XCOM

Scattered and primary photons reaching the detector plane 150 cm from the source were transported through a 20 cm diameter by 20 cm long uniform cylindrical water phantom centered on isocentre. The variable LATCH was assigned to a particle if it interacted with a component within the model; this was used to identify scattered and primary photons reaching the detector plane. The simulation was run for iris diameters ranging from 2.4 to 21.2 cm defined at isocentre. The SPR was calculated for each simulation within a 1.5 cm radius about central axis at the detector plane (this did not include simulation of the detector and anti-scatter grid).

Absolute dose per mAs of the x-ray tube for both the bowtie filter and the iris collimation were determined following the TG-61 protocol[90]. An Exradin A12 ionization chamber was used with collecting volume of 0.65 cm^3. As per the protocol, measurements were taken at a depth of 2 cm, with a source-to-surface distance (SSD) of 100 cm. A 10 x 10 cm^2 blade-defined field was used for measurements with the bowtie filter. Similarly, iris measurements were taken with a 10 cm diameter iris defined field, with the blades set to 27.2 x 20.6 cm^2. Once the absolute dose per mAs was known, dose was measured for iris-defined fields ranging from 2.4 to 19.9 cm diameter at isocentre using the same setup as above. A 0.015 cm^3 cylindrical ion chamber (PTW N31010, Freiburg, Germany) was cross-calibrated and used for in phantom measurements for a 22.2 cm diameter by 20 cm long cylindrical water phantom.

3.4.4 CNR VERSUS VOI DIMENSION

Image CNR was investigated as a function of VOI diameter ranging 2.4 to 21.2 cm in diameter. The same cylindrical water phantom described in the previous section was centered on isocentre. A 9 mm diameter by 3 cm long cylindrical bone insert (density of 1.82 g/cm^3) was place within the center of the cylindrical phantom. A dose of approximately 18 mGy was given to isocentre for each iris diameter (measured using cross-calibrated ion chamber). This was done by replacing the bone insert with a 0.015 cm^3 cross-calibrated ionization chamber and adjusting the mAs for each CBCT acquisition to account for the decrease scattered dose contribution to isocentre with decreasing iris diameter (Figure 3.5a). The changes in mAs are displayed in Figure 3.5b. Ten acquisitions were acquired for each iris diameter, five with the bone insert in place and five with just water to give a pure noise image. CNR was calculated as

$$CNR = \frac{|P_{Bone} - P_{Water}|}{\sigma_{Water}}$$

Eq 3.1

where P_{Bone} is the average pixel value within the bone insert, P_{Water} is the average value of the water within the same area as the bone and σ_{water} is the average noise within the water. Error bars were found by calculating the mean and standard deviation of CNR measured in ten 0.2 cm spaced slices a centimeter above and below the central slice, and over five reconstructed image sets.
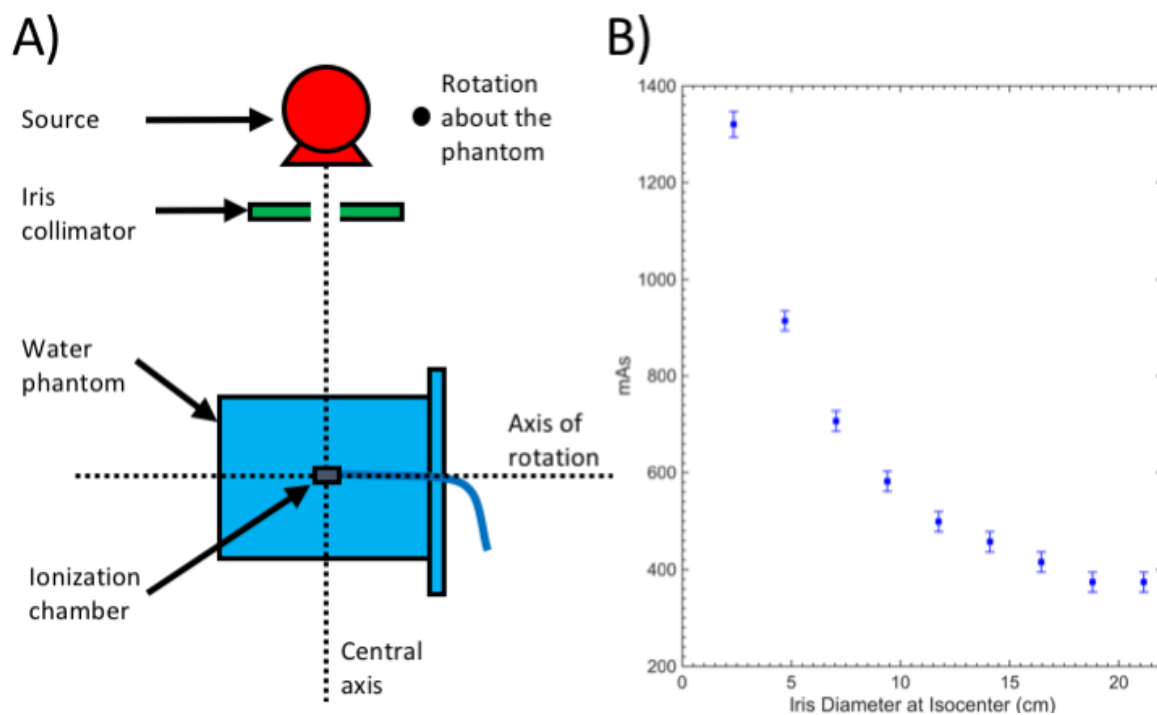
Figure 3.5   a) Sketch of experimental setup and b) mAs as a function of iris diameter used to acquire CNR versus VOI dimension to deliver the same dose to isocentre.

3.4.5 VOI DOSE CALCULATION USING 4D MONTE CARLO

Source 20 in DOSXYZnrc developed by Lobo and Popescu[80] was used to simulate the synchronized iris stage and radial translations with gantry angle. The BLOCK component module used to simulate the copper iris within the static BEAMnrc model was replaced with the SYNCVMLC component module. The use of this component module allowed iris translations to be synchronized with gantry rotation in DOSXYZnrc. The acquisition was divided into 360 control points over the 360° arc. The CT DICOM information was exported from the TPS and used to create an EGSPHANT file, containing the material and density composition of the phantom. This allowed the dose distribution to be simulated

97

on the imaged phantom. Dose distributions were simulated using the same cylindrical water phantom previously described for iris diameters of 44.2 and 110.7 mm, as well as an off-axis acquisition and with the bowtie filter.

Absolute dose measurements were made at isocentre for each of the simulated image trajectories. These were taken with the 0.015 cm^3 cylindrical ion chamber discussed in section 3.4.3. All dose measurements were taken using the same image protocol described in section 3.4.2. Dose ratios between the VOI dose distributions and bowtie dose distributions were then calculated.

3.4.6 QUALITATIVE ASSESSMENT OF kV VOI CBCT

A 2.8 cm diameter by 3 cm long cylindrical marrow insert (density of 1.12 g/cm^3, 1.09 electron density relative to water) was placed within the center of the cylindrical phantom. A 5 cm diameter on axis VOI and corresponding full field were acquired. The same dose to the VOI was maintained in both acquisitions. This required adjusting the mAs from 1340 (VOI) to 750 mAs (bowtie).
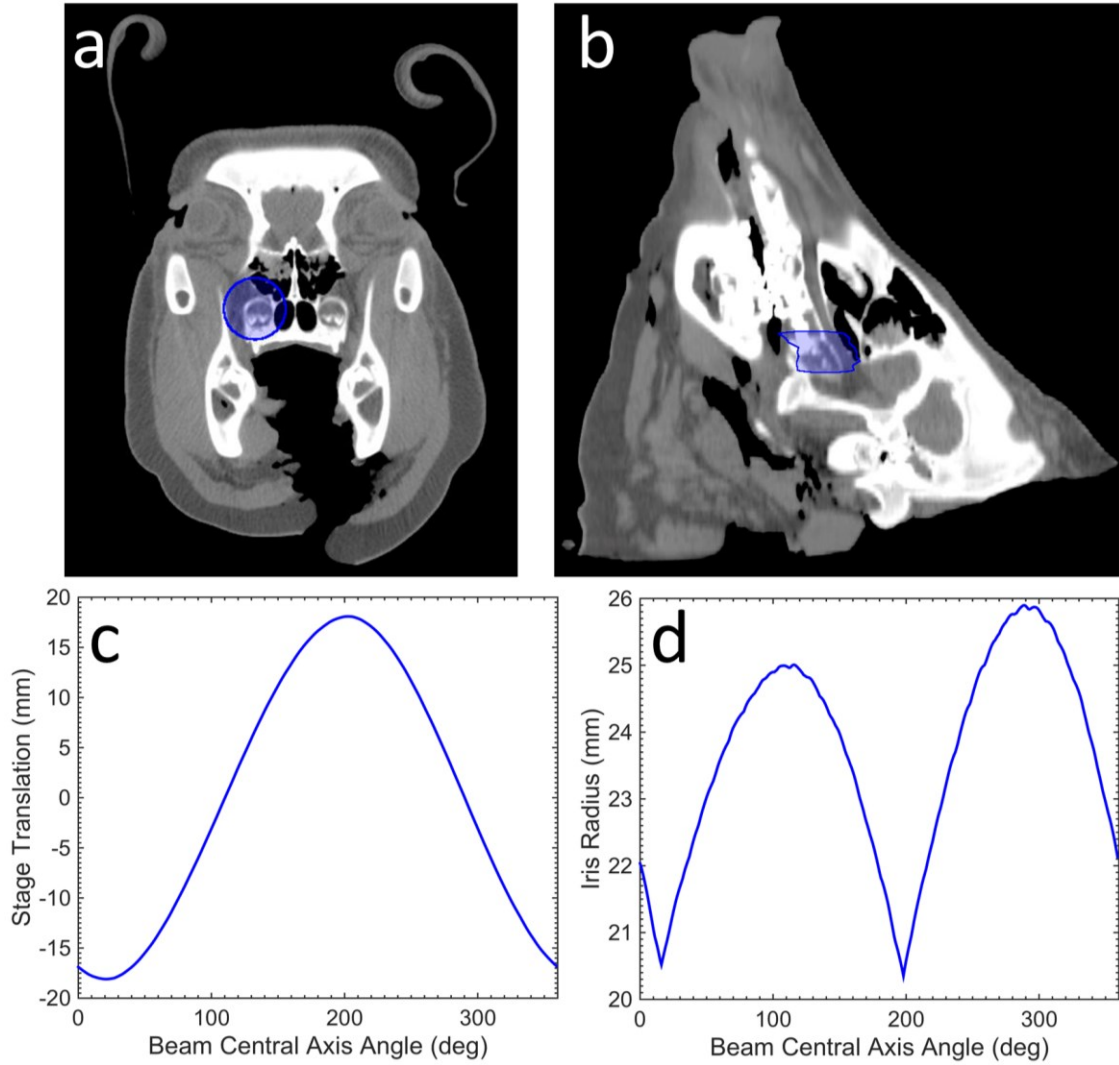
Figure 3.6   (a) Axial and (b) sagittal views of the VOI in the Eclipse (Varian Medical Systems, Inc., Palo Alto, CA) treatment planning system. Below are the corresponding (c) stage and (d) radial iris translations for the VOI.

The head-and-neck region of a pig was used to examine image quality improvement with a more realistic geometry and material. Figure 3.6 displays the location of the VOI within the pig. A full-bowtie image volume was acquired of the entire head for comparison. The same dose to the VOI was maintained in both acquisitions, which required adjusting the

99

mAs from 1340 (VOI) to 1055 mAs (bowtie). The image dose distributions were simulated as described in the previous section using Source 20 in DOSXYZnrc.

3.5   RESULTS AND DISCUSSION

3.5.1   SCATTERED PHOTON REDUCTION WITH VOI DIAMETER

A Figure 3.7a displays the magnitude of scattered and primary photon fluence Monte Carlo simulated from the uniform cylindrical water phantom, at the detector plane 150 cm from the source, for two iris diameters of 2.4 and 21.2 cm defined at isocentre. The primary photon fluence was unchanged within the VOI between the two iris diameters. The scattered contribution inside the VOI was decreased by approximately a factor of 9 and 22 inside and lateral to the projected VOI, respectively. Figure 3.7b displays the corresponding SPR within a 1.5 cm radius about central axis at the detector plane as a function of iris diameters ranging from 2.4 to 21.1 cm defined at isocentre. The variation in SPR was approximately linear with diameter, decreasing SPR by 0.13 per centimeter, with a decrease in SPR by a factor of 8.4 when decreasing iris diameter from 21.2 cm to 2.4 cm. Lai *et al.*[13] had previously report a measured SPR reduction ranging from 6.6 and 10.3 for an 11 and 15 cm diameter by 12 cm long polycarbonate cylindrical phantom, respectively, at 100 cm from the source, using a 2.5 x 2.5 cm^2 aperture compared to full field.
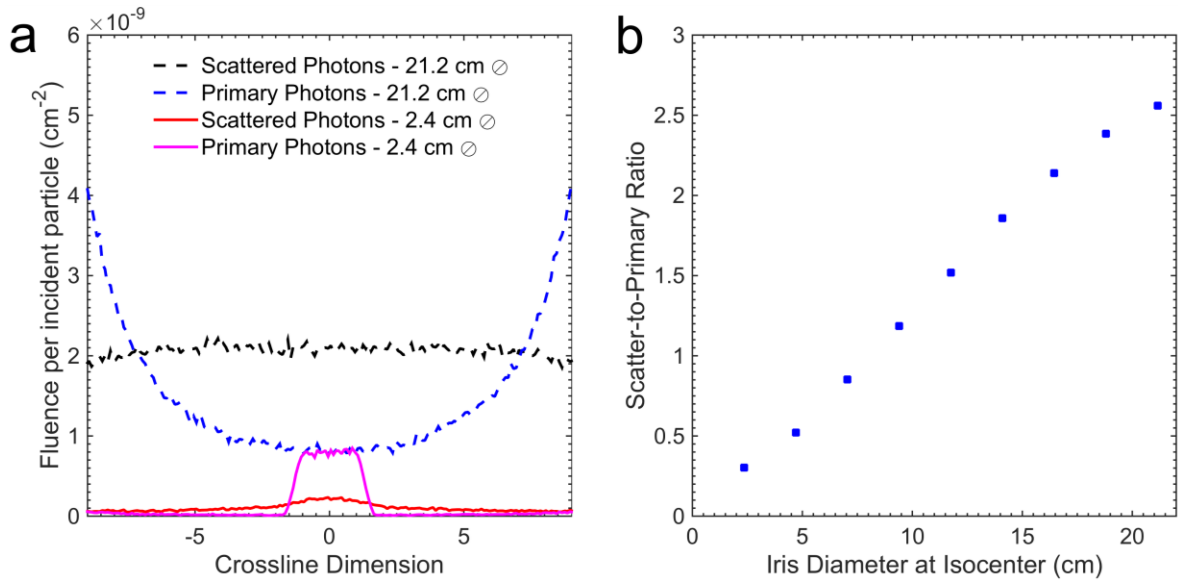
Figure 3.7   (a) Simulated scatter and primary photon fluence at the detector plane 150 cm from the source along the crossline (normal to the linac gun-target direction) direction one centimeter wide for a 2.4 and 21.2 cm iris diameter field defined at isocentre. (b) Scattered-to-primary photon ratio as a function of iris diameter, about central axis at the detector plane. A uniform cylindrical water phantom centered on isocentre was used.
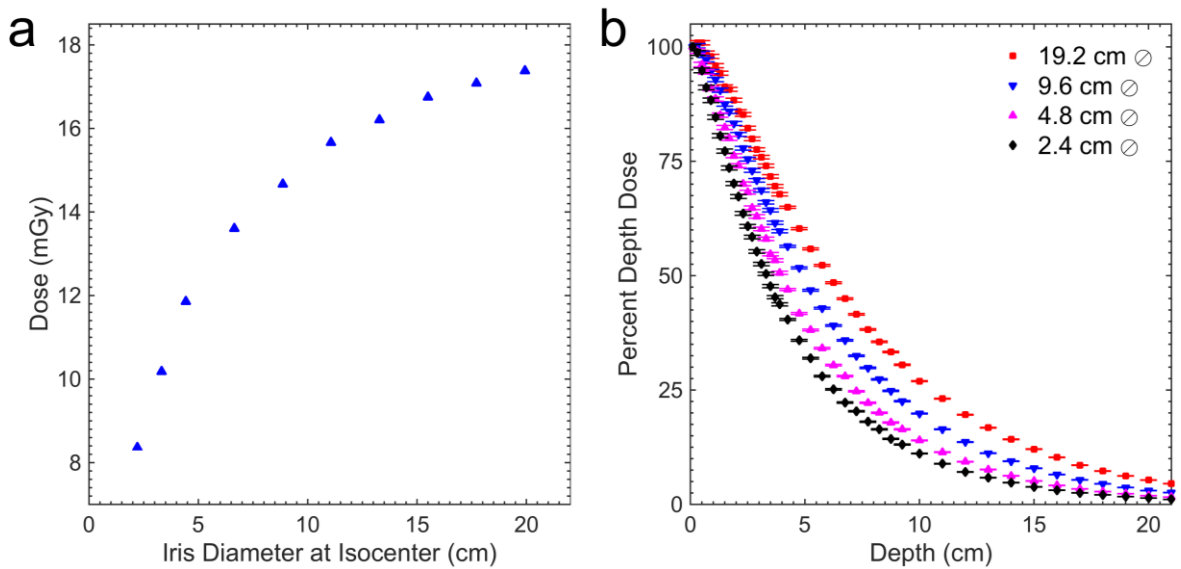
Figure 3.8   (a) Measured dose in mGy for iris diameters ranging from 2.2 cm to 19.9 cm. Measurements were taken at a depth of 2 cm and 100 cm SSD using a 120 kVp beam and 100 mAs. (b) Modeled percent depth dose curves for iris diameters ranging from 2.4 cm to 19.2 cm at a SSD of 100 cm

3.5.2 Dose reduction using VOI

Figure 3.8a displays the effect of decreased phantom scatter on measured dose at a depth of 2 cm in a water tank, with a static beam for iris diameters ranging from 2.2 to 19.9 cm. Within this diameter range, measured dose was decreased by a factor of 2.1, with the most dramatic decrease in dose occurring at iris diameters less than 6.6 cm. Figure 3.8b displays modeled percent depth dose curves for iris diameters ranging from 2.4 to 19.2 cm, at a SSD of 100 cm. We believe that the decrease in dose with depth for decreasing imaging aperture occurs through the same mechanism as megavoltage beams, in which, relative to the surface dose the scatter contribution to dose increases with depth for increasing imaging apertures[91]. Accordingly, for fixed surface dose, central dose is lower for small fields. This effect is demonstrated in Figure 3.9 for VOI dose distributions of 11.1 cm diameter and a 4.4 cm diameter located on and off-axis compared to a full-bowtie dose distribution, for the uniform cylindrical water phantom centered on isocentre, using the protocol described in section 3.4.2. As demonstrated, the imaging dose was drastically reduced when using the VOI technique, with doses to isocentre of 55, 48 and 26 mGy for the full-bowtie, 11.1 cm and 4.4 cm diameter VOI, respectively. A dose of 31 mGy was given to the center of the off-axis VOI with an isocentre dose of 11 mGy.
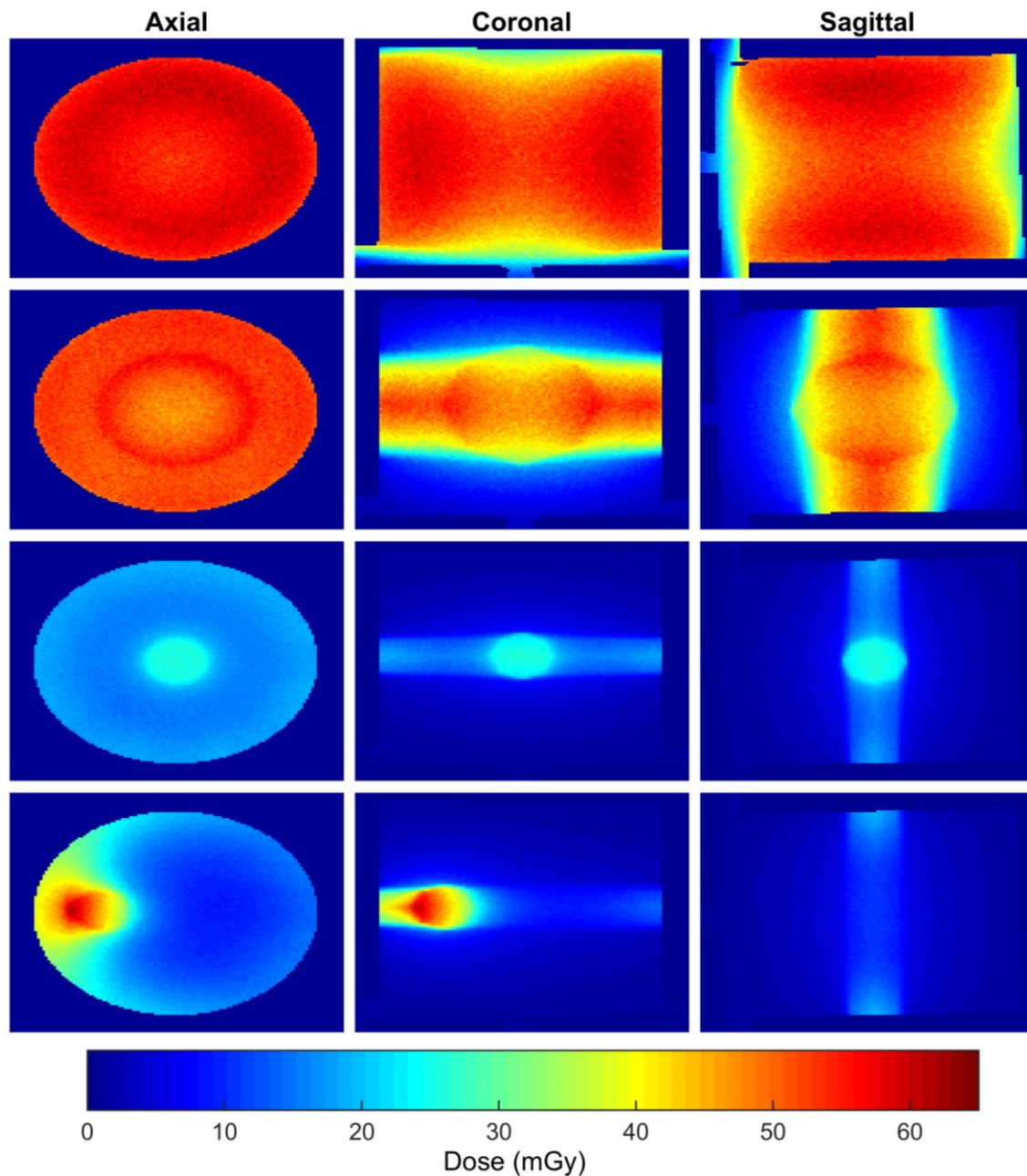
Figure 3.9   (from top down) Monte Carlo simulated dose distributions using the uniform cylindrical water phantom, for 360° CBCT acquisitions of a full-bowtie and three volumes-of-interest: a 11.1 cm diameter, a 4.4 cm diameter on and off-axis.

Corresponding dose ratios between the VOI and the full-bowtie dose distribution are also

displayed in Figure 3.9. For a large VOI, such as 11.1 cm diameter, dose is reduced to 80%

of the full field value. SI to the VOI, reductions to 16% of the full field are observed along the axis of rotation. For a 4.4 cm diameter VOI, the dose reductions are more significant, with a reduction to 55% and 26% of the full field value to the center and lateral to the VOI, respectively. As the VOI is shifted off-axis, the superficial dose reduction is lost proximal to the VOI, with minimal sparing. Dose sparing is reduced when the imaged volume is superficial as demonstrated in the off-axis VOI compared to the full-bowtie. This effect is largely due to the shape of the bowtie filter, which at a distance of 10 cm from central axis offers maximum attenuation of the x-ray beam. However, lateral to the VOI sparing is maintained, with a reduction down to 16% of the full-field dose. For both on and off axis 4.4 cm diameter VOI, SI dose was reduced down to 4% of the full field value. Lai *et al.*[13] reported a similar dose reduction of approximately 56% for a 2.5 x 2.5 cm^2 aperture compared to a 12 x 16 cm^2 full field. They observed similar dose reductions outside the VOI with dose reductions of approximately 11% and 7% of the full-field value, lateral and inferior to the VOI, respectively.

3.5.3 IMAGE QUALITY IMPROVEMENT USING VOI CBCT

Figure 3.10 displays CNR measurements for the cylindrical water phantom with a bone insert centered on isocentre, for iris diameters ranging from 2.4 to 21.2 cm. Over this iris diameter range CNR was improved by a factor of approximately 2.0 when decreasing from largest to smallest acquired diameter. Similar trends were observed for image contrast and noise, in which contrast was improved by a factor of approximately 1.6 and noise was decreased by a factor of approximately 1.2, when decreasing iris diameter over the same

range. These results appear to contradict the results present by Lai *et al.*[13], where a similar trend was observed for contrast, however noise increased with decreasing imaging aperture, thus yielding marginal gains in image CNR. However, this can be explained by the difference in which the images were acquired with varying imaging aperture. The premise of our current work is to maintain the dose to the phantom constant while observing the effect of the dynamic iris collimation on image quality, and thus the x-ray tube mAs was adjusted to provide the same imaging dose to isocentre within the phantom for each iris diameter. This leads to an increase in the primary quanta detected within the projected VOI for smaller diameters. In the study by Lai *et al.*[13], the image protocol was held constant with changing imaging aperture, which would lead to approximately the same number of primary quanta detected, with a greatly reduced overall signal due to the decrease in scatter. This is also apparent within the work by Siewerdsen and Jaffray[92], which for a given protocol image noise increases with decreasing cone angle. Our work demonstrates that, for example, an increase in tube current by 55% is possible for the phantom demonstrated in Figure 3.7 for a 5 cm diameter VOI, compared to a full field protocol, without increasing dose to the patient. This is qualitatively demonstrated in Figure 3.11.
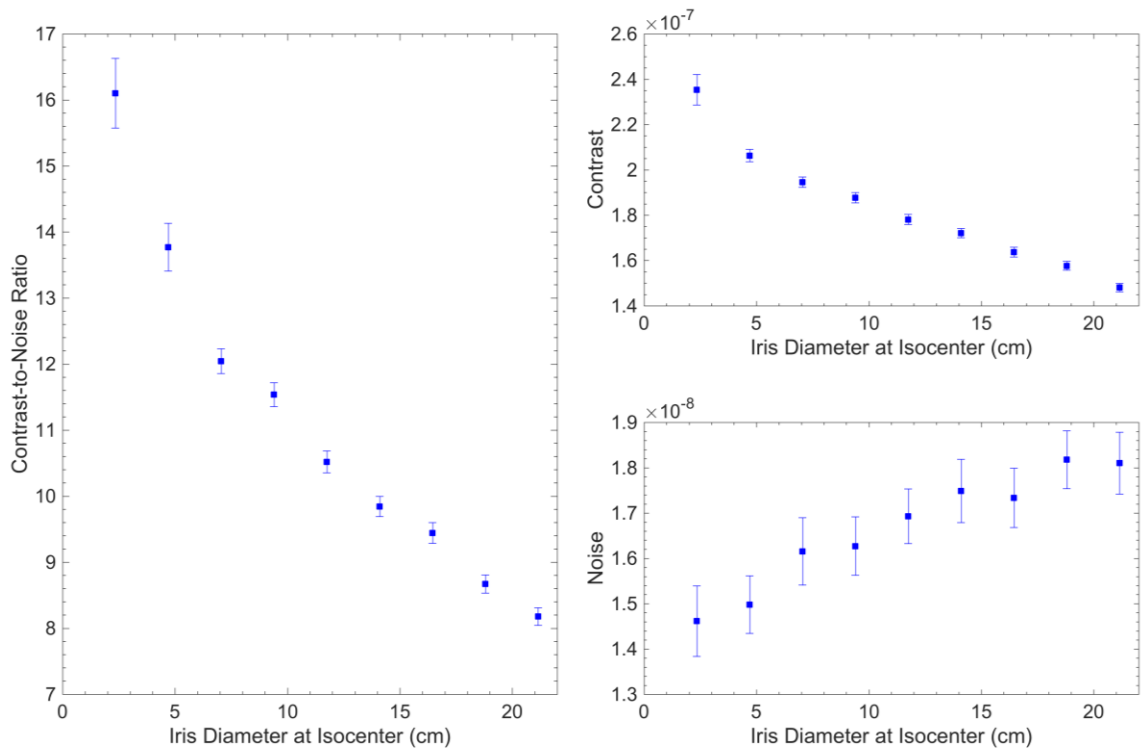
Figure 3.10   (clockwise from the left) CNR as a function of iris diameter for cylindrical water phantom with a bone insert centered on isocentre. Corresponding contrast and noise measurements as a function of iris diameter.

3.5.4 QUALITATIVE ASSESSMENT OF kV VOI CBCT

Figure 3.11 displays reconstructed images of a marrow insert in a cylindrical water phantom for a 5 cm diameter VOI (top left) and full-bowtie (top right), using the same dose to the center of the VOI. The two images share the same window level. The corresponding line profile demonstrates improved contrast between the insert and water in the VOI compared to the full-field acquisition. Compared to full-field, the VOI approach offers an improvement in contrast, by a factor of approximately 1.8. Also demonstrated

is some image degradation immediately adjacent to the VOI boundary. This effect extents approximately 4 mm into the VOI.

Figure 3.12 displays reconstructed images of the VOI displayed in Figure 3.6 as well as the corresponding full-bowtie image. Similar to Figure 3.11, the two images are displayed with common windowing. Profiles are displayed through the VOI and full-bowtie image.
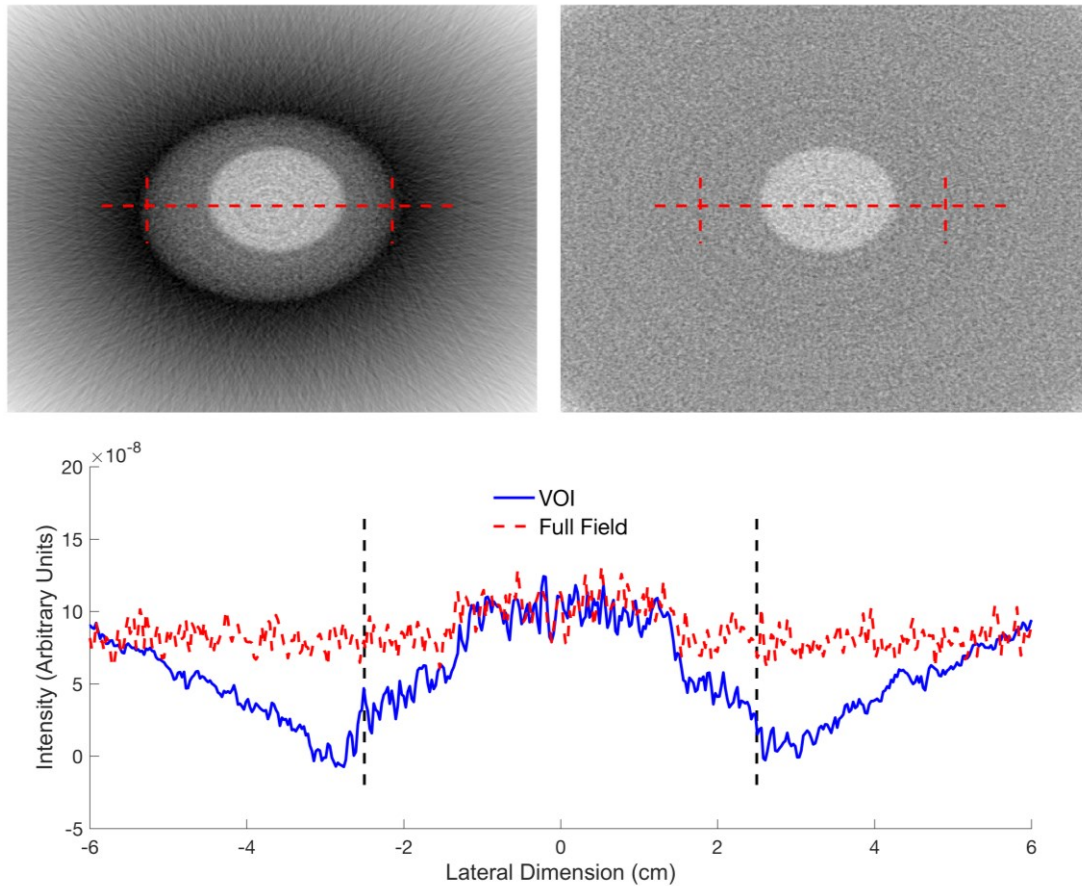
Figure 3.11   (top row) reconstructed volumes for the VOI and corresponding full-bowtie image of a marrow insert in water. Horizontal and vertical dashed line marks the profile and VOI boundary location, respectively. (bottom row) Profiles for both VOI (blue) and bowtie (red) volumes, the vertical dashed line indicated the VOI boundary.
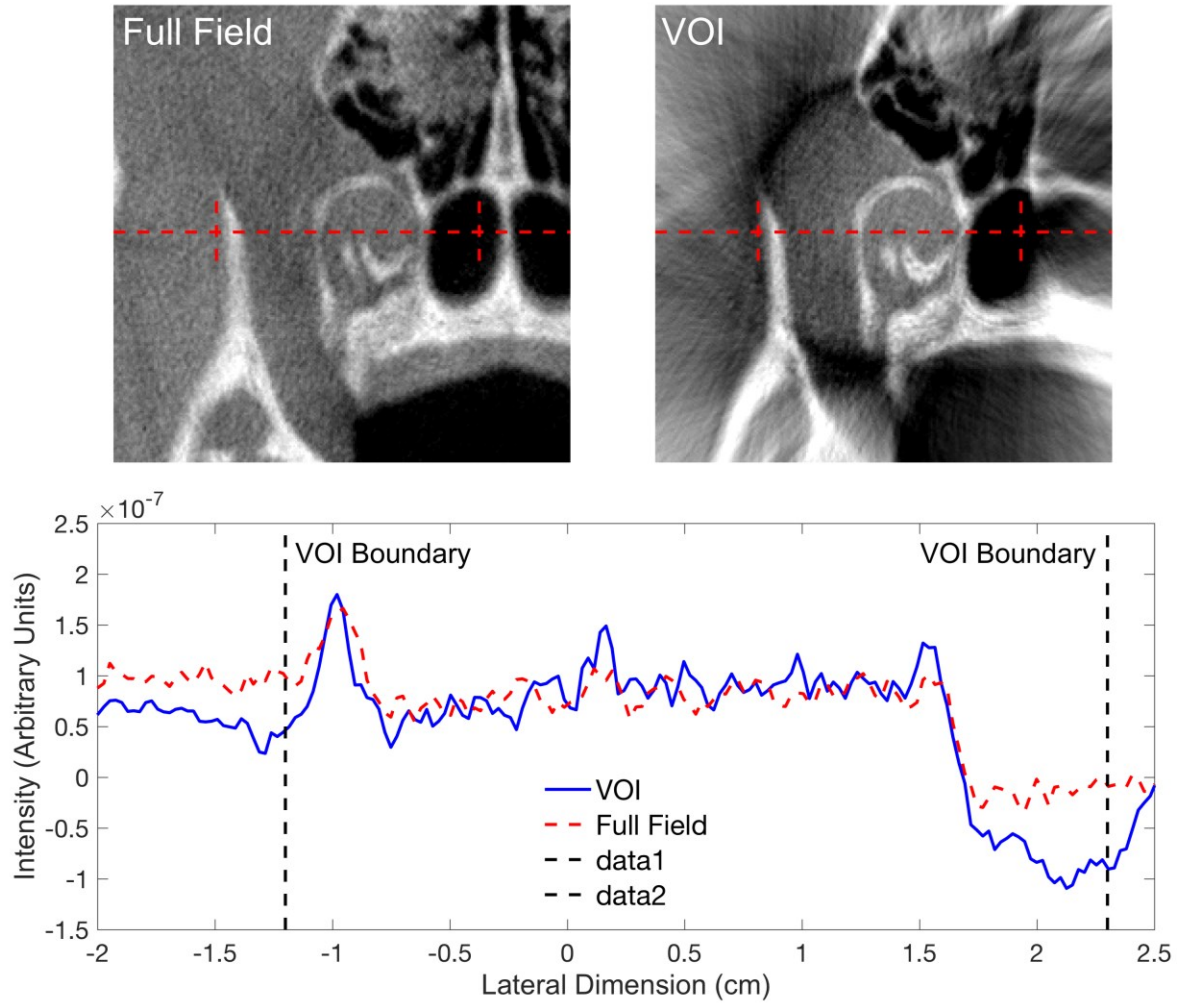
Figure 3.12   (top row) reconstructed volumes for the VOI displayed in Figure 3.6 and corresponding full-bowtie image. Horizontal and vertical dashed line indicate the profile and VOI boundary location, respectively. (bottom) Profiles through soft tissue for both image VOI (solid) and bowtie (dashed) volumes, the dashed line indicated the VOI boundary.
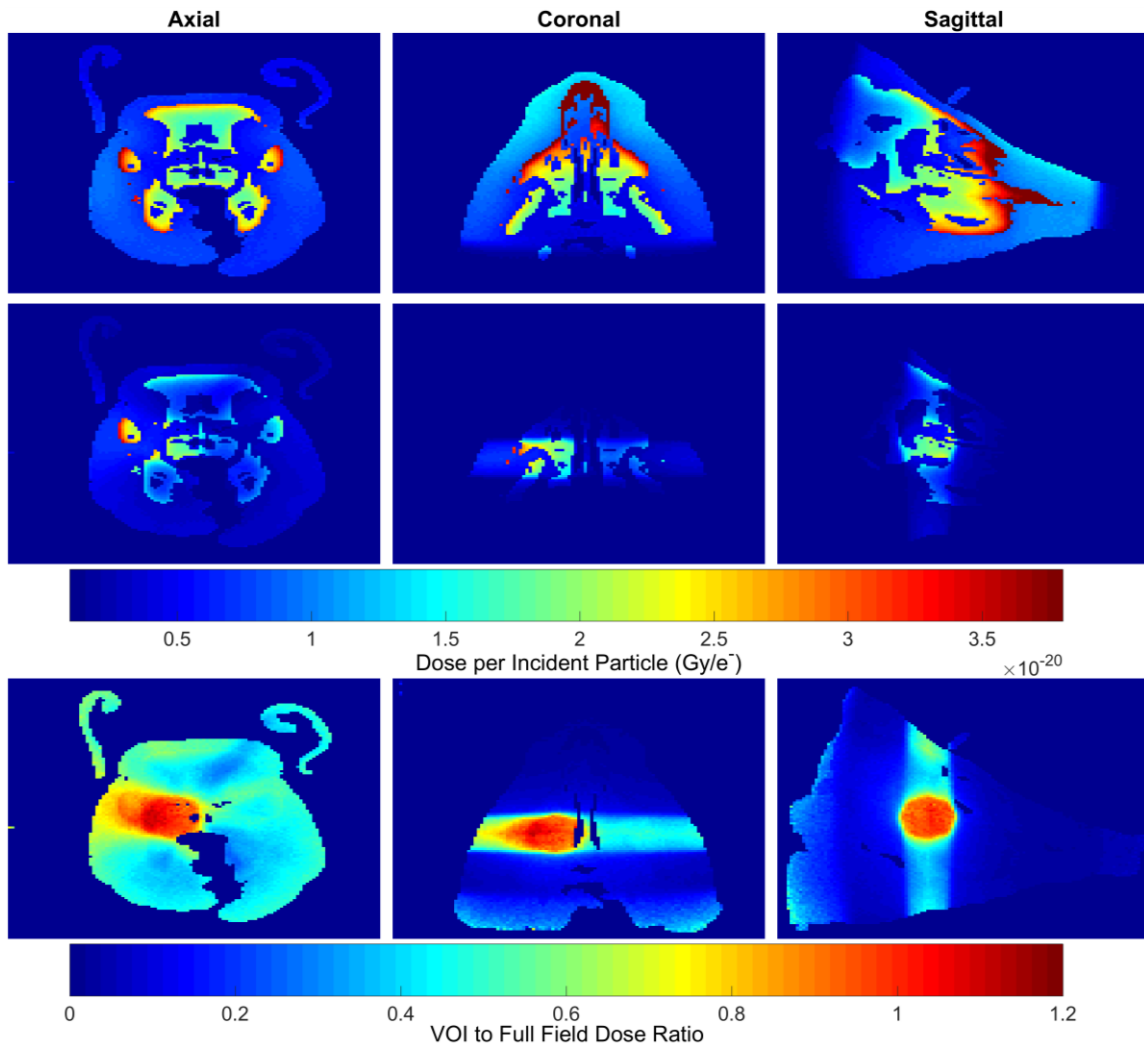
Figure 3.13   Dose distributions for the full-bowtie (top row) and VOI (middle row) acquisitions for image volumes displayed in Figure 3.12, in Gy per incident history. (bottom row) Dose ratios of the VOI to full-bowtie acquisitions.

Figure 3.13 displays the corresponding simulated dose distributions in Gy per incident particle, for the image volumes displayed in Figure 3.12. As with the previous dose distributions displayed in Figure 3.9, the high dose region is isolated to the imaged volume, with a smooth fall-off laterally within the scan plane and rapid decrease superior-inferiorly. When a full-bowtie is used, the high dose region is located within the central

region of the head where attenuation of the filter is minimal and decreases laterally with increasing filter thickness or within the thinner sections of the head. Figure 3.14 displays profiles of axial and sagittal slices through the dose ratio distribution. The highest ratio outside the VOI occurs adjacent to the right side of the VOI. Outside the VOI, 1%, 30% and 50% of the full-bowtie dose were observed superior, posterior and lateral to the VOI, respectively. Dose to the mandibles within the scan plane was reduced to 32% of the full field value. This offers improved sparing in bone compared to the surrounding normal tissue (43% of full field value).

One limitation of the VOI approach presented here, is all information outside the VOI is lost during reconstruction. This could prove problematic when the VOI includes only soft tissue and could be challenging to register to the planning CT. Iris thickness could be reduced to implement the method presented by Cho *et al*.[15] in which the collimator was partially attenuating. This allowed for a high quality VOI image with reduced quality outside. A nested VOI sequence is an alternative approach, in which a sequential pattern of large (outer) VOI and small (inner) VOI are acquired. The result is a high image quality inner VOI, surrounded by a reduced image quality VOI. This approach has been demonstrated by Leary and Robar[18] using an MLC on a linac with a carbon target and Szczykutowicz *et al*.[19] using a TomoTherapy system. This approach could be readily implemented on the current prototype with minor software modifications.
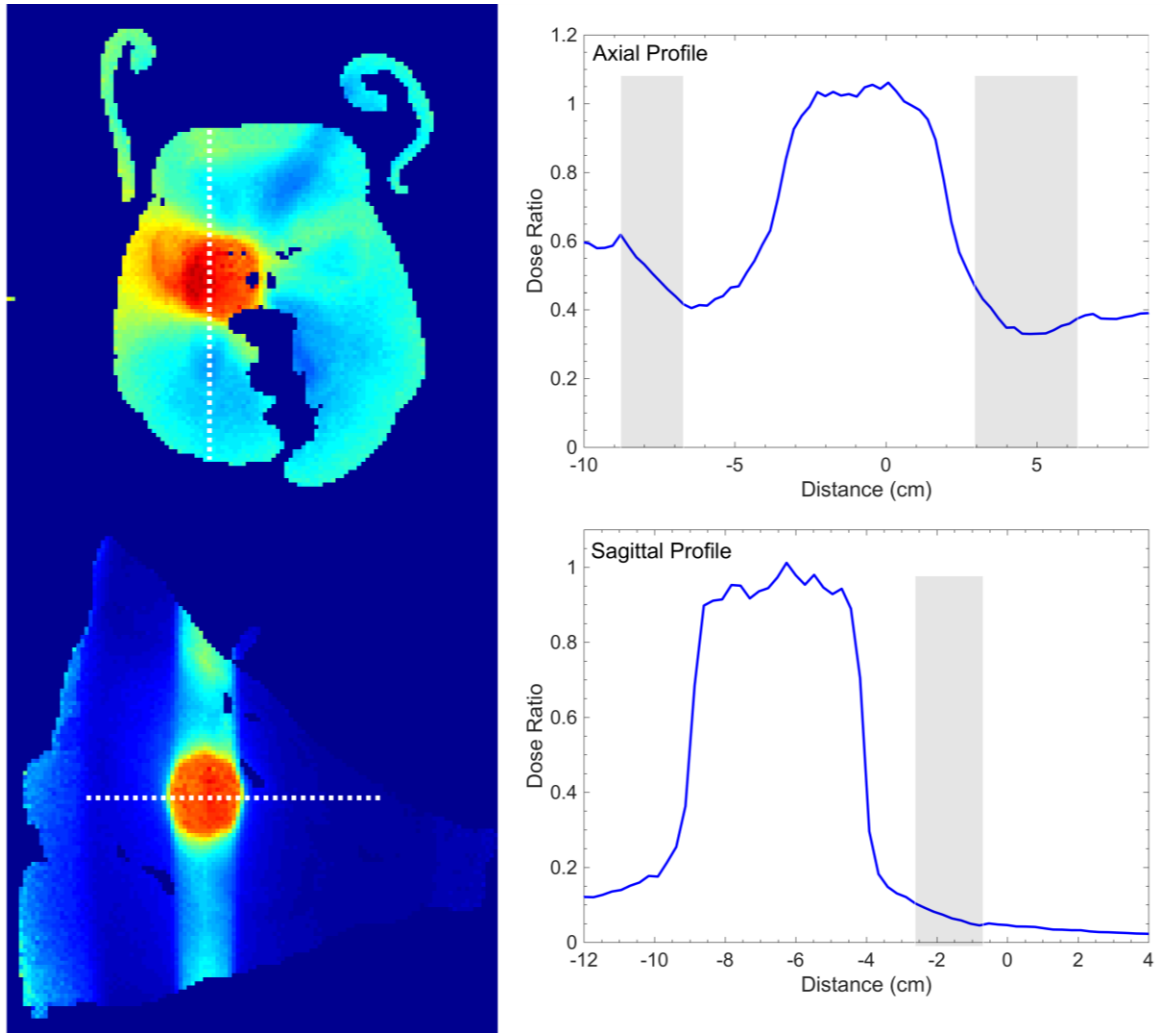
Figure 3.14   VOI to full-field dose ratio maps (left) with profiles corresponding to dotted lines. Shaded regions mark the location of bone.

3.6   CONCLUSIONS

In this work, we have demonstrated the feasibility and advantages of dynamic collimation for kilovoltage VOI CBCT in imaged guided radiotherapy. Other than its coupling to treatment unit, the robotic aperture used in this work is modular and independent, and therefore could be implemented on any OBI, or e.g., C-arm imaging system. The workflow

presented uses information from the treatment planning system to guide image acquisition (i.e. VOI shape and location) and establishes a link between the planning and image guidance steps. When maintaining constant tube mAs, the amount of dose reduction in CBCT was dependent on the size and location of the VOI within the phantom. Assuming a deeply seated VOI, when maintaining constant dose to the VOI, CNR can be greatly improved with a factor increase of 2.0 over the imaging apertures examined.

CHAPTER 4 MANUSCRIPT 2: VOLUME OF INTEREST CBCT AND TUBE CURRENT MODULATION FOR IMAGE GUIDANCE USING DYNAMIC KV COLLIMATION

4.1 PROLOGUE

The following manuscript describes the development of a robotic collimation system consisting of four independent blades. This system was designed for the TrueBeam STx platform, which allowed for the implementation of the novel imaging arcs necessary for TCM. The compatibility and advantages of TCM VOI are assessed for CBCT in this manuscript. Additionally, this manuscript lays the groundwork for current modulated VOI used for intrafraction monitoring of the prostate.

4.2 ABSTRACT

Purpose: The focus of this work is the development of a novel blade collimation system enabling VOI CBCT with tube current modulation using the kV image guidance source on a linear accelerator. Advantages of the system are assessed, particularly with regard to reduction and localization of dose and improvement of image quality.

Materials and Methods: A four blade dynamic kV collimator was developed to track a VOI during a CBCT acquisition. The current prototype is capable of tracking an arbitrary volume defined by the treatment planner for subsequent CBCT guidance. During gantry rotation, the collimator tracks the VOI with adjustment of position and dimension. CBCT image quality was investigated as a function of collimator dimension, while maintaining the same dose to the VOI, for a 22.2 cm diameter cylindrical water phantom with a 9 mm diameter bone insert centered on isocentre. Dose distributions were modeled using a dynamic BEAMnrc library and DOSXYZnrc. The resulting VOI dose distributions were compared to full-field CBCT distributions to quantify dose reduction and localization to the target volume. A novel method of optimizing X-ray tube current during CBCT acquisition was developed and assessed with regard to CNR and imaging dose.

Results: Measurements demonstrated that the VOI CBCT method using the dynamic blade system yields an increase in CNR by a factor of approximately 2.2. Depending upon the anatomical site, dose was reduced to 15%–80% of the full field CBCT value along the central axis plane and down to less than 1% out of plane. The use of tube current modulation allowed for specification of a desired SNR within projection data. For

approximately the same dose to the VOI, CNR was further increased by a factor of 1.2 for modulated VOI CBCT, giving a combined improvement of 2.6 compared to full field CBCT.

Conclusions: The present dynamic blade system provides significant improvements in CNR for the same imaging dose and, localization of imaging dose to a pre-defined VOI. The approach is compatible with tube current modulation, allowing optimization of the imaging protocol.

4.3 INTRODUCTION

VOI CBCT offers improved image quality and dose reduction compared to full-field CBCT through reduction of scatter generation within the patient[8, 12, 13, 93]. Chen *et al.*[12] and Lai *et al.*[13] have demonstrated that using a static copper collimator, scatter reductions of a factor of 6.6, compared to full field CBCT, for example. This resulted in a CNR improvement of a factor of approximately 1.45, with dose reductions by a factor of 1.2 and 2.7 inside and outside the VOI, respectively, compared to full field CBCT. Chen *et al.*[12] and Lai *et al.*[13] used an 11 cm breast phantom, with an 80 kVp beam and the same x-ray tube parameters for both VOI and open-field CBCT. Similarly, Kolditz *et al.*[14] have developed a two arc VOI technique using a static collimator and two isocentres, one arc for a low dose full field acquisition and the second for a high dose collimated VOI acquisition. These data sets were combined using a combination of forward projection, registration and weighting to reconstruct using the FDK algorithm[68]. The result is a high quality VOI image with reduced noise and increased spatial resolution compared to outside the VOI, with 93.1% reduction in dose compared to a conventional full field scan

with equivalent spatial resolution. Previously[93] we demonstrated implementation of kV VOI CBCT using a robotic, octagonal iris collimator that replaces the bowtie filter on an OBI of a 2100 iX Varian linear accelerator (Varian Medical Systems, Inc., Palo Alto, CA). This was capable of increasing image CNR by up to a factor of 2 compared to large fields for the same imaging dose, while decreasing the lateral dose to the VOI to 30% to 60% and less than 1% SI to the VOI, of the full-field value. However, the geometry of the x-ray aperture is restricted to an octagon which must encompass the longest dimension of the VOI in each projection, thus limiting imaging dose conformity for elongated or irregular VOIs. In addition, the robotic collimator was implemented on a previous generation of linac on-board imaging (Clinac OBI, Varian Medical Systems, Inc., Palo Alto, CA) providing limited control over novel acquisition protocols.

Another possible degree of freedom in improving image quality per unit dose is TCM, which has widely been used in diagnostic CT for the last several decades[94]. This technique aims at adapting tube current to the attenuation of the body region for a given angle, thereby reducing imaging dose yet maintaining image quality. TCM may be applicable to VOI CBCT, given that the longitudinal extent of typical VOIs may be comparable to current generation multi-detector CT[95]. The combination of VOI and tube-current modulation could also be considered a simple form of fluence-field modulated CT[19–23, 96]. Gies *et al.*[27] have previously described a method to calculate tube current modulation in CT based on the attenuation through the central axis, which results in a desired number of quanta at the detector plane for every projection, demonstrating that dose and image noise could be reduced[28, 29]. For CBCT, Szczykutowicz and Mistretta[21–23]

described an approach in which fluence is modulated by ten overlapping iron wedge pairs creating a piecewise-constant dynamic attenuator. By modulating fluence as a function of projection angle, Szczykutowicz and Mistretta have demonstrated that this technique is capable of decreasing dose and image noise while providing regions of high SNR compared to unmodulated CBCT. Similarly for CT, Hsieh *et al*.[24] and Hsieh and Pelc[25] have described a piecewise-linear dynamic attenuator using two sets of abutting triangular wedges composed of iron, one offset laterally from the other by half of the triangle base. Hsieh *et al*.[24] and Hsieh and Pelc[25] demonstrated that fluence could be modulated as a function of position and projection angle, resulting in decreases in dose and scatter-to-primary ratio. Bartolac *et al*.[20] described a framework which calculates an optimal fluence distribution using prescribed image quality and dose objectives to various structures within the patient. This framework could potentially be implemented for a kV system using any of the mentioned above attenuator techniques. Recently Leary and Robar[18] and Szczykutowicz *et al*.[19] have successfully demonstrated this concept using a MLC in combination with a 2.5 MV carbon target on a Clinac (Varian Medical Systems, Inc., Palo Alto, CA) and a standard 3.5 MV beam on a TomoTherapy unit (Accuray, Madison WI), respectively.

In the current work, we demonstrate VOI CBCT with dynamic collimator and the enhancement of this imaging approach by incorporating TCM. This is done by extending the functionality of the standard kV blades on a linear accelerator image guidance platform using a newly-developed prototype dynamic collimator. We demonstrate the

utility and advantages of this technology with regard to image quality and dose reduction in VOI CBCT. Finally, the compatibility and advantages of TCM is examined.

4.4   MATERIALS AND METHODS

4.4.1   PROTOTYPE DYNAMIC COLLIMATOR

A robotic blade system was developed to collimate the radiation field produced by the imaging system as a function of gantry angle (Figure 4.1). Similar to that in the commercial system, the blades are composed of 2 mm of steel with an added 3 mm of lead within the radiation field. The y-blades and x-blades are located on either side of an aluminum base plate, which attaches to the frame of the x-ray tube. The y-blades (translating parallel to the axis of rotation) and x-blades (translating perpendicular to the axis of rotation) are located approximately 20.2 and 22.9 cm from the anode, respectively. Blade translations are accomplished using stepper motors (E28H43-05-900, Haydon Kerk Motion Solutions, Inc., Waterbury, CT), one for each blade. This system is slightly more massive than the previously developed iris collimator [93], however remains well below the weight tolerance of the source arm and has negligible impact on gravitational sag. The dynamic collimator interface was designed to be modular, i.e., allowing it to be easily ported to other CBCT imaging systems, and therefore largely independent of the linac on-board imaging. The collimator dynamics are controlled using a microcomputer (Raspberry Pi 2 model B V1.1, Raspberry Pi Foundation, Caldecote, UK) located within the gantry. Each stepper motor is controlled using an A4983 micro-stepping driver chip (Allegro MicroSystems, Inc., Worcester, MA), coordinating simultaneous motion of each blade. The maximum imaging

aperture is 27.2 by 27.2 cm^2, with complete over-travel of each blade. To determine

gantry angle, a triple-axis digital accelerometer (ADXL345, Analog Devices, Inc., Norwood,

MA) was used.
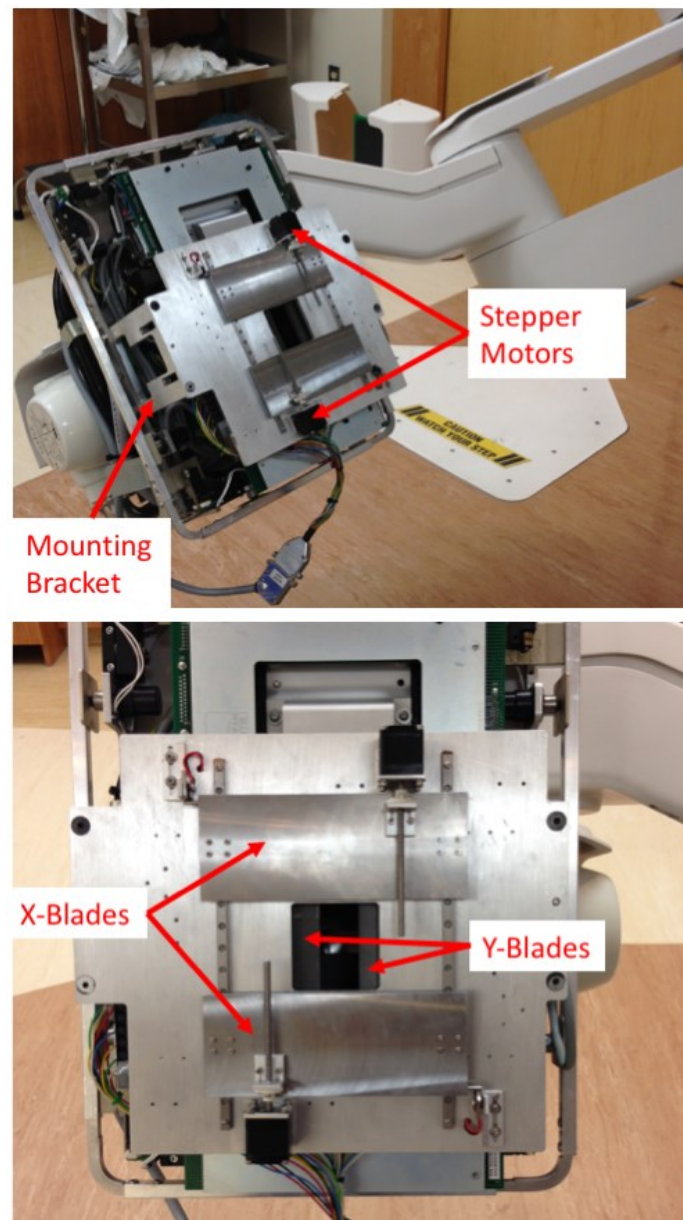
Figure 4.1   (Top) Robotic blade collimator attached to the x-ray tube on a Varian TrueBeam
              STx unit.

4.4.2 VOI CBCT Imaging

The previously described imaging paradigm by Parsons and Robar[93] was used within this work. Briefly, a VOI is defined using the Eclipse TPS (Varian Medical Systems, Inc., Palo Alto, CA). To calculate blade locations, the DICOM structure set of the VOI is exported from the TPS and loaded into software to determine collimator trajectory. For each projection angle, the structure set is projected onto a two-dimensional plane intersecting isocentre and perpendicular to the source. Each blade is then fitted to the projection. The translation trajectories are calculated over a 360-degree arc. An example of this is displayed in Figure 4.2 for an ATOM head phantom with a VOI offset from the axis of rotation. At the time of imaging, the calculated translations serve as a lookup table for the angular position of the gantry. For the present work, all translations and imaging apertures are specified at the plane orthogonal to the central axis and intersecting isocentre.

Images were acquired using Developer Mode on a TrueBeam STx unit. Our institutional clinical CBCT imaging protocol for head and neck patients was adapted for this work, using the following base x-ray tube parameters of a potential of 120 kVp, current of 20 mA, pulse width of 20 ms, SAD of 100 cm, SDD of 150 cm, and a 200° arc.

The CBCT projections were reconstructed using the FDK algorithm[68] within iTools (Varian Medical Systems, iLab GmbH, Baden, Switzerland). The preprocessing steps were simplified from previous VOI CBCT methods[93] to account for the truncation artifacts associated when reconstructing VOI projections. Prior to reconstruction the VOI projection is masked using the *a priori* blade locations, eroded, the boundary of the VOI

extrapolated and normalized. For comparison to previous work with the robotic iris collimator[93], image CNR was investigated for the same dose to isocentre for each aperture size, using a 9 mm diameter by 3 cm long cylindrical bone insert (density of 1.82 g/cm^3) centered on isocentre contained within a 22.2 cm diameter by 20 cm long cylindrical water phantom. CNR was calculated using Eq 3.1. Error bars were found by calculating the mean and standard deviation of CNR measured among ten 1 mm slices above and below the central slice.
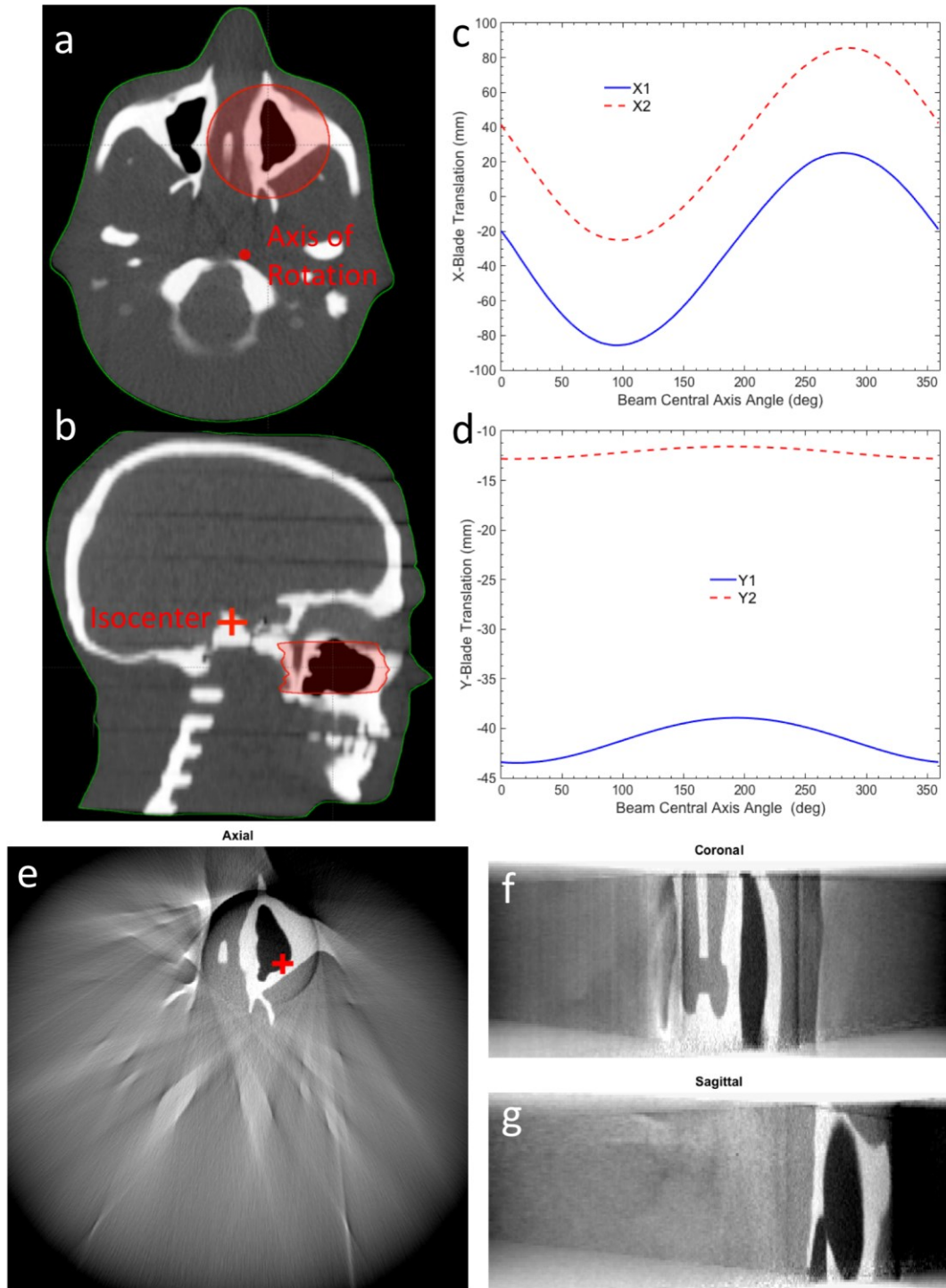
Figure 4.2   (a-b) CT volume of the ATOM head phantom in the treatment planning with the VOI in red and isocentre indicated with a crosshair. (c) X- and (d) Y-blade translations as a function of beam central axis angle at isocentre (using the Varian IEC coordinate system). (e-g) Reconstructed VOI, cross in axial image marks the coronal and sagittal planes.

4.4.3 4D MONTE CARLO FOR VOI CBCT

To calculate (modulated and unmodulated) VOI CBCT dose distributions Monte Carlo simulations were used. The x-ray tube with prototype dynamic blade collimator was modeled in BEAMnrc[76] using exact geometric and material specifications provided by Varian Medical Systems. A phase-space was first generated immediately above the dynamic blade collimation. This phase-space was then used as an input for the VOI CBCT dose calculations. This was done for efficiency purposes as the bremsstrahlung distribution throughout the rotation is constant, with only the blade collimation changing. A 120 keV mono-energetic electron beam was incident on the x-ray target. The incident electron beam angle relative to the x-ray tube was simulated according to manufacturer's specifications. The DBS variance reduction technique was used, with a splitting radius of 17 cm for standard open field of 27.2 x 20.6 cm^2 and bremsstrahlung splitting number of 2000. Similar to previous work where similar kV sources were modeled[89, 93], the EGSnrc parameters listed in Table 3.1 were used; where not mentioned the default values were used. Global ECUT and PCUT of 0.521 MeV and 0.010 MeV, respectively, were used.

Source 20 in DOSXYZnrc and the SYNCJAWS component module developed by Lobo and Popescu[80] were used to simulate the synchronized blade translations with gantry rotation in DOSXYZnrc. The simulation was divided into 200 control points. The CT DICOM information was exported from the TPS and used to create an EGSPHANT file containing the material and density composition of the phantom.
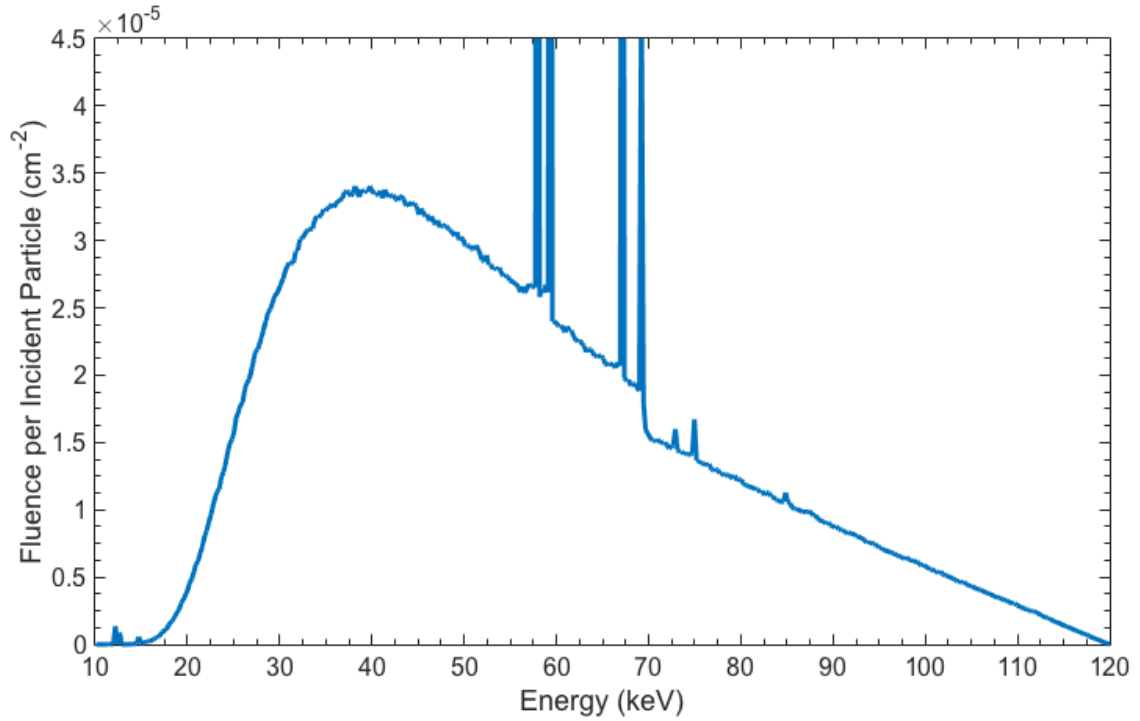
Figure 4.3　　　120 kVp open-field spectrum from the kV source on TrueBeam.

4.4.4 Tube Current Modulation

The CT DICOM information was exported from the TPS and used to create linear attenuation coefficients matrix using air, lung, tissue and bone (as defined in ICRU-44 [97]) for a 60 keV photon from the NIST database[98]. 60 keV was chosen as it is approximately the mean energy (63 keV calculated using BEAMdp[99]) of the 120 kVp spectrum from the x-ray tube on TrueBeam displayed in Figure 4.3. Siddon's method[72] was then used to calculate an attenuation map (DRR) in MATLAB, mimicking the physical setup of an SAD and SDD of 100 and 150 cm, respectively. This was repeated in one degree increments for a full rotation around the phantom. The attenuation maps were then masked with the corresponding blade positions. The formulation developed by Gies *et al.*[27] and modified

by Szczykutowicz and Mistretta[21, 23] was used to determine variation of fluence as a function of projection angle. Briefly, this calculation is described using the following equation from Gies *et al.*[27]

$$N_i = \frac{N_o}{\sum_{i=1}^{P} \sqrt{A_i}} A_i \qquad \text{Eq 4.1}$$

where N_i is desired number of quanta after traversing the phantom for an angle i, N_o is the total number of emitted throughout an acquisition, P is the number of projections and $A_i = e^{\alpha (\overline{\mu L})_i}$ is the amount of attenuation through the phantom for an angle i. Following the work of Szczykutowicz and Mistretta[21, 23], an α parameter of 1 was chosen such that modulation is proportional to attenuation. Similarly, a q value was used to calculate $(\overline{\mu L})_i$ for an angle i. This parameter is used to determine a threshold below which the mean is taken and can be used to account for soft tissue/bone interfaces. Figure 4.4 displays three values of q for a projection of the VOI displayed in Figure 4.2 at a source angle of 180 degrees. As demonstrated, by reducing q, a greater portion soft tissue relative to bone is used in determining $(\overline{\mu L})_i$. Within Developer Mode on TrueBeam version 2.0, currently only the pulse width can be altered between projection acquisitions, as stated in 4.4.2 a tube current of 20 mA was always used with a minimum allowed exposure per image of 0.4 mAs, therefore a 20 ms pulse width was taken to be the lower bound for modulation. The above was then used to create an extensible markup language (XML) script for Developer Mode.
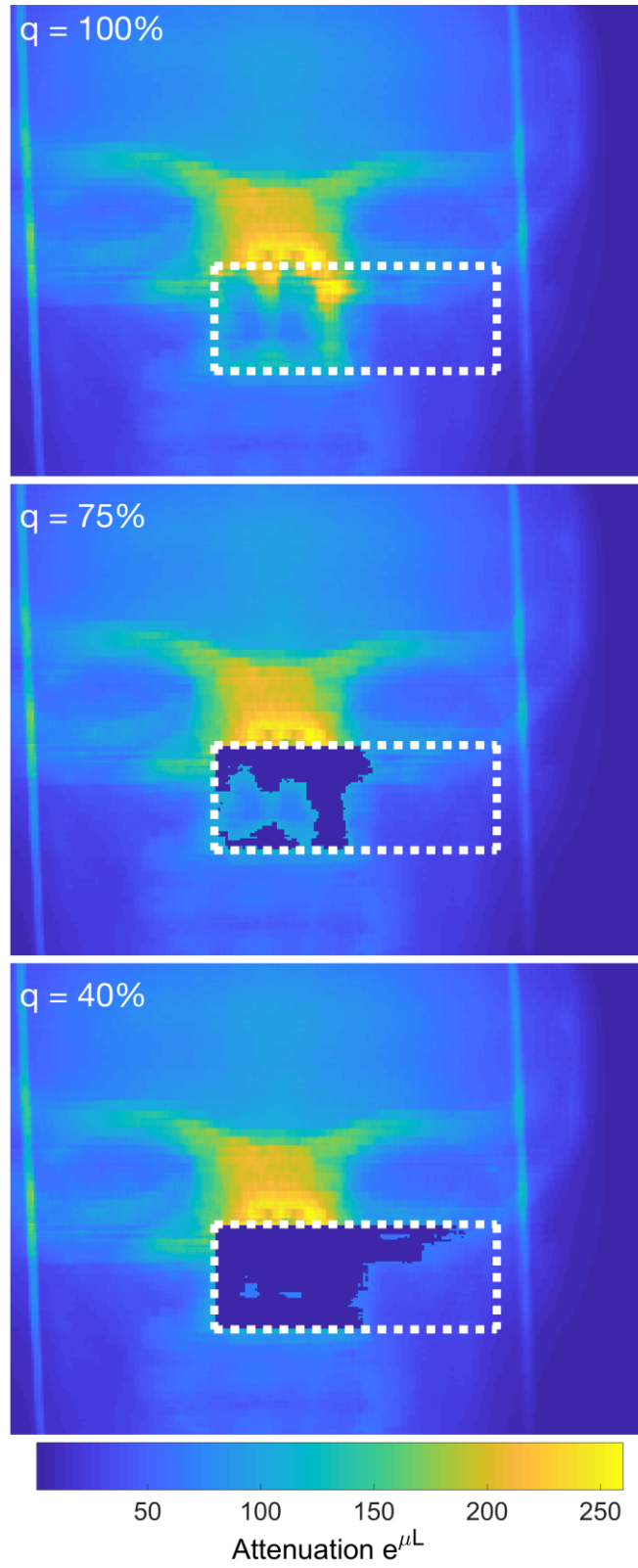
Figure 4.4   Attenuation maps for q equal to 100%, 75% and 40%. Dashed box highlights the location of the blades and data used in calculating $\overline{(\mu L)}_i$.

To demonstrate that desired number of quanta was arriving at the detector signal, projection SNR was measured through ten acquisitions of the VOI in phantom displayed in Figure 4.2. At each angle the mean and standard deviation of each pixel value were recorded. SNR was then calculated as the average mean over the average standard deviation, among acquisitions, for each angle. Image CNR was investigated using the phantom described in 4.4.2 except the cylindrical bone insert was placed 5.5 cm off-axis. The VOI was located off-axis to provide variation in attenuation. A 6.5 cm diameter by 2.5 cm long VOI was used with the bone insert at the center. Dose was measured by replacing the bone insert with a 0.015 cm^3 cross-calibrated ionization chamber (PTW N31010, Freiburg, Germany). Primary calibration was done using an Exradin A12 ionization chamber (Standard Imaging, Inc., Middleton, WI) with collecting volume of 0.65 cm^3 using the TG-61 protocol[90]. This process was done for q values of 25%, 50% and 100% as well as unmodulated acquisition using a pulse width of 82 ms. 82 ms represent the pulse width which gives approximately the same total mAs as a q value of 100%.

4.5   Results and Discussion

4.5.1 Dynamic blade VOI CBCT

Figure 4.5 displays CNR measurements for the cylindrical water phantom with a bone insert centered on isocentre, for imaging apertures ranging from 2x2 cm^2 to 18x18 cm^2. Compared to the previous iris collimator[93] (field areas ranging from 3.9 to 316.3 cm^2), VOI CBCT with the dynamic blade system provides a similar contrast increase by a factor of 1.3 and noise reduction by a factor of 1.7 compared to full field CBCT, and thus an increase

in CNR by a factor of approximately 2.2. The results in Figure 4.5 also demonstrate that the rate of CNR improvement is most pronounced as imaging aperture is reduced below approximately 10x10 cm^2.

Figure 4.6 displays VOI CBCT imaging dose distributions for an open-field and the VOI acquisition of the phantom displayed in Figure 4.2. Similar to previous work[93], this demonstrates that the high dose is mainly isolated to the VOI, however on the axial planes containing the VOI a dose ranging from 20 to 50% of the full field value exists, while the dose outside the plane is decreased to less than 1%. Extrapolating the above results to other anatomy would be challenging as the associated gains in image quality and dose reduction are highly dependent on the anatomy of interest, as well as the size and location of the VOI.
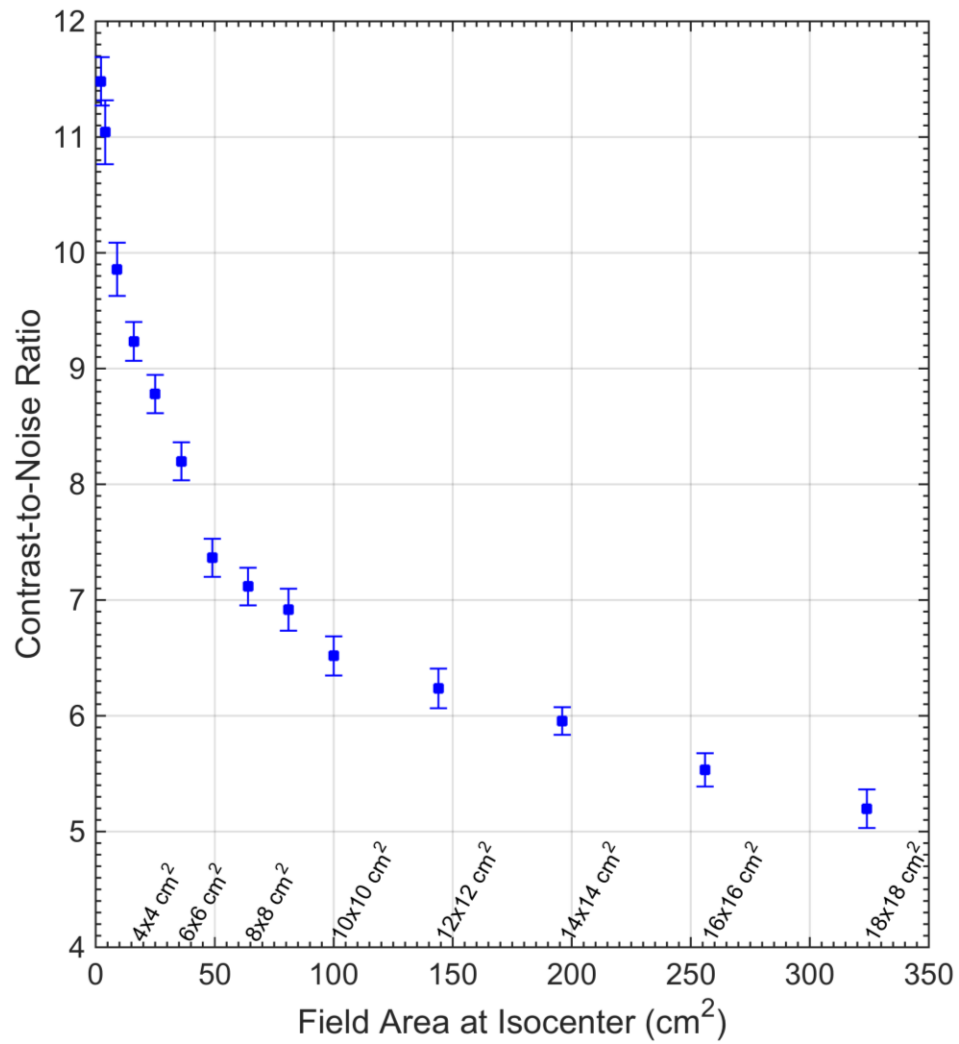
Figure 4.5   CNR measurements for a cylindrical water phantom with a bone insert centered on isocentre, for imaging apertures ranging from 2x2 cm^2 to a 18x18 cm^2 field.

| Axial | Coronal | Sagittal |

Dose per Incident Particle (Gy/e⁻)

$\times 10^{-20}$

VOI to Full Field Dose Ratio
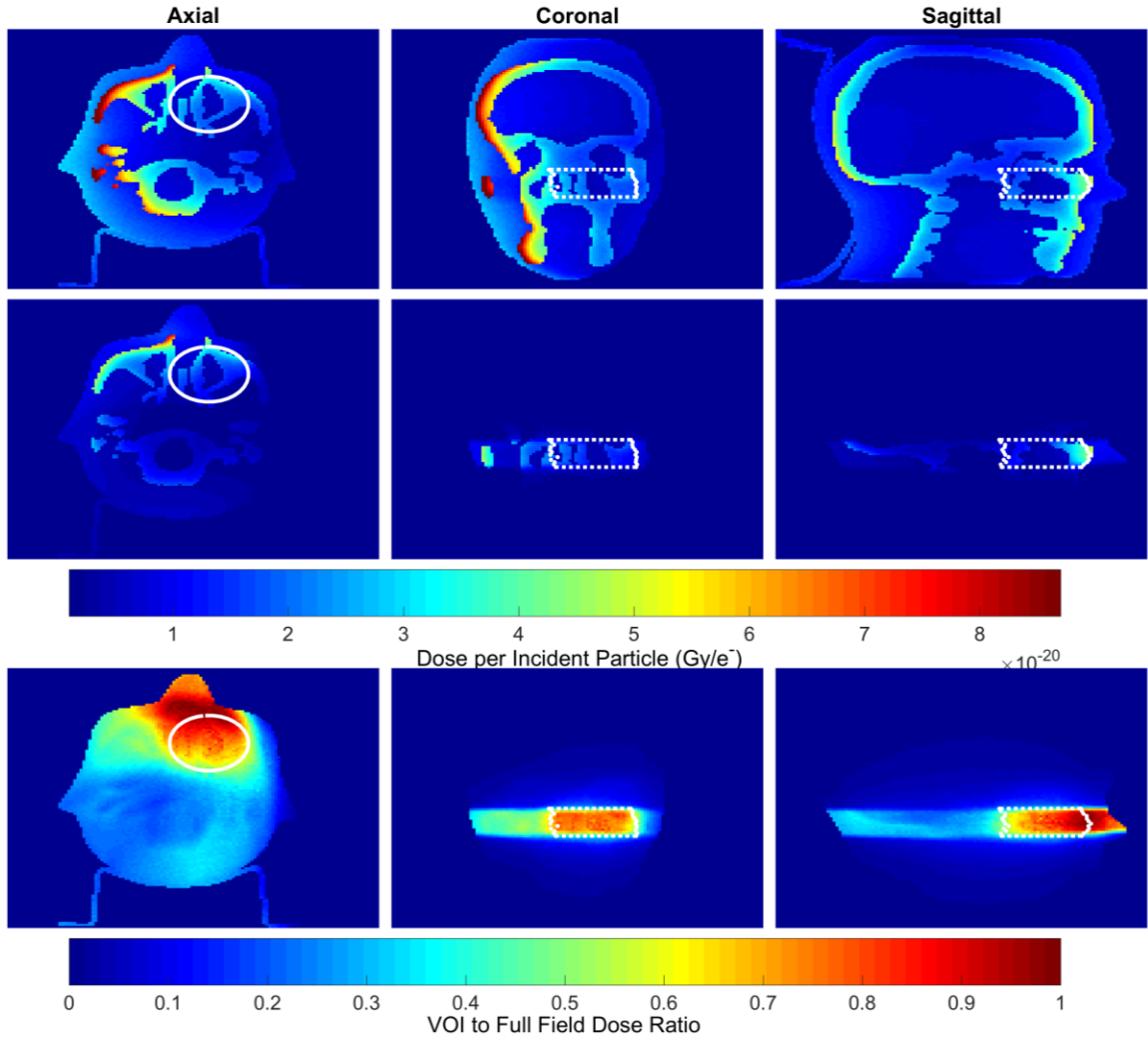
Figure 4.6   Dose distributions for the open field (top row) and VOI (middle row) acquisitions for image volumes displayed in Figure 4.2, in Gy per incident electron striking the x-ray target. (bottom row) Dose ratios of the VOI to open field acquisitions. White contour highlights the location of the VOI.

4.5.2 Modulated VOI CBCT

Figure 4.7 displays attenuation as a function of projection angle for the VOI displayed in Figure 4.2a-b using a *q* value of 100% as well as the arc path that represents the minimum integral attenuation. Variation is approximately sinusoidal but will depend on the shape

of the patient, radiologic attenuation and location of the VOI. For comparison, when using a linear attenuation coefficient 0.19 cm^{-1} for a water phantom, the attenuation values are comparable to those calculated by Gies *et al.*[27] using the central ray-line method. Figure 4.7 also displays the pulse width as a function of beam central axis angle using a q value of 100%, in which a 20 ms pulse sets the lower bound. An unmodulated acquisition using the same total mAs would equate to a pulse width of approximately 80 ms.

Figure 4.8 displays projection SNR within the VOI as function of beam central axis angle for a modulated and unmodulated VOI CBCT acquisition of the VOI displayed in Figure 4.2. This demonstrates that modulated VOI CBCT results in approximately equivalent SNR throughout the rotation compared to the sinusoidal SNR of an unmodulated acquisition (with an inverse relationship with the amount of attenuation). Furthermore, the SNR of the unmodulated acquisition follows an inverted relationship of the attenuation. The above suggests that projection SNR could be prescribed using this method.

Figure 4.9 displays dose ratios for unmodulated and modulated VOI acquisitions compared to an unmodulated open field dose distribution. The use of modulation results in a slight increase to the maximum dose to the VOI, with an increase of approximately 10% compared to unmodulated acquisition using the same integral mAs. However, the dose to the VOI can be reduced by lowering the q value, as demonstrated for q values of 50% and 25%, giving dose reductions of 38% and 50% compared to a q value of 100%, respectively. Little variation in the dose outside the VOI is observed, with a reduction of approximately 10% two centimeters posterior to the VOI, when changing q value from

100% to 25%. Figure 4.9 also highlights how the use attenuation could be used to guide the arc path for an unmodulated acquisition.
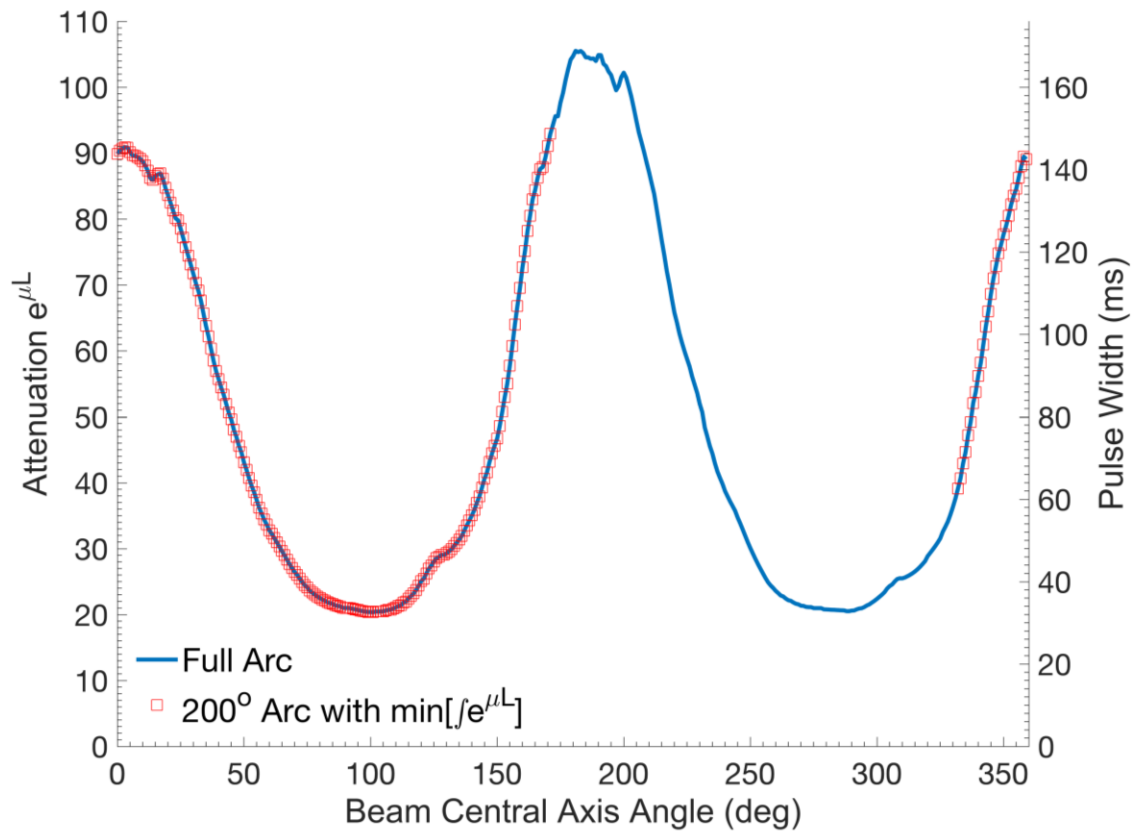
Figure 4.7   Attenuation and pulse width as a function of beam central axis angle for the VOI displayed in Figure 4.2a-b using a q value of 100% for a complete rotation and the 200° arc with the lowest integral attenuation.
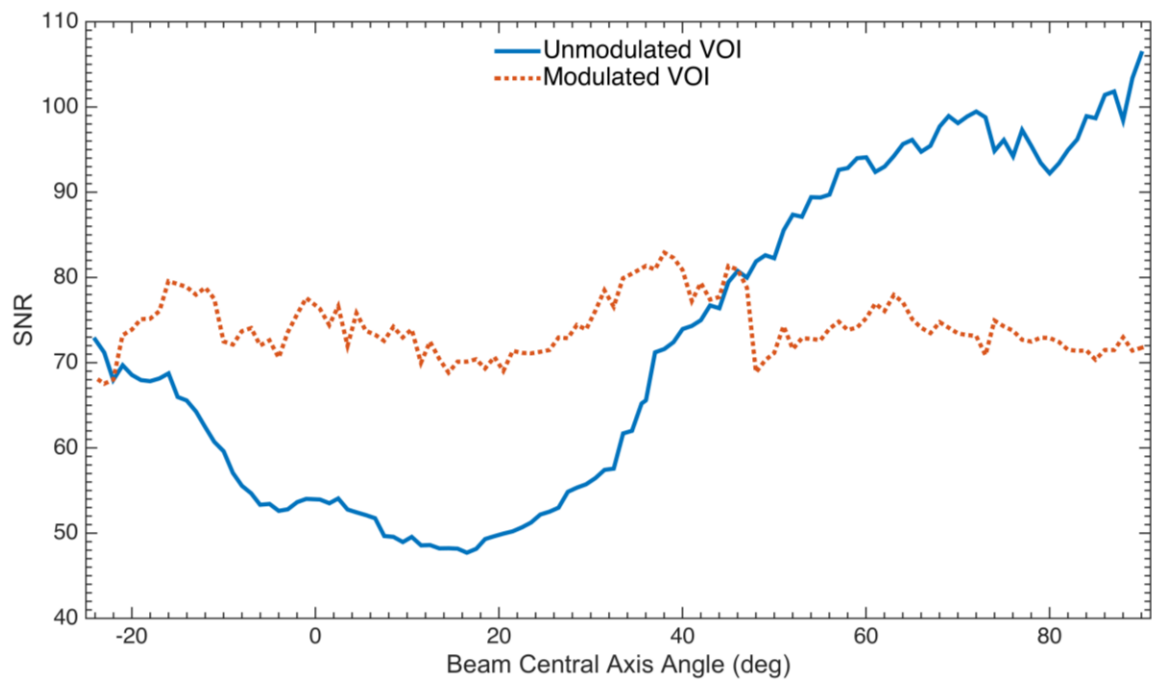
Figure 4.8   Projection signal-to-noise ratio as a function of projection angle for a modulated (q=100%) and unmodulated VOI acquisition for the VOI displayed in Figure 4.2.
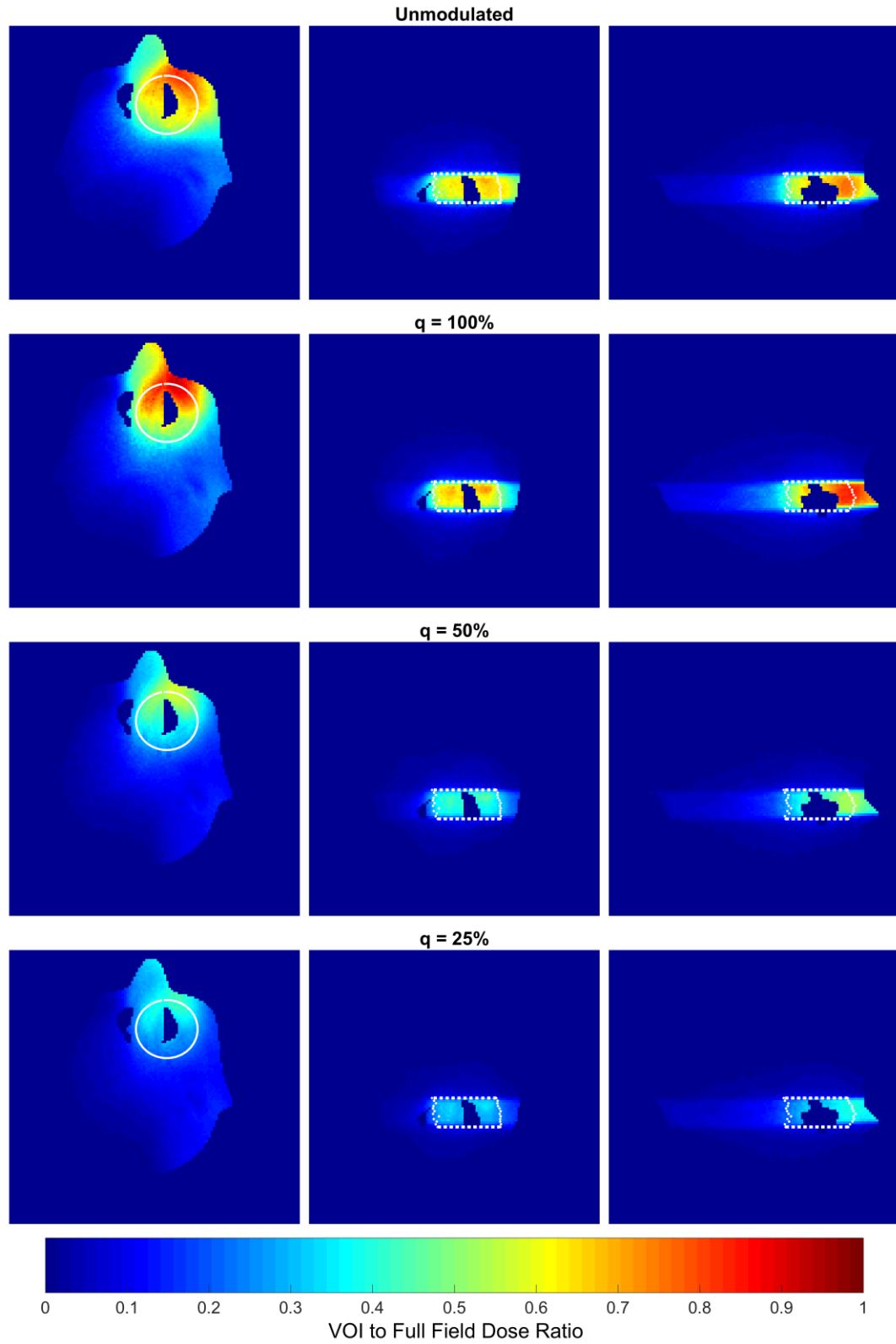
Figure 4.9   (top down) VOI to full field ratio for an unmodulated and modulated for q values of 100%, 50% and 25%. White contour highlights the location of the VOI.

Figure 4.10 displays CBCT image CNR, VOI dose and total mAs for unmodulated and modulated acquisitions using a 6.5 cm diameter by 2.5 cm long VOI centered on a bone insert located 5.5 cm off axis in the phantom described in section 4.4.2. This demonstrates that for approximately the same total mAs and dose, a modulated (q=100%) acquisition results in an increase in CNR by a factor of 1.2 compared to an unmodulated acquisition. Also demonstrated is that for approximately the same CNR, modulation with q=25% gives a dose reduction by a factor of 1.6, compared to the unmodulated case. Interpolating from these results, q=96% would deliver approximately the same dose to the VOI. This would correspond to a CNR of approximately 23.9, giving an improvement by a factor of 1.16 compared to an unmodulated acquisition. It should be noted that, compared to full field CBCT imaging, these improvements are incremental to those realized by use of the VOI approach alone, i.e., those demonstrated in Figure 4.5 and Figure 4.6. Modulated VOI CBCT could result in a CNR improvement as high as a factor of 2.6 compared to open field. Additionally, Figure 4.10(d-f) displays the dose difference from the unmodulated and modulated acquisitions. The region anterior to the VOI has a maximum dose reduction of approximately 10 mGy and 30 mGy for q values of 100% and 25%, respectively, compared to no modulation. For a q value of 100% the surface dose adjacent to the VOI is increased by approximately 8 mGy. For q values of 25% and 50%, the start angle was shifted compared to the unmodulated acquisition, and there is an increase of dose near the end of the arc by approximately 5 mGy.
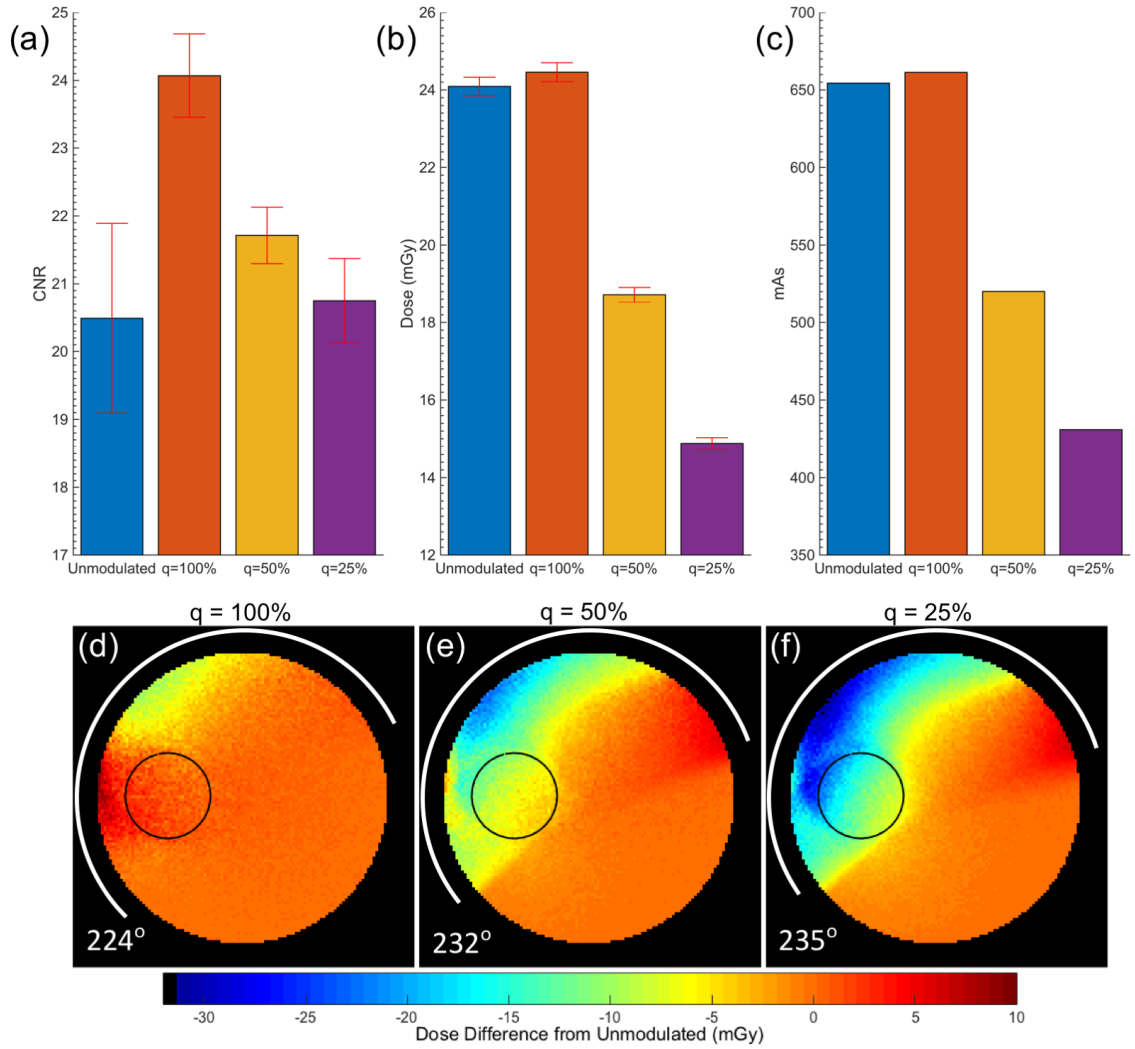
Figure 4.10   (a) CNR, (b) VOI point dose measurement and (c) total mAs for a diameter for a cylindrical water phantom with a bone insert located 5.5 cm off axis. A 6.5 cm diameter by 2.5 cm long VOI was used with the bone insert at the center. Monte Carlo simulated dose difference from the unmodulated acquisition for (d) q=100%, (e) q=50% and (f) q=25% with the bone insert removed. The white arc indicates the 200° arc path and start angle in Varian IEC coordinates. VOI location marked with a black circle.

The main limitation of the technique presented within this work is that the planning CT set is required to calculated the attenuation maps used in determining A_i. While these data are always available for image guidance, it would be difficult to implement in its

current form in the diagnostic imaging. An approach similar to Szczykutowicz and Mistretta[21, 23] could be used, in which previous angle projections are used to determine the desired signal in the current projection. This would require the first few angles of the arc to be unmodulated. Additionally, when the planning CT is available, calculating attenuation maps at one degree increments can be a lengthy process, however Jia *et al*.[100] have demonstrated that this process can efficiently be calculated using GPUs. Using a tool such as this would also allow the use of polyenergetic spectra, which would improve the calculation for a variety of anatomical sites. This would also allow for the management of beam hardening.

A premise of the VOI CBCT as implemented here is that all image data outside the VOI is discarded during reconstruction. However, the current modulation approach described here could provide an additional degree of freedom, e.g., in the nested VOI sequences demonstrated by Leary and Robar[18] and Szczykutowicz *et al*[19], allowing imaging of larger anatomical volumes while controlling levels of image quality and dose throughout the imaged anatomy. Although more complex apertures would be involved, this approach may also assist in an evolution toward true fluence field modulation as described by Bartolac *et al*.[20] in which detailed volumes could be prescribed individual image quality and dose objectives.

4.6 CONCLUSIONS

In this work, we have combined two advantageous approaches in image acquisition for guidance of radiotherapy: i) VOI CBCT, which localizes imaging dose to, for example, the

planning target volume, and ii) modulation of mAs as a function of projection angle. For

the same imaging dose, the VOI CBCT method offers CNR improvements by up to a factor

of 2.2 within the VOI. Peripheral dose outside of the VOI is reduced to 20% to 50% of the

dose value with a full field CBCT approach.   When mAs modulation is applied, an

additional enhancement of CNR (e.g., factor of 1.2) are observed, without a further

increase in dose.

CHAPTER 5 MANUSCRIPT 3: CURRENT MODULATED VOLUME-OF-INTEREST IMAGING FOR KILOVOLTAGE INTRAFRACTION MONITORING OF THE PROSTATE

Authors: David Parsons, Tynan Stevens and James Robar

Contribution: Primary author, development and manufacture of device, development

of methodology, data collection and analysis

5.1 PROLOGUE

The following manuscript applies current modulated VOI for intrafraction monitoring of

the prostate using the kV system on TrueBeam. The focus of this paper is to improve the

available image quality during simultaneous kV and MV irradiation. This was done by

utilizing the increased image quality associated with small fields demonstrated in Chapter

3 and Chapter 4 as well as modulating the fluence in accordance with kV attenuation.

Variations in MV scatter at the detector plane were simulated to investigate the

observations during simultaneous kV imaging. This was done using Monte Carlo

simulation by varying the field size and rotation about the phantom. Finally, the corresponding kV dose distributions are demonstrated for the various modulated and unmodulated VOI acquisitions used in this manuscript.

5.2 ABSTRACT

Purpose: The focus of this work is to improve the available kV image quality for continuous intrafraction monitoring of the prostate during volumetric modulated arc therapy. This is investigated using a novel blade collimation system enabling TCM and VOI imaging of prostate fiducial markers during radiotherapy, and Monte Carlo simulation of MV scatter.

Materials and Methods: A four-blade dynamic kV collimator was used to track a VOI containing gold fiducial markers embedded in a dynamic pelvis phantom during gantry rotation. For each fiducial marker, a VOI margin around each marker was set to be 2σ of the population covariance matrix characterizing prostate motion. This was used to conform to a single or several fiducial markers and compared to a static field. DRRs were used to calculate the kV attenuation for each VOI as a function of angle and used to optimize x-ray tube current during acquisition. Image quality was assessed with regard to CNR, fiducial marker detectability and imaging dose. Monte Carlo simulations in EGSnrc were used to calculate the imaging dose to the phantom and MV scatter fluence to the imaging panel.

Results: Fiducial markers can be accurately located using a VOI containing a single or several fiducial markers using a relatively high constant kV mAs. However, when using a

6x6cm^2 field the dose can be upwards of 1.5 Gy in bone for constant kV mAs and 3.1 Gy when applying TCM at 1 Hz imaging over the course of 40 fractions. This can be mitigated through tailoring the imaging field to a single or several fiducial markers, in which the integral dose is reduced by a factor of 15.6 and 3.7, respectively. For a constant MV treatment field size, the scattered fluence reaching the kV panel varies by less than a factor of two for a completely rotation of the gantry. However, the MV scatter spectrum overlaps with the detector response for a deleterious effect, with a peak MV scatter energy of approximately 100 keV. TCM can be used to overcome the variability in image quality throughout the rotation and therefore improve fiducial marker CNR and detectability during periods of high kV attenuation.

Conclusions: The combination of VOI and TCM introduces an advantageous approach in intrafraction monitoring of the prostate during radiotherapy by both reducing and localizing the imaging dose, while improving image quality and fiducial marker detectability during periods of high kV attenuation. Additionally, the influence of MV scatter has been demonstrated to be most important in low attenuation regions, with a variation by a factor of two.

5.3   INTRODUCTION

The use of SBRT for the treatment of prostate cancer is promising due to the relatively low α/β ratio[4, 34, 35] (1.5 Gy) compared to the surrounding normal tissue (rectum ranging from 4 to 6 Gy)[4, 34]. As a result, a hypo-fractionated regimen would offer a greater therapeutic ratio compared to conventional fractionation regimens. Aside from the

clinical benefits, SBRT would also offer increased patient convenience, throughput, and can be less overall cost compared to conventional fractionation regimens[34, 101]. However, when the number of fractions is decreased to as few as five over two weeks, compared to the traditional 28 to 35 fractions over six to seven weeks, the consequence of geographic miss is greatly increased[4]. A commonly-used approach to account for this is to expand the CTV. This approach can cause an increase in GU and GI toxicity. Recent studies by Alongi *et al.*[102] and Jabbari *et al.*[103] have demonstrated that much of these effects can be limited by decreasing the CTV expansion. Importantly, the above margins are population-based and do not account for individual patient motion. Ng *et al.*[38] and Langen *et al.*[37] have established that prostate motion can deviate over 15 mm from isocentre for long durations of an individual fraction. Recently, Colvill *et al.*[53] demonstrated that a persistent excursion with a mean displacement of 9.9 mm during VMAT reduces the CTV $D_{99\%}$ and PTV $D_{95\%}$ by 19.2% and 34.2%, respectively, while increasing rectum $V_{65\%}$ by 100.7%. These effects may be mitigated through either gating or dynamic MLC[53] by utilizing intrafraction monitoring of the prostate. There are several techniques available for intrafraction motion monitoring, including implanted RF transponders[37, 55, 56], stereoscopic x-ray imaging[57–59], or monoscopic imaging[38, 58, 60].

Monoscopic kilovoltage intrafraction monitoring (KIM), developed by Poulsen *et al.*[60], utilizes the gantry-mounted x-ray system to perform prostate monitoring of implanted gold fiducial markers during treatment, making it possible on modern linear accelerators with planar kV image guidance. When imaging the projection of a fiducial marker, two directions of motion are resolvable, i.e., those of the detector plane.

However, the position along a ray line is unresolved. Poulsen *et al.*[60] recognized that due to i) the highly correlated motion that exists between SI and AP motion for the prostate, ii) the fact that the SI direction always being identified during imaging, and iii) minimal lateral motion of the prostate, the 3D position of the prostate could be estimated. This is accomplished by calculating the expectation value of the unresolved dimension along ray line that intersects the probability distribution. This technique provides absolute localization in two dimensions (in the rotated coordinate system) and utilizes correlations between the SI and AP prostate motion to determine the unresolved dimension with a mean error less than 0.6 mm[61]. However, the effects of MV scatter from the patient to the kV detector and kV beam attenuation have been demonstrated to have deleterious effects on available image quality[62, 63, 104]. The magnitude of MV scatter can vary throughout the treatment delivery, more specifically it depends on patient geometry, dose rate and field shape[62, 63]. However, these effects have yet to be fully investigated, and limited to techniques to retaining kV CBCT image quality during treatment. These involved adding kV control points in the treatment plan and holding off the MV beam[62], or holding off the kV beam to acquire an MV scatter image[63].

Previously, we have demonstrated that the kV CBCT image CNR can be improved by a factor of 1.3 when decreasing from an $6x6cm^2$ to $2x2cm^2$ field for a given dose[104] when using a VOI approach. Additionally, the effects of kV attenuation can be greatly mitigated through using TCM in combination with VOI in which the variance in SNR throughout a complete rotation can be greatly reduced, leading to a further improvement

in CBCT CNR by a factor of 1.2 compared to an unmodulated acquisition with the equal dose to the VOI[104].

Within this work, we demonstrate the application of TCM and VOI to KIM. Specifically, we examine the feasibility of a VOI conforming to a single or several fiducial markers compared to a static field based on the entire prostate volume, and demonstrate the corresponding dosimetric impact. Given that the MV beam is expected to be on during this guidance, the variation in MV scatter radiation is investigated for varying field sizes and rotation using Monte Carlo modeling. Finally, to improve the method, TCM is implemented and fiducial marker CNR is examined as a function of gantry rotation compared to an unmodulated constant mAs acquisition. Although this work utilizes the KIM method to estimation prostate motion, it could be readily applied to any kV intrafraction imaging such as the kV-MV methods proposed by Ren *et al.*[105], Cho *et al.*[106] or Wiersma *et al.*[57]

5.4 MATERIALS AND METHODS

Within this work, and as illustrated in Figure 5.1, three systems are used simultaneously to investigate current modulated volume-of-interest (CMVOI) for intrafractional monitoring of the prostate: the kV and MV systems of a TrueBeam STx, a novel dynamic kV collimator, and 3D dynamic prostate phantom. In the following sections, each of these components are described in detail.
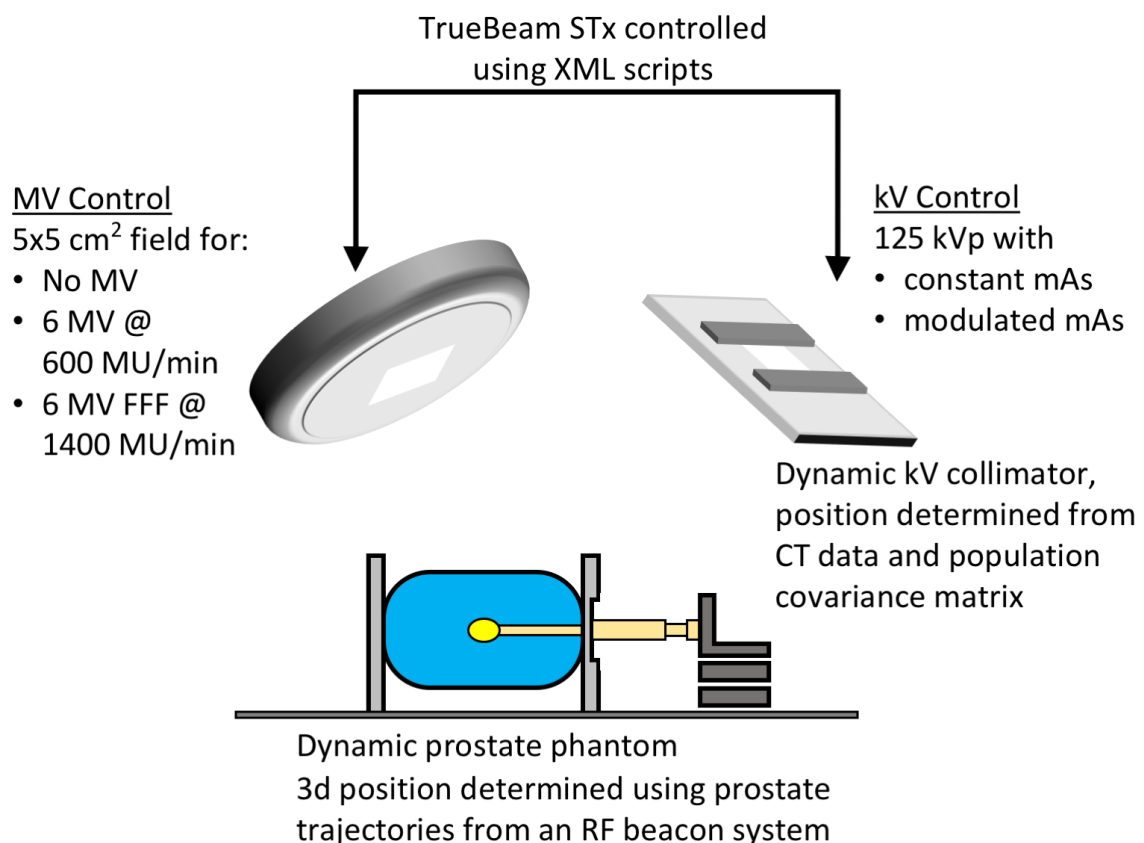
Figure 5.1   Key components used in this work to explore CMVOI for intrafractional monitoring of the prostate.

5.4.1 PROTOTYPE DYNAMIC COLLIMATOR

The previously described robotic collimation system[104] was used to define the radiation field produced by the imaging system as a function of gantry angle (Figure 4.1). Briefly, the prototype consists of four blades composed of 2 mm of steel with an added 3 mm of lead, this mimics the design of the commercial system. The dynamic collimator interface is modular and independent from the clinical system. Blade motions are controlled using a microcomputer (Raspberry Pi 2 model B V1.1, Raspberry Pi Foundation, Caldecote, UK)

and a triple-axis digital accelerometer (ADXL345, Analog Devices, Inc., Norwood, MA) located within the gantry.

5.4.2 Dynamic Prostate Phantom

To simulate the motion of the prostate we developed a novel dynamic pelvis phantom. Previous prostate tracking experiments with fiducial markers used a Styrofoam phantom and embedded fiducial markers on a translation stage[107] or fiducial markers placed on the robotic treatment couch[58]. This implementation is sufficient for verification of tracking algorithms but does not provide the necessary conditions to degrade image quality (i.e. MV scatter and kV attenuation) including surrounding tissue and bony anatomy. The resulting dynamic phantom (Figure 5.2) is composed of two major components a three-dimensional translation stage (LNR50S, Thorlabs, Inc., Newton, NJ) and four slices of an ATOM phantom. The central soft tissue (bordering the pubis, ischium tuberosity and sacrum) of slices 34 to 37 of the ATOM phantom were removed to create an irregularly-shaped water filled cavity for translation of a 3D printed prostate with three embedded gold fiducial markers. Both ends of the phantom where sandwiched between plates of PMMA. The inferior PMMA plate is composed to two 1.2 cm slabs, the central 27 cm diameter of each slab was recessed 3.2 mm. Within this recess a 2.9 mm thick by 12.7 cm diameter PMMA drive plate was set (surrounded by lubricant). This drive plate was attached to a 32 mm nylon drive rod which created AP and lateral translations. Inside the drive rod was a 19 mm nylon shaft which allowed for SI translations. This shaft was connected to an 11 mm nylon rod which attaches to a 3D printed simulated prostate

gland. Additionally, to allow for the displacement of water by the insertion of the nylon rod, a latex bladder was stretched over a 38 mm diameter opening in the superior PMMA plate. The phantom was made water tight using a silicon sealant, the exception being the inferior PMMA plates which sealed to the phantom using lubricant. The superior and inferior PMMA plates were held together using four 9.5 mm threaded nylon rods. Motions of approximately 5 mm, 30 mm and 40 mm are possible laterally, AP and SI, respectively.
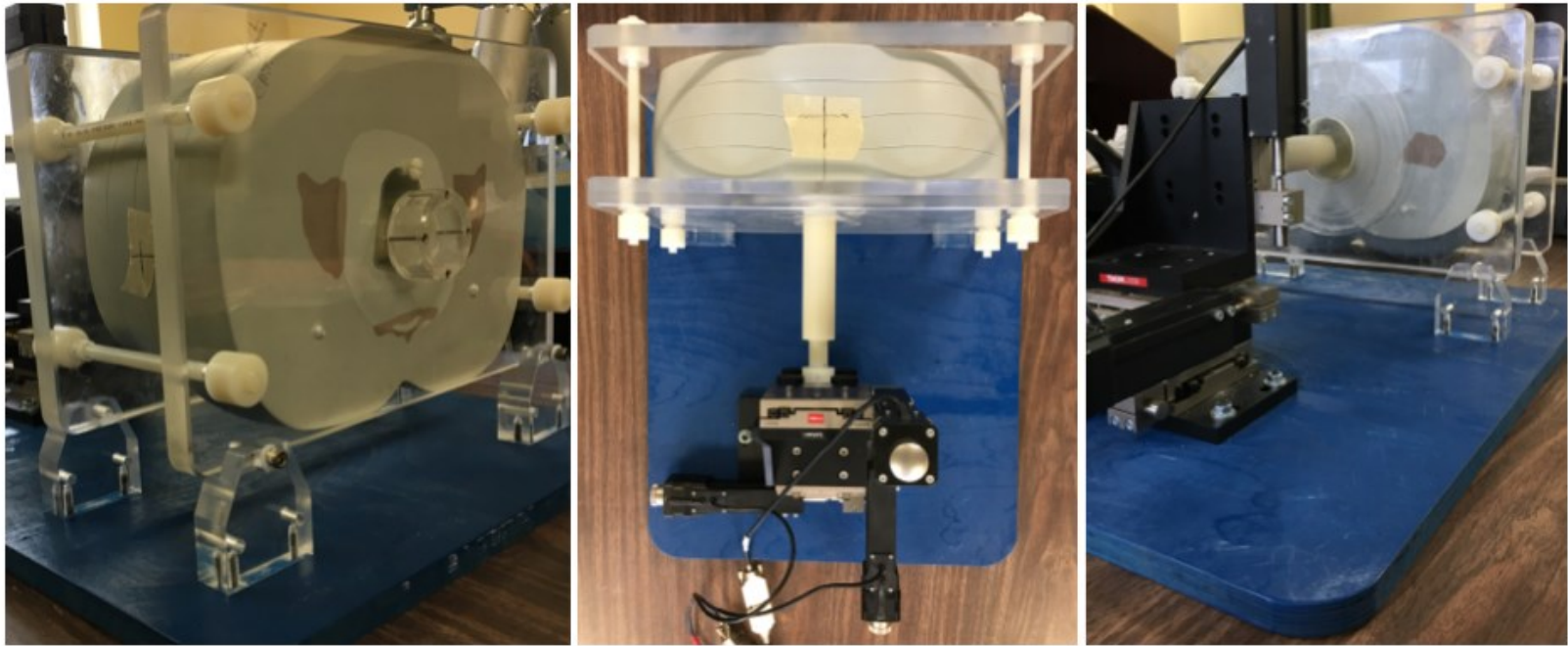
Figure 5.2   Dynamic prostate phantom with three-dimensional translation stage.

Stage translations were controlled using ActiveX controls with MATLAB. Actual prostate trajectories from an RF beacon system were provided by Langen *et al*.[37] These were used as lookup tables to guide stage translations. The software has a latency of 0.02 s at 4 Hz and increases to 0.1 s at 10 Hz. Within this work 4 Hz was used for all translations.

5.4.3 VOI INTRAFRACTIONAL IMAGING

The CT and structure DICOM data of the phantom were exported from the Eclipse TPS (Varian Medical Systems, Inc., Palo Alto, CA). To calculate blade locations necessary to image a fiducial marker, a distribution of random points and their corresponding probability were generated at the fiducial marker location within the phantom. These points were generated using the population covariance matrix from Poulsen *et al*.[60], future implementations would use the standard pre-treatment arc[38] to construct the patient specific motion model. A shell was then made at 2σ and expanded by 5 mm in each direction to account for the finite size of the fiducial marker. The shell was then projected onto a two-dimensional plane intersecting isocentre and perpendicular to central axis. Each blade is then fitted to the projection. This is repeated for each fiducial marker in the phantom (where either one or three markers were used within this work) and calculated for a 360° arc. Mean imaging apertures of 1.4x1.5 cm^2 and 3.0x3.2 cm^2 were used for conformal to a single and several fiducial markers, respectively. For tracking experiments, three collimation trajectories were generated for a static 6x6 cm^2, conformal to all fiducial markers and only to the central fiducial marker (Figure 5.3). These were used to demonstrate the feasibility of the conformal and single fiducial marker

tracking compared to a static field as well as the corresponding dosimetric impact for

each.
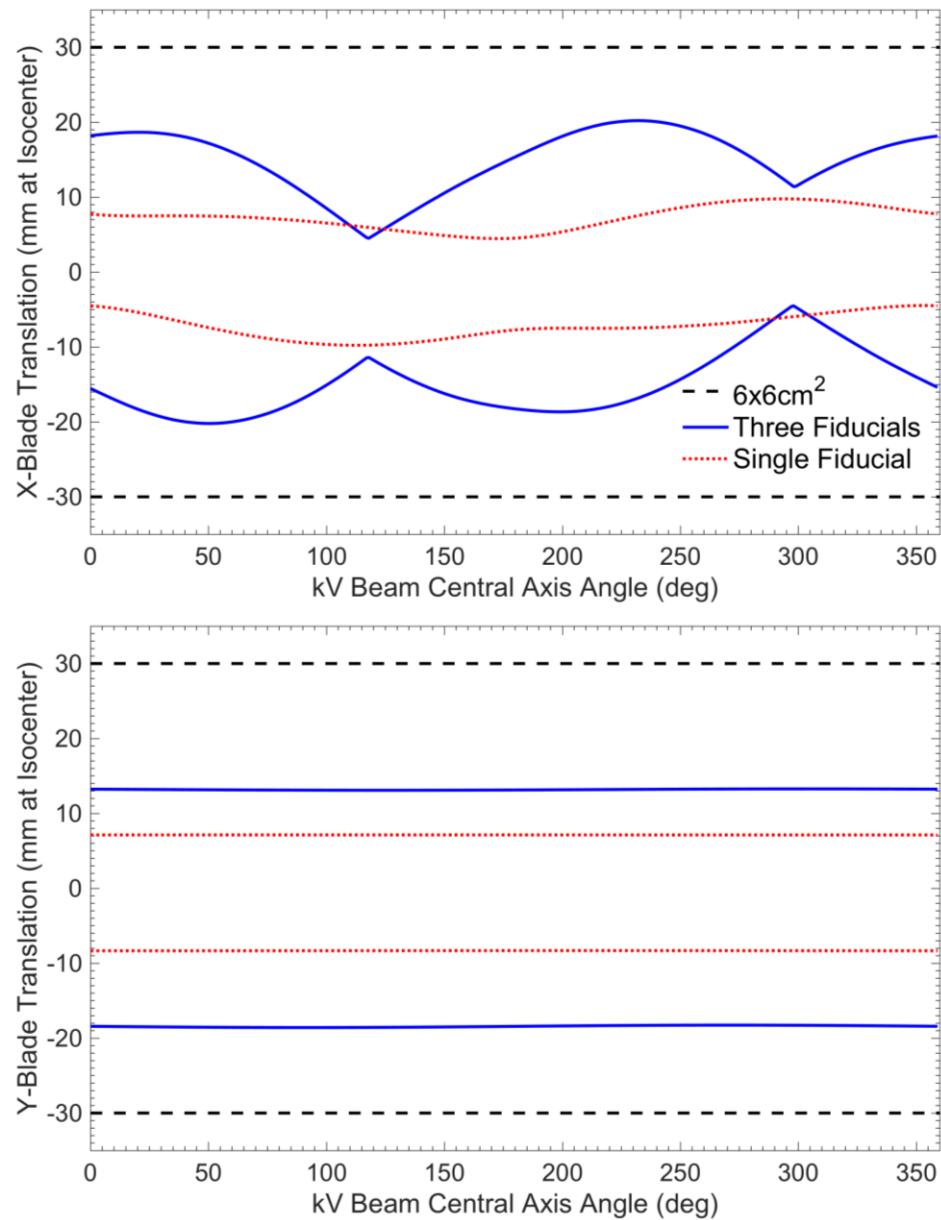
Figure 5.3   X (travel along the plane of rotation) and Y (travel perpendicular to the plane of rotation) blade translations as a function of beam central axis angle at isocentre, defined using the Varian IEC coordinate system, for a 6x6 cm^2 static field, VOI conformal to three and a single fiducial marker.
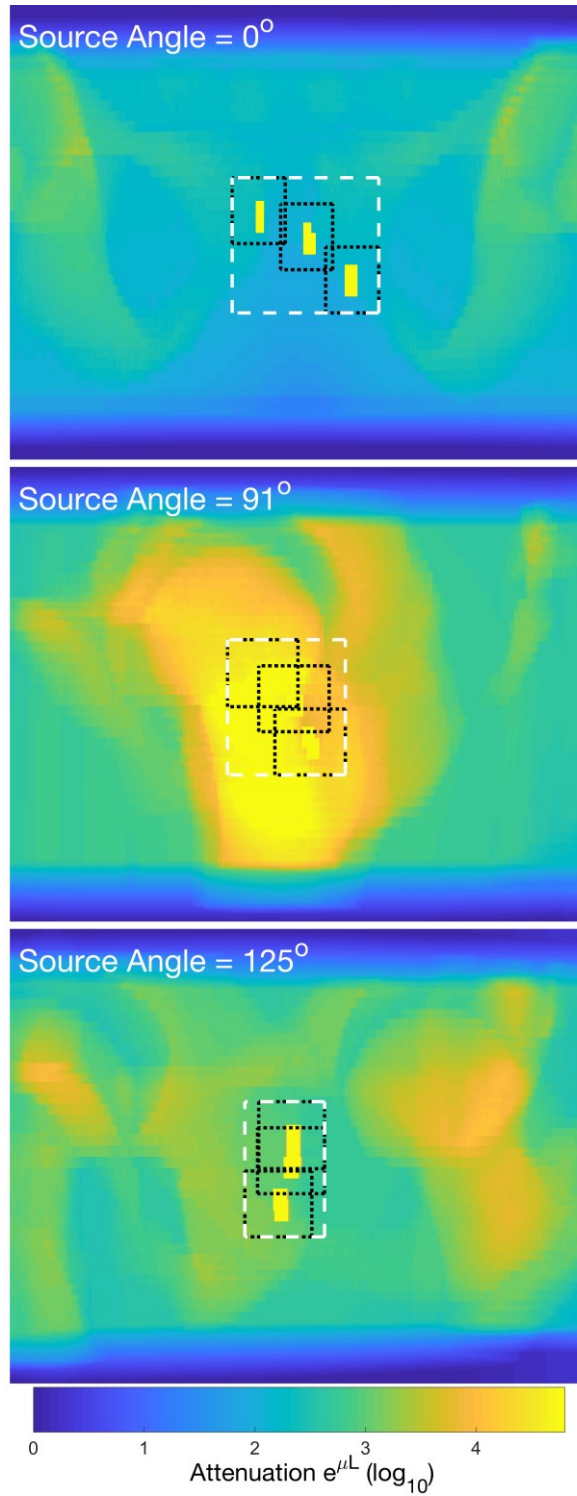
Figure 5.4   Attenuation maps for kV source angles of 0°, 91° and 125°. Dashed boxes highlight the location of collimation necessary to image for each fiducial marker or all three fiducial markers. Fiducial markers are displayed for visualization purposes; in the calculation, these voxels are given the same linear attenuation value as tissue.

5.4.4 TUBE CURRENT MODULATION

To calculate TCM, CT data were used to create linear attenuation coefficients matrix using air, lung, tissue and bone (as defined in ICRU-44 [97]) for a 60 keV photon from the NIST database[98]. Siddon's method[72] was then used to calculate an attenuation map (DRR) in MATLAB, mimicking the physical setup of an SAD and SDD of 100 and 150 cm, respectively. This was repeated in one degree increments for a full rotation around the phantom (Figure 5.4). The attenuation maps were then masked with the corresponding blade positions to give the mean attenuation through the phantom for an angle i. The attenuation curve is optimized for tube current modulation. This is done using the formulation developed by Gies *et al.*[27] Briefly, this calculation is described using Eq 4.1 where N_i is desired number of quanta after traversing the phantom for an angle i, N_o is the total number of emitted throughout an acquisition, P is the number of projections and $A_i = e^{\overline{(\mu L)}_i}$ is the amount of attenuation through the phantom for an angle i. The standard pelvis CBCT clinical protocol (at our center) of 1.6 mAs per projection was used as a baseline for modulation. Figure 5.5 displays an ideal mAs curve, but due to the limitations of Developer Mode on the TrueBeam platform, a step-wise mAs approach was needed. This was necessary to allow for simultaneous MV and kV irradiation. Unlike previous work[104], this slightly increases projection SNR variance compared to an ideal modulation. The mAs steps were optimized by minimizing the difference from ideal with a minimum arc length per segment of at least 30°. Additionally, the lowest allowable mAs in Developer Mode is 0.2 mAs per projection, which sets the global minimum. For gantry angles centered around ±90° for a 6 MV photon beam a lower mAs is ideal.
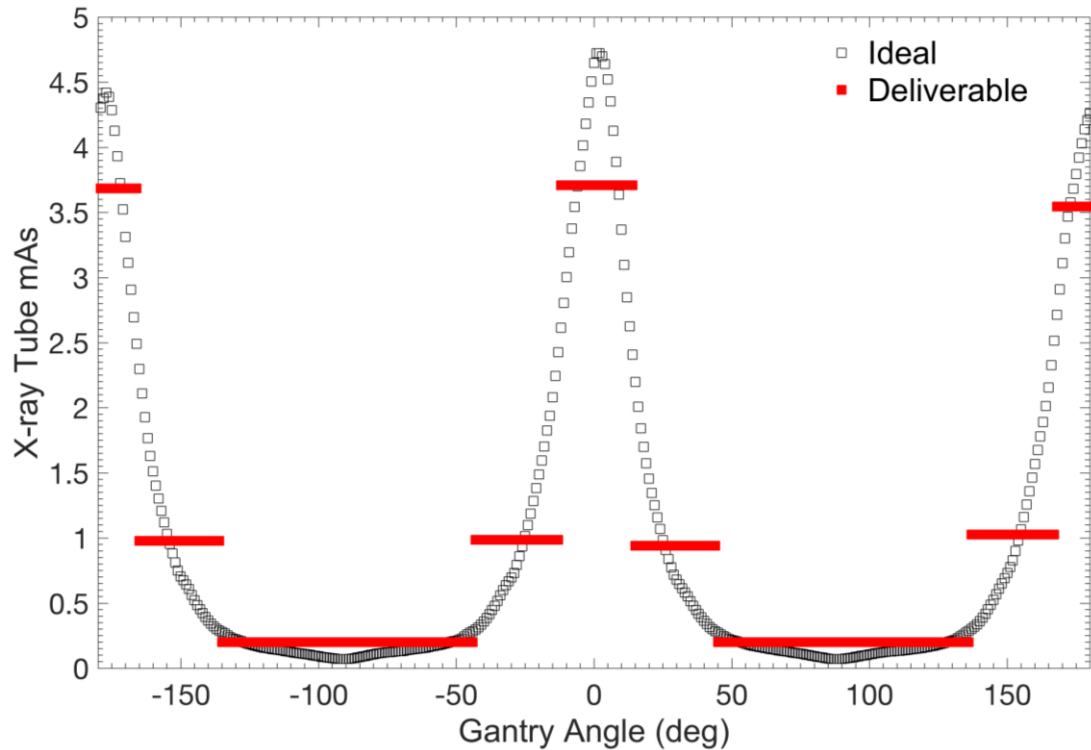
Figure 5.5   Tube current modulation for a single fiducial marker located within the ATOM pelvic phantom. Displayed are the ideal mAs and the deliverable step-wise mAs.

5.4.5 IMAGING ON THE TREATMENT UNIT

All acquisitions on the linac were accomplished using XML scripts generated with a modified version of Veritas (Varian Medical Systems, Inc., Palo Alto, CA)[108]. Veritas was modified to allow dynamic imaging arcs during MV irradiation. Four sets of experiments were conducted. The first included imaging a moving prostate with a constant mAs and simultaneous 6 MV irradiation (static 5x5 cm^2 at 600 MU/min) for the following VOIs:

    i.   a static 6x6cm^2

    ii.   conformal to three fiducial markers

    iii. conformal to a single fiducial marker

153

The second included investigating the variation in fiducial marker CNR as a function of gantry angle. This involved imaging a static prostate for a single rotation of the gantry for a:

    i.   constant mAs during 6 MV treatment

    ii.   constant mAs during no MV treatment

    iii.   TCM during 6 MV treatment

For each projection, image CNR was calculated using Eq 3.1. The CNR at each angle is averaged over four acquisitions.

The third included investigating the variation in fiducial marker CNR and displacement from known using a static prostate for an mAs ranging from 0.5 to 3.0 in approximately 0.5 mAs increments for a left-right kV beam using a 2x2 cm^2 and 6x6 cm^2 collimation during:

    i.   no MV treatment

    ii.   6 MV treatment at 600 MU/min

    iii.   6 MVFFF treatment at 1400 MU/min

Finally, a single fiducial marker was monitored using a low mAs per projection (approximately half the clinical protocol for CBCT) with and without mAs modulation for a complete rotation. A simultaneous 6 MVFFF was used at 1400 MU/min. This represents a scenario in which image quality would degrade for constant mAs but could be improved using modulation. Practically this emulates a larger patient (greater than 18 cm AP and 32 cm left-right) or hypo-fraction with a greater MV dose-rate.

5.4.6 FIDUCIAL MARKER TRACKING

In each acquisition, the kV collimation, dynamic phantom and linac were started in sequence. For kV imaging the default frame rate in Developer Mode of 11 Hz was used. This produced approximately 1000 projections for a single rotation of the gantry at a speed of 6°/s. The machine dynalog file (a log file containing the recorded position of every moving axis every 20 ms) was recorded for each acquisition and used to determine the temporal location of each projection by matching gantry location in the image header.

Similar to previous work[58], in each projection the fiducial markers were automatically detected using a maximum convolution approach. This involved using a convolution kernel with the central pixels set to one and surrounded by a one-pixel border with a negative value such that the total value of the kernel is zero. When convolved with the projection, the result is zero for objects larger than the fiducial marker and maximum values for objects with the same size and orientation as the fiducial markers. Note that, within the phantom, all fiducial markers were placed such that the long axis was along the axis of rotation for the linac. With the fiducial marker locations determined in image coordinates, the 3D location of the fiducial markers in phantom coordinates were then calculated using the solution described by Poulsen *et al*[60] using the population covariance matrix. These trajectories were then compared to the ground truth, i.e. the programed trajectory of the translation stage. All acquisitions were analyzed off-line.

5.4.7 Monte Carlo model of MV scatter

A model of MV scatter was required to determine whether this source of image degradation was sufficiently variable with gantry angle, and significant to be integrated into the modulation of mAs. The treatment head of the TrueBeam STx platform was simulated using previously[109] validated phase spaces for a 6 MV photon beam generated in VirtuaLinac (Varian Medical Systems, Inc., Palo Alto, CA). The phase space was located 73 cm above isocentre and was validated as accurate to within better than 2% compared to measured depth dose and off-axis profiles. This served as the input for a BEAMnrc[76] model containing the jaws, MLC and mylar exit window. These three components were modeled using exact geometric and material specifications provided by Varian Medical Systems. This was used as an input to DOSXYZnrc[77].

To model MV scattered fluence to the kV detector plane an approach similar to that from Asuni et al.[110] was used. This involved generating a new EGSphant file for each control point of the simulation. At each control point, the MV beam was held stationary and the CT phantom was rotated about isocentre. This is illustrated in Figure 5.6 for MV beam angles of 0°, 45° and 110°. The phantom composition has been simplified to use only air, tissue and bone. For each angle the 6 MV beam is incident from the top of the image. Additionally, between the CT data and the kV detector plane a single column of air was added with variable width to ensure a distance of was 50 cm from isocentre. MV scattered fluences were scored (displayed as a dashed line in Figure 5.6) using IAEA phase space format for 2.5 x 2.5 cm², 5 x 5 cm², and 10 x 10 cm² jaw defined square fields. For the 10x10 cm² field, scattered fluences were scored for MV beam angles ranging from 0

to 180 degrees in 11.25° increments. All MV scatter fluences were analyzed from the central 10x10 cm^2 of the detector plane. The EGSnrc parameters listed in Table 3.1 were used; where not indicated the default values were used. Global ECUT and PCUT of 0.7 MeV and 0.010 MeV, respectively, were used. These scattered spectra were compared to the detector response of x-ray detector (4030CB, Varian Medical Systems, Inc., Palo Alto, CA). Similar to the work by Roberts *et al*[111]. and Faddegon *et al.*[112], detector response was modeled using mono-energetic pencil beams of varying energy from 0.010 MeV to 7.00 MeV incident on the detector, and the detector response was quantified by scoring dose deposited in the 0.6 mm thick CsI per incident particle. The detector was modeled in DOSXYZnrc using exact geometric and material specifications provided by Varian Medical Systems. This model does not include light generation or transport in the CsI and assumes that the amount of light generation is proportional to the dose. Furthermore, this model does not include the 60 lines per centimeter anti-scatter grid and was approximated using the suggested thickness of equivalent aluminum. This model was used to demonstrate how the MV scattered spectrum could be detrimental.

MV 0°	MV 45°	MV 110°
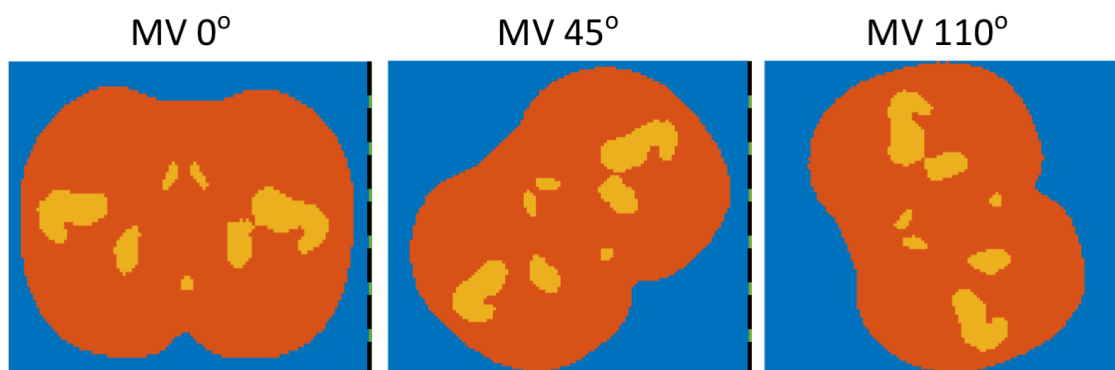
Figure 5.6   EGSphant files of the pelvis generated using CT phantom rotations for MV beam angles of 0°, 45° and 110°. The simplified phantom is composed of air, tissue and bone. The vertical dashed line marks the location of the phase space (detector surface).

5.4.8 4D Monte Carlo for kV dose calculation

The kV source was modeled in BEAMnrc[76] using the kV Imaging System Monte Carlo package provided by Varian Medical Systems. Similar to previous work[93, 104], a phase space was first generated immediately above the dynamic blade collimator for a 125 keV mono-energetic electron beam. DBS was used, with a splitting radius of 17 cm for maximum field of 27.2 x 20.6 cm^2 and bremsstrahlung splitting number of 2000. Similar to previous work where similar kV sources were modeled[89, 93], the EGSnrc parameters listed in Table 3.1 were used; where not mentioned the default values were used. Global ECUT and PCUT cut-off energies of 0.521 MeV and 0.010 MeV, respectively, were used. Source 20 in DOSXYZnrc and the SYNCJAWS component module developed by Lobo and Popescu[80] were used with the above phase space to simulate the synchronized blade translations with gantry rotation in DOSXYZnrc. Similar to the experimental setup, the

158

simulation was divided into 360 control points. Dose distributions were calculated for constant mAs and TCM using a VOI of:

  i.   static 6x6 cm^2

  ii.   conformal to three fiducial markers

  iii. conformal to a single fiducial marker

5.5   RESULTS AND DISCUSSION

5.5.1 VOI IMAGING

Figure 5.7 displays the detected locations of the fiducial marker trajectory compared to ground truth for various kV imaging apertures using a constant mAs during an arc treatment, during treatment delivery with a 6 MV, 600 MU/min photon beam a 5x5 cm^2. This demonstrates the validity of the using a VOI approach for intrafraction monitoring, including the monitoring of a single imaging aperture using a very small kV field. The main disadvantage of using only a single fiducial marker is the inability to calculate rotations[113] in addition to translations, which have been demonstrated to cause meaningful dosimetric errors[114, 115]. However, in concept this can be overcome by periodically opening the collimation to include additional fiducial markers as well. Ideally, the fiducial marker positions could be incorporated into the collimation position to either open the collimation at moments of high translation to include addition fiducial markers or to further reduce the imaging aperture used during periods of stability. However, in this work all image analysis was done offline.
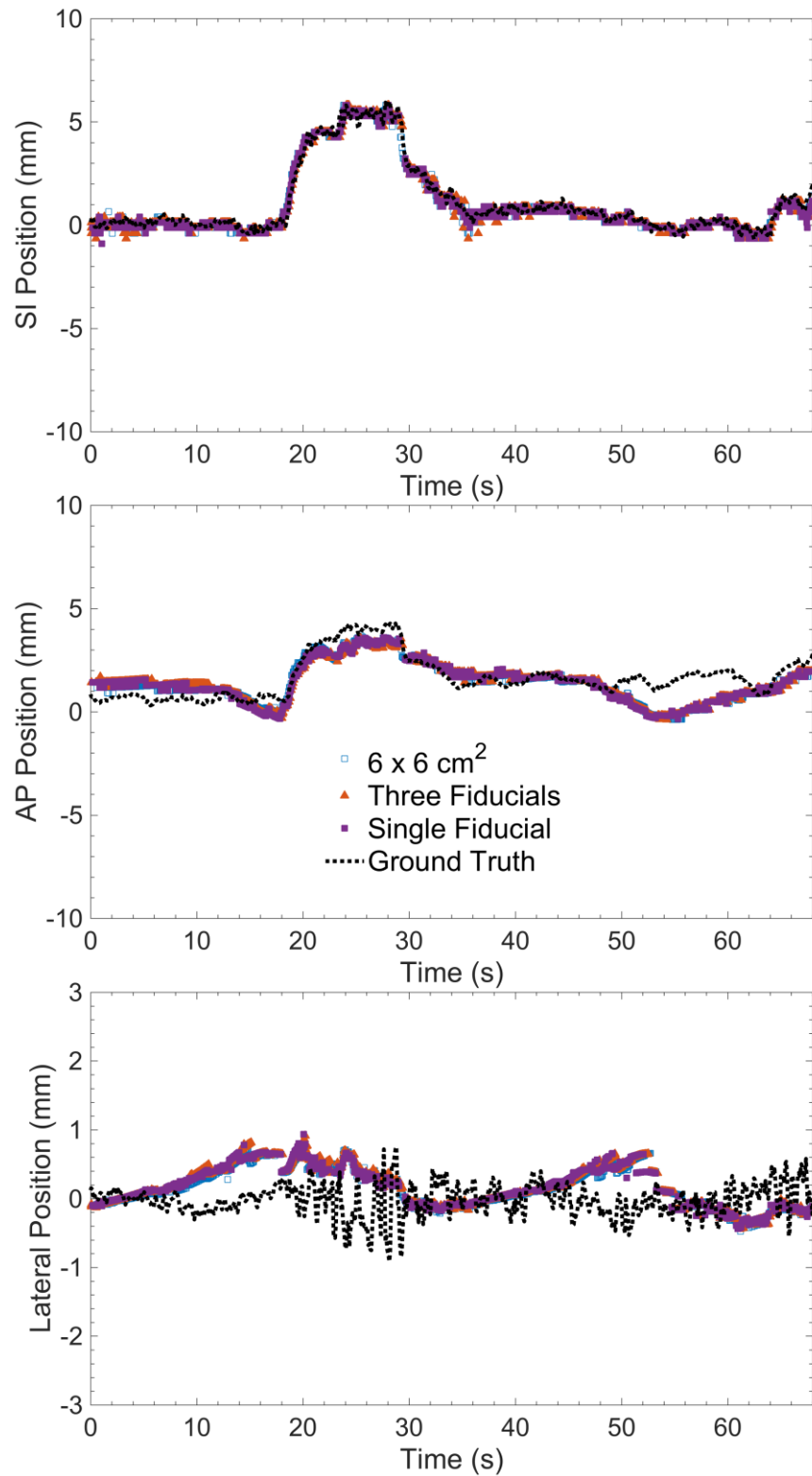
Figure 5.7   Fiducial marker locations for various kV imaging apertures during an arc treatment using a 6 MV photon beam with a 5x5 cm² field and constant dose rate of 600 MU/min.

5.5.2 Current modulated VOI

Figure 5.8 displays projection CNR as a function of gantry angle for a single fiducial marker embedded within the ATOM pelvis phantom using constant mAs and TCM with a simultaneous 6 MV beam irradiation, acquired with the same integral mAs. To highlight the variation in CNR throughout the rotation, attenuation is displayed as well. Ideally using mAs modulation should largely eliminate the variability in CNR, however due to the necessary quantized approach in modulating tube current, CNR is correspondingly higher when more mAs is used than necessary and is similarly lower for less mAs (Figure 5.5). As demonstrated for constant mAs, there exists a ~20° span centered around gantry angles of 0° and ±180° in which the noise within the projection is greater than the available contrast, which could lead to the inability to detect the fiducial marker.

In this work, an equal integral mAs has been used to compare constant and modulate imaging dose and CNR. In reality the maximum mAs could be chosen for the worst angle (gantry angle of ±180°), this would serve as the constant mAs per projection throughout the rotation or the upper bound for modulation. Therefore, a lower integral mAs and dose would be used in the TCM scenario.
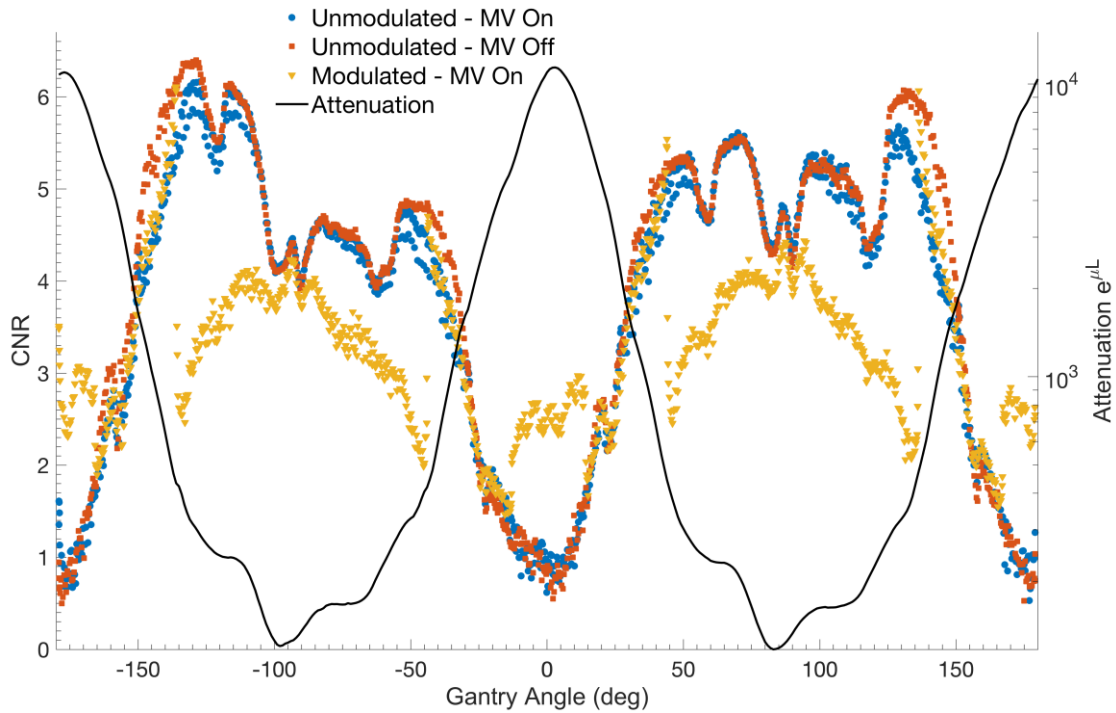
Figure 5.8   Measured fiducial marker CNR as a function of gantry angle for constant (with and without simultaneous MV irradiation) and modulated mAs. Overlaid with corresponding kV attenuation.

Figure 5.9 demonstrates the variability of CNR for decreasing mAs for a 2x2 cm^2 or 6x6 cm^2 kV fields with increasing MV scatter contribution per projection, with no MV beam, 6 MV or 6 MVFFF. As demonstrated in the absence of MV scatter, fiducial marker CNR is degraded as mAs decreases, but is visible at mAs greater than 0.5. However, as MV scatter increases to the conditions of 6 MVFFF this increases the minimum mAs to 1.0. This figure also highlights an observation by Siewerdsen and Jaffray[8], in which the 6x6 cm^2 has lower noise than the 2x2 cm^2, giving a higher CNR for the 6x6 cm^2. However, the 6x6 cm^2 gives approximately 1.6 times the imaging dose to the VOI[93] as the 2x2 cm^2, for a slight improvement in CNR (approximately 1.15). Previously[93, 104], this was leveraged by

162

maintaining the same VOI dose for smaller fields as larger fields, this results in greater

primary photon contribution for smaller fields and therefore reduced noise.
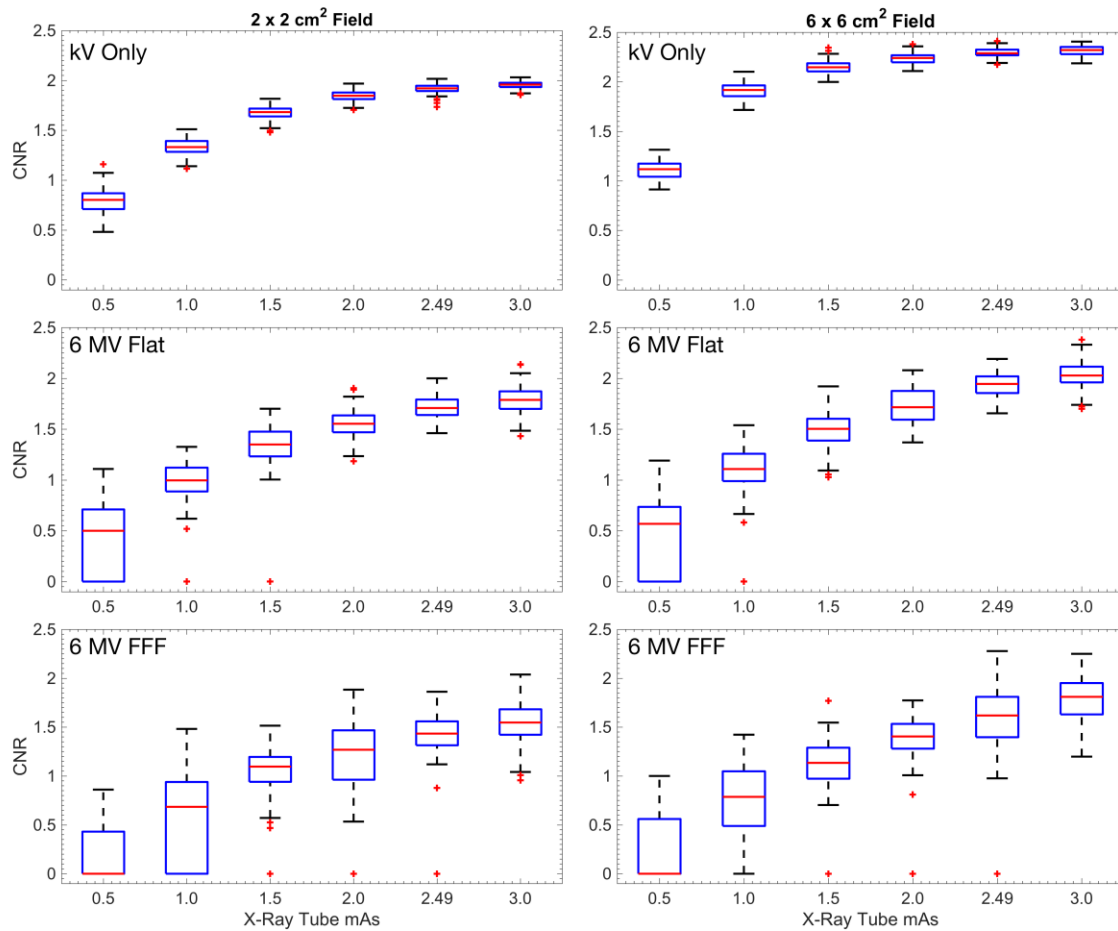
Figure 5.9   Fiducial marker CNR for a 2x2 cm2 and 6x6 cm² kV fields for no MV beam, 6 MV
and 6 MVFFF. The MV photon beams used a 5x5 cm² field.

Figure 5.10 displays the corresponding spatial error from the ground truth for decreasing

mAs for a 2x2 cm² or 6x6 cm² kV field with increasing MV scatter contribution per

projection, for no MV beam, 6 MV and 6 MVFFF. This demonstrates in the absence of MV

scatter even though the CNR is very low at 0.5 mAs, the fiducial marker is accurately detected with a median error of 0.38 mm (pixel width). Similar to CNR, for a 6 MVFFF beam the median error at 0.5 mAs increases to 2.10 and 1.94 mm for a 2x2 and 6x6 cm^2 kV field, respectively, with the 75th percentile extending to 8.0 mm. At greater than 0.5 mAs, the median error is less than 0.6 mm in all scenarios.
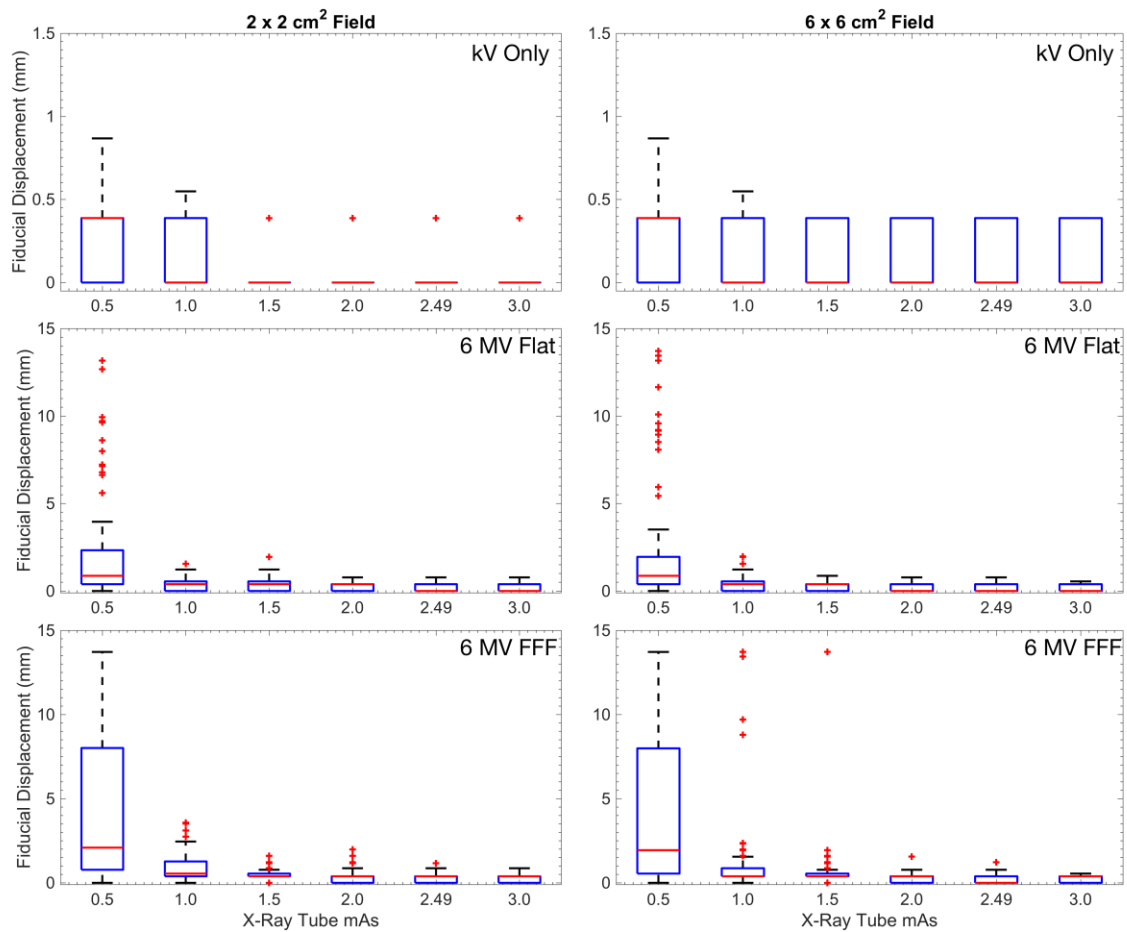
Figure 5.10   Corresponding fiducial marker displacement from known position for a 2x2 cm^2 and 6x6 cm^2 kV fields for no MV beam, 6 MV and 6 MVFFF. The MV photon beams used a 5x5 cm^2 field.

Figure 5.11 displays the fiducial marker trajectory compared to ground truth for a constant mAs (0.75 mAs per projection) and TCM (with equal integral mAs). The regions of high variance in the constant acquisition correspond with the previously noted (Figure 5.8) ~20° range centered around gantry angles of 0° and ±180°, in which the error in detected SI position can be as high as ±9.2 mm. As demonstrated, TCM greatly reduces these errors in detection during periods of high attenuation. However, three projections (time equal to 10.1, 11.6 and 53.1 seconds) in regions of low attenuation exhibit errors up to 4.9 mm, this would indicate that the minimum mAs of 0.2 was insufficient for the magnitude of MV scatter at those angles. This could also be a disadvantage of single fiducial marker tracking, however this could be overcome in a future implementation in which the estimated position can be communicated to the collimator in near real time. The envisioned system would function as follows. For periods of high stability, the imaging aperture would be reduced to a set minimum about the single fiducial marker. As motion is detected, the imaging aperture would be increased field limits modified to match the shift in fiducial marker position, such that the fiducial marker is centered in the field or expanded to image several fiducial markers. Additionally, as previously stated, the latter would also allow for the calculation of rotations.
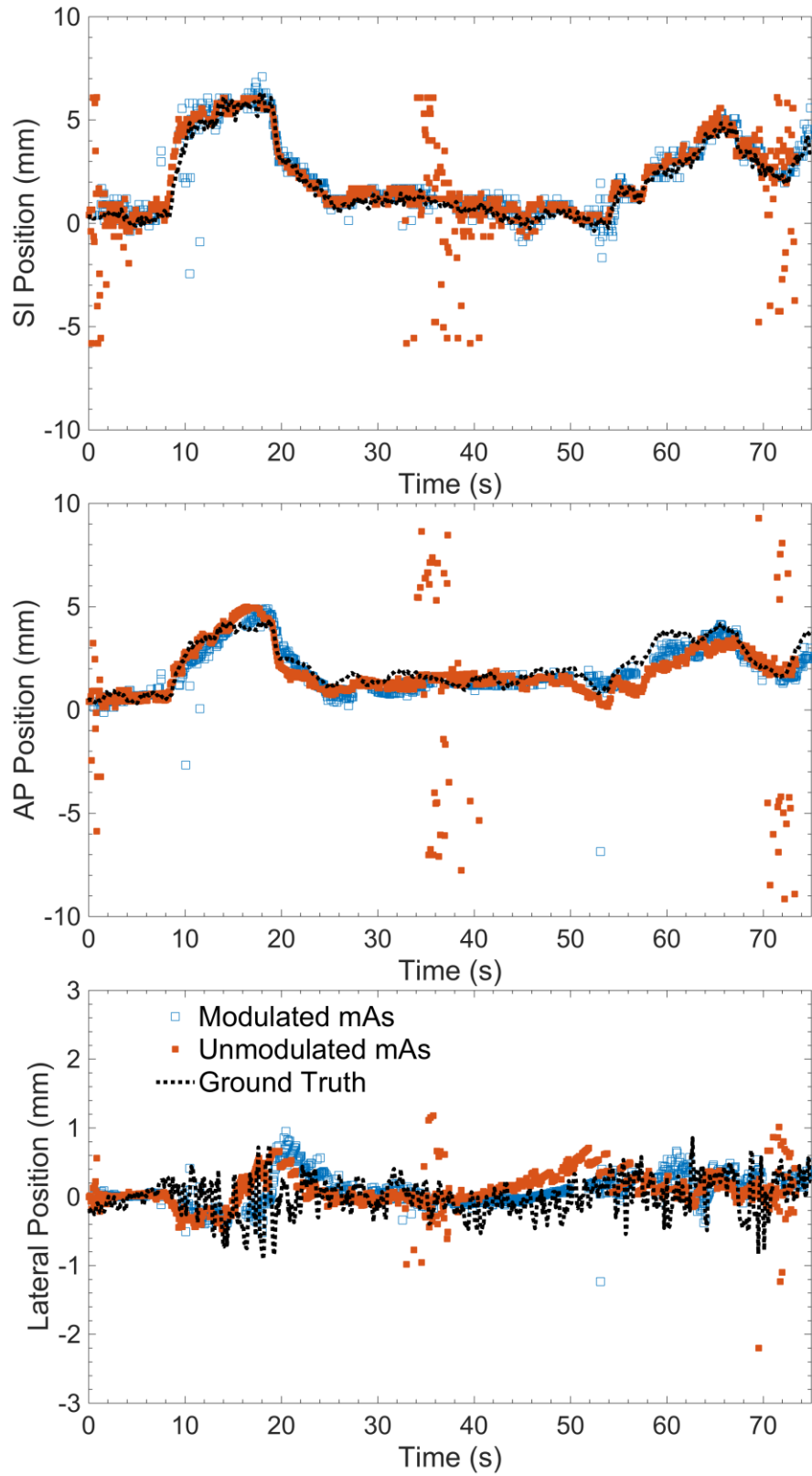
Figure 5.11   Detected fiducial marker positions compared to ground truth during 6 MVFFF irradiation with either constant or modulated mAs.
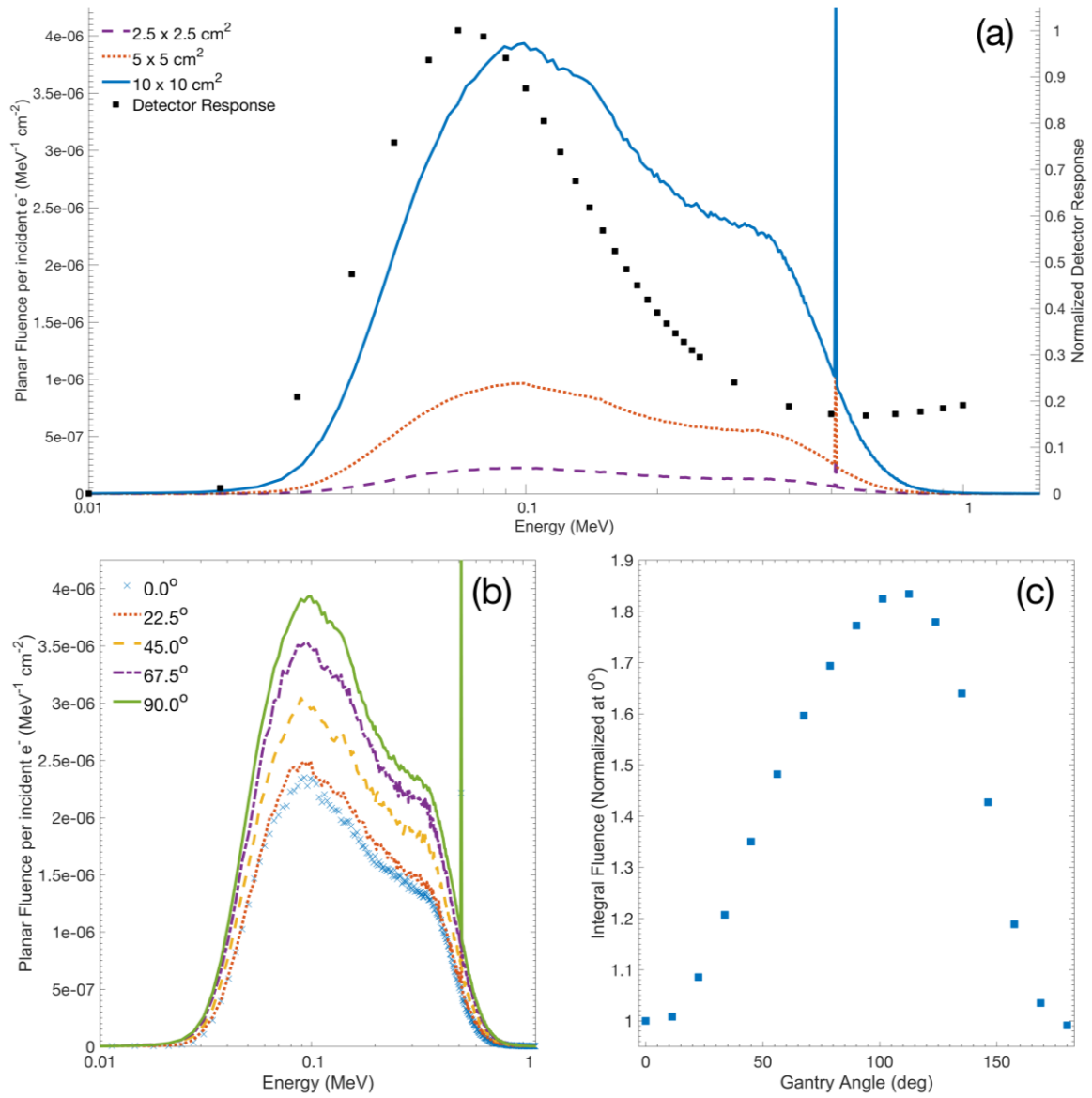
Figure 5.12   (A) MV scatter fluence at the kV detector plane for 2.5x2.5 cm^2, 5x5 cm^2 and 10x10 cm^2 treatment fields incident on the ATOM phantom for a lateral beam. Detector response is overlaid for comparison. (B) MV scatter fluence for a 10x10 cm^2 for rotations ranging from 0° (anterior-posterior) to 90° (lateral). (C) Integral fluence as a function of rotation normalized at 0° for 10x10 cm^2.

5.5.3 MV Scatter

As highlighted in the previous several figures, MV scatter can cause significant localization errors at low mAs. Figure 5.12 demonstrates the variation and magnitude of MV scatter for several field size and angular positions. Figure 5.12a displays MV phantom scatter fluence at the kV detector plane (50 cm from isocentre) for a 6 MV beam for fields sizes of 2.5x2.5 cm^2, 5x5 cm^2 and 10x10 cm^2. The energy response of the x-ray detector is displayed for comparison. The overlap highlights the observation that for kV intrafraction imaging this could be problematic as the majority of the fluence resides in the energy range that coincides with the maximal response of the kV detector. Increasing MV field size from 2.5x2.5 cm^2 to 10x10 cm^2 increases integral scatter fluence by approximately a factor of 17.4, however the relative fluence is comparatively independent of field size for this phantom. As demonstrated in Figure 5.12b, the magnitude of scatter varies with gantry rotation by up to a factor of 1.8, but the relative fluence is fairly independent of rotation.

Similar to the results demonstrated for TCM in Figure 5.11, this would indicate that, at least for this pelvic geometry, a gantry angle specific correction for MV scatter will be less important compared to adjustment for kV attenuation. This is due to the comparatively small variation in MV scatter of less than a factor of two compared to the factor of 300 observed in kV attenuation through the phantom. Additionally, when MV scatter is generally the greatest (gantry ±90°) kV attenuation is at a minimum (Figure 5.5). Therefore, as highlighted in Figure 5.11, if an MV scatter correction was to be used it would set the lower mAs bound in the low attenuation regions.

5.5.4 VOI IMAGING DOSE

Figure 5.13 displays the corresponding Monte Carlo simulated kV dose distributions for a constant mAs acquisition of the three imaging fields as well as the corresponding TCM distributions for equal integral mAs. This demonstrates the dosimetric impact of using a VOI approach compared to a static 6x6 cm^2 field. Crocker *et al.*[64] demonstrated that the mean kV imaging dose to the prostate ranges from 2 to 30 cGy using a 5.3 × 6.1 cm^2 field at 120 kVp and 1.02 mAs per projection at 1 Hz for various treatments regimes. However, as demonstrated in Figure 5.13 this would increase to approximately 0.1 to 1.5 Gy in bone, and up to 3.1 Gy if using TCM. A reduction of 3.7 in integral dose is observed when changing from a generic 6x6 cm^2 static field to an angle specific conformal field that encompasses all fiducial markers. This is further reduced by a factor of 4.26 when imaging the central fiducial marker alone. Additionally, Figure 5.13 highlights the dosimetric effect of TCM, where a trade-off is necessary to realize improved image quality at angles of high attenuation. For example, switching to TCM for a single fiducial marker, the dose is increased by up to a factor of 5.5 in the lateral regions of the pelvis. However, a corresponding decrease is observed in the AP regions of the pelvis where the dose is decreased to a factor of 0.2 compared to the constant mAs protocol. This results in a change of integral dose ranging from $\pm 12\%$, depending on the field technique used, for an equal integral mAs.
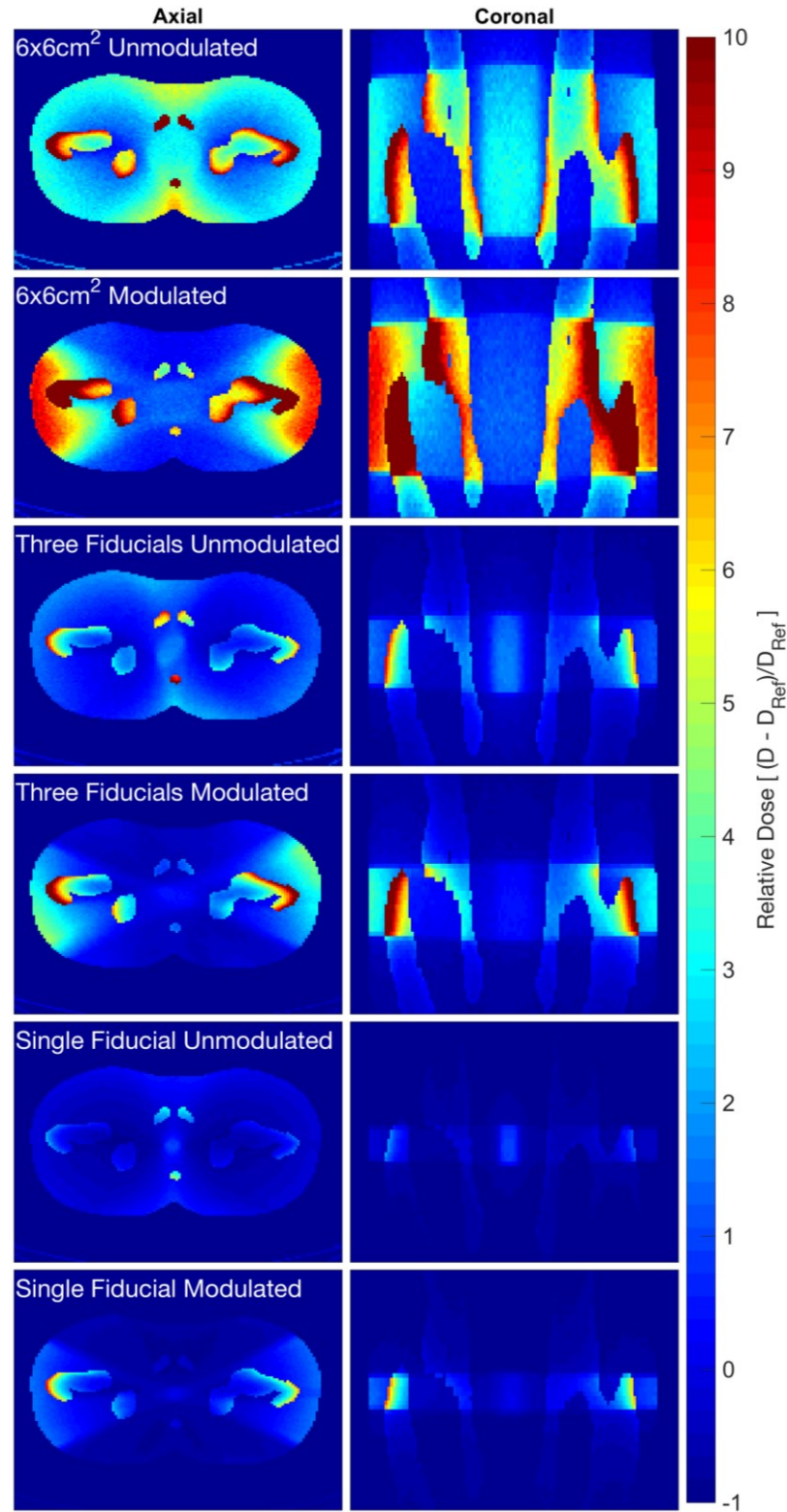
Figure 5.13   Relative kV dose distributions for a static 6x6cm^2 field, VOI conformed to several and a single fiducial marker with unmodulated and modulated mAs. D_{Ref} is the isocentre dose for the single fiducial unmodulated acquisition.

5.6   CONCLUSIONS

In this work, we have demonstrated two promising approaches in intrafractional monitoring of the prostate during radiotherapy: VOI imaging, which localizes and reduces the imaging dose, and TCM which offers improved image quality and fiducial marker detectability during periods of high attenuation. The VOI method is able to improve image quality by a factor increase of CNR of 1.3 for single marker imaging compared to a 6x6 cm^2 for a given dose, or reduce image dose by a factor of 15.6. TCM allows CNR variability to be minimized throughout gantry rotation and is able to recover detection of a fiducial marker where kV attenuation is greatest, for example. MV scatter was demonstrated to be a maximum during periods of low kV attenuation and if included MV scatter would set the lower limit of modulation.

CHAPTER 6   CONCLUSIONS

6.1   SUMMARY

The purpose of this thesis was to further develop VOI imaging to include arbitrarily located and shaped VOI. This was accomplished through the development of two unique dynamic collimators. The iris collimator, introduced in manuscript one (Chapter 3), was implemented by replacing the bowtie mount on a 2100 iX Varian linear accelerator. Using this collimator for CBCT, we demonstrated that for a given dose to the VOI, image CNR could be improved up to a factor of two as imaging aperture decreases compared to an open field. This corresponds to a factor reduction in SPR of 8.4. We additionally demonstrated, that for this gain in image quality, large dose reductions were possible outside the VOI, both in and out of plane. Reduction of peripheral dose to 4% of the full field value out of plane was achieved. The functionality of a dynamic iris collimator was demonstrated through phantom studies using data readily available from the TPS to generate radial and translation trajectory data required in image acquisition. This implementation was limited with regard to the ability to manipulate image acquisition parameters throughout rotation of the gantry and with regard to imaging aperture having one parameter, i.e., iris diameter, thereby limiting imaging dose conformity.

The dynamic blade collimator, introduced in manuscript two (Chapter 4), further improved upon the VOI method. This was implemented on the TrueBeam STx platform and incorporated four individually controlled blades which mimicked the commercial

system. The blade collimator reproduced comparable image quality improvements as the iris collimator for CBCT. The blade collimator resulted in dose reductions to less than 1% of the full-field value out of plane. The amount of dose reduction in-plane depends on the size and location of the VOI within the anatomy of interest. By using Developer Mode on TrueBeam, tube current modulated VOI CBCT was implemented, thereby further enhancing performance with regard to image quality per unit dose. For approximately equal dose to the VOI, image CNR was improved by a factor of 1.2, compared to an unmodulated VOI acquisition. Additionally, for approximately equal CNR, dose was reduced by a factor of 1.6 within the VOI, with more substantial reductions possible in-plane.

Manuscript three (Chapter 5) focused on applying current modulated VOI acquisition to intrafraction motioning of the prostate. This work built upon the previously established methods and tools developed for VOI CBCT. In this work, the VOI approach has been demonstrated to be as accurate as the commonly used larger static fields, however required the VOI to be conformed to just a single fiducial marker. The influence of MV scatter and kV attenuation on image CNR and fiducial detectability were quantified. Unlike unmodulated acquisition, current modulated VOI imaging was used to demonstrate that accurate fiducial detectability could be preserved even in the presence of unfavourable imaging conditions. Although the integral imaging dose is approximately equal to that for the unmodulated case, the modulated VOI method requires higher maximum dose for projection angles associated with high attenuation.

6.2 FUTURE WORK

The techniques developed in this thesis demonstrate the promise for improved image quality with reduced peripheral dose for patients. However, there exist several avenues that may be explored further.

6.2.1 NESTED VOI CBCT

The major disadvantage of the VOI approach used in the thesis is that all information outside the VOI is discarded during reconstruction. The next evolution of this work could be to implement modulation of the field similar to that demonstrated by Leary and Robar[18] or Szczykutowicz *et al.*[19] for MV beams. In combination with TCM, this would result in a true implementation of fluence field modulated CBCT as described by Bartolac *et al.*[20]. However, this implementation would require considerable effort in developing an optimizer to calculate a solution that adheres to specified dose limits and image quality objectives. The optimizer would likely contain a simple dose and image noise calculation engine as described by Bartolac *et al.*[20]
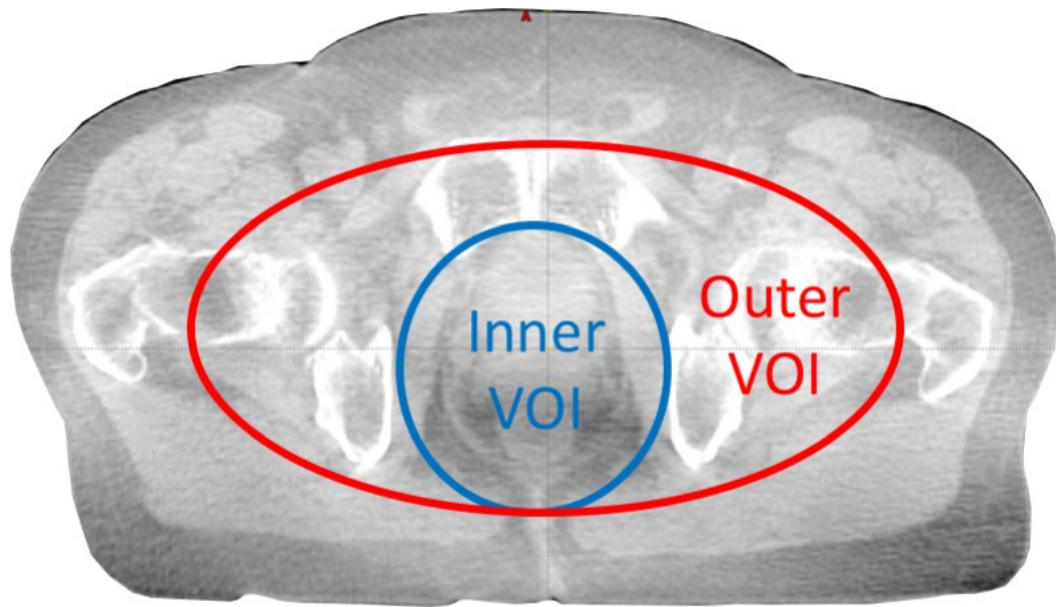
Figure 6.1   Nested VOI approach, in which the inner VOI would contain high quality image data and the outer VOI would contain lower quality image data acquired at a lower dose.

However, the simpler approach would be to implement the nested VOI approach demonstrated by Leary and Robar[18] and Lu *et al.*[116] and illustrated in Figure 6.1 for a patient with prostrate cancer. In this approach, a high quality inner VOI is acquired with reduced quality outer VOI. This approach is important as it addresses one of the disadvantages of the VOI approach, in which the information outside the VOI is lost. A possible scenario in which this could become important is one in which the inner VOI may appear to be aligned relative to the treatment plan, however, the surrounding anatomy may not be. Within this approach, the inner VOI will maintain a higher image quality while the outer VOI will be used for rigid information. Figure 6.2a displays blade trajectories for an inner and outer VOI acquisition. The nested VOI acquisition could be one in which the

collimation transitions between the two VOIs at set frequency. This is demonstrated in Figure 6.2b for a ten degree transition frequency between the inner and outer VOI, with two degrees for transition to and from the outer VOI trajectory.

A key research question would be optimization of the blade trajectory, balancing dose reduction in the outer VOI while still providing adequate image quality for the guidance task. If implemented, this approach would increase the imaging dose to the patient but could greatly expand the available information for image guidance in peripheral anatomy.
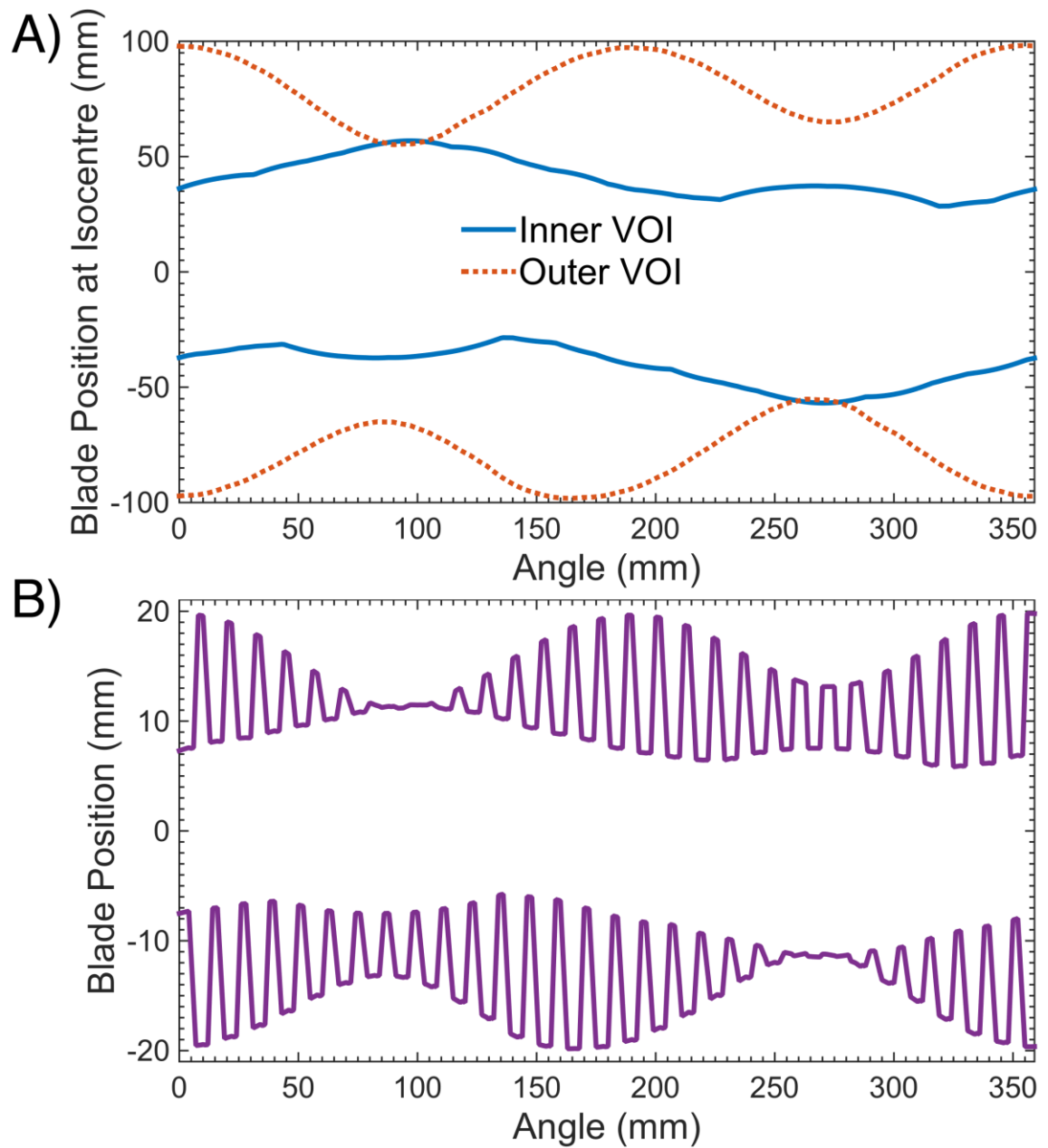
Figure 6.2   A) Inner and outer VOI blade trajectories. B) Potential blade translations for a combined inner and outer (nested) VOI acquisition sampled in ten degree intervals with two degrees of transition.

6.2.2 Soft Tissue Enhancement with VOI CBCT

The improvements in image quality reported have all been for simple phantoms. It would be of interest to investigate how this translates to a realistic anatomy, particularly to investigate improvement of soft tissue contrast using a VOI technique. This could be accomplished in a cadaver or in patients following approval by a research ethics board. However, in the latter, TCM would not be possible in the current version of TrueBeam, as the time required for acquisition is simply too long. However, a patient study using the intrafraction monitoring approach described herein would be possible. A further question worth examining is whether, given the improved image quality afforded by the VOI approach, the prostate and rectal wall interface is conspicuous. If it is, the requirement to insert fiducial markers could be alleviated for conventional fractionation schemes.

6.2.3 VOI CBCT Integrity and Limitations

It would be of interest to examine the integrity and limitations of VOI placement within a realistic anatomy. All this work has been focused on developing the technology and demonstrating the image quality (CNR) and dosimetric consequences of the VOI approach. This involved using relatively simple phantoms, i.e. cylindrical water phantom with a tissue equivalent insert. However, the placement of VOI within a complex geometry was not a focus. An example of poor VOI placement can be observed in Figure 4.2e using the ATOM head phantom, in which the extrapolation method fails to fully compensate for the truncation artifact near VOI boundaries on a sharp attenuation

gradient (e.g., a transition from bone to soft tissue or soft tissue to air). This can be further demonstrated using a synthetic phantom. Figure 6.3 displays FBP of a synthetic phantom containing a bone ring surrounded with soft tissue, in which the projection data has been truncated 5 mm after, centered on and 5 mm before the 10 mm thick bone ring. As illustrated in Figure 6.3, when the projection data is truncated on the bone ring, the integrity of the interior is diminished (truncation induced cupping) compared to when the projection data is truncated 5 mm before or after the bone ring. The simplest solution could be to ensure VOI boundaries avoid sharp attenuation gradients. Additional problematic scenarios could be established in exploration of a range of synthetic phantoms using a variety of geometries and compositions. However, this problem could possibly be remedied using information from previously mentioned nested VOI approach. In which the outer VOI projections could help guide the extrapolation of the inner VOI projections. Figure 6.4 displays an ideal sinogram for a nested VOI acquisition of the phantom in Figure 6.3. Figure 6.4 utilized a parallel beam geometry for the purposes of the demonstrate, additional work is required in translating this approach to a fan beam geometry. Additionally, the outer VOI will need to be adequately sampled as to avoid aliasing artifacts. With this approach, the outer VOI data could be used to optimize the extrapolation or interpolation of adjacent data attenuated outside the inner VOI. An alternative, could be to revisit the DRR approach to fill the truncated data utilized by Robar *et al*.[16].
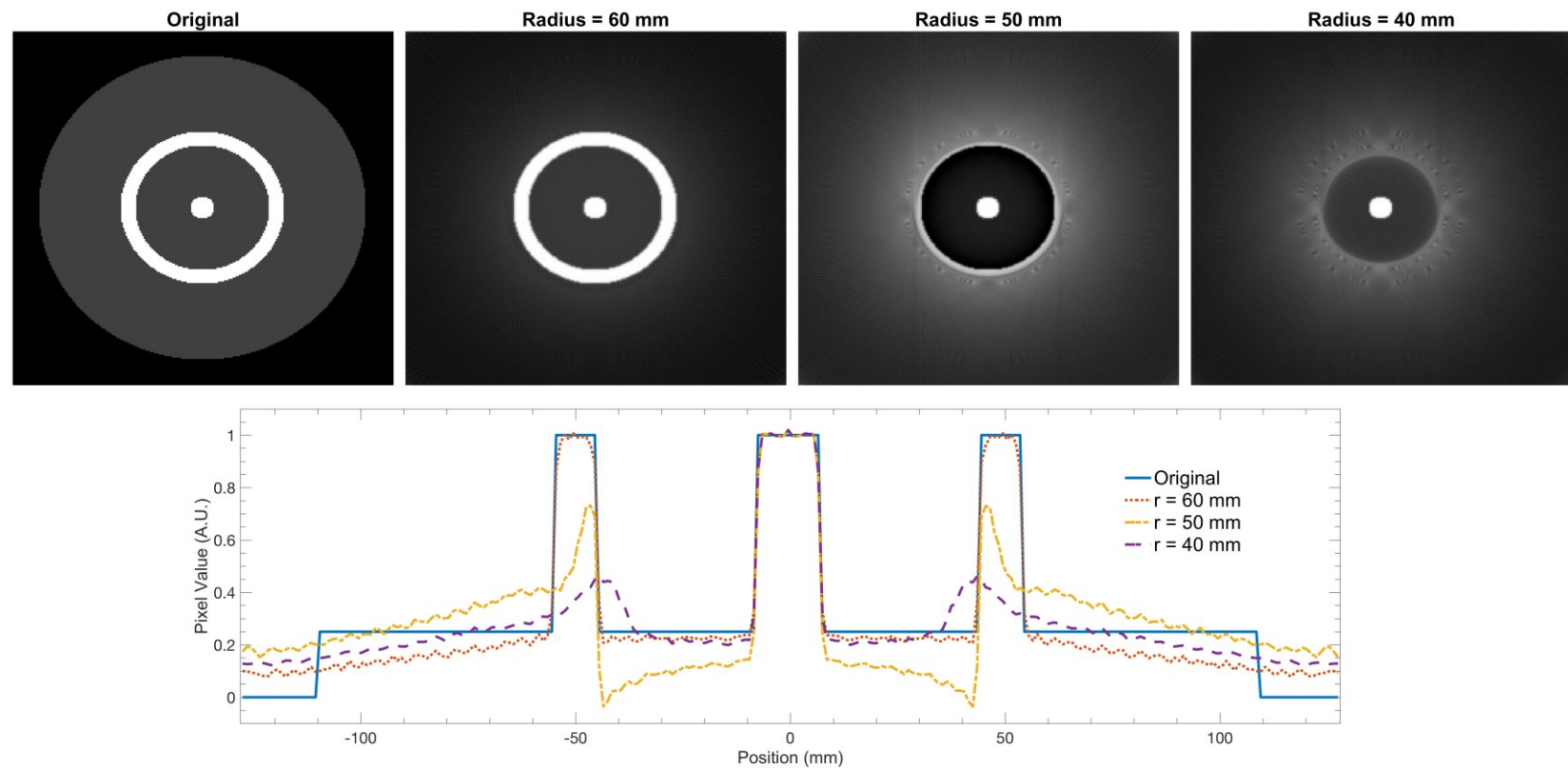
Figure 6.3   FBP of truncated projections of a synthetic bone and tissue phantom. The data truncated either just before, in the middle or after the 10 mm thick bone ring with a centre radius of 50 mm. Profiles are horizontal through the center of the phantom.
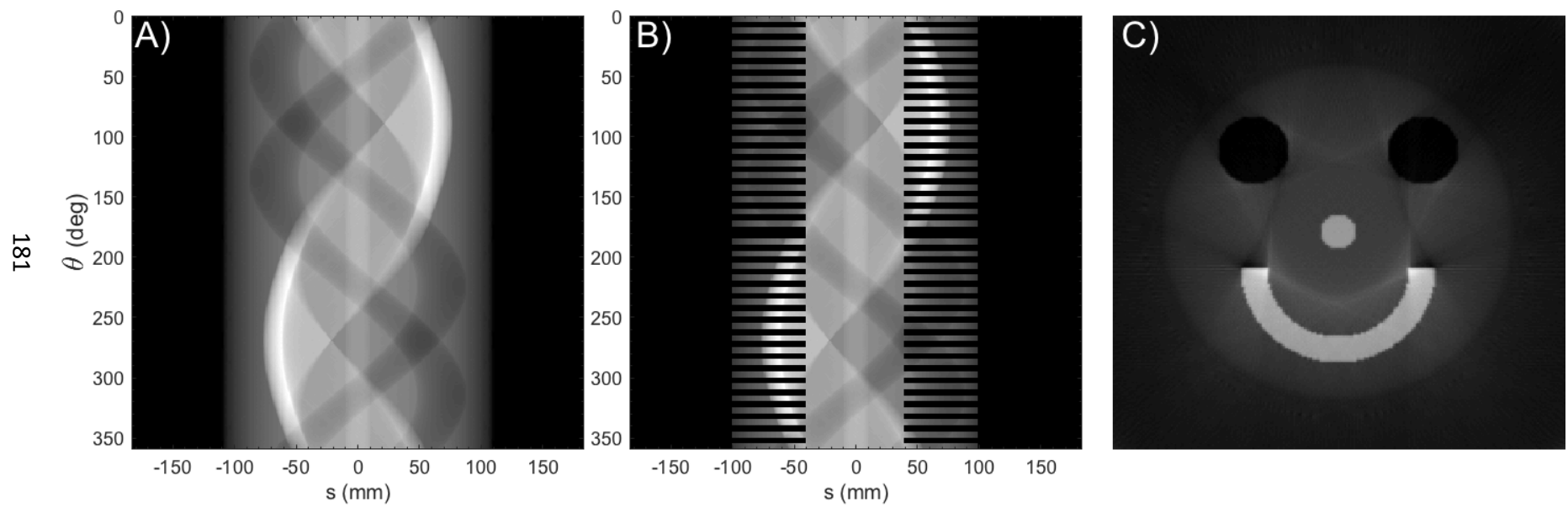
Figure 6.4   A) complete sinogram of the phantom from Figure 2.2 sampled over 2π, for a parallel beam geometry. B) Sinogram for an inner and outer VOI of the phantom sampled in five degree intervals. C) Reconstruction using extrapolation of both the inner and outer VOI boundary.

6.2.4   DENTAL APPLICATION OF VOI CBCT

Another area in which the VOI approach would be advantageous is dentistry. Dental x-rays are currently the most common means of exposure to man-made ionizing radiation for Americas and Canadians[117]. Currently, the Health Canada guidelines (Safety Code 30)[118] for the use of x-rays in dental applications are do not include recommendations for the CBCT or digital detectors, which are currently employed. The implementation of CBCT in a dental setting has been linked to increased usage of x-rays, with an estimated sevenfold increase for the average person over the last several decades[119]. The addition of the VOI technique could significantly reign in the amount of dose from these procedures, which is not germane to the diagnosis. For VOI CBCT in dental applications, the challenge is in calculating the collimation trajectory as no CT or structure set is available as *a priori* information. However, a rudimentary trajectory could be calculated from a backprojected structure drawn on two projections 90° apart. This could be applied to any CBCT system without *a priori* data. This implementation will greatly decrease the imaging dose of repeat scans, which could commence in early childhood.

6.2.5   DYNAMIC COLLIMATION FOR INTRAFRACTION MONITORING

The next step in applying a VOI approach to intrafraction monitoring would be to enable a system in which the estimated position can be communicated to the collimator in near real time. This would allow for reduction in the margin placed on the projected covariance matrix.

a) Initial Setup b) Fiducial Marker Motion

c) Expand and Centre d) Contract for stable motion
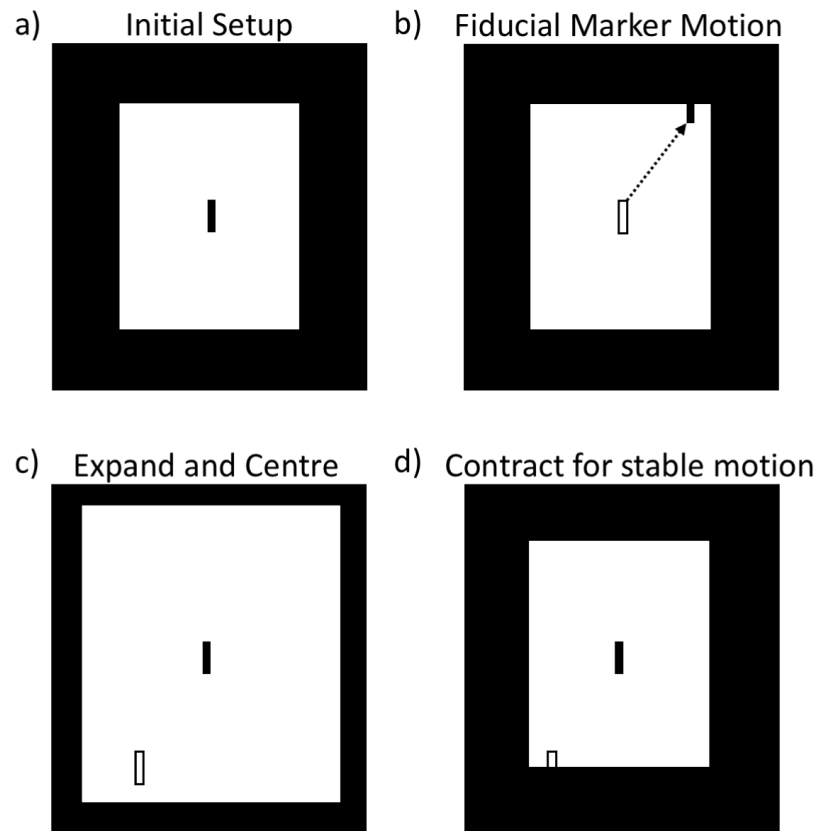
Figure 6.5 Graphical illustration of the proposed dynamic fiducial marker collimation for periods of stable and unstable motion.

The envisioned system would function as follows and is illustrated in Figure 6.5. For periods of high stability (Figure 6.5a), the imaging aperture would be reduced to a set minimum. As motion is detected (Figure 6.5b), the imaging aperture would be increased field to limits modified to match the shift in fiducial position, such that the fiducial is centered in the field (Figure 6.5c). Finally, as motion stabilizes again the aperture would be reduced to a set minimum (Figure 6.5d).

This approach can also be demonstrated using the blade trajectories utilized in Chapter 5. Figure 6.6 displays VOI trajectories conformal to a single and several fiducial markers used in 5.5.1. The proposed dynamic VOI collimation is demonstrated using these two VOI trajectories, in which for stable motion the VOI includes only a single fiducial, however as unstable motion is observed, the aperture would expand to include several fiducial markers. Once the motion stabilizes, the aperture would again centre on a single fiducial marker located at a shifted location. This implementation would increase the imaging dose to the patient, but would eliminate periods in which the fiducial marker may travel outside the field of view. In addition, the patient specific covariance matrix should be used to generate the collimation. In practice this could be derived from a pre-treatment arc or the VOI CBCT data acquired to initially align the patient for treatment.
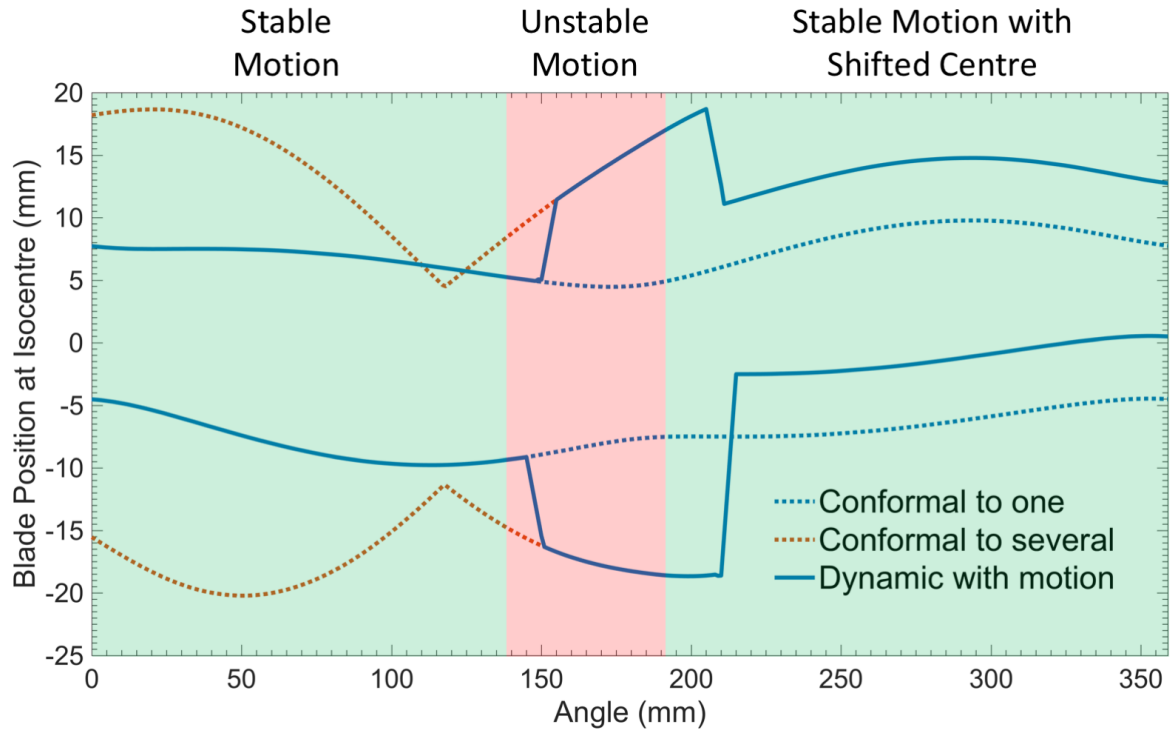
Figure 6.6   Demonstration of the blade position as a function of angle for detected fiducial marker motion. Blade positions for the VOIs used in 5.5.1 are displayed for a VOI conformal to a single and several fiducial markers. The proposed dynamic collimation is displayed using these two blade trajectories for periods of stable and unstable motion. In which for unstable motion the collimation conformal to a single fiducial marker would expand to encompass several fiducial markers. The collimation would then contract to a single fiducial once the motion stabilizes.

6.2.6 ADDITIONAL INVESTIGATION INTO MV SCATTER

It would also be of interest to investigate the variation in MV scatter for wide range of patient sizes and other anatomy for which intrafraction monitoring is applicable. Additionally, it would be of interest to examine whether the modulated field sizes and dose rates common with SBRT vary the conclusions of 5.5.3. This would allow for a more comprehensive description of MV scatter. Currently, the current modulation is independent of the magnitude of MV scatter as a function of gantry angle, but as

demonstrated this does set the lower limit of modulation, and in a future implementation this could be taken into consideration either with a calibrated Monte Carlo model or (a more sophisticated approach) using active feedback from image data to increase or decrease tube current. Figure 6.7 displays integral fluence at the detector plane for a modulated MLC pattern during a VMAT arc using the same phantom used in 5.5.3. As demonstrated in Figure 6.7, the magnitude of scatter varies greatly as a function of angle for a modulated field compared to the static fields investigated in 5.5.3, in which the scatter fluence was sinusoidal with angle.
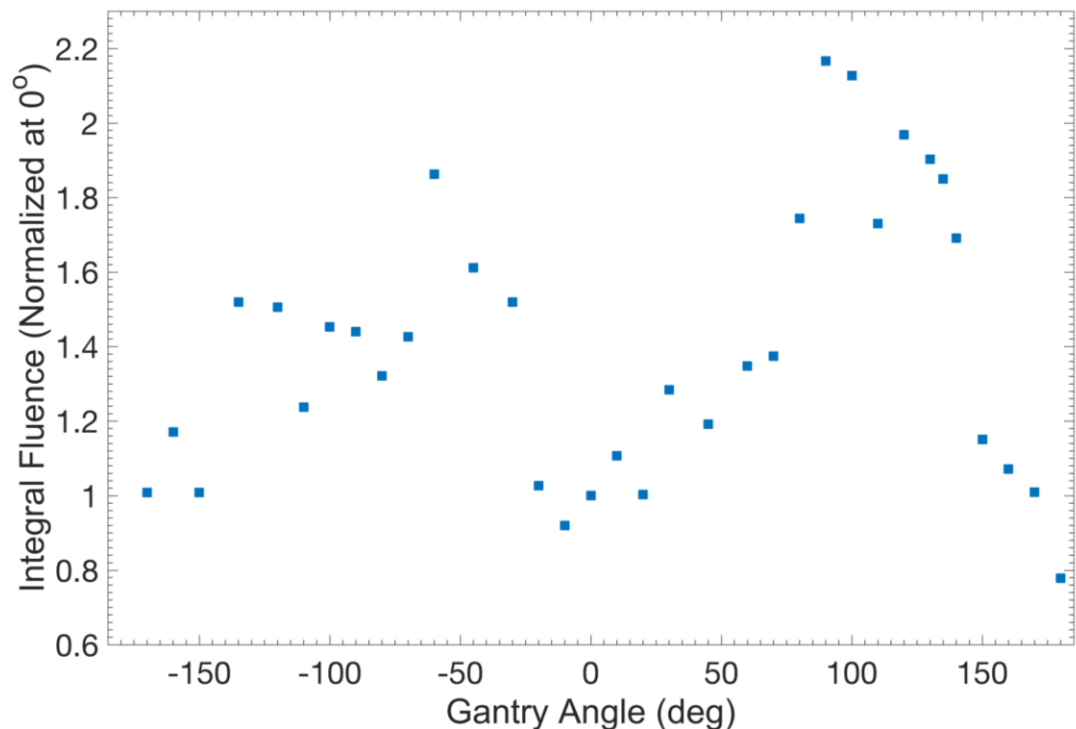
Figure 6.7   Simulated integral scatter fluence as a function of rotation normalized at 0° for a modulated MLC pattern during a VMAT arc.

186

6.3 Conclusions

Overall, this thesis has demonstrated the advantages of the VOI approach for IGRT. In general, VOI offers improved image quality with localized and reduced imaging dose. Specifically, **the advantageous are**:

For CBCT

- Simulated SPR was decreased by a factor of 8.9 when decreasing iris diameter from 21.2 cm to 2.4 cm (defined at isocentre) for a uniform cylindrical water phantom.

- Imaging dose is both reduced and localized to the VOI as field size decreases. For example, a VOI with a diameter of 4.4 cm centered on isocentre has a dose reduction to 55% and 4% of the full field value inside and outside the VOI, respectively. Maximum dose reductions occur superior or inferior to the VOI and can be reduced to less than 1% of the full field value.

- The reduction in dose to the VOI as aperture size decreased allowed for further improvement in image CNR. This was accomplished by maintaining equal dose to the VOI for each aperture size investigated. Using this approach, CNR can be improved up to a factor of 2.2 when decreasing from an 18x18 cm^2 to a 2x2 cm^2 aperture (defined at isocentre).

- Image CNR is further enhanced by a factor of 1.2 when TCM is utilized compared to an unmodulated acquisition for equal imaging dose.

Alternatively, image CNR can be maintained for a reduced imaging dose compared to an unmodulated acquisition.

For intrafraction monitoring

- Fiducial markers can be detected accurately using a VOI conforming to a single or several fiducial markers. This reduces the integral imaging dose by a factor of 15.6 and 3.7 for a VOI conformal to a single or several fiducial markers, respectively, compared to a conventional 6x6 cm^2 field.

- TCM can be applied to offset the effects of kV attenuation thereby maintaining accuracy of fiducial detection compared to an unmodulated acquisition, especially for scenarios with poor imaging conditions.

- MV scatter is greatest for lateral beams and can vary by a factor of 1.8 throughout the gantry rotation for a static field in the phantom investigated. The highest MV scatter occurs during a period of lowest kV attenuation and if included in TCM it would set the lower bound for modulation.

The disadvantages are:

For CBCT

- In the reconstruction method used all information outside the VOI is discarded. This could lead to a scenario in which mis-alignment could occur when using a VOI, if the anatomy outside the VOI is relevant. A solution could be to implement a nested VOI approach similar to that described by Leary and Robar[18] and Lu *et al.*[116].

- As illustrated in 6.2.3, the extrapolation approach used at the VOI boundary may not be sufficient for all VOI placement within a given anatomy. This can result in truncation induced cupping when the VOI boundary is positioned on a sharp attenuation gradient. This requires further investigation using synthetic phantoms, or to established guidelines when implementing the VOI approach for anatomical site. Also, any possible effects could be minimized when implementing a nested VOI approach.

For intrafraction monitoring

- A dosimetric trade-off is required when implementing TCM. At least for the patient geometries examined herein, for equal integral mAs, the use of TCM increases the maximum dose to the lateral regions of the pelvis up to a factor of 5.5 compared to an unmodulated acquisition. However, little variation in integral dose is observed. In practice the integral dose for TCM

acquisition would not be equal to an unmodulated acquisition. For an

unmodulated acquisition, the mAs per projection would be set for the

greatest kV attenuation. Whereas for TCM acquisition, this mAs would set

the upper bound for modulation, with the lower bound set for MV scatter,

thereby giving a lower integral dose.

These improvements are realized without substantial changes in system design. Although

a novel prototype dynamic iris or blade kV collimator were used, the latter is close in

design to that used commercially, and TCM acquisition is already permitted by the

TrueBeam linear accelerator platform, albeit through Developer Mode.

REFERENCES

1   Statistics Canada, *Table 102-0561: Leading causes of death, total population, by age group and sex, Canada* (2015).

2   Canadian Cancer Society, Statistics Canada, Public Health Agency of Canada, and Provincial/Territorial Cancer Registries, *Canadian cancer statistics 2015* (2015).

3   B.W. Stewart and C.P. Wild, *World cancer report 2014* (Lyon, France, 2014).

4   E.J. Hall and A.J. Giaccia, *Radiobiology for the Radiologist*, 7th ed. (Wolters Kluwer Health/Lippincott Williams & Wilkins, Philadelphia, PA, 2012).

5   International Atomic Energy Agency, *Inequity in cancer care: A global perspective* (Vienna, Austria, 2011).

6   M.B. Barton *et al.*, "Estimating the demand for radiotherapy from the evidence: A review of changes from 2003 to 2012," Radiother. Oncol. **112**(1), 140–144 (2014).

7   D.A. Jaffray, D.G. Drake, M. Moreau, A.A. Martinez, and J.W. Wong, "A radiographic and tomographic imaging system integrated into a medical linear accelerator for localization of bone and soft-tissue targets," Int. J. Radiat. Oncol. Biol. Phys. **45**(3), 773–89 (1999).

8   J.H. Siewerdsen and D.A. Jaffray, "Cone-beam computed tomography with a flat-panel imager: Magnitude and effects of x-ray scatter," Med. Phys. **28**(2), 220–231 (2001).

9   G.H. Glover, "Compton scatter effects in CT reconstructions," Med. Phys. **9**(6), 860–7 (1982).

10   W. Zhao, D. Vernekohl, J. Zhu, L. Wang, and L. Xing, "A model-based scatter artifacts correction for cone beam CT," Med. Phys. **43**(4), 1736–1753 (2016).

[11] J.T. Bushberg, J.A. Seibert, E.M. Leidholdt, and J.M. Boone, *The Essential Physics of Medical Imaging*, 3rd ed. (Lippincott Williams & Wilkins, Philadelphia, PA, 2011).

[12] L. Chen *et al.*, "Feasibility of volume-of-interest (VOI) scanning technique in cone beam breast CT—a preliminary study," Med. Phys. **35**(8), 3482–3490 (2008).

[13] C.-J. Lai *et al.*, "Reduction in x-ray scatter and radiation dose for volume-of-interest (VOI) cone-beam breast CT—a phantom study," Phys. Med. Biol. **54**(21), 6691–6709 (2009).

[14] D. Kolditz, Y. Kyriakou, and W.A. Kalender, "Volume-of-interest (VOI) imaging in C-arm flat-detector CT for high image quality at reduced dose," Med. Phys. **37**(6), 2719–2730 (2010).

[15] S. Cho, E. Pearson, C.A. Pelizzari, and X. Pan, "Region-of-interest image reconstruction with intensity weighting in circular cone-beam CT for image-guided radiation therapy," Med. Phys. **36**(4), 1184–92 (2009).

[16] J.L. Robar, D. Parsons, A. Berman, and A. Macdonald, "Volume-of-interest cone-beam CT using a 2.35 MV beam generated with a carbon target," Med. Phys. **39**(7), 4209–4218 (2012).

[17] D. Parsons and J.L. Robar, "Beam generation and planar imaging at energies below 2.40 MeV with carbon and aluminum linear accelerator targets," Med. Phys. **39**(7), 4568–4578 (2012).

[18] D. Leary and J.L. Robar, "CBCT with specification of imaging dose and CNR by anatomical volume of interest," Med. Phys. **41**(1), 11909 (2014).

[19] T. Szczykutowicz, J. Hermus, M. Geurts, and J. Smilowitz, "Realization of fluence field modulated CT on a clinical tomotherapy megavoltage CT system," Phys. Med. Biol. **60**(18), 7245–57 (2015).

[20] S. Bartolac, S. Graham, J. Siewerdsen, and D. Jaffray, "Fluence field optimization for noise and dose objectives in CT," Med. Phys. **38**(7), S2–S17 (2011).

21 T.P. Szczykutowicz and C.A. Mistretta, "Design of a digital beam attenuation system for computed tomography: Part I. System design and simulation framework," Med. Phys. **40**(2), 21905 (2013).

22 T.P. Szczykutowicz and C.A. Mistretta, "Experimental realization of fluence field modulated CT using digital beam attenuation," Phys. Med. Biol. **59**(5), 1305–1326 (2014).

23 T.P. Szczykutowicz and C.A. Mistretta, "Design of a digital beam attenuation system for computed tomography. Part II. Performance study and initial results," Med. Phys. **40**(2), 21906 (2013).

24 S.S. Hsieh, D. Fleischmann, and N.J. Pelc, "Dose reduction using a dynamic, piecewise-linear attenuator," Med. Phys. **41**(2), 21910 (2014).

25 S.S. Hsieh and N.J. Pelc, "The feasibility of a piecewise-linear dynamic bowtie filter," Med. Phys. **40**(3), 31910 (2013).

26 H. Greess *et al.*, "Dose reduction in computed tomography by attenuation-based on-line modulation of tube current: evaluation of six anatomical regions," Eur. Radiol. **10**(2), 391–394 (2000).

27 M. Gies, W.A. Kalender, H. Wolf, C. Suess, and M.T. Madsen, "Dose reduction in CT by anatomically adapted tube current modulation. I. Simulation studies," Med. Phys. **26**(11), 2235–47 (1999).

28 W.A. Kalender, H. Wolf, C. Suess, M. Gies, H. Greess, and W.A. Bautz, "Dose reduction in CT by on-line tube current control: Principles and validation on phantoms and cadavers," Eur. Radiol. **9**, 323–8 (1999).

29 W.A. Kalender, H. Wolf, and C. Suess, "Dose reduction in CT by anatomically adapted tube current modulation. II. Phantom measurements," Med. Phys. **26**(11), 2248–53 (1999).

30   J. Hsieh, *Computed Tomography: Principles, Design, Artifacts, and Recent Advances*, 2nd ed. (SPIE Press, Bellingham, WA, 2010).

31   C.E. DeSantis *et al.*, "Cancer Treatment and Survivorship Statistics, 2014," CA Cancer J Clin **64**, 252–271 (2014).

32   T.M. Pisansky *et al.*, "Clinical Outcomes and Prognostic Factors in 4839 Patients Treated with External Radiotherapy for Stage T1-T2 Prostate Cancer," Int. J. Radiat. Oncol. Biol. Phys. **60**(S1), S167 (2004).

33   M.J. Zelefsky *et al.*, "High-dose intensity modulated radiation therapy for prostate cancer: Early toxicity and biochemical outcome in 772 patients," Int. J. Radiat. Oncol. Biol. Phys. **53**(5), 1111–1116 (2002).

34   T.-J. Tan, S. Siva, F. Foroudi, and S. Gill, "Stereotactic body radiotherapy for primary prostate cancer: A systematic review," J. Med. Imaging Radiat. Oncol. **58**(5), 601–11 (2014).

35   S.M. Bentzen and M.A. Ritter, "The alpha/beta ratio for prostate cancer: What is it, really?," Radiother. Oncol. **76**(1), 1–3 (2005).

36   X. Tong *et al.*, "Intrafractional prostate motion during external beam radiotherapy monitored by a real-time target localization system," J. Appl. Clin. Med. Phys. **16**(2), 5013 (2015).

37   K.M. Langen *et al.*, "Observations on real-time prostate gland motion using electromagnetic tracking," Int. J. Radiat. Oncol. Biol. Phys. **71**(4), 1084–90 (2008).

38   J.A. Ng *et al.*, "Kilovoltage intrafraction monitoring for prostate intensity modulated arc therapy: First clinical results," Int. J. Radiat. Oncol. Biol. Phys. **84**(5), 655–661 (2012).

39   C.I. Tang *et al.*, "Phase I/II study of a five-fraction hypofractionated accelerated radiotherapy treatment for low-risk localised prostate cancer: Early results of pHART3," Clin. Oncol. **20**(10), 729–737 (2008).

40   H.C. Quon *et al.*, "Dose-escalated stereotactic body radiation therapy for prostate cancer: Quality-of-life comparison of two prospective trials," Front. Oncol. **6**, 185 (2016).

41   H.B. Musunuru *et al.*, "Dose-escalation of five-fraction SABR in prostate cancer: Toxicity comparison of two prospective trials," Radiother. Oncol. **118**(1), 112–117 (2016).

42   A.J. Katz and J. Kang, "Stereotactic body radiotherapy as treatment for organ confined low- and intermediate-risk prostate carcinoma, a 7-year study," Front. Oncol. **4**, 240 (2014).

43   C.R. King, J.D. Brooks, H. Gill, and J.C. Presti, "Long-term outcomes from a prospective trial of stereotactic body radiotherapy for low-risk prostate cancer," Int. J. Radiat. Oncol. Biol. Phys. **82**(2), 877–882 (2012).

44   G. Bolzicco, M.S. Favretto, N. Satariano, E. Scremin, C. Tambone, and A. Tasca, "A single-center study of 100 consecutive patients with localized prostate cancer treated with stereotactic body radiotherapy," BMC Urol. **13**(1), 1 (2013).

45   L.N. Chen *et al.*, "Patient-reported urinary incontinence following stereotactic body radiation therapy (SBRT) for clinically localized prostate cancer," Radiat. Oncol. **9**(1), 148 (2014).

46   R. Hannan *et al.*, "Stereotactic body radiation therapy for low and intermediate risk prostate cancer-Results from a multi-institutional clinical trial," Eur. J. Cancer **59**, 142–151 (2016).

47   C. Oliai *et al.*, "Stereotactic body radiation therapy for the primary treatment of localized prostate cancer," J. Radiat. Oncol. **2**(1), 63–70 (2013).

48   S.M. McBride *et al.*, "Hypofractionated stereotactic body radiotherapy in low-risk prostate adenocarcinoma: Preliminary results of a multi-institutional phase 1 feasibility trial," Cancer **118**(15), 3681–3690 (2012).

49 H.B. Musunuru *et al.*, "Predictive parameters of symptomatic hematochezia following 5-fraction gantry-based SABR in prostate cancer," Int. J. Radiat. Oncol. Biol. Phys. **94**(5), 1043–1051 (2016).

50 L.N. Chen *et al.*, "Stereotactic body radiation therapy (SBRT) for clinically localized prostate cancer: The Georgetown University experience," Radiat. Oncol. **8**(1), 58–68 (2013).

51 J.W. Lischalk, I.D. Kaplan, and S.P. Collins, "Stereotactic body radiation therapy for localized prostate cancer," Cancer J. **22**(4), 307–313 (2016).

52 C.R. King, J.D. Brooks, H. Gill, T. Pawlicki, C. Cotrutz, and J.C. Presti, "Stereotactic Body Radiotherapy for Localized Prostate Cancer: Interim Results of a Prospective Phase II Clinical Trial," Int. J. Radiat. Oncol. Biol. Phys. **73**(4), 1043–1048 (2009).

53 E. Colvill *et al.*, "DMLC tracking and gating can improve dose coverage for prostate VMAT," Med. Phys. **41**(9), 91705 (2014).

54 Q.J. Wu, T. Li, L. Yuan, F.-F. Yin, and W.R. Lee, "Single institution's dosimetry and IGRT analysis of prostate SBRT," Radiat. Oncol. **8**(1), 215 (2013).

55 A. Sawant *et al.*, "Toward submillimeter accuracy in the management of intrafraction motion: The integration of real-time internal position monitoring and multileaf collimator target tracking," Int. J. Radiat. Oncol. Biol. Phys. **74**(2), 575–582 (2009).

56 T.P. Mate, D. Krag, J.N. Wright, and S. Dimmer, "A new system to perform continuous target tracking for radiation and surgery using non-ionizing alternating current electromagnetics," Int. Congr. Ser. **1268**, 425–430 (2004).

57 R.D. Wiersma, W. Mao, and L. Xing, "Combined kV and MV imaging for real-time tracking of implanted fiducial markers," Med. Phys. **35**(4), 1191–1198 (2008).

58   M.T.R. Stevens, D. Parsons, and J.L. Robar, "Continuous monitoring of prostate position using stereoscopic and monoscopic kV image guidance Continuous monitoring of prostate position using stereoscopic and monoscopic kV image guidance," Med. Phys. **35**(5), 2558–68 (2016).

59   M.S. Hoogeman, J.J. Nuyttens, P.C. Levendag, and B.J.M. Heijmen, "Time dependence of intrafraction patient motion assessed by repeat stereoscopic imaging," Int. J. Radiat. Oncol. Biol. Phys. **70**(2), 609–618 (2008).

60   P.R. Poulsen, B. Cho, K. Langen, P. Kupelian, and P.J. Keall, "Three-dimensional prostate position estimation with a single x-ray imager utilizing the spatial probability density," Phys. Med. Biol. **53**(16), 4331–4353 (2008).

61   P.J. Keall *et al.*, "EP-1490: Accuracy results from the first clinical trial of a new real-time IGRT system, Kilovoltage Intrafraction Monitoring," Radiother. Oncol. **115**(S1), S810 (2015).

62   C. Ling *et al.*, "Acquisition of MV-scatter-free kilovoltage CBCT images during RapidArc™ or VMAT," Radiother. Oncol. **100**(1), 145–149 (2011).

63   M. van Herk, L. Ploeger, and J.-J. Sonke, "A novel method for megavoltage scatter correction in cone-beam CT acquired concurrent with rotational irradiation," Radiother. Oncol. **100**(3), 365–369 (2011).

64   J.K. Crocker, J.A. Ng, P.J. Keall, and J.T. Booth, "Measurement of patient imaging dose for real-time kilovoltage x-ray intrafraction tumour position monitoring in prostate patients," Phys. Med. Biol. **57**(10), 2969–2980 (2012).

65   Canadian Institute For Health Information, *Medical Imaging in Canada 2012* (2013).

66   A.C. Kak and M. Slaney, *Principles of Computerized Tomographic Imaging* (IEEE Press, 1988).

67   T.M. Buzug, *Computed Tomography: From Photon Statistics to Modern Cone-Beam CT*, 1st ed. (Springer-Verlag, Berlin, Germany, 2008).

68   L. Feldkamp, L. Davis, and J. Kress, "Practical cone-beam algorithm," JOSA A **1**(6), 612–9 (1984).

69   D.L. Parker, "Optimal short scan convolution reconstruction for fanbeam CT," Med. Phys. **9**(2), 254–257 (1982).

70   General Electric Healthcare, *LightSpeed Series Learning and Reference Guide* (GE Healtcare, Little Chalfont, UK, 2007).

71   J. Haaga, F. Miraldi, W. MacIntyre, J. LiPuma, P. Bryan, and E. Wiesen, "The effect of mAs variation upon computed tomography image quality as evaluated by in vivo and in vitro studies," Radiology **138**(2), 449–54 (1981).

72   R.L. Siddon, "Fast calculation of the exact radiological path for a three-dimensional CT array," Med. Phys. **12**(2), 252–5 (1985).

73   P. Mayles, A. Nahum, and J.C. Rosenwald (eds.), *Handbook of Radiotherapy Physics: Theory and Practice*, 1st ed. (CRC Press, Boca Raton, FL, USA).

74   R.L. Ford and W.R. Nelson, *The EGS code system: Computer programs for the Monte Carlo simulation of electromagnetic cascade showers*, 3rd ed. (SLAC, La Joila, CA, 1978).

75   I. Kawrakow, E. Mainegra-Hing, D.W.O. Rogers, F. Tessier, and B.R.B. Walters, *The EGSnrc Code System: Monte Carlo Simulation of Electron and Photon Transport NRCC Report PIRS-701* (NRC, Ottawa, Canada, 2011).

76   D.W. Rogers, B.A. Faddegon, G.X. Ding, C.M. Ma, J. We, and T.R. Mackie, "BEAM: a Monte Carlo code to simulate radiotherapy treatment units," Med. Phys. **22**(5), 503–524 (1995).

77   I. Kawrakow, "Accurate condensed history Monte Carlo simulation of electron transport. I. EGSnrc, the new EGS4 version," Med. Phys. **27**(3), 485–498 (2000).

78   I. Kawrakow, M. Fippel, and K. Friedrich, "3D electron dose calculation using a voxel based Monte Carlo algorithm (VMC)," Med Phys **23**(4), 445–57 (1996).

79   B. Walters, I. Kawrakow, and D.W.O. Rogers, *DOSXYZnrc Users Manual* (Ottawa, Canada, 2011).

80   J. Lobo and I.A. Popescu, "Two new DOSXYZnrc sources for 4D Monte Carlo simulations of continuously variable beam configurations, with applications to RapidArc, VMAT, TomoTherapy and CyberKnife," Phys. Med. Biol. **55**(16), 4431–4443 (2010).

81   D.A. Jaffray, J.H. Siewerdsen, J.W. Wong, and A.A. Martinez, "Flat-panel cone-beam computed tomography for image-guided radiation therapy," Int. J. Radiat. Oncol. Biol. Phys. **53**(5), 1337–1349 (2002).

82   American College of Radiology, *Image Wisely*, (2014).

83   The Alliance for Radiation Safety in Pediatric Imaging, *Image Gently*, (2014).

84   M.J. Murphy *et al.*, "The management of imaging dose during image-guided radiotherapy: Report of the AAPM Task Group 75," Med. Phys. **34**(10), 4041–4063 (2007).

85   E.E. Graves *et al.*, "Design and evaluation of a variable aperture collimator for conformal radiotherapy of small animals using a microCT scanner," Med. Phys. **34**(11), 4359–4367 (2007).

86   A.O. Macdonald, Investigation of volume-of-interest megavoltage cone-beam computed tomography (MSc Thesis, Dalhousie University, 2010).

87   L. Yu, Y. Zou, E.Y. Sidky, C.A. Pelizzari, P. Munro, and X. Pan, "Region of interest reconstruction from truncated data in circular cone-beam CT," IEEE Trans. Med. Imaging **25**(7), 869–881 (2006).

88   D.J. Kadrmas, R.J. Jaszczak, J.W. McCormick, R.E. Coleman, and C.B. Lim, "Truncation artifact reduction in transmission CT for improved SPECT attenuation compensation," Phys. Med. Biol. **40**(6), 1085–1104 (1995).

89   G.X. Ding, D.M. Duggan, and C.W. Coffey, "Characteristics of kilovoltage x-ray beams used for cone-beam computed tomography in radiation therapy," Phys. Med. Biol. **52**(6), 1595–1615 (2007).

90   C.M. Ma *et al.*, "AAPM protocol for 40–300 kV x-ray beam dosimetry in radiotherapy and radiobiology," Med. Phys. **28**(6), 868–893 (2001).

91   F.M. Khan, *The Physics of Radiation Therapy*, 3rd Ed. (Lippincott Williams & Wilkins, Philadelphia, PA, 2003).

92   D.A. Jaffray and J.H. Siewerdsen, "Cone-beam computed tomography with a flat-panel imager: Initial performance characterization," Med. Phys. **27**(6), 1311–1323 (2000).

93   D. Parsons and J.L. Robar, "An investigation of kV CBCT image quality and dose reduction for volume-of-interest imaging using dynamic collimation," Med. Phys. **42**(9), 5258–5269 (2015).

94   GE Medical Systems (ed.), *CT Hispeed Advantage RP System*, 15th ed. (GE Technical Publications, 1994).

95   E.M. Hsiao, F.J. Rybicki, and M. Steigner, "CT coronary angiography: 256-slice and 320-detector row scanners," Curr. Cardiol. Rep. **12**(1), 68–75 (2010).

96   D. Heuscher and F. Noo, "CT dose reduction using dynamic collimation," in *2nd Int. Conf. Image Form. X-ray Comput. Tomogr.*(2012), pp. 115–8.

97   International Commission of Radiation Units and Measurements, *Tissue substitutes in radiation dosimetry and measurement ICRU Report 44* (International Commission on Radiation Units and Measurements, Bethesda, MD, 1989).

98   J.H. Hubbell and S.M. Seltzer, *Report No. NISTIR 5632: Tables of x-ray mass attenuation coefficients and mass energy-absorption coefficients 1 keV to 20 MeV for elements Z=1 to 92 and 48 additional substances of dosimetric interest* (National Institute of Standards and Technology, Gaithersburg, MD, 1995).

99   C.M. Ma and D.W.O. Rogers, *BEAMdp Users Manual NRCC Report PIRS-0509(C)revA* (NRCC, Ottawa, Canada, 2009).

100   X. Jia, H. Yan, L. Cerviño, M. Folkerts, and S.B. Jiang, "A GPU tool for efficient, accurate, and realistic simulation of cone beam CT projections," Med. Phys. **39**(12), 7368–78 (2012).

101   J.B. Yu, L.D. Cramer, J. Herrin, P.R. Soulos, A.L. Potosky, and C.P. Gross, "Stereotactic body radiation therapy versus intensity-modulated radiation therapy for prostate cancer: Comparison of toxicity," J. Clin. Oncol. **32**(12), 1195–1201 (2014).

102   F. Alongi *et al.*, "Linac based SBRT for prostate cancer in 5 fractions with VMAT and flattening filter free beams: Preliminary report of a phase II study," Radiat. Oncol. **8**(8), 171–179 (2013).

103   S. Jabbari *et al.*, "Stereotactic body radiotherapy as monotherapy or post-external beam radiotherapy boost for prostate cancer: Technique, early toxicity, and PSA response," Int. J. Radiat. Oncol. Biol. Phys. **82**(1), 228–234 (2012).

104   D. Parsons and J.L. Robar, "Volume of interest CBCT and tube current modulation for image guidance using dynamic kV collimation," Med. Phys. **43**(4), 1808–17 (2016).

105   L. Ren, Y. Zhang, and F.-F. Yin, "A limited-angle intrafraction verification (LIVE) system for radiation therapy," Med. Phys. **41**(2), 20701 (2014).

[106]   M.K.K. Leung, J.C.L. Chow, B.D. Chithrani, M.J.G. Lee, B. Oms, and D.A. Jaffray, "Irradiation of gold nanoparticles by x-rays: Monte Carlo simulation of dose enhancements and the spatial properties of the secondary electrons production," Med. Phys. **38**(2), 624 (2011).

[107]   P.R. Poulsen, B. Cho, A. Sawant, and P.J. Keall, "Implementation of a new method for dynamic multileaf collimator tracking of prostate motion in arc radiotherapy using a single kV imager," Int. J. Radiat. Oncol. Biol. Phys. **76**(3), 914–23 (2010).

[108]   P. Mishra, J. Lewis, T. Etmektzoglou, and M. Svatos, "TH-C-12A-12: Veritas: An open source tool to facilitate user interaction with TrueBeam Developer Mode," Med. Phys. **41**(6), 563 (2014).

[109]   D. Parsons, J.L. Robar, and D. Sawkey, "A Monte Carlo investigation of low-Z target image quality generated in a linear accelerator using Varian's VirtuaLinac," Med. Phys. **41**(2), 21719 (2014).

[110]   G. Asuni, T.A. van Beek, S. Venkataraman, I.A. Popescu, and B.M.C. McCurdy, "A Monte Carlo tool for evaluating VMAT and DIMRT treatment deliveries including planar detectors," Phys. Med. Biol. **58**(11), 3535–50 (2013).

[111]   D.A. Roberts, V.N. Hansen, A.C. Niven, M.G. Thompson, J. Seco, and P.M. Evans, "A low Z linac and flat panel imager: comparison with the conventional imaging approach," Phys. Med. Biol. **53**(22), 6305–6319 (2008).

[112]   B.A. Faddegon, V. Wu, J. Pouliot, B. Gangadharan, and A. Bani-Hashemi, "Low dose megavoltage cone beam computed tomography with an unflattened 4 MV beam from a carbon target," Med. Phys. **35**(12), 5777–5786 (2008).

[113]   C.Y. Huang, J.N. Tehrani, J.A. Ng, J. Booth, and P. Keall, "Six degrees-of-freedom prostate and lung tumor motion measurements using kilovoltage intrafraction monitoring," Int. J. Radiat. Oncol. Biol. Phys. **91**(2), 368–375 (2015).

[114]   E. Dabrowska, B. Brzozowska, B. Chaber, P. Kukolowicz, J. Starzynski, and A. Zawadzka, "EP-1501: Influence of prostate rotation on dose distribution in the target volume," Radiother. Oncol. **115**(S1), S817–S818 (2015).

[115] S. Ipsen, R. Bruder, R. O'Brien, P.J. Keall, A. Schweikard, and P.R. Poulsen, "Online 4D ultrasound guidance for real-time motion compensation by MLC tracking," Med. Phys. **43**(10), 5695–5704 (2016).

[116] W. Lu *et al.*, "Reconstructing cone-beam CT with spatially varying qualities for adaptive radiotherapy: a proof-of-principle study," Phys. Med. Biol. **59**(20), 6251 (2014).

[117] E.B. Claus, L. Calvocoressi, M.L. Bondy, and J.M. Schildkraut, "Dental X-Rays and Risk of Meningioma," Cancer **118**(18), 4530–4537 (2012).

[118] Health Canada, *Radiation Protection in Dentistry - Recommended Safety Procedures for the Use of Dental X-Ray Equipment - Safety Code 30* (Ottawa, Canada, 2000).

[119] National Council on Radiation Protection and Measurements, *Ionizing radiation exposure of the population of the United States* (Bethesda, MD, 2009).

APPENDIX A   COPYRIGHT PERMISSION

A.1   PERMISSION FOR: AN INVESTIGATION OF KV CBCT IMAGE QUALITY AND DOSE REDUCTION FOR

VOLUME-OF-INTEREST IMAGING USING DYNAMIC COLLIMATION

Halifax, NS B3H 1V7
Canada
Attn: David Parsons

Publisher Tax ID	EU826007151
Billing Type	Invoice
Billing Address	David Parsons
	Dalhousie University
	Dept of Physics and Atmospheric Science
	5820 University Avenue
	Halifax, NS B3H 1V7
	Canada
	Attn: David Parsons
Total	0.00 CAD

JOHN WILEY AND SONS LICENSE
TERMS AND CONDITIONS

Mar 01, 2017

This Agreement between David Parsons ("You") and John Wiley and Sons ("John Wiley and Sons") consists of your license details and the terms and conditions provided by John Wiley and Sons and Copyright Clearance Center.

License Number	4060310595426
License date	March 1, 2017
Licensed Content Publisher	John Wiley and Sons
Licensed Content Publication	Medical Physics
Licensed Content Title	Volume of interest CBCT and tube current modulation for image guidance using dynamic kV collimation
Licensed Content Author	David Parsons, James L. Robar
Licensed Content Date	Nov 30, 2016
Licensed Content Pages	10
Type of use	Dissertation/Thesis
Requestor type	Author of this Wiley article
Format	Print and electronic
Portion	Full article
Will you be translating?	No
Title of your thesis / dissertation	Volume of interest imaging for image guided radiotherapy
Expected completion date	Apr 2017
Expected size (number of pages)	210
Requestor Location	David Parsons Dalhousie University Dept of Physics and Atmospheric Science 5820 University Avenue Halifax, NS B3H 1V7 Canada Attn: David Parsons

Publisher Tax ID   EU826007151

Billing Type   Invoice

Billing Address   David Parsons
                          Dalhousie University
                          Dept of Physics and Atmospheric Science
                          5820 University Avenue
                          Halifax, NS B3H 1V7
                          Canada
                          Attn: David Parsons

Total   0.00 CAD

JOHN WILEY AND SONS LICENSE
TERMS AND CONDITIONS

Apr 20, 2017

This Agreement between David Parsons ("You") and John Wiley and Sons ("John Wiley and Sons") consists of your license details and the terms and conditions provided by John Wiley and Sons and Copyright Clearance Center.

License Number	4093111427973
License date	Apr 20, 2017
Licensed Content Publisher	John Wiley and Sons
Licensed Content Publication	Medical Physics
Licensed Content Title	Current modulated volume-of-interest imaging for kilovoltage intrafaction monitoring of the prostate
Licensed Content Author	David Parsons, M. Tynan R. Stevens, James L. Robar
Licensed Content Date	Mar 22, 2017
Licensed Content Pages	15
Type of use	Dissertation/Thesis
Requestor type	Author of this Wiley article
Format	Print and electronic
Portion	Full article
Will you be translating?	No
Title of your thesis / dissertation	Volume of interest imaging for image guided radiotherapy
Expected completion date	Apr 2017
Expected size (number of pages)	210
Requestor Location	David Parsons Dalhousie University Dept of Physics and Atmospheric Science 5820 University Avenue Halifax, NS B3H 1V7 Canada Attn: David Parsons

Publisher Tax ID   EU826007151

Billing Type   Invoice

Billing Address   David Parsons
                          Dalhousie University
                          Dept of Physics and Atmospheric Science
                          5820 University Avenue
                          Halifax, NS B3H 1V7
                          Canada
                          Attn: David Parsons

Total   0.00 CAD